A N N U A L R E P O R T

2015

and list of publications

Bayerisches Forschungsinstitut
für Experimentelle Geochemie und Geophysik
Universität Bayreuth

Bayerisches Geoinstitut
Universität Bayreuth
D-95440 Bayreuth
Germany

Telephone: +49-(0)921-55-3700
Telefax: +49-(0)921-55-3769
e-mail: bayerisches.geoinstitut@uni-bayreuth.de
www: http://www.bgi.uni-bayreuth.de

Editorial compilation by: Stefan Keyssner and Petra Buchert
Section editors: Andreas Audétat, Tiziana Boffa Ballaran, Leonid Dubrovinsky, Dan Frost, Gregor Golabek, Tomoo Katsura, Takaaki Kawazoe, Hans Keppler, Hauke Marquardt, Katharina Marquardt, Catherine McCammon, Nobuyoshi Miyajima, Dave Rubie, Gerd Steinle-Neumann

Staff and guests of the Bayerisches Geoinstitut in **July 2015**:

Die Mitarbeiter und Gäste des Bayerischen Geoinstituts im **Juli 2015**:

First row, from left (1. Reihe, v. links) Ahmed El Goresy, Ananya Mallik, Leyla Ismailova, Michelle Wenz, Andrea Adams, Rong Huang

Second row, from left (2. Reihe, v. links) Gertrud Gollner, Stella Chariton, Anna Pakhomova, Joanna Emilien, Catherine McCammon, Kirsten Schulze, Nicki Siersch, Zsanett Pintér, Elena Bykova, Lanlan Shi, Anke Potzel

Third row, from left (3. Reihe, v. links) Stefan Keyssner, Nicole Fischer, Caroline Bollinger, Christopher Beyer, Takayuki Ishii, Sven Linhardt, Holger Kriegl, Vera Laurenz, Jellie de Vries, Robert Arato

Fourth row, from left (4. Reihe, v. links) Maxim Bykov, Katherine Armstrong, Dan Frost, Fanny Sorbadere, Florian Heidelbach, Gerd Ramming, Yang Li, Leonid Dubrovinsky, Daohan Zhang, Fabian Wagle, Ulrike Trenz

Fifth row, from left (5. Reihe, v. links) Robert Myhill, Stephan Blaha, Anja Rosenthal, Ryosuke Sinmyo, Katharina Marquardt, Tomoo Katsura, Oliver Rausch, Stefan Übelhack, Takahiro Yoshioka, Lydia Kison-Herzing

Sixth row, from left (6. Reihe v. links) Nobuyoshi Miyajima, Takaaki Kawazoe, Robert Farla, Hans Keppler, Sergey Ovsyannikov, Mickaël Laumonier, Enrico Bruschini, Hauke Marquardt, Gerd Steinle-Neumann

Seventh row, from left (7. Reihe v. links) Steven Jacobsen, Ulrich Böhm, Svyatoslav Shcheka, Haihao Guo, Dmitry Druzhbin, Alok Chaudhari, Matteo Masotta, Alexander Kurnosov

Absent (Es fehlten) Andreas Audétat, Tiziana Boffa Ballaran, Johannes Buchen, Petra Buchert, Thomas Chust, Heinz Fischer, Gregor Golabek, Kurt Klasinski, Detlef Krauße, Raphael Njul, Sylvain Petitgirard, Esther Posner, Dave Rubie, Romina Scharfenberg, Hubert Schulze, Vojtech Vlcek, Nico Walte, Lin Wang

Contents

Foreword

In the 29th Annual Report of the Bayerisches Geoinstitut we present the research activities of the institute over the past year in its efforts to understand processes occurring within the Earth and other planets. The research projects described in these pages are diverse in many aspects. They range in scale, for example, from studies of the atomic imperfections within mineral structures that allow them to deform and flow within the Earth, to those that simulate collisions between planet-sized objects that have consequences for the formation of planetary atmospheres. In this, as in previous years, these research objectives have been mainly achieved through experiments performed at the elevated pressures and temperatures of planetary interiors. However, these are increasingly being supported by computer simulations of processes occurring at various scales. In this respect we were very pleased at the beginning of the year to welcome Gregor Golabek from ETH Zurich to the institute, who accepted the Professorship in Geodynamic Modelling. Dynamic models that track the flow of heat and mass within the Earth and planets are able to explore the influence of mineral and rock properties on the development of planetary structure. Professor Golabek's work, therefore, allows the consequences of properties determined in the laboratory to be realized at the planetary scale.

2015 saw a record number of employees at the institute reflecting in turn considerable success in the attainment of external funding. These numbers are set to rise further next year because the institute has obtained funding for an ‚International Research and Training Group' from the DFG. This graduate school, which is a collaboration with the Department of Earth Sciences at Tohoku University in Sendai, Japan, will start in 2016 and fund 12 PhD positions over the next 4.5 years. Students will study aspects of the deep cycling of volatile elements through the interior of the Earth. The aim will be to quantify how volatile elements, principally carbon, hydrogen and nitrogen, are transported, stored and expelled from the interior. As part of their studies students will spend 6 to 12 months performing research at Tohoku University and we look forward to also welcoming exchange students from Tohoku University to Bayreuth over the next years. Professor Ohtani of Tohoku University is an internationally recognized leader in high pressure research and has been a long term BGI collaborator since his time as a guest professor here in 1995. At Tohoku University, however, students will be exposed to a broader range of disciplines within fields such as geochemistry, volcanology and geophysics, where the study of Earth's volatiles is also of major interest.

As in previous years, many of the projects described in the Annual Report were only made possible as a result of innovative developments in experimental methods. Projects in the Methodological Developments section (3.8) of the Annual report are of interest in this respect as they often form the basis for studies reported in subsequent yearbooks. Over the last years a series of developments have been reported concerning a double stage diamond anvil cell design, in which extreme pressures are obtained by compressing an inner stage of opposing diamond spheres. In the past year results obtained with this device were published in the journal Nature, where the compression of the metal osmium was reported to over 7.5 megabars, a current world record in static pressure attainment. Anomalies in the unit cell parameters during this compression implicate the involvement of inner electrons of the

osmium atom, which under normal conditions would play no role in atomic bonding. Pressure therefore provides a tool to probe the fundamental electronic structure of materials. Further developments of this technique reported in this yearbook indicate that pressures near to 10 megabars may have been reached. The main problem that arises now is that currently there is no accurate method for measuring pressures at these highly extreme conditions.

A further notable study reported in this yearbook employs the absorption of X-rays to probe the density of quenched silicate melts in a diamond anvil cell at conditions compatible with the core-mantle boundary. The results provide the first convincing evidence that the density of a silicate magma at the base of the mantle would be greater than that of the minerals crystallizing from it. Models for the formation of the Earth predict that the entire mantle likely melted at various times as a result of giant impacts. This study implies that rather than such a magma ocean crystallizing from the base upwards, flotation of crystallizing minerals may have caused a long term magma ocean to persist at the base of the mantle. This could explain geophysical anomalies that can still be detected in this region of the mantle and might also explain geochemical signatures interpreted to arise from an early formed reservoir that may still be enriched in volatile and radiogenic elements today.

Towards the end of the year I received the surprising but tremendous news that I would receive the Gottfried Wilhelm Leibniz Prize of the DFG in 2016. It is indeed quite outstanding that 4 members of the BGI leadership have now been Leibniz Prize winners. As a long term BGI member I have benefited greatly from the remarkable culture and atmosphere of the institute that has been fostered and maintained by the leadership over many years. I take this opportunity to also emphasize the role of present and past colleagues in this achievement and recognize our outstanding technical support.

As in previous years, and also on the behalf of my colleagues, I would like to thank the *Free State of Bavaria* as represented by the *Bavarian State Ministry of Science, Research and Art* as well as the *Commission for High-Pressure Research in Geoscience* for their continuing support and strong commitment to the Bayerisches Geoinstitut. In addition we would like to thank the *President and Leadership of the University of Bayreuth* for their steadfast and continuing support of the profile field “High Pressure and High Temperature Research”. We also gratefully acknowledge generous support from external funding agencies, in particular the *Alexander von Humboldt Foundation*, the *European Union*, the *German Science Foundation*, and the *Federal Ministry of Education and Research*, which continue to contribute greatly to the further development and success of the Geoinstitut.

Bayreuth, March 2016 Dan Frost

Vorwort

Im 29sten Jahresbericht des Bayerischen Geoinstituts stellen wir die Forschungsaktivitäten des Instituts über Prozesse in der Erde und in anderen Planeten vor. Die Forschungsprojekte sind in vielerlei Hinsicht sehr breit gefächert. Im Größenmaßstab reichen sie zum Beispiel von Untersuchungen atomarer Fehlerstellen in Kristallstrukturen, die diesen ein plastisches Fließen im Erdinneren ermöglichen, bis zur Simulation der Kollisionen von Protoplaneten und der Entwicklung planetarer Atmosphären. Wie in früheren Jahren sind die Forschungsziele hauptsächlich durch Experimente bei den hohen Drücken und Temperaturen erreicht worden, die im Inneren der Planeten herrschen. Die Experimente werden jedoch zunehmend durch Computersimulationen beteiligter Prozesse auf unterschiedlichen Größenskalen unterstützt. In dieser Hinsicht schätzen wir uns sehr glücklich, dass wir Gregor Golabek von der ETH Zürich Anfang des letzten Jahres an unserem Institut willkommen heißen konnten. Er hat die Professur für geodynamische Modellierung übernommen. Dynamische Modelle, die die Bewegung von Wärme und Masse im Erdinneren und in anderen Planeten simulieren, helfen dabei, den Einfluss von Mineral- und Gesteinseigenschaften auf die Entwicklung der Struktur eines Planeten zu erforschen. Professor Golabeks Arbeiten können daher helfen, die Auswirkungen von im Labor bestimmten Eigenschaften auf planetare Prozesse zu verstehen.

Im Jahr 2015 erreichte das Bayerische Geoinstitut eine neue Rekordzahl von Beschäftigten, was in erster Linie auf die großen Erfolge bei der Einwerbung von Drittmitteln zurückzuführen ist. Diese Zahl wird vermutlich in den kommenden Jahren noch steigen, da sich das Institut erfolgreich um eine ‚International Research and Training Group' der DFG beworben hat. Diese Graduiertenschule in Zusammenarbeit mit der Tohuku-Universität in Sendai (Japan) wird 2016 beginnen und 12 Doktoranden in den kommenden 4,5 Jahren finanzieren. Die Studenten werden sich mit verschiedenen Aspekten des Kreislaufs von flüchtigen Elementen zwischen dem tiefen Erdinneren und der Erdoberfläche befassen. Das Ziel wird es sein, den Transport, die Speicherung und die Freisetzung von Kohlenstoff, Wasserstoff und Stickstoff in der Erde zu quantifizieren. Die Doktoranden werden dabei 6 bis 12 Monate an der Tohoku-Universität verbringen, um dort Teile ihrer Forschungsarbeiten durchzuführen. Wir freuen uns darauf, im Austausch Studenten der Tohoku-Universität über die nächsten Jahre hier in Bayreuth zu Gast zu haben. Professor Ohtani von der Universität Tohoku ist ein international anerkannter Experte für Hochdruckforschung und arbeitet schon seit seinem ersten Aufenthalt als Gastprofessor im Jahr 1995 mit Forschern des BGI zusammen. An der Tohoku-Universität haben die Studenten des BGI dagegen die Möglichkeit, einen weiten Bereich verschiedener Disziplinen wie Geochemie, Vulkanologie oder Geophysik kennenzulernen, in denen allen die Untersuchung von flüchtigen Elementen von großem Interesse ist.

Wie in früheren Jahren wurden viele der in diesem Jahresbericht vorgestellten Projekte erst als Resultat innovativer technischer Entwicklungen von experimentellen Methoden möglich. Die Sektion ‚Methodological Developments' (3.8) ist in dieser Hinsicht besonders interessant, weil sie oft die Basis für wissenschaftliche Resultate in den folgenden Jahrbüchern liefert. In den letzten Jahren wurde über eine Reihe von technischen Fortschritten in der Entwicklung einer zweistufigen Diamantstempelzelle berichtet, in der extreme Drücke dadurch erzeugt werden, dass ein zusätzliches Paar von runden Diamantstempeln in der Zelle zusammengedrückt wird. Im vergangenen Jahr wurden nun mit diesem Aufbau Resultate

erzielt und in der Fachzeitschrift *Nature* publiziert. Dabei wurde das Metall Osmium auf 7,5 Megabar komprimiert, was derzeit den Weltrekord in statischen Hochdruckexperimenten darstellt. Anomalien in den Gitterparametern während dieser Kompression deuten auf eine Beteiligung der inneren Elektronen an der Bindung der Osmium-Atome hin, was unter normalen Bedingungen nicht zu erwarten wäre. Der Druck ist damit ein Werkzeug zur Untersuchung der fundamentalen elektronischen Struktur der Materie. Weitere Entwicklungen dieser Technik, die in dem vorliegenden Jahrbuch vorgestellt werden, deuten darauf hin, dass bis zu 10 Megabar erreicht werden können. Das gegenwärtig wichtigste Problem in diesem Bereich ist das Fehlen eines akkuraten Barometers unter solch extremen Bedingungen.

Eine weitere bemerkenswerte Studie in diesem Jahrbuch nutzt die Absorption von Röntgenstrahlen, um die Dichte abgeschreckter Silikatschmelzen in einer Diamantstempelpresse bei p,T-Bedingungen zu messen, die der Kern-Mantel-Grenze in der tiefen Erde entsprechen. Die Ergebnisse liefern den ersten überzeugenden Hinweis, dass die Dichte eines Silikatmagmas an der Basis des Erdmantels höher ist als die der Minerale, die aus derselben Schmelze kristallisieren. Modelle der Bildung der Erde sagen voraus, dass zu unterschiedlichen Zeiten der gesamte Mantel aufgrund von Impaktprozessen geschmolzen war. Die vorliegende Studie legt daher nahe, dass – statt einer Kristallisationsabfolge von unten aufwärts – das Aufschwimmen von kristallisierenden Mineralen einen über lange Zeit stabilen Magmaozean an der Basis des Mantels verursacht hat. Dieses Szenario könnte durchaus geophysikalische Anomalien erklären, die man in diesem Bereich des Mantels heute noch beobachtet. Es wäre auch konsistent mit geochemischen Daten, die auf die Existenz eines tiefen, an flüchtigen und radiogenen Elementen angereicherten Reservoirs hindeuten.

Zum Ende des letzten Jahres erhielt ich die überraschende und großartige Nachricht, dass ich 2016 den Gottfried Wilhelm Leibniz Preis der DFG erhalten würde. Es ist sehr bemerkenswert, dass damit nun vier ehemalige und gegenwärtige Professoren des BGI den Leibniz Preis gewonnen haben. Als ein langjähriges Mitglied des BGI habe ich enorm von der außergewöhnlichen Kultur und Atmosphäre des Instituts profitiert, die durch die Institutsleitung über viele Jahre gepflegt und erhalten wurde. Ich möchte deshalb die Gelegenheit nutzen, um die wichtige Rolle gegenwärtiger und früherer Kollegen in meiner Arbeit zu betonen und insbesondere auch die ausgezeichnete technische Unterstützung am BGI zu würdigen.

Meine Kollegen und ich möchten dem *Freistaat Bayern*, vertreten durch das *Bayerische Staatsministerium für Wissenschaft, Forschung und Kunst*, und der *Kommission für Geowissenschaftliche Hochdruckforschung der Bayerischen Akademie der Wissenschaften* unseren Dank für ihre fortwährende Unterstützung des Bayerischen Geoinstituts aussprechen. Darüber hinaus möchten wir dem Präsidenten und der Hochschulleitung der Universität Bayreuth ausdrücklich für ihre zuverlässige und kontinuierliche Unterstützung des Profilfeldes ‚Hochdruck- und Hochtemperaturforschung' danken. Wir sind auch für die großzügige Förderung durch externe Geldgeber dankbar, insbesondere der *Alexander-von-Humboldt-Stiftung*, der *Europäischen Union* und der *Deutschen Forschungsgemeinschaft*, die ebenfalls wesentlich zur Entwicklung und zum Erfolg des Bayerischen Geoinstituts beigetragen haben.

Bayreuth, im März 2016 Dan Frost

1. Advisory Board and Directorship

1.1 Advisory Board

The *Kommission für Geowissenschaftliche Hochdruckforschung der Bayerischen Akademie der Wissenschaften* advises on the organisation and scientific activities of the institute. Members of this board are:

Prof. Dr. G. BREY	Institut für Geowissenschaften der Johann Wolfgang Goethe-Universität, Frankfurt am Main
Prof. Dr. U. CHRISTENSEN	Max-Planck-Institut für Sonnensystemforschung, Katlenburg-Lindau
Prof. Dr. R. KNIEP	Emeritus, Max-Planck-Institut für Chemische Physik fester Stoffe, Dresden
Prof. Dr. H. PALME	Emeritus, Institut für Mineralogie und Geochemie der Universität zu Köln – Senckenberg Forschungsinstitut und Naturmuseum Frankfurt/M.
Prof. Dr. M. RIEDERER (Chairman)	Julius-von-Sachs-Institut für Biowissenschaften, Würzburg
Prof. Dr. R. RUMMEL (Vice Chairman)	Institut für Astronomische und Physikalische Geodäsie der TU München
Prof. Dr. E. SALJE, FRS, FRSA	Department of Earth Sciences, University of Cambridge
Prof. Dr. H. SOFFEL	Emeritus, Institut für Allgemeine und Angewandte Geophysik der Universität München

The Advisory Board held a meeting in Bayreuth (17.04.2015).

1.2 Leadership

Prof. Dr. Dan FROST (Director) from 01.10.
Prof. Dr. Tomoo KATSURA (Deputy Director) from 01.10.
Prof. Dr. Hans KEPPLER

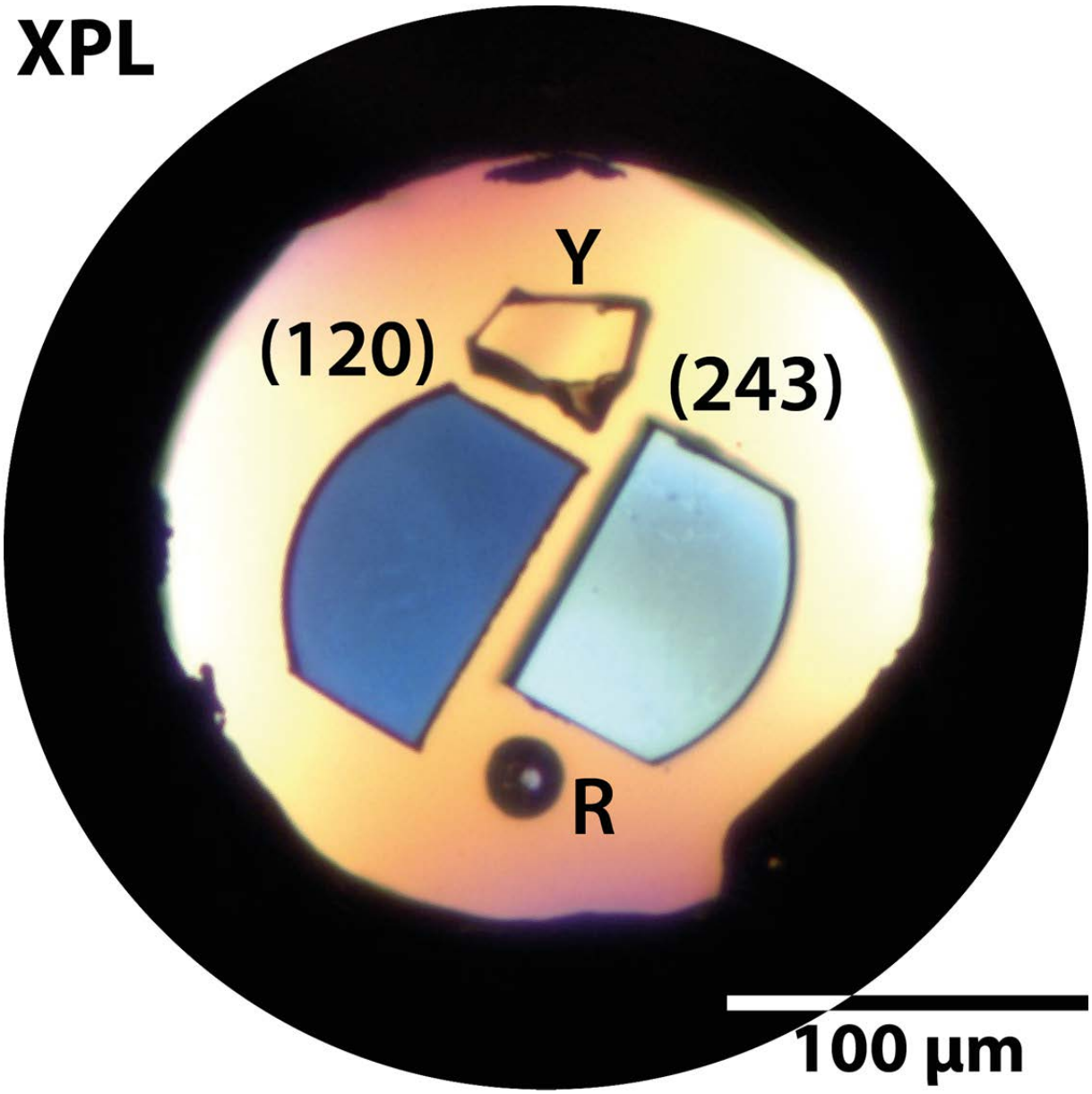

Wadsleyite in crossed polarized light (XPL): Focused ion beam cut single-crystal segments of wadsleyite with different crystallographic orientations (indicated) inside the pressure chamber of a diamond anvil cell along with Sm:YAG (Y) and ruby (R) for pressure/temperature determination. (Photo by Johannes Buchen, BGI)

Mikroskopische Aufnahme von Wadsleyit mit polarisiertem Licht unter gekreuzten Nicols; mit fokussiertem Ionenstrahl (FIB) geschnittene Einkristallsegmente von Wadsleyit mit unterschiedlichen Kristallorientierungen (markiert) in der Druckkammer einer Diamant-stempelzelle zusammen mit Sm:YAG (Y) and Rubin (R) Kristallen zur Druck-/ Temperaturbestimmung. (Foto von Johannes Buchen, BGI)

2. Staff, Funding and Facilities

2.1 Staff

At the end of 2015 the following staff positions existed in the Institute:

- Scientific staff: **13**
- Technical staff: **15**
- Administrative staff: **3**
- Administrative officer: **1**

During 2015, 46 scientific positions (395 months) were funded by grants raised externally by staff members of the institute. In addition 7 long-term scientific positions (44 months) were funded by the resources of the BGI Visiting Scientists' Programme (see Sect. 7) which also supported short-term visits for discussing future projects or presenting research results (see Sect. 5). 18 scientists (124 months) were supported by personal grants (stipends).

2.2 Funding

In 2015, the following financial resources were available from the Free State of Bavaria:

- Visiting Scientists' Programme: 208.000 €
- Consumables: 617.000 €
- Investment funding: 8.000 €

The total amount of national/international external funding (*"Drittmittel"*) used for ongoing research projects in 2015 was 3.138.000 € (Positions: 1.935.000 €; equipment, consumables and travel grants: 1.203.000 €).

	positions	**equipment, consumables, travel grants**	**total**
• AvH	194.000 €	39.000 €	233.000 €
• BMBF	194.000 €	696.000 €	890.000 €
• DFG	1.144.000 €	386.000 €	1.530.000 €
• EU	335.000 €	73.000 €	408.000 €
• Others	68.000 €	9.000 €	77.000 €
			3.138.000€

(AvH = Alexander von Humboldt Foundation; BMBF = Federal Ministry of Education and Research; DFG = German Science Foundation; EU = European Union; Others: DAAD, Univ. Bayreuth, Chinese Science Council, Japanese Society for the Promotion of Science, Azerbaijan National Academy of Science)

In the following list only the BGI components of the funding is listed in cases where joint projects involved other research institutions. Principal investigators and the duration of the grants are listed in brackets. Total project funding refers to the funding over the entire duration of this project.

Funding institution	Project, Funding	Total Project Funding
BMBF	05K12WC1 (L.S. Dubrovinsky – 8.12-7.15) "Single crystal crystallography at extreme pressures and variable temperatures" Total funding:	448.000 €
BMBF	056K13WC4 (L.S. Dubrovinsky – 7.13-6.16) "NANORES: Nanofokussierende Röntgenoptiken und Probenumgebungen für die resonante Kernstreuung zum Studium von schnellen Prozessen in Chemie, Biologie und in Materie unter extremen Bedingungen" Total funding:	475.300 €
BMBF	KEI0500009612 (T. Katsura – 7.13-6.16) "Aufbau einer experimentellen Station mit einer großvolumigen Hochdruckapparatur an der Damping-Wiggler-Beamline des Deutschen Elektronen Synchrotron (DESY)" Total funding:	1.186.000 €
BMBF	05K13WC1 (H. Keppler – 7.13-6.16) "Aufbau einer Hochdruckpresse vom Multi-Anvil-Typ an der Forschungs-Neutronenquelle FRM II in Garching" Total funding:	3.499.590 €
DFG	AU 314/5-1 (A. Audétat – 10.14-9.17) "Development of new oxybarometers for silicic magmas" Position: E13/2, 36 months 90.900 € student assistant 5.000 € Consumables: 35.000 € Overhead: 26.100 €	157.000 €
DFG	BO 2550/7-1 (T. Boffa Ballaran, A. Woodland – 8.13-7.16) "Crystal chemistry of ferric iron in the deep upper mantle and transition zone" Position: student assistant 5.000 € Consumables and travel funding: 9.500 € Overhead: 2.900 €	17.400 €
DFG	BO 2550/8-1 (T. Boffa Ballaran – 9.14-8.16) DFG SPP 1385 'The first 10 Million Years of the Solar System – a Planetary Materials Approach' "Der Einfluss von Mantel Rheologie auf die frühe Differenzierung eisiger Satelliten" Positions: E 13, 24 months 127.200 € student assistant 10.000 € Consumables: 12.285 € Equipment: 27.216 € Overhead: 35.300 €	212.001 €

DFG	DU 393/9-1 (L.S. Dubrovinsky – 1.15-12.17) DFG TP 7 'Chemische Reaktionen zwischen Karbonaten und pyrolitischem Erdmantel und Entstehung ultratiefer Diamanten' "Structures, properties and reactions of carbonates at high temperatures and pressures" Position: E 13 (66 %), 36 months 120.600 € Consumables: 32.250 € Overhead: 30.600 €	183.450 €
DFG	DU 393/10-1 (L.S. Dubrovinsky, C.A. McCammon – 8.15-7.17) DFG SPP 1833 'Building a Habitable Earth' "Leichte Elemente im Kern einer bewohnbaren Erde" Position: E 13, 36 months 206.700 € Consumables: 20.250 € Overhead: 45.400 €	272.350 €
DFG	FR 1555/9-1 (D.J. Frost – 2.15-1.16) "Die Phasenbeziehungen mafischer Gesteine im Erdmantel und Geo-Barometer für Eklogit und Pyroxenit bis zu den Bedingungen der Mantel-Übergangszone" Position: E 13 (75 %), 12 months 44.500 € Overhead: 8.900 €	53.400 €
DFG	FR 1555/10-1 (D.J. Frost – 8.15-7.18) DFG SPP 1833 'Building a Habitable Earth' "Die Ermittlung des Mechanismus der frühzeitigen Oxidation des Erdinneren" Position: E 13 (75 %), 36 months 143.600 € Consumables: 22.250 € Overhead: 33.200 €	199.050 €
DFG	HE 3285/2-1 (F. Heidelbach – 4.13-3.16) "Reaction kinetics and plastic deformation in mantle rocks" 1 position: 36 months 188.900 € Consumables and travel funding: 21.500 € Overhead: 42.100 €	252.500 €
DFG	KA 3434/3 (T. Katsura – 4.13-3.16) "Dislocation recovery experiment of hydrous olivine as a function of water content and crystallographic orientation" 1 position: E 13, 36 months 196.200 € Consumables and travel funding: 20.000 € Overhead: 43.000 €	249.300 €
DFG	KA 3434/7-1 (T. Katsura – 6.14-5.17) "Messung der Korngrenzendiffusion von Forsterit in Abhängigkeit des Wassergehalts" 1 position: E 13, 36 months 196.200 € student assistant 5.000 € Consumables and travel funding: 20.388 € Overhead: 31.700 €	253.288 €

DFG	KA 3434/8-1 (T. Katsura – 4.15-3.18) "Bestimmung des Drei-Phasen-Stabiliätsfelds des Post-spinell-Übergangs in $(Mg,Fe)_2SiO_4$: Erörterung der extremen Schärfe der 660-km-Diskontinuität und deren Bedeutung für die chemische Struktur und die Dynamik des tiefen Erd-mantels" 1 position: E 13, 36 months 196.200 € student assistant 5.000 € Consumables and travel funding: 16.000 € Overhead: 43.300 €			260.500 €
DFG	KA 3434/9-1 (T. Katsura – 9.15-8.18) "Messung von Si-Selbstdiffusionskoeffizienten in Wadsleyit als Funktion des Wassergehaltes" 1 position: E 13, 36 months 196.200 € student assistant 5.000 € Consumables and travel funding: 45.750 € Overhead: 49.500 €			296.450 €
DFG	Forschungsgroßgeräte (T. Katsura) INST 91/291 "Ultrahochdruck-Vielstempelapparatur"			371.000 €
DFG	Forschungsgroßgeräte (T. Katsura) INST 91/302 "Fräsmaschine für Keramikteile"			241.000 €
DFG	KE 501/10-1 (H. Keppler – 7.13-6.16) "DFG Core Facility: High-pressure laboratories of Bayerisches Geoinstitut" Total funding:			544.600 €
DFG	KE 501/11-1 (H. Keppler – 2013-2016) "Electrical conductivity and dissociation of fluids in crust and mantle" Total funding:			267.800 €
DFG	KE 501/8-2 (H. Keppler – 2014-2017) "In-situ observation of the crystallization kinetics and texture evolution of basalts" Total funding:			174.000 €
DFG	KO 3958/2-1 (N. de Koker, G. Steinle-Neumann – 2.11-3.16) DFG SPP 1488 (PlanetMag) "Thermal and electrical conductivity of iron at planetary core conditions from ab initio computations" Positions: E 13, 36 months 186.300 € student assistant (79 h/month) 12 months 7.965 € Consumables and travel funding: 9.000 € Publication costs: 2.250 € Overhead: 41.100 €			246.615 €
DFG	MA 4534/4-1 (H. Marquardt – 9.15-8.18) "Deformationsexperimente an (Mg,Fe)O Ferroperiklas bei hohen Drücken und gleichzeitig hohen Temperaturen" Positions: E13 2/3, 36 months: 123.000 € Consumables: 33.850 € Overhead: 31.400 €			188.250 €

DFG	MA 6287/2-1 (K. Marquardt – 11.14-7.16) "Korngrenzcharakterverteilung in Olivin" Travel funding: 7.800 € Overhead: 1.600 €	9.400 €
DFG	MA 6287/3-1 (K. Marquardt – 9.15-8.18) "Elementverteilung in Geomaterial-Korngrenzen unter Berücksichtigung ihrer Geometrie" Positions: E13 2/3, 36 months: 123.000 € student assistant 2.500 € Consumables: 26.445 € Overhead: 30.400 €	182.345 €
DFG	MC 3/18-1 (C.A. McCammon, L.S. Dubrovinsky, D.J. Frost – 7.13-6.16) "The effect of pressure, temperature and oxygen fugacity on the stability of subducted carbonates and implications for the deep carbon cycle" Positions: E 13/2, 36 months 88.000 € student assistant 5.000 € Equipment, consumables and travel funding: 31.650 € Overhead: 24.900 €	149.550 €
DFG	MC 3/19-2 (C.A. McCammon, S. Gilder – 9.13-8.16) DFG SPP 1488 (PlanetMag) "How pressure influences the magnetic properties of titanomagnetite and iron with implications for magnetic anomalies and core fields" Equipment, consumables and travel funding: 6.400 € Overhead: 1.300 €	7.700 €
DFG	MC 3/20-1 (C.A. McCammon – 10.15-9.18) DFG FOR 2125 (CarboPaT) "Elastic properties of carbonates at high pressure and high temperature" Positions: E13 2/3, 36 months: 123.000 € Equipment, consumables and travel funding: 32.250 € Overhead: 30.600 €	185.850 €
DFG	OV 110/1-2 (S.V. Ovsyannikov – 9.13-8.15) "Structural and electronic properties of sesquioxides at high pressures and temperatures: new forms, new insights and new possible applications" Positions: E 13, 24 months 125.900 € Consumables and travel funding: 20.000 € Overhead: 29.200 €	175.100 €
DFG	OV 110/1-3 (S.V. Ovsyannikov – 9.15-11.15) "Structural and electronic properties of sesquioxides at high pressures and temperatures: new forms, new insights and new possible applications" Positions: E 13, 3 months 16.400 € Overhead: 3.300 €	19.700 €

DFG	PE 2334/1-1 (S. Petitgirard – 10.15-9.17) DFG SPP 1833 'Building a Habitable Earth' "Dichte und Verbleib von Silikatschmelzen im frühen Erdmantel" Positions: E 13, 36 months 206.700 € student assistant 5.000 € Consumables: 42.750 € Overhead: 50.900 €	305.350 €
DFG	RU 1323/2-2 (D.C. Rubie, D.J. Frost, H. Palme – 6.12-5.16) DFG SPP 1385 'The first 10 Million Years of the Solar System – a Planetary Materials Approach' "Conditions, timescales and cosmochemical evolution during the early accretion of terrestrial planets" Positions: E 13/2, 24 months 56.500 € Consumables and travel funding: 40.000 € Publication costs: 1.500 € Overhead: 19.600 €	117.600 €
DFG	RU 1323/9-1 (D.C. Rubie – 3.14-2.16) DFG SPP 1385 'The first 10 Million Years of the Solar System – a Planetary Materials Approach' "Chemische Entwicklung der Metallkerne von Kleinplaneten in der Frühgeschichte des Sonnensystems" Positions: E 13 (75 %), 24 months 88.000 € student assistant 10.000 € Consumables and travel funding: 20.572 € Overhead: 23.700 €	142.272 €
DFG	STE 1105/10-1 (G. Steinle-Neumann – 4.14-3.17) DFG SPP 1488 (PlanetMag) "Structure and electronic transport properties of metallic liquids at conditions of planetary cores" Positions: E 13, 24 months 125.500 € student assistant 18.798 € Consumables: 9.820 € Overhead: 30.800 €	184.918 €
DFG	Emmy Noether-Programm (H. Marquardt – 2014-2019) "Structure and Elasticity of GeoMaterials at Extreme Conditions (GeoMaX)" Positions: group leader, E14/E15, 60 months: 375.400 € post doc, E13, 60 months: 317.200 € 2 PhD students, 2/3 E13, 36 months: 264.400 € student assistant: 11.904 € Consumables, travel funding: 222.550 € Investments: 127.714 € Overhead: 184.400 €	1.503.568 €
EU	European Research Council (ERC) Advanced Grant No. 290568 (D.C. Rubie – 5.12-4.17) "Accretion and Early Differentiation of the Earth and Terrestrial Planets" ("ACCRETE") Positions, consumables and travel funding:	1.826.200 €

2.3 Laboratory and office facilities

The institute occupies an area of

ca. 1350 m^2	laboratory space
ca. 480 m^2	infrastructural areas (machine shops, computer facilities, seminar room, library)
ca. 460 m^2	office space

in a building which was completed in 1994.

2.4 Experimental and analytical equipment

The following major equipment is available at the Bayerisches Geoinstitut:

I. High-pressure apparatus
- 15 MN/1500 tonne Kawai-type multianvil high-pressure apparatus (40 GPa, 2000 K)
- 6 x 8 MN/6x800 tonne independently acting-anvil press (25 GPa, 3000 K)
- 50 MN/5000 tonne multianvil press (25 GPa, 3000 K)
- 12 MN/1200 tonne multianvil press (25 GPa, 3000 K)
- 10 MN/1000 tonne multianvil press (25 GPa, 3000 K)
- 5 MN/500 tonne multianvil press (20 GPa, 3000 K)
- 5 MN/500 tonne press with a deformation DIA apparatus
- 4 piston-cylinder presses (4 GPa, 2100 K)
- Cold-seal vessels (700 MPa, 1100 K, H2O), TZM vessels (300 MPa, 1400 K, gas), rapid-quench device
- Internally-heated autoclave (1 GPa, 1600 K)
- High-pressure gas loading apparatus for DAC

II. Structural and chemical analysis
- 1 X-ray powder diffractometer
- 1 X-ray powder micro-diffractometer
- 1 X-ray powder diffractometer with furnace and cryostat
- 2 automated single-crystal X-ray diffractometers
- High-brilliance X-ray system
- Single crystal X-ray diffraction with super-bright source
- 1 Mössbauer spectrometer (1.5 - 1300 K)
- 3 Mössbauer microspectrometers
- 2 FTIR spectrometers with IR microscope
- FEG transmission electron microscope (TEM), 200 kV analytical, with EDS and PEELS
- FEG scanning TEM, 80-200 kV analytical, with 4-SDDs EDS and post-column energy filter (EFTEM/EELS)

FEG scanning electron microscope (SEM) with BSE detector, EDS, EBSD and CL

Dual beam device, focused ion beam (FIB) and FEG SEM. In situ easy-lift manipulator, STEM and EDS detector, and beam deceleration option

3 Micro-Raman spectrometers with ultraviolet and visible lasers

Tandem-multipass Fabry-Perot interferometer for Brillouin scattering spectroscopy

JEOL JXA-8200 electron microprobe; fully-automated with 14 crystals, 5 spectrometer configuration, EDX, capability for light elements

193 nm Excimer Laser-Ablation ICP-MS

ICP-AES sequential spectrometer

Water content determination by Karl-Fischer titration

GC/MS-MS for organic analyses

Confocal 3D surface measurement system

III. *In situ* determination of properties

Diamond anvil cells for powder and single crystal X-ray diffraction, Mössbauer, IR, Raman, optical spectroscopy, electrical resistivity measurements up to at least 100 GPa

Facility for in situ hydrothermal studies in DAC

Externally heated DACs for in situ studies at pressures to 100 GPa and 1200 K

1-atm furnaces to 1950 K, gas mixing to 1600 K, zirconia fO2 probes

1-atm high-temperature creep apparatus

Gigahertz ultrasonic interferometer with interface to resistance-heated diamond-anvil cells

Heating stage for fluid inclusion studies

Impedance/gain-phase analyser for electrical conductivity studies

Apparatus for in situ measurements of thermal diffusivity at high P and T

Laser-heating facility for DAC

Portable laser heating system for DAC

The Geoinstitut is provided with well equipped machine shops, an electronic workshop and sample preparation laboratories. It has also access to the university computer centre.

3. Forschungsprojekte

3.1 Struktur und Dynamik der Erde und Planeten

Die terrestrischen Planeten im Sonnensystem entstanden über einen Zeitraum von etwa 100 Millionen Jahren durch Kollisionen, zuerst von Planetesimalen untereinander und in späteren Stadien der Akkretion durch Zusammenstöße von mehrere tausend Kilometer messenden planetaren Embryos mit verbleibenden Planetesimalen und untereinander. Durch die Freisetzung kinetischer Energie wurden die entstehenden terrestrischen Planeten zumindest teilweise aufgeschmolzen, was in die Bildung eines Magmaozeans mündete und die Entstehung eines dichten Eisenkerns erleichterte. Die terrestrischen Planeten waren jedoch auch weiterhin, nach Abschluss der Kernbildung, dem Bombardement durch chondritische Einschlagskörper ausgesetzt. Unter anderem gelangten auf diese Weise nach der Kernbildung wieder siderophile Elemente in den Mantel der Erde.

Der erste Beitrag dieses Kapitels beschäftigt sich mit der Frühphase der Akkretion von Planeten, als in der protoplanetaren Scheibe die ersten Bausteine der Planeten, die sogenannten Planetesimale, entstanden. Moderne astrophysikalische Modelle deuten darauf hin, dass diese wenige Dutzend bis Hundert Kilometer großen Körper innerhalb kurzer Zeit durch Gravitationskollaps in einer Scheibe, bestehend aus Mikro- bis Millimeter großen Partikeln, entstanden. Da der Druck in solch kleinen Körpern relativ gering war, kann man anfangs eine hochporöse innere Struktur erwarten. Die Porosität hat insbesondere einen Einfluss auf die thermische Leitfähigkeit der Silikate. Um den Einfluss einer zu Beginn porösen Struktur auf die thermomechanische Entwicklung des Planetesimals zu studieren, wurden 2D und 3D-Simulationen durchgeführt, die zu dem Schluss führten, dass nur in Körpern mit weniger als 30 km Radius eine poröse Oberflächenschicht erhalten bleibt, welche die innere Entwicklung des Körpers beeinflusst. Auf größeren Körpern werden die Hohlräume durch Sinterprozesse bereits innerhalb weniger hunderttausend Jahre komplett geschlossen.

Die zweite Studie widmet sich der Phase der Planetenentstehung, in der planetare Embryos miteinander kollidierten und so größere Körper bildeten. Hierfür wurden dreidimensionale SPH-Modelle (SPH = *smoothed particle hydrodynamics*) mit geodynamischen 3D-Modellen kombiniert, um sowohl die Kollision als auch die längerfristige Entwicklung des Zielkörpers zu modellieren. Dies bietet die Möglichkeit, die Limitierung sowohl der SPH-Modelle, nämlich, dass nur wenige Tage nach der Kollision modelliert werden können, als auch die der geodynamischen Modelle, dass nur vertikale Einschläge mittels Parametrisierung simuliert werden können, zu beseitigen. Zu diesem Zweck wird das Endresultat einer spezifischen SPH-Simulation als Anfangsbedingung für das geodynamische Modell genutzt. In ausführlichen Tests wurde ermittelt, wann nach der Kollision der Datentransfer durchgeführt werden kann, ohne dass mit der Zeit weiterhin zurückfallendes Auswurfmaterial die langfristige thermomechanische Entwicklung des Körpers beeinflusst.

Wie bereits erwähnt, entsteht während der Akkretion terrestrischer Planeten auch deren Eisenkern. Dabei heizt sich der entstehende Planet durch die Freisetzung potentieller Energie immer stärker auf, was zur Bildung eines tiefen Magmaozeans führen kann. Laborexperimente deuten darauf hin, dass die Eisenkerne von einschlagenden planetaren Embryos im Magmaozean auseinanderbrechen und sich mit dem Magmaozean thermisch und chemisch ausgleichen. Dies würde jedoch bedeuten, dass sich das mit leichten Elementen angereicherte Material an der Kern/Mantel-Grenze befinden würde, während das Material in tieferen Schichten des Erdkerns dichter wäre. Das hätte jedoch zur Folge, dass im Eisenkern keine thermische Konvektion stattfinden und somit in der Frühzeit kein internes Magnetfeld erzeugt werden könnte. Jedoch ist heutzutage bekannt, dass die Erde bereits vor 3.4 Milliarden Jahren ein Magnetfeld besaß, also zu einer Zeit als der innere Erdkern höchstwahrscheinlich noch nicht existierte. Somit muss thermische Konvektion im Kern stattgefunden haben. Im dritten Beitrag wird ermittelt, unter welchen Bedingungen die größten Einschläge während der letzten Phase der Planetenentstehung diese Stratifikation des Kerns mechanisch aufbrechen können, um somit die Existenz eines frühen Magnetfelds zu ermöglichen.

Der vierte Beitrag beschäftigt sich, mit numerischen *ab-initio* Modellen zur elektrischen und thermischen Leitfähigkeit von Eisen unter Bedingungen des Erdkerns. Insbesondere der Wert der thermischen Leitfähigkeit wurde in den letzten Jahren in der Literatur wiederholt kontrovers diskutiert. Dies ist von großer Bedeutung, da verbesserte Kenntnisse eine präzise Bestimmung ermöglichen, wie groß der Wärmefluss an der Kern/Mantel-Grenze sein muss, um einen thermisch angetriebenen Dynamo im Erdkern zu ermöglichen. Zusammen mit paläomagnetischen Daten für das Erdmagnetfeld erlaubt dies, verfeinerte Modelle der thermischen Entwicklung des Erdkerns zu erstellen. Diese wiederum ermöglichen letztendlich auch eine bessere Eingrenzung des Entstehungsalters für den inneren Erdkern.

In den ersten 500 Millionen Jahren nach der Entstehung des Sonnensystems bombardierte übrig gebliebenes oder aus dynamisch instabilen Regionen des Sonnensystems stammendes Material die jungen terrestrischen Planeten. Neben der Anlieferung von siderophilem Material kann dieses Bombardement auch die Atmosphäre eines terrestrischen Planeten beeinflussen, indem der Einschlag zu Atmosphärenverlusten führt, was in der Folge die Oberflächentemperatur beeinflusst. Geodynamische Modelle wiederum deuten darauf hin, dass die Oberflächentemperatur einen entscheidenden Einfluss auf das tektonische Regime des Planeten haben kann. Der letzte Beitrag beschreibt, wie der Effekt dieser Einschläge auf die Entwicklung eines terrestrischen Planeten studiert wurde. Es wurde dafür ein detailliertes zweidimensionales, gekoppeltes Mantel-Atmosphärenmodell für den Planeten Venus entwickelt. Die Resultate zeigen, dass genügend große Einschläge in dieser Epoche nach der Planetenentstehung zwar einen Teil der Atmosphäre entfernen, dies aber durch Vulkanismus, der durch den massiven Einschlag ausgelöst wird, aufgewogen werden kann. Durch den massiven Vulkanismus wird auch Wasser aus der Atmosphäre entfernt. Da die Atmosphärentemperatur in diesem Fall stets hoch bleibt, wird das Wasser durch UV-Strahlung aufgespalten und geht verloren. Zusammen resultiert dies in einem Szenario, in dem auf der Venus niemals Plattentektonik auftreten kann.

3.2 Geochemie

Ursprung, Verteilung und Einfluss flüchtiger Elemente sind gemeinsame Hauptthemen einiger Beiträge dieses Kapitels. Zumeist stehen jedoch volatile Elemente nicht im direkten Fokus der Untersuchungen, sondern es werden vielmehr andere Elemente genutzt um die geochemischen Einflüsse von Fluiden, Schmelzen und Gasen zu bestimmen. Diese Thematik wird in Untersuchungen von Meteoriten und zur Akkretion der Erde, die am Anfang dieses Kapitels stehen, offensichtlich. Sie findet sich auch in Studien über die Diamantentstehung im mittleren Teil, und in Untersuchungen über magmatische und erzbildende Prozesse am Ende dieser Sektion.

Das Kapitel beginnt mit einer Beschreibung von Abfolgen mineralischer Überwachsungen in Komponenten eines undifferenzierten Meteorits. Generell wird angenommen, dass derartige Minerale aus der Abkühlung von Gasen des solaren Nebels entstehen und dass unter hohen Temperaturen gebildete refraktäre Minerale von flüchtigen Mineralen überwachsen wurden, die bei niedrigeren Temperaturen kondensierten. Unter den sauerstoffarmen Bedingungen in denen sich der untersuchte Meteorit bildete, kondensierten jedoch Elemente wie Kohlenstoff und Schwefel, die normalerweise fllüchtig sind, schon sehr früh. Dies stellt die Idee in Frage, dass Materie, die früh aus dem solaren Nebel kondensierte und aus der die Proto-Erde zusammengewachsen wäre, nur geringe Anteile an volatilen Elementen gehabt hat. Die nachfolgenden zwei Studien untersuchen die späten Stadien der Erdakkretion mit Hilfe des Verhaltens stark siderophiler Elemente. Stark siderophile Elemente wie Platin und Iridium reichern sich im Vergleich zu Silikatschmelzen stark in Eisenschmelzen an. Experimente, die in der ersten Studie beschrieben sind, zeigen, dass stark siderophile Elemente in geringerem Maß in Metallen aufgenommen werden, sobald der Metallschmelze Schwefel hinzugefügt wird. Diese Ergebnisse werden in der anschließenden Studie verwendet, um aufzuzeigen, dass die in einem späten Stadium aufgetretene Abtrennung einer sulfidreichen Schmelze in den Erdkern einen Abdruck im Muster der hoch siderophilen Elemente im Erdmantel hinterlassen hat. Der Ursprung dieses Elementmusters wurde bisher mit der Akkretion eines unbekannten Typs meteoritischer Materie erklärt.

Im nächsten Projekt werden thermodynamische Modelle verwendet, um Verteilungs-koeffizienten leichter Elemente zwischen Mantel und Kern unter Mantelbedingungen zu bestimmen. Diese Bedingungen stellen für experimentelle Arbeiten eine große Herausforderung dar; deshalb sind derartige Modelle, die zahlreiche Arten thermo-dynamischer Daten kombinieren, zur Klärung widersprüchlicher experimenteller Resultate sehr nützlich. Der letzte Beitrag, der sich mit der Entstehung der frühen Erde befasst, untersucht den Effekt von Druck auf den Oxidationszustand von Eisen in Silikatschmelzen. Der frühe Magmaozean der Erde hat an seiner Untergrenze wahrscheinlich mit dem erdkernbildenden metallischen Eisen im Gleichgewicht gestanden; im Falle eines seichten Magmaozeans hätte dies zu einem sehr niedrigen Gehalt an dreiwertigem Eisen im Magma geführt, und somit zu generell niedrigem Oxidationszustand im Mantel. Im Falle eines tiefen

Magmaozeans wären theoretisch größere Fe^{3+}-Anteile möglich. Experimente dieser letzten Studie zeigen jedoch, dass bis zu einer Tiefe von ungefähr 500 km keine erhöhten Gehalte an dreiwertigem Eisen vorhanden sind. Weitere Experimente müssen klären, ob diese Erkenntnisse auch für größere Tiefen zutreffen.

Die nachfolgenden zwei Untersuchungen gelten dem Verständnis von Bildung und Einlagerung von Granateinschlüssen in Diamanten aus dem tiefen Erdmantel. Die erste präsentiert eine Kalibrierung, die die Zusammensetzung von Granateinschlüssen sowohl mit der Tiefe, in der die Einlagerung geschah, als auch mit der Zusammensetzung der Gesteine, in denen die Einschlüsse und Diamanten gebildet wurden, ins Verhältnis setzt. Aus den Ergebnissen wird deutlich, dass sich Diamanten in Mantelgesteinen nur in Tiefen von weniger als 200 km bilden. Stattdessen bildeten sie sich in heterogenen Bereichen, die entweder bei tiefreichender Subduktion ozeanischer Kruste oder durch Reaktionen zwischen Teilschmelzen aus der subduzierten Kruste und dem umgebenden Erdmantel entstanden sind. Die nächste Studie versucht, diese Schmelzreaktionen und die Zusammensetzung der dabei entstandenen Granate zu reproduzieren. Ein faszinierendes Ergebnis dieser Studie ist, dass durch die Schmelzreaktion eine Mineralzone geschaffen wird, die für weitere einsickernde Schmelze undurchdringlich ist. Das könnte möglicherweise zur Bildung und Konservierung von mit siliziumreicher Schmelze gefüllten Taschen tief im oberen Erdmantel führen. Das abschließende Projekt zum tiefen Erdmantel nutzt die *in situ*-Röntgenbeugung an einer Synchrotron-Einrichtung zur Überprüfung von Drücken, die mit Hilfe von Mineralgleichgewichten innerhalb bestimmter Gesteinsgesellschaften berechnet wurden. Die Verteilung einiger Elemente zwischen den Mineralphasen ist druckabhängig und kann für Abschätzungen des Druck-Gleichgewichts in Mantelgesteinen verwendet werden. Die Ergebnisse weisen für Drücke, die für Gleichgewichte typischer Mantelgesteine üblicherweise eingesetzt werden, einige Unstimmigkeiten auf und verdeutlichen, dass Neukalibrierungen erforderlich sind.

Die nächste Untersuchung befasst sich mit dem Kreislauf flüchtiger Bestandteile entlang von Subduktionszonen. Durch Anwendung eines Dreilagen-Modells für die subduzierte Platte und thermodynamischen Daten zur Prognose von Phasengleichgewichten in jeder einzelnen Lage bis 7 GPa und 1000 °C wird ein quantitatives Modell zur Freisetzung von H_2O und CO_2 in unterschiedlichen Subduktionstiefen aufgestellt. Die Ergebnisse zeigen, dass entlang typischer P-T-Pfade bis in 200 km Tiefe nur die untere Lage aus serpentinisiertem Harzburgit vollständig entgast. Dagegen transportieren sowohl die ozeanische Kruste als auch die darüber liegende Lage aus Sedimenten einen Teil der Volatilen in größere Tiefen hinab, hauptsächlich bedingt durch die Stabilität von Phengit.

Einem recht kontroversen Thema widmet sich der nächste Artikel. Eine Theorie besagt, dass ein Teil der in der Erdkruste vorhanden Kohlenwasserstoffe abiogenen statt biogenen Ursprungs sei, und dass diese Kohlenwasserstoffe innerhalb des Erdmantels durch Reaktionen von Methan entstanden seien. Daher wurden Experimente mit Diamantstempelzellen bei

Drücken bis 4,5 GPa und Temperaturen bis 1500 °C durchgeführt, um nachzuprüfen, ob Öl in der Präsenz von Mantelgestein reagiert, und in welchem Ausmaß dadurch die Stabilität komplexer Kohlenwasserstoffe beeinflusst wird.

Die nächsten zwei Untersuchungen befassen sich mit dem Verhalten von Volatilen und Metallen in Magmenkammern der oberen Erdkruste. Die erste ist eine experimentelle Untersuchung zur Bestimmung der Zusammensetzung von Fluiden, die aus kristallisierenden mafischen Magmen entweichen und in überlagernde felsische Magmen migrieren. Die Studie kommt zu dem Ergebnis, dass die Elemente S, Cl, Cu, Se, Te, Br und Cd am stärksten in diesen Fluiden angereichert sind und deswegen auch am geeignetsten sind, in felsischen Magmen solche Prozesse nachzuweisen. Die andere Studie konzentriert sich auf eine der weltweit größten porphyrischen Kupferlagerstätte. Sie geht der Frage nach, warum gerade dieses Magmasystem so intensiv mineralisiert wurde. Durch die Untersuchung von Schmelz- sowie Sulfideinschlüssen in Phänokristallen lässt sich der Gehalt an Metallen und Volatilen in dem erzbringenden Latit-Magma rekonstruieren und mit Vergleichsdaten aus entsprechenden unmineralisierten Schmelzsystemen vergleichen. Es stellt sich heraus, dass die erzbringenden Schmelzen im Bingham Canyon und die zweier anderer porphyrischen Cu-Mo-Au-Lagerstätten im Vergleich mit ihren unmineralisierten Gegenstücken weder an Metallen noch an Volatilen angereichert waren. Die Studie kommt zu dem Schluss, dass eher ungewöhnlich große Magmenkammern als spezialisierte Magmen der Schlüssel für abbauwürdige Erzlagerstätten sind.

Der dieses Kapitel abschließende Beitrag stellt eine Erweiterung einer früheren Untersuchung zur Verteilung von Vanadium zwischen Magnetit und felsischer Silikatschmelze dar (vgl. Jahresbericht von 2011), mit dem Ziel, ein Oxy-Barometer zu entwickeln, das auch für langsam abgekühlte Gesteine wie Granit anwendbar ist. Der Schlüssel für die letztere Anwendung ist, dass kleine Mengen an silikatischer Schmelze und Magnetit oft als Einschlüsse in großen Quarzkristallen zu finden sind; wenn diese Einschlüsse mit Laser-Ablation (LA-ICP-MS) als Ganzes abgetragen werden, zeigen sie daher die ursprünglichen V-Gehalte an und ermöglichen die Berechnung der Verteilungskoeffizienten für Vanadium. Die Studie kommt zur Erkenntnis, dass die V-Verteilung zwischen Magnetit und Schmelze in erster Linie von der Sauerstofffugazität abhängt, gefolgt von Schmelzzusammensetzung und Temperatur. Druck und Magnetit-Zusammensetzung haben dagegen nur einen geringen Einfluss.

3.3 Mineralogie, Kristallchemie und Phasenübergänge

Die Verknüpfung mikroskopischer Eigenschaften und makroskopischer Beobachtungen spielt weiterhin eine sehr wichtige Rolle in unserem Bestreben, das Erdinnere und die Prozesse, die seine Dynamik und Entwicklung beeinflussen, besser zu verstehen. Die experimentelle Bestimmung von Strukturen und Stabilitätsbereichen umfasst einen weiten Bereich an

Variablen, zu denen nicht nur Druck und Temperatur, sondern auch wichtige Faktoren für die Zusammensetzung zählen, wie zum Beispiel Sauerstofffugazität und Wassersättigung. Mit theoretischen Ansätzen kann dieser Parameterraum sogar noch weiter ausgedehnt werden. In diesem Kapitel des Jahresberichts werden die neuesten Ergebnisse derartiger Untersuchungen beschrieben.

Bridgmanit, das häufigste Mineral der Erde, steht weiter im Fokus der Untersuchungen. Neue Ergebnisse zeigen, dass die Eisenverteilung zwischen Kationenstellen wie auch das Auftreten von Leerstellen sowohl mit der Temperatur als auch mit der Sauerstofffugazität in Beziehung stehen; der Einbau von Argon kann die Zustandsgleichung und auch die thermodynamische Stabilität beeinflussen. Die Entdeckung neuer Eisenoxide führt zu weiteren, neuen Wirtsmineralen für dreiwertiges Eisen; Untersuchungen zu Spin-Übergängen bei dreiwertigem Eisen lassen überraschende Regelmäßigkeiten erkennen, die mit seiner Elektronenstruktur verknüpft sind. Kristallstruktur und -morphologie liefern auch Informationen über die Bildungsbedingungen, so dient zum Beispiel die Elementarzelle von Olivin als Geobarometer für den Zeitpunkt ihres Einschlusses in Diamant; Spinell-Entmischungen aus Ferroperiklas in Diamant deuten auf vorher vorhandene Versetzungs-strukturen hin. Die Substitution von scheinbar gering vorhandenen Elementen in Wadsleyit, wie zum Beispiel Übergangsmetallen, beeinflusst das Ladungsgleichgewicht und den Einbau flüchtiger Bestandteile wie Wasserstoff und beeinflusst so deren tiefreichende Stoffkreisläufe. In ähnlicher Weise können Polymorphe von Siliziumdioxid durch eine gekoppelte Substitution von Silizium mit dreiwertigen Atomen Wasserstoff einbauen. Untersuchungen von Phasenübergangssequenzen in Siliziumdioxid liefern darüberhinaus auch Einblicke in die Entstehung extraterrestrischer Materie.

Phasenübergänge verbinden auch mikroskopische Eigenschaften mit makroskopischen Beobachtungen und führen zu genaueren Kenntnissen über seismische Diskontinuitäten. Die Mächtigkeit der Diskontinuität in 660 Km Tiefe wird durch die Ausdehnung des drei-Phasen-Feldes Ringwoodit + Bridgmanit + Ferroperiklas bestimmt; neue Entwicklungen bei *in situ*-Röntgenbeugungsmessungen versprechen eine präzise Bestimmung dieses Stabilitätsfeldes. Phasenübergänge in Karbonaten liefern genauere Hinweise zum tiefen Kohlenstoff-Kreislauf, wenn sie entsprechend vorhandener seismischer Daten aufgelöst werden können; neue Resultate über Kobalt- und Mangan-Karbonate ermöglichen Einblicke in die Systematik von Phasenübergängen, was auch auf die weiter verbreiteten Karbonate zutrifft, die im tiefen Erdmantel erwartet werden. Bei sehr extremen Bedingungen ermöglichen theoretische Berechnungen die Bestimmung von MgO-Phasenübergangen, die für die Kerne von Riesenplaneten oder von felsigen Exoplaneten relevant sind. Theoretische Ansätze lassen erweiterte Berechnungen zu Phasenbeziehungen und seismischen Eigenschaften von Mischkristallen zu. Prognosen über Mischkristall-Stabilitäten können auf der Basis der Eigenschaften ihrer Endglieder vorgenommen werden, wie es am Beispiel der Rutilstruktur mit den Endglieder-Dioxiden aus Silizium und Germanium experimentell bestätigt werden konnte.

3.4 Physikalische Eigenschaften von Mineralen

Ein quantitatives Verständnis der physikalischen Mineraleigenschaften ist von grundlegender Bedeutung um den Zusammenhang zwischen geophysikalischen Beobachtungen und der Struktur und Zusammensetzung des Erdinneren zu verstehen und um die Dynamik unseren Planeten verlässlich zu modellieren.

In diesem Jahr wurde besonderer Wert darauf gelegt, die elastischen Eigenschaften von verschiedenen Mineralen mit hoher Genauigkeit zu bestimmen, wie in den ersten vier Beiträgen dieses Kapitels beschrieben. Die Mantel-Übergangszone, welche sich in einer Tiefe von 410 bis 660 km befindet, ist von großer Bedeutung für die Dynamik des Erdinneren und stellt möglicherweise einen großen Speicher für Wasser und flüchtige Elemente dar. Die ersten beiden Beiträge zielen darauf ab, die elastischen Eigenschaften der Olivin-Polymorphe Wadsleyit und Ringwoodit, welche das größte Volumen der Übergangszone ausmachen, besser zu verstehen. Hierzu wurden Experimente in der Diamantstempelzelle durchgeführt, die Röntgenbeugung und Brillouin-Streuung verbinden. Eine Besonderheit dieser Studien ist die Ladung einer Diamantstempelzelle mit mehreren Einkristallen deren Größe und Form mit der fokussierten Ionenstrahl (FIB) Präparation angepasst wurden. Mit diesem Ansatz können direkte Informationen über die Effekte von Eisen- und OH-Gehalt auf die elastischen Eigenschaften von Wadsleyit und Ringwoodit bei hohen Drücken und hohen Temperaturen erhalten werden, ohne die Notwendigkeit einen sekundären Druckstandard zu verwenden. Im dritten Beitrag wird ebenfalls die FIB-Präparation mit Röntgenbeugung und Brillouin-Streuung kombiniert, um einen konsistenten Datensatz der elastischen Eigenschaften von Al-Fe-haltigem Bridgmanit bei den Drücken des unteren Erdmantels zu erhalten. Al-Fe-haltiger Bridgmanit ist die bei Weitem häufigste Mineralphase unterhalb der seismologischen Diskontinuität bei 660 km Tiefe und die gemessenen Daten werden benötigt um seismologische Beobachtungen mit möglichen chemischen Variationen dieses Minerals in Verbindung zu bringen.

Im vierten Beitrag wird über Elastizitätsmessungen an polykristallinem SiO_2 Stishovit berichtet, ein weiteres potentiell wichtiges Mineral des unteren Erdmantels. Die Experimente wurden mittels Synchrotron-Röntgenbeugung am Petra III Ring (DESY) bis 60 GPa durchgeführt. Weiterhin werden gerade Brillouin-Messungen an diesem Material durchgeführt, um die akustischen Scherwellengeschwindigkeiten über den Phasenübergang von tetragonal zu orthorhombisch oberhalb von 50 GPa zu messen.

Die FIB-Probenpräparation wurde auch im fünften Beitrag für drei Glas-Proben mit verschiedenen chemischen Zusammensetzungen angewandt (SiO_2, $MgSiO_3$, $(Mg,Fe)SiO_3$). Die Gläser wurden gleichzeitig in eine Diamantstempelzelle geladen, um einen direkten Vergleich des Kompressionsverhaltens zu ermöglichen und den Effekt des Druckmediums auf das Kompressionsverhalten zu verstehen.

Die folgenden drei Beiträge beschreiben Hochdruck-Röntgenbeugungsexperimente an Mantelmineralen mit dem Ziel ein systematisches Verständnis der Zusammenhänge zwischen Struktur, Zusammensetzung, Spin-Zuständen und Kompressionsverhalten zu erlangen. Beitrag (**f**) berichtet über das Kompressionsverhalten und assoziierte Strukturänderungen in einem neuen Oxid $Mg_2Fe_2O_5$, welches als Zerfallsprodukt von Magnesioferrit ($MgFe_2O_4$) bei hohen Drücken entsteht. Eine wichtige Beobachtung dieser Studie ist ein stark anisotropes axiales Kompressionsverhalten, wobei die c-Achse die weichste Richtung darstellt.

In Beitrag (**g**) werden Hochdruck-Einkristall-Röntgenbeugungsexperimente und Synchrotron-Mössbauer-Messungen an eisenhaltigem silikatischem Granat vorgestellt, die darauf abzielen, die Effekte des Eisenoxidations- und Spin-Zustands auf die Granatstruktur innerhalb der Mischkristallreihe zwischen Skiagit ($Fe^{2+}_3Fe^{3+}_2Si_3O_{12}$) und Majorit ($Fe_4Si_3O_{12}$) systematisch zu verstehen. Erstaunlicherweise zeigen die vier Granate trotz unterschiedlicher Zusammensetzungen ein sehr ähnliches Kompressionsverhalten und zeigen eine Volumenreduktion bei Drücken zwischen 50 und 60 GPa, welche mit einem Spin-Übergang von Fe^{3+} auf dem Oktaederplatz in der Granatstruktur assoziiert wird.

Im folgenden Beitrag wurden die synthetischen Skiagit-Majorit-Granate in einer Diamantstempelzelle bei Drücken oberhalb von 45 GPa mit einem Laser geheizt. Eines der Zerfallsprodukte war eine orthorhombische Perovskit-phase mit einer Zusammensetzung von $(Fe^{2+}_{0.64}Fe^{3+}_{0.24})SiO_3$. Das Kompressionsverhalten dieser Phase wurde bis 130 GPa mittels Synchrotron-Röntgenbeugung gemessen und mit dem Verhalten von $MgSiO_3$ und $(Mg,Fe)(Si,Al)O_3$ Bridgmaniten verglichen, um die Effekte von chemischer Zusammensetzung, Valenz-Zuständen und Spin-Zuständen auf das Kompressionsverhalten zu verstehen.

Transporteigenschaften sind von grundlegender Bedeutung für die Modelle der Dynamik des Erdinneren und werden in den Beiträgen (**i**) und (**j**) diskutiert. Zn-Co-Diffusionsexperimente an $NaCoF_3$ post-Perovskit Einkristallen, die als Niedrigdruck-Analogmaterialien für Silikat-Perovskit dienen, wurden in der Vielstempelzelle durchgeführt und sind in Kapitel (**i**) beschrieben. Die Ergebnisse zeigen, dass chemische Diffusion entlang <100> drei Größenordnungen schneller abläuft als entlang <010>/<001>. Die Resultate von *in situ*-Messungen der elektrischen Leitfähigkeit von partiell geschmolzenen Olivin-Aggregaten mit verschiedenen Anteilen an basaltischer Schmelze (0 bis 100 %) bei Bedingungen des oberen Erdmantels werden in Beitrag (**j**) vorgestellt. Die Ergebnisse zeigen, dass die Schmelze bereits bei einem Volumenanteil von 0,5 % ein verbundenes Netzwerk bildet. Diese Beobachtung legt nahe, dass keine Verformung notwendig ist, um die elektrische Leitfähigkeit von partiell geschmolzenen Gesteinen zu erhöhen.

Im letzten Kapitel dieser Sektion, werden verschiedene Formulierungen der Wärmekapazität kritisch diskutiert und deren Genauigkeit verglichen mit dem Ziel ein besseres Verständnis der Ansätze zu gewinnen, welche in verschiedenen thermodynamischen Modellen Anwendung finden.

3.5 Fluide, Schmelzen und ihre Wechselwirkung mit Mineralen

In den 90er Jahren wurde die globale Erwärmung in der Öffentlichkeit nur relativ wenig diskutiert. Der Hauptgrund hierfür war der Ausbruch des Vulkans Pinatubo auf den Philippinen im Jahr 1991. Die von diesem Ausbruch erzeugten Schwefelsäure-Aerosole in der Stratosphäre wirkten wie ein Filter, der Sonnenstrahlung zurückstreute und für mehrere Jahre die Auswirkungen der anthropogenen CO_2-Emissionen kompensierte. Da diese Effekte von der Menge des Schwefels abhängen, die bei einer Eruption in die Stratosphäre injiziert werden, ist es nicht nur von akademischem Interesse, die Schwefel-Freisetzung durch Vulkane quantitativ zu verstehen. Ein Hauptproblem ist hier, dass sehr unterschiedliche Messdaten für den Fluid/Schmelze-Verteilungskoeffizienten von Schwefel existieren. Ein erster Beitrag in diesem Kapitel enthält daher die Ergebnisse einer systematischen Untersuchung dieses Verteilungskoeffizienten für einen weiten Bereich von Magmen unterschiedlicher Zusammensetzung. Die Daten zeigen, dass $D_S^{Fluid/Schmelze}$ stark von der Zusammensetzung der Schmelze abhängt, aber praktisch unabhängig von der Temperatur ist. Ein neues numerisches Modell erlaubt quantitative Vorhersagen der Schwefel-Freisetzung und damit der klimatischen Auswirkung von Vulkaneruptionen.

Alle vulkanischen Eruptionen werden letztlich angetrieben durch die Entmischung von Gasen – überwiegend Wasserdampf – die sich in der Schmelze tiefer im Erdinneren unter hohem Druck gelöst hatten. Die Geschwindigkeit dieses Entmischungsprozesses wird weitgehend durch den Diffusionskoeffizienten von Wasser bestimmt. Für basaltische Schmelzen gibt es hier, im Gegensatz zu den SiO_2-reicheren rhyolitischen Schmelzen, kaum Daten. Diese Lücke füllt der zweite Beitrag in diesem Kapitel. Die Ergebnisse zeigen, dass der Diffusionskoeffizient stark mit dem Wassergehalt zunimmt. Damit es zu Vulkaneruptionen an der Erdoberfläche kommt, ist es nicht nur notwendig, dass in der Tiefe Schmelze gebildet wird, sondern diese Schmelze muss sich auch vom umgebenden Gestein trennen können. Ein entscheidender Parameter ist hier der Kontaktwinkel der Schmelze. Dieser Winkel wurde in einem Enstatit-Forsterit-Modellsystem bei 1 bar untersucht.

Die kontinentale Kruste wurde zum größten Teil durch Magmen gebildet, die in Subduktionzonen entstanden sind. Obwohl dieser Prozess seit Jahrzehnten untersucht wird, gibt es immer noch Kontroversen über den genauen Mechanismus der Schmelzbildung. Eine systematische Studie von publizierten Daten von nicht-entgasten Schmelzeinschlüssen in der Georoc-Datenbasis zeigt, dass die Konzentrationen von Spurenelementen wie Sr, Rb, U, Ce und La in den Magmen mit dem Cl/H_2O-Verhältnis stark ansteigen. Dies kann nur erklärt werden, wenn diese Elemente von einer salzhaltigen, wasserreichen Fluidphase von der subduzierten Platte in die Zone der Schmelzbildung im Mantelkeil transportiert worden sind. Der NaCl-Gehalt dieser Fluide verbesserte die Effizienz dieses Transportprozesses durch die Stabilisierung von Chloridkomplexen.

Arbeiten am Bayerischen Geoinstitut haben in den letzten Jahrzehnten gezeigt, dass flüchtige Elemente wie Wasserstoff und Stickstoff in Mineralen des Erdmantels gelöst werden können

und dass der Erdmantel deshalb ein erhebliches Reservoir für diese Elemente darstellt. Ein weiterer Beitrag in diesem Kapitel beschreibt die ersten Messungen der Löslichkeit von Stickstoff in $(Mg,Fe)_2SiO_4$-Wadsleyit im Gleichgewicht mit Olivin. Anscheinend wird Stickstoff im Wadsleyit im Vergleich zum Olivin stark angereichert. Möglicherweise ist die Übergangszone des Erdmantels daher nicht nur ein wichtiges Reservoir für Wasser, sondern auch für Stickstoff.

Die letzten beiden Beiträge in diesem Kapitel beschäftigen sich mit zwei Prozessen, die in der frühen Erdgeschichte abliefen, während der Bildung des Erdkerns und der Kristallisation des Magmenozeans. Neue Röntgen-Absorptionsmessungen von Gläsern unter hohem Druck legen die Vermutung nahe, dass Silikatschmelzen im untersten Mantel immer dichter sein werden als kristalline Phasen. Dies bedeutet, dass möglicherweise der Kern noch von einem tiefen Magmenozean umgeben war, als der größte Teil des Mantels sich bereits verfestigt hatte. Inwieweit bei der Bildung des Erdkerns chemisches Gleichgewicht zwischen dem Kern und dem Mantel erreicht wurde, wird teilweise bestimmt durch die Diffusionskoeffizienten von Elementen wie Si, O und Cr. Eine Kombination von experimentellen Daten und *ab-initio* molekulardynamischen Simulationen zeigt, dass diese Diffusionskoeffizienten in einfacher Weise von der Schmelztemperatur des Eisens abhängen.

3.6 Rheologie and Metamorphose

Verschiedene geologische und geophysikalische Naturerscheinungen, wie beispielsweise Vulkanismus und Erdbeben, haben ihren Ursprung in der Dynamik des Erdinneren. Die rheologischen Eigenschaften der Minerale und der aus ihnen aufgebauten Gesteine steuern das dynamische Verhalten im Erdinneren. Zur Bestimmung ihrer rheologischen Eigenschaften gelten Verformungsexperimente unter kontrollierten Umgebungsbedingungen als die geeignetste Methode. Das Verhältnis von gerichtetem Druck und Verformungs-geschwindigkeit kann hierbei direkt bestimmt werden. Die sechsachsige Vielstempelpresse am Bayerischen Geoinstitut ermöglicht es, Scherspannungen zu erzeugen, indem ein Druckstempelpaar relativ zu den anderen Druckstempeln druckentlastend oder druck-verstärkend eingesetzt wird, wodurch eine Verformung der Proben unter Drücken von einigen GPa erzielt wird. Vergleichbare Verformungsexperimente bei Drücken im GPa-Bereich können mit der D-DIA-Apparatur des Instituts durchgeführt werden. Der erste Beitrag dieses Kapitels konzentriert sich auf den Einfluss von deviatorischem Druck und gleichzeitiger plastischer Verformung bei der Bildung von Granat in Eklogit. Es zeigte sich, dass die Produktionsrate von Granat bei 10 GPa, im Vergleich mit der Produktionsrate unter hydrostatischem Druck, um bis zu 40 % zunimmt. Die Bestimmung der rheologischen Eigenschaften eines bimineralischen Eklogits in seinem Stabilitätsfeld sind Untersuchungsziel des zweiten Beitrags. Für jedes Mineral werden am ESRF/Grenoble kleinste Gitterverformungen durch einen kombinierten Einsatz einer D-DIA-Presse und einem für *in situ*-Messungen geeigneten Röntgendiffraktometer bestimmt. In Ergänzung zu diesen

Verformungsstudien mit großvolumigen Pressen wurden rheologische Untersuchungen auch mit Hilfe von Diamantstempelzellen durchgeführt. Im dritten hier vorgestellten Projekt wird die Einkristall-Röntgendiffraktometrie zur Erforschung von Eis IV eingesetzt, um Kenntnisse über das Innere von eisigen Trabanten zu gewinnen. Die folgende vierte Studie befasst sich mit möglichen Veränderungen im Deformationsverhalten von Ferroperiklas bei 30-40 GPa und bei hohen Temperaturen, um die kürzlich veröffentlichte Zunahme seiner Fließfestigkeit zu verstehen. Daraus ergeben sich weitere Kenntnisse über die Anisotropie des unteren Mantels. Hierfür wurden an der Strahllinie für Extreme Bedingungen am DESY (PETRA III) Röntgenbeugungsanalysen an pulverförmigen Ferroperiklas-Proben bei 40-80 GPa und bei Temperaturen von 1100-1500 K durchgeführt.

Obwohl Verformungsexperimente die direkteste Methode zur Untersuchung der Mineralrheologie darstellen, werden bei der Überprüfung von Ergebnissen aus Verformungsexperimenten unterschiedliche Strategien verfolgt. Druck und Verformungsraten sind in Verformungspressen um viele Größenordnungen höher als in der Natur. Die Eigendiffusion von Si wird als limitierender Faktor im Deformationskriechenregime angesehen. Der fünfte Beitrag beschreibt die Entwicklung einer Methode zur Messung von Si- und O-Eigendiffusionen in Einkristall-Wadsleyit, mit der sich feststellen ließ, dass der Sauerstoff-Diffusionskoeffizient von Forsterit eine positive Druckabhängigkeit aufweist, im Gegensatz zu anderen Selbstdiffusionskoeffizienten wie der von zum Beispiel Silizium.

Diffusionskoeffizienten liefern nur indirekte Informationen über die Effektivität von Versetzungskriechen, das als wichtigster Kriechmechanismus im Erdmantel gilt. Folglich könnten Experimente zur Versetzungsannihilation bei quasi-hydrostatischem Druck unsere Kenntnisse über Deformationsprozesse vergrößern. Die Versetzungsmobilität zeigt bei geringer Belastung eine Abhängigkeit vom Wassergehalt, im Gegensatz zur Temperaturabhängigkeit, die sowohl bei Versetzungsmobilitäten als auch bei Verformungs-exerimenten übereinstimmt. Vergleicht man das Maß der Versetzungsannihilation von Bridgmanit und Ringwoodit mit unterschiedlichen Wassergehalten, so stellt sich heraus, dass die Versetzungsgeschwindigkeit in Bridgmanit höher als in wasserfreiem Ringwoodit ist, jedoch niedriger als diejenige in Ringwoodit mit einem Wassergehalt von 1 %. Es lässt sich spekulieren, dass sich mit diesen Ergebnissen globale Variationen bei der Stagnation von Erdplatten erklären lassen. Eine wasserführende Übergangszone im Erdmantel lässt sich ebenfalls vermuten. Experimente zur Versetzungsannihilation liefern traditionell nur Ergebnisse zur Kletter-Mobilität von Versetzungen. Neuartige Analysen erlauben die gleichzeitige Bestimmung von Gleit- und Kletter-Mobilitäten zu bestimmen. Die Analysen lassen vermuten, dass die Versetzungsmobilität in Verformungsexperimenten durch das Gleiten kontrolliert wird.

Mikrotexturelle Betrachtungen am Transmissionselektronenmikroskop (TEM) liefern wichtige Informationen zu rheologischen Eigenschaften von Mineralen. Neuen Erkenntnisse über Versetzungen ergeben sich aus genauen transmissionselektronischen Untersuchungen

von verformtem Wadsleyit. Um Vorgänge des Feststoff-Kriechens besser zu verstehen wurden im achten Beitrag Veränderungen von Mikrostrukturen bei *in situ*-Verformung im TEM untersucht. In der Metallurgie ist bekannt, dass Cottrell-Wolken, also Segregation von Spurenelementen in den Kern von Versetzungen, Verhärtungen und Versprödung in FCC- und BCC-Metallen bewirkt. Im neunten Beitrag werden Versuche beschrieben, mit denen Auswirkungen von Cottrell-Wolken in Mantelmineralen geprüft werden. Der letzte Beitrag dieses Kapitels beschreibt Untersuchungen von Phasenübergängen von Olivin nach Ringwoodit und Ahrensit im Tissint-Meteorit auf der Basis genauer Analysen mit SEM-, EPMA- und FIB-TEM-Methoden.

3.7 Materialwissenschaften

Die Entwicklung neuer Methoden im Feld der Hochdruckforschung (sowohl im Labor als auch in der Theorie) wurde über lange Zeit aus dem Interesse am inneren Aufbau der Erde und anderer Planeten vorangetrieben. Die dabei entwickelten Techniken sind allerdings auch für die Materialwissenschaften von zunehmendem Interesse. Zum einen erlaubt eine verstärkte Wechselwirkung von Atomen unter hohem Druck die Untersuchung fundamentaler chemischer und physikalischer Prozesse und Veränderungen, zum anderen werden Methoden bei hohem Druck zur Materialsynthese untersucht und auch genutzt. Um wissenschaftlichen Fortschritt in beide Richtungen zu ermöglichen, müssen Analysemethoden bei hohem Druck – also *in situ* – ausreichend entwickelt sein. Ein wichtiger Durchbruch in dieser Hinsicht fand in der Einkristall-Röntgenbeugung unter hohem Druck statt, bei der zugängliche Druckbereich von ca. 15 GPa auf über 150 GPa erweitert wurde. Dabei haben Wissenschaftler am Bayerischen Geoinstitut eine wichtige Rolle gespielt, und die Anwendung der neuentwickelten Technik steht im Mittelpunkt dieses Abschnitts des Jahresberichts. Verschiedenste Materialklassen von Festkörpern werden dabei untersucht: Elemente, Oxide und metallorganische Verbindungen.

Bor und Bor-Verbindungen bleiben auch nach Jahrzehnten von Untersuchungen im Fokus wissenschaftlichen Interesses, da sie einzigartige physikalische Eigenschaften aufweisen (hohe Härte, Stabilität und chemische Trägheit), die sie technologisch interessant machen. Experimente an elementarem Bor sowie Kobaltborid zeigen deren niedrige Kompressibilität auf und geben Hinweise auf die Mechanismen, die ihre hohe Härte kontrollieren.

Unter den Oxiden der Übergangsmetalle hat Sc_2O_3 (Scandia) die höchste bekannte elektronische Bandlücke, was es für industrielle Anwendungen extrem interessant macht. Es wird unter anderem in Lichtquellen mit hoher Intensität, in Verbundkeramiken und optischen Beschichtungen verwendet. Auf der Basis von Pulverbeugungs-Daten wurde das Hochdruckverhalten von Sc_2O_3 bisher kontrovers diskutiert. Im dritten Beitrag dieses Kapitels wird auf der Basis von Daten aus Röntgenbeugung an Einkristallen und Raman-Spektroskopie die Sequenz von Phasenübergängen geklärt.

Die Kristallchemie von Phosphaten unter hohem Druck ist sowohl in der Materialwissenschaft als auch der Mineralogie von Interesse, da sie dort traditionell als Analogmaterialien von Silikaten verwendet werden. Hochdruck-Experimente an $TiPO_4$ zeigen im Druckbereich bis 55 GPa vier neue Phasen, von denen eine Phosphor in ungewöhnlicher fünffacher Koordination zeigt.

Dichte metallorganische Verbindungen sind wichtige Kandidaten für eine neue Generation von multiferroischen Materialien, die in mehrstufigen Schaltelementen verwendet werden. Der Einfluss von mechanischer Spannung oder Druck auf metallorganische Verbindungen ist bisher nicht untersucht – aber erste Experimente, deren Ergebnisse hier präsentiert werden, zeigen, dass verschiedene Metallzentren zu Variationen bei Phasenübergängen führen.

Der letzte Beitrag in diesem Kapitel nutzt theoretische Methoden zur Untersuchung der Ladungsverteilung in organischen Molekülen, wenn diese ionisiert werden. Zusätzlich zu den lange bekannten Mechanismen der Lokalisierung, wie Polaronen und Solitonen, wird hier beschrieben, dass Ladung spontan lokalisiert, wenn die Länge eines Polymers einen kritischen Wert übersteigt.

3.8 Methodische Entwicklungen

Bei experimentellen Untersuchungen in den Erd- und Materialwissenschaften ist die Verbesserung bestehender und die Entwicklung neuer Methoden ein weiterhin wichtiges Ziel. Solche Fortschritte sind zum Beispiel hilfreich für 1) die Ausdehnung des zugänglichen Druck- und Temperaturbereichs und ihre präzisere Bestimmung, was für ein besseres Verständnis des tiefen Erdinneren erforderlich ist, 2) bei neuartigen Messungen zur Bestimmung physikalischer und chemischer Eigenschaften von Materie und 3) für die Bestimmung von chemischer Zusammensetzung und von Kristallgitter-Fehlern in natürlichen und experimentell synthetisierten Proben. Die Beiträge dieses Kapitels stellen zahlreiche Aspekte der methodischen Weiterentwicklung vor.

Mit einer neuen Vielstempelpresse („IRIS-15“), die bereits 2014 installiert wurde, zielen die hier durchgeführten Experimente auf obere und mittlere Regionen des unteren Erdmantels ab, wo Drücke oberhalb von 23 GPa herrschen. Der erste Beitrag widmet sich technischen Entwicklungen bei der Verwendung von angeschrägten Würfeln aus Wolframkarbid, mit denen Experimente bei Drücken bis zu 44 GPa und Temperaturen von 2000 K bei einem relativ großen Probenvolumen und stabilen Heizbedingungen ermöglicht werden.

Neutronenbeugungsexperimente liefern wichtige Informationen über das Verhalten leichter Elemente (z. B. H und C) sowie ihnen benachbarter Elemente (z. B. Mg, Al und Si) in Kristallstrukturen, da sich der Streuquerschnitt von dem von Röntgenstrahlen unterscheidet. Der zweite Beitrag in diesem Kapitel stellt neue Entwicklungen und die Leistungsfähigkeit von Detektoren für Neutronenbeugung vor, die am Forschungsreaktor FRM II in Garching an der dort seit 2011 installierten Multianvil-Presse (6-Stempel) zum Einsatz kommen.

Weitere vier Beiträge stellen neue methodischen Fortschritte bei der Generierung und Erfassung hoher Drücke und Temperaturen in Diamantstempelzellen (DAC) vor. Der dritte Artikel beschreibt, wie der Druckbereich bei DAC-Experimenten auf 800-1000 GPa ausgedehnt werden konnte, indem man auch für die doppelstufige DAC-Technik Dichtungen einführte. Drei Beiträge schildern erreichte Erfolge bei der Erzeugung und Messung hoher Temperaturen in der DAC. Eine stabile Beheizung der Probe ist unbedingte Voraussetzung für die Bestimmung von Materialeigenschaften bei hohen Temperaturen mit Hilfe von Einkristall-Röntgenbeugungsmessungen und durch Brillouin- und Ramanspektroskopie. Der vierte Artikel stellt ein temperaturstabiles Heizsystem bis 1500 K vor, das aus einem inneren Hochtemperatur-Aufbau mit einem Heizelement aus Graphit besteht. Weiterhin ermöglicht das Beheizen mit einem gepulsten statt einem Dauerstrich-Laser die Bestimmung der Wärmeleitfähigkeit und der Kinetik chemischer Reaktionen und von Phasenübergängen in der DAC. Der fünfte Beitrag stellt den Aufbau und die Leistungsfähigkeit eines doppelseitigen Heizsystems mit Puls-Lasern vor, der eine Temperaturbestimmung mit hoher räumlicher Auflösung ermöglicht. Zur Untersuchung von Temperatureffekten auf Materialeigenschaften ist die Bestimmung des Temperaturgradienten über eine laserbeheizte Probe ebenfalls sehr wichtig. Der sechste Artikel verdeutlicht, dass mit der isomerischen Verschiebung von Mössbauerspektren aus Synchrotron-Messungen Aussagen zum Temperaturgradienten in laserbeheizten Proben getroffen werden können.

Zwei folgende Projekte befassen sich mit Neuentwicklungen bei DAC und Moissonitstempelzellen (MAC) zur Untersuchung wasserhaltiger Fluide und Magmen. Kenntnisse über die Eigenschaften wasserhaltiger Fluide sind notwendig, um das Wachstum kontinentaler Kruste nachzuvollziehen, da sie die Magmenbildung in Subduktionszonen kontrollieren. Der siebte Beitrag beschreibt die Entwicklung eines neuen Aufbaus zur Bestimmung elektrischer Leitfähigkeiten in wässrigen Fluiden, um deren Dissoziationsgrad (z. B. pH) zu erfassen. Kenntnisse über Prozesse von Blasenbildung und -wachstum in Magmen einer vulkanischen Magmakammer sind für unser Verständnis für den Verlauf von Vulkanausbrüchen wichtig. Die mit einer MAC erreichbaren Druck-Temperatur-Bedingungen konnten auf die Bedingungen ausgedehnt werden, die in Magmenkammern vorhanden sind. Das beschreibt der achte Beitrag, der ausführt, dass dadurch genaue Untersuchungen über das Verhalten von Blasen im Magma bei Vulkaneruptionen ermöglicht werden.

Die beiden das Kapitel abschließenden Beiträge stellen Fortschritte in der Probenanalytik vor. Die Beobachtung und Bestimmung von Versetzungen in Kristallen spielt bei Untersuchungen zu rheologischen Eigenschaften, die durch Versetzungsbewegungen gesteuert werden, eine wichtige Rolle. Der vorletzte Artikel präsentiert eine in den Geowissenschaften neue Methode (*electron channeling contrast imaging* - ECCI) zur Beobachtung von Versetzungen in Oxiden mit einem Rasterelektronenmikroskop (Feld-Emission). Das Transmissionselektronen-mikroskop Titan G^2 80-200 - FEI wurde am Geoinstitut im Jahre 2013 installiert. Der abschließende Beitrag stellt den Ursprung von Kristallnegativen in Diamanten aus dem unteren Erdmantel auf der Basis detaillierter Analysen mit diesem neuen Gerät vor.

3. Research Projects

3.1 Earth and Planetary Structure and Dynamics

The terrestrial planets in our solar system formed within roughly 100 million years after the start of the solar system. In the beginning, collisions involved planetesimals; during the later stages of accretion, planetary embryos collided with remaining planetesimals and with other embryos. Due to the release of kinetic energy, magma oceans formed repeatedly on the nascent terrestrial planets allowing for effective core segregation. However, even after core formation ceased, material was delivered to the terrestrial planets first during the late veneer epoch and later on during the late heavy bombardment. One consequence of this bombardment was the reintroduction of siderophile elements into Earth's mantle.

The first contribution in this section deals with the early phase of planet formation when planetesimals, small building blocks of terrestrial planets, formed in the protoplanetary disc. Modern astrophysical research indicates that these objects with a size of a dozen to hundreds of kilometers formed within a short time from micro- to millimeter-sized particles. Since pressures are low inside planetesimals, these objects are expected to be initially highly porous, and the material porosity has a significant influence on the thermal conductivity of the silicates. 2D and 3D numerical models were used to study the thermomechanical evolution of planetesimals. Results indicate that only objects with less than 30 km radius can retain a porous outer shell that can influence their internal evolution. On the other hand, inside larger objects sintering processes close the pores efficiently within a few hundred thousand years.

The second contribution discusses the phase of planet formation when planetary embryos collided among each other and formed larger terrestrial objects. For this purpose, a 3D SPH (smoothed particle hydrodynamics) model was serially coupled with a 3D geodynamical model to study both the impact process and the longer-term evolution of the target body. This method allows overcoming the limitations of both SPH models and geodynamical models. Namely, SPH models describe a short time after the impact process. On the other hand, impacts can be only prescribed in a simplified way in geodynamical models. Therefore the final state of each SPH simulation serves as input data for the geodynamical model. Since ejecta material falling back onto the target body can affect the thermomechanical evolution, detailed tests were performed to assess the sensitivity of the handoff between both models.

As mentioned above Earth's accretion and differentiation are contemporary processes. Due to impact heating, the internal temperatures rise and a magma ocean forms. Laboratory experiments indicate that the iron cores of impactor bodies will emulsify in this magma ocean, resulting in their thermal and chemical equilibration with the magma ocean. This would result in a stratified core with material containing more light alloying elements resting on top of the core. Under these conditions thermal convection in the core is not viable and no internal magnetic field can be generated. However, paleomagnetic data prove the Earth's magnetic field already, formed 3.4 billion years ago. Since it is rather unlikely that the Earth's inner

core already formed at that time, chemical convection is not yet a viable option. Thus thermal convection had to occur in the core. The third abstract discusses how major impacts mechanically stirred the core and were able to overcome the core stratification.

The fourth contribution describes *ab initio* calculations of the electrical and thermal conductivity of iron under the conditions of Earth's core. Especially the thermal conductivity was in recent years a matter of debate. Thus reduced error bars enable better estimates of the heat flux across the core mantle boundary necessary to operate a thermally driven dynamo. Combined with paleomagnetic data, this allows for refined thermal evolution models for the Earth's core, thus allowing to put better constraints on the age of Earth's inner core.

In the first 500 million years after the formation of the solar system both leftover material from accretion and material derived from dynamically unstable regions bombarded the young terrestrial planets. This epoch is known as the late veneer. Not only siderophile material was delivered this way to the planets, but also the planetary atmospheres were affected since impacts can remove part of the atmosphere and in this way influence the surface temperature. Recent geodynamical models indicate that the surface temperature can have a significant influence on the tectonic regime of a planet. The last contribution describes a 2D coupled atmosphere-interior model applied to Venus that takes the late veneer bombardment into account. The results show that sufficiently large impacts remove some atmosphere, but that the resulting volcanic activity replenishes atmospheric gases efficiently. The resulting high surface temperatures allow for efficient loss of water from the atmosphere. Finally, this results in a scenario where plate tectonics never occurred on Venus.

a. *The impact of short-lived radionuclides and porosity on the early thermomechanical evolution of planetesimals (G.J. Golabek, T. Lichtenberg, T.V. Gerya and M.R. Meyer/ Zurich)*

The thermal history and internal structure of chondritic planetesimals, assembled before the giant impact phase of chaotic growth, potentially yield important implications for the final composition and evolution of terrestrial planets. These parameters critically depend on the internal balance of heating versus cooling, which is mostly determined by the presence of short-lived radionuclides (SLRs), such as ^{26}Al and ^{60}Fe, as well as the heat conductivity of the material. The heating by SLRs depends on their initial abundances, the formation time of the planetesimal and its size. It has been argued that the cooling history is determined by the porosity of the granular material, which undergoes dramatic changes via compaction processes and tends to decrease with time.

In this study we assess the influence of these parameters on the thermomechanical evolution of young planetesimals with both 2D and 3D simulations. Using the code family I2ELVIS/I3ELVIS we have run numerous 2D and 3D numerical finite-difference fluid dynamic models with varying planetesimal radius, formation time and initial porosity (Fig. 3.1-1). Our results indicate that powdery materials lower the threshold for melting and

convection in planetesimals, depending on the amount of SLRs present. A subset of planetesimals retains a powdery surface layer which lowers the thermal conductivity and hinders cooling. However, the effect of initial porosity is small compared to those of planetesimal size and formation time, which dominate the thermomechanical evolution and are the primary factors for the onset of melting and differentiation (Fig. 3.1-2).

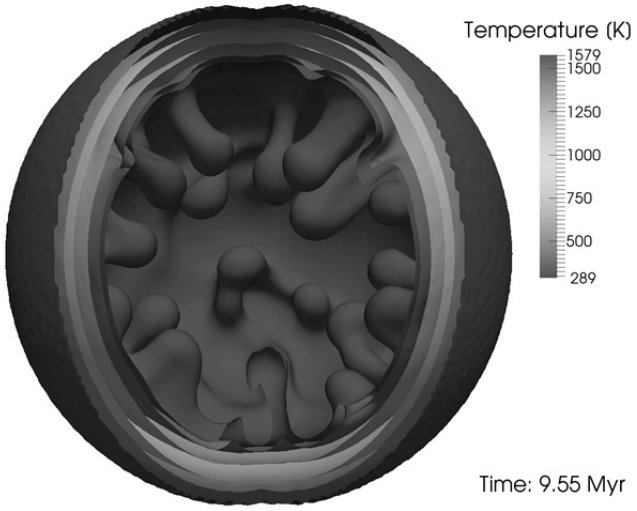

Fig. 3.1-1: Density isocontours in a 3D model with 110 km radius, 0.25 as initial porosity and formation time of 0.1 Myr after CAI.

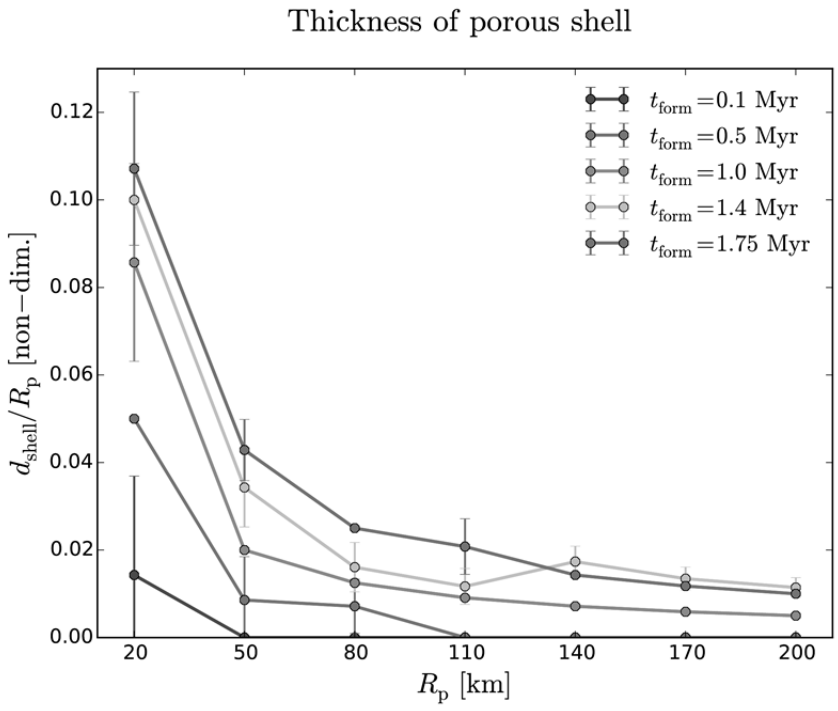

Fig. 3.1-2: Fraction of porous shell versus planetesimal radius after all thermomechanical processes have ended. The values represent the arithmetic means over the results for all initial porosities, the errorbars showing the corresponding standard deviations. The shell fraction decreases with increasing size of the body and with earlier formation time.

b. *Coupling collision and geodynamical models (G.J. Golabek, M. Jutzi/Bern, A. Emsenhuber/Bern and T.V. Gerya/Zurich)*

The crustal dichotomy is the dominant geological feature on planet Mars. The exogenic approach to the origin of the crustal dichotomy assumes that the northern lowlands correspond to a giant impact basin formed after primordial crust formation. However these simulations only consider the impact phase without studying the long-term repercussions of such a collision.

The endogenic approach, suggesting a degree-1 mantle upwelling underneath the southern highlands, relies on a high Rayleigh number and a particular viscosity profile to form a low degree convective pattern within the geological constraints for the dichotomy formation. Such vigorous convection, however, results in continuous magmatic resurfacing, destroying the initially dichotomous crustal structure in the long-term.

A further option is a hybrid exogenic-endogenic approach, which proposes an impact-induced magma ocean and subsequent superplume in the southern hemisphere. However these models rely on simple scaling laws to impose the thermal effects of the collision.

Here we use impact simulations performed with a SPH code serially coupled with geodynamical computations performed using the code I3VIS to improve the latter approach and test it against observations. We are exploring collisions varying the impactor velocities, impact angles and target body properties, and are gauging the sensitivity to the handoff from SPH to I3VIS.

As expected, our first results indicate the formation of a transient hemispherical magma ocean in the impacted hemisphere, and the merging of the cores (Fig. 3.1-3). We also find that impact angle and velocity have a strong eff ect on the post-impact temperature field and on the timescale and nature of core merger.

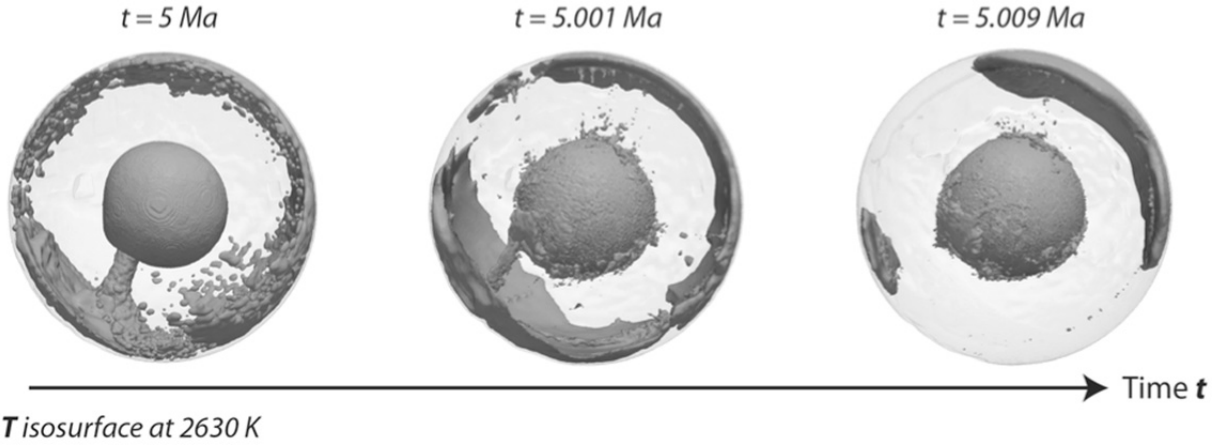

Fig. 3.1-3: I3ELVIS result for the evolution of a Mars-sized planet after a grazing collision with a 1000 km radius impactor. Temperature isosurface at 2630 K, corresponding to the liquidus of peridotite at martian CMB pressure.

c. *Stratification of terrestrial cores (S.A. Jacobson and D.C. Rubie, in collaboration with A. Morbidelli/Nice and J. Hernlund/Tokyo)*

We continued this year to develop our model of the construction and evolution of the Earth's core. Numerical N-body simulations of successful solar system formation scenarios like the Grand Tack create Earth-like planets with realistic accretion histories. These models connect the growth of Earth with the provenance of the projectile material, so assuming that refractory elements have near CI chondritic compositions and using a model for the oxidation and water gradients in the disk, we have a simulated record of Earth's evolving composition. We model the planetary differentiation process after each accretion event using a metal-silicate equilibration model. This model uses a mass balance approach and partition coefficients determined from high-pressure experiments. One of the outputs of this model is the composition of a metal liquid that is added to the core.

This core addition is, of course, primarily iron and nickel, but it also contains light elements such as Si and O. The concentration of these light elements in each core addition is a function of the projectile core composition and the conditions of metal-silicate equilibration such as temperature, pressure, and oxygen fugacity. In general, since the equilibration temperatures and pressures naturally increase during accretion, the concentration of light elements included in each newer core addition increases as a function of time. This means that typically later delivered core layers are less dense than earlier delivered layers, so this process establishes a stable density stratification (Fig. 3.1-4a). Some core layers as accreted are denser than the layers accreted before them, so they are initially unstable. It is not clear how two unstable layers interact with each other, so we model two end-member scenarios. In the first, the two layers are mixed (Fig. 3.1-4b). This model is appropriate if the stabilizing flows of core material are turbulent. If the flows are laminar, then the swapping model is more appropriate (Fig. 3.1-4c). In this model, the two layers are just exchanged in radial location. These layer exchanges occur until the core is stable after every core addition.

The density of a core addition depends on its composition but also on its temperature. This is determined by two thermal end-member models. In the cold thermal end-member model, the layers are heated by adiabatic compression as its sinks into the mantle and then into the core. In the hot thermal end-member model, the layers are heated adiabatically and by the release of gravitational potential energy as heat. This model produces a significantly hotter central temperature of Earth and a significantly colder core-mantle boundary, so the core-mantle boundary heat flux should be high, while the cold thermal end-member produces the opposite and a low heat flux is expected.

The critical Rayleigh number, which determines whether heat transfer is convective in the core, is generally positive unless the thermal profile is an adiabat as established by the cold end-member scenario or after heat has been transferred out of the hot thermal end-member scenario. However, composition and temperature deviations from an adiabat can create

boundary regions where the local density gradient deviation, which is proportional to the Rayleigh number, is less than zero. These deviations create conductive barriers where convection cannot occur regardless of the heat flux.

These conductive barriers prevent single cell convection of the core, and hence homogenization of the core's composition and the onset of a long-lasting geodynamo. Late energetic giant impacts can disrupt these conductive barriers by mechanically mixing large regions of the core.

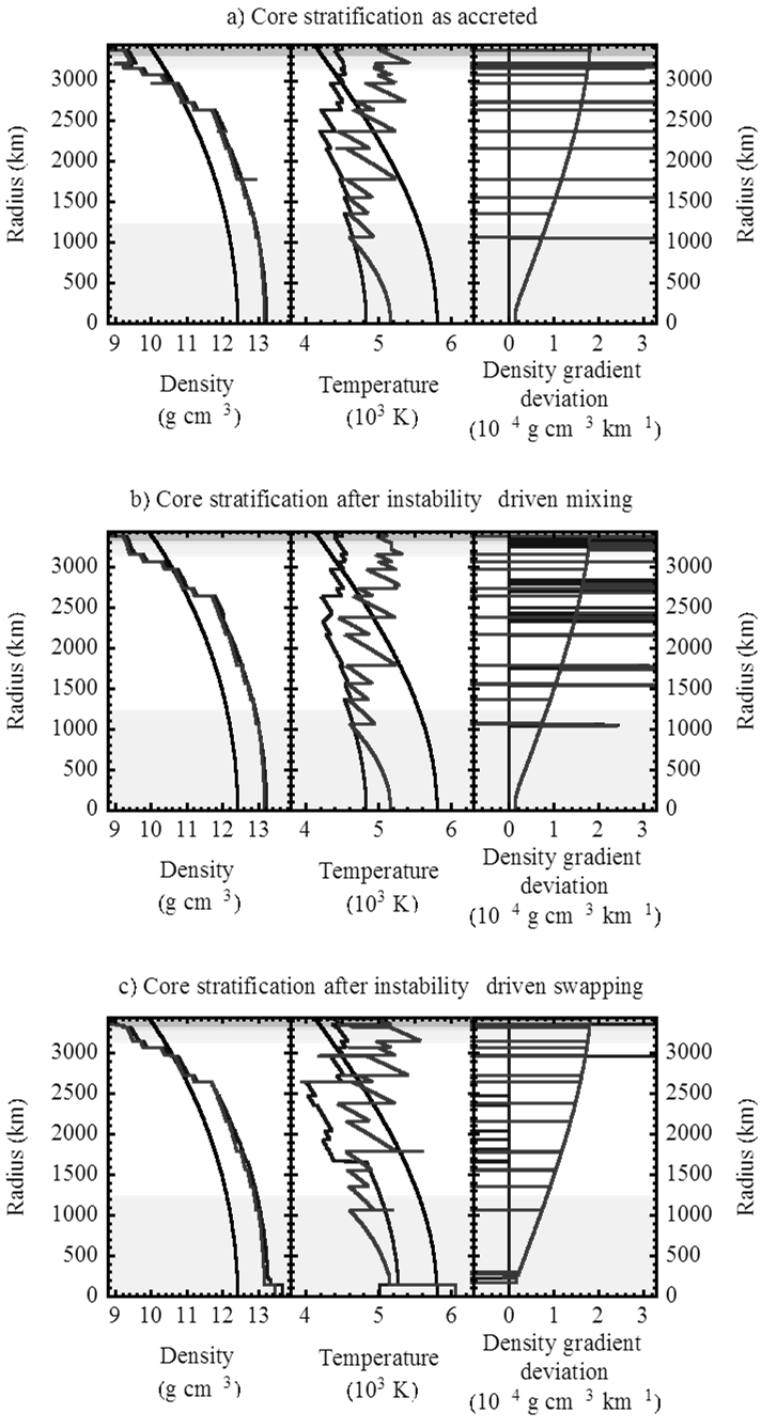

Fig. 3.1-4: In each panel, the density (lefthand plot), temperature (center plot), and deviation of the density gradient (righthand plot) profiles for Earth's core are shown as a function of radius. The profiles are shown as accreted (panel a), which preserves some unstable layering, and as final core profiles after a layer exchange model (mixing in panel b, and swapping in panel c) has stabilized the density profile. Both the cold (dark grey) and hot (light grey) thermal model end-members are shown and compared to an empirical Earth model (black) derived from the PREM. The extent of the inner core is marked by a gray region, and the two estimates of an upper stratified layer are shown: an approximate 300 km layer from seismic modeling (light gray) and a 140 km layer from geomagnetic modeling (dark grey).

d. *Conductivity of iron along its melting curve (F. Wagle, V. Vlček and G. Steinle-Neumann)*

Electrical and thermal conductivity are critical parameters in the assessment of the evolution of convection-driven planetary dynamos and the diffusion of heat. While a planet is slowly cooling, a portion of the conducting fluid in the core solidifies and imposes constraints in terms of geometry and physical properties on the dynamo. In order to better understand these constraints for dynamo evolution of terrestrial planets, we investigate electronic transport properties upon freezing of pure iron, the predominant core material.
A widely successful way of computing electrical resistivity ρ_{el} at ambient pressure is by Ziman's formula

$$\rho_{el} = \frac{3\pi\Omega_0}{\hbar e^2 {v_F}^2} \langle S(k)|\mathcal{U}_k|^2\rangle, \tag{1}$$

with

$$\langle S(k)|\mathcal{U}_k|^2\rangle = \frac{1}{4k_F}\int_0^{2k_F} S(k)|\mathcal{U}_k|^2\, k^3 \mathrm{d}k, \tag{2}$$

where k is the wave number of the scattering vector, $S(k)$ the static ion-ion structure factor, $\mathcal{U}_k$ the Fourier transform of the pseudo-potential, Ω_0 the volume per atom, v_F the Fermi velocity, e the elementary charge, k_F the Fermi wave number and $\hbar$ the reduced Planck constant. By following Ziman's approximation

$$\frac{\rho_{el}^{liquid}}{\rho_{el}^{solid}} \simeq \frac{S(0)^{liquid}}{S(0)^{solid}}, \tag{3}$$

we can relate electrical resistivity to isothermal compressibility in the thermodynamic limit $\lim_{k\to 0} S(k) = \varrho k_B T \beta_T$ at the melting point and therefore write

$$\frac{\rho_{el}^{liquid}/\rho_{el}^{solid}}{\beta_T^{liquid}/\beta_T^{solid}} \simeq 1. \tag{4}$$

In the equations above, ϱ denotes density, k_B Boltzmann's constant and $\beta_T = -\varrho\, \partial(1/\varrho)/\partial p$ is the isothermal compressibility. For iron at ambient conditions this relation holds well and resistivity measurements up to 6 GPa indicate that it remains valid at high pressure.

Since β_T can be computed from an equation of state and an expression for $\rho_{el}^{liquid}(V,T)$ has been reported in the literature, we can estimate ρ_{el}^{solid} along the melting curve of iron from equation (4), as shown in Fig. 3.1-5a. Thermal conductivity λ_{th} for both the liquid and solid phase can then be obtained by the law of Wiedemann-Franz, as shown in Fig. 3.1-5b.

We predict a decrease of ρ_{el}^{solid} at the fcc $(\gamma) \rightarrow$ hcp(ε) phase transition, which corresponds to a decrease of the unit cell volume and the associated increase of charge carrier density. For conditions at the Earth's present-day inner core boundary, we find $\rho_{el}^{solid} = 59.7\ \mu\Omega \cdot$ cm and $\lambda_{th}^{solid} = 215$ W·m^{-1}·K^{-1}.

This method provides a framework for reliably and quickly estimating electrical and thermal conductivity at inner core boundaries of terrestrial planets, up to $p-T$ conditions of the Earth's center. The objective of ongoing work is the understanding of the weight of every material-specific quantity in relation (1), in order to find the driving mechanism for the high-pressure behaviour of conductivity of metals and alloys.

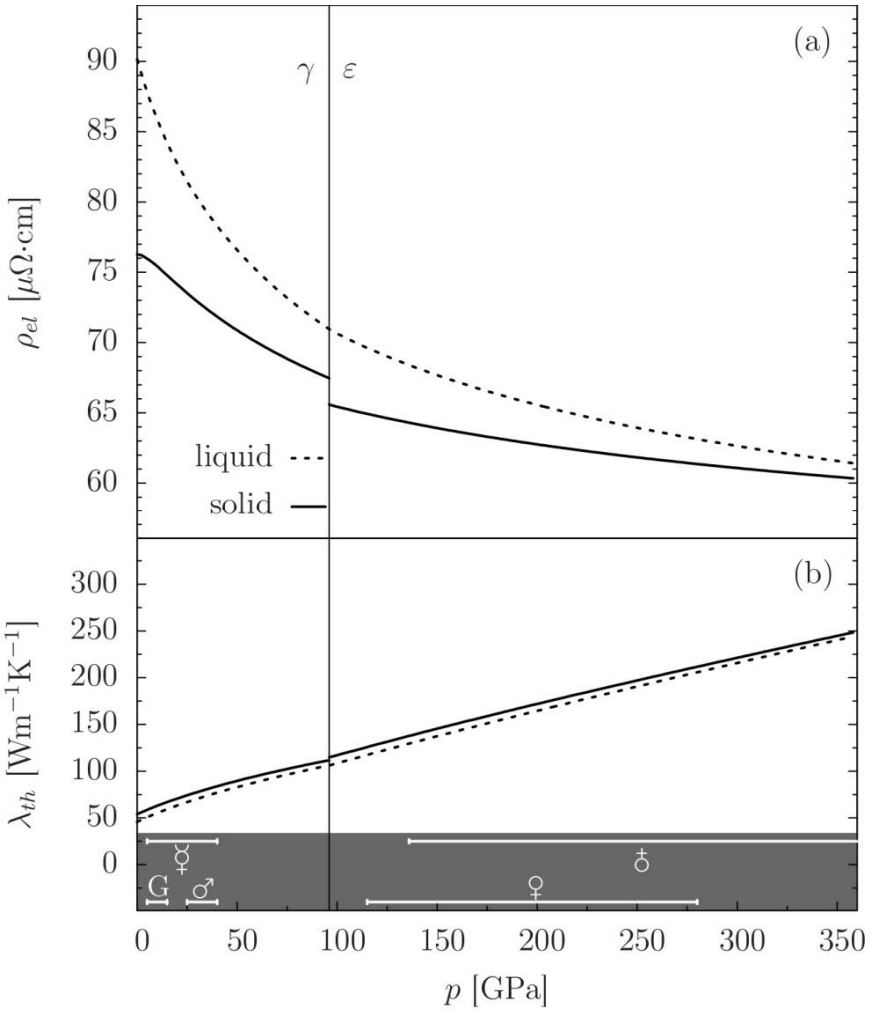

Fig. 3.1-5: (a) Electrical resistivities in both the liquid (dashed curve) and the solid (solid curve) phase of pure iron along its melting curve as a function of pressure. (b) Electronic contributions to the thermal conductivity of both liquid (dashed curve) and solid (solid curve) phase of pure iron along its melting curve as a function of pressure. This has been computed from (a) and the law of Wiedemann-Franz using a power-law fit to the Lorenz number which depends on p and T. Pressure ranges for the cores of terrestrial planets and Ganymede are indicated along the p-axis.

e. *Effect of a single large impact on the coupled atmosphere-interior evolution of Venus (G.J. Golabek, C. Gillmann/Brussels and P.J. Tackley/Zurich)*

We investigate the effect of a single large impact either during the Late Veneer or Late Heavy Bombardment on the evolution of the mantle and atmosphere of Venus. We use a coupled interior/exterior numerical code based on the code StagYY. Single vertical impacts are simulated as instantaneous events affecting both the atmosphere and mantle of the planet by (i) eroding the atmosphere, causing atmospheric escape, and (ii) depositing energy in the crust and mantle of the planet. The main impactor parameters include timing, size/mass, velocity and efficiency of energy deposition. We observe that impact erosion of the atmosphere is a minor effect compared to melting and degassing triggered by energy deposition in the mantle and crust. We are able to produce viable pathways that are consistent with present-day Venus, especially considering large Late Veneer Impacts. Small collisions (< 100 km radius) have only local and transient effects. Medium-sized impactors (100-400 km) do not have much more consequence unless the energy deposition is enhanced, for example by a fast collision. In that case, they have comparable effects to the largest category of impacts (400-800 km): a strong thermal anomaly affecting both crust and mantle and triggering melting and a change in mantle dynamics patterns (Fig. 3.1-6). Such an impact is a global event and can be responsible for volcanic events focused at the impact location and near the antipode. Depending on the timing of the impact, it can also have major consequences for the long-term evolution of the planet and its surface conditions by either (i) efficiently depleting the upper mantle of the planet, leading to the early loss of its water or (ii) imposing a volatile-rich and hot atmosphere for billions of years.

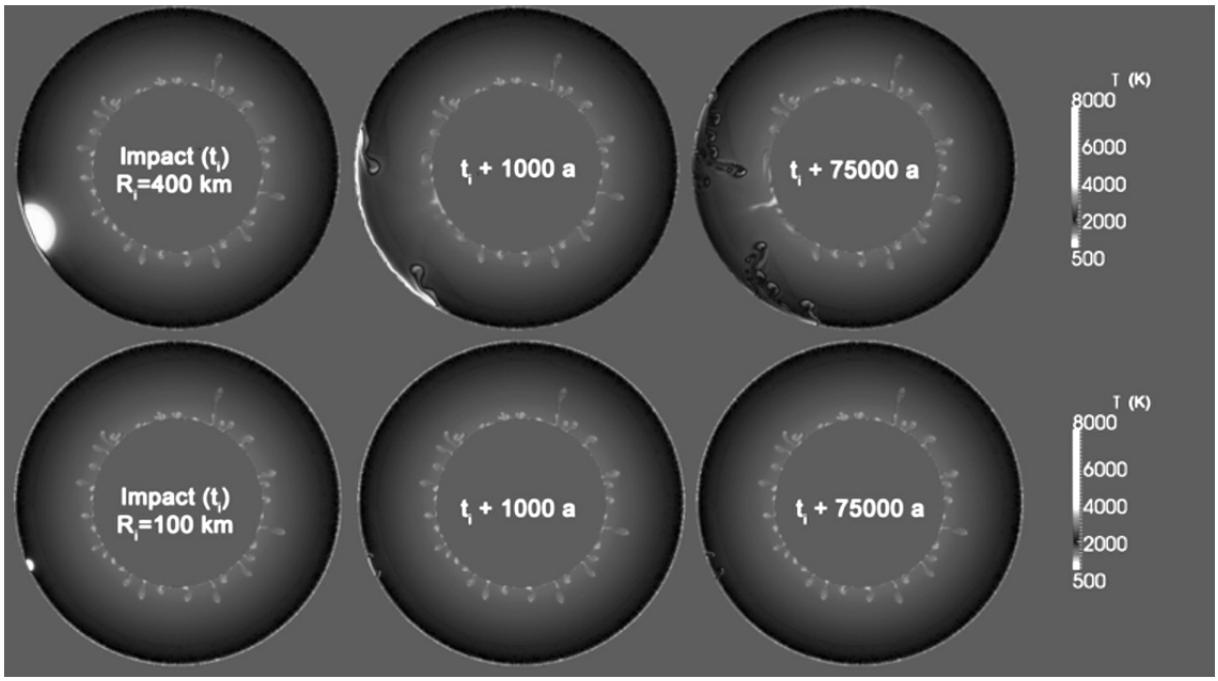

Fig. 3.1-6: Immediate effects on the mantle of Venus for an impactor with (upper panel) 400 km radius and (lower panel) with 100 km radius.

3.2 Geochemistry

The origin, distribution and influence of volatile elements are major themes linking many of the studies in this section. In most cases, however, volatile elements themselves are not under direct investigation but rather other elements are being employed to trace the geochemical effects of fluids, melts and gases stabilised by the presence of volatiles. These themes are apparent in studies on meteorites and Earth's accretion that appear at the start of this section, they recur in studies that examine diamond formation towards the middle of this section and are apparent in the final studies that examine magmatic and ore forming processes.

This section commences with a study describing sequences of mineral overgrowths within the components of an undifferentiated meteorite. It is generally assumed that such minerals grew from cooling nebula gases and that high temperature refractory minerals should be overgrown by volatile minerals that condense at lower temperatures. Under the oxygen-poor conditions at which the meteorite in question formed, however, normally volatile elements such as carbon and sulphur condense to form quite refractory minerals at relatively high temperatures. This brings into question the idea that the material that condensed early from the solar nebula, from which the proto-Earth would have accreted, was poor in volatile elements. The next two studies examine the final stages of Earth's accretion by tracing the behaviour of highly siderophile elements. Highly siderophile elements, such as platinum and iridium, partition strongly into liquid iron in preference to silicate melt. In the first study experiments demonstrate that as sulphur is added to metallic liquid, highly siderophile elements partition less strongly into the metal. In the following study these results are used to demonstrate that the late stage separation of a sulphide rich liquid to the core left an imprint in the highly siderophile element signature of the Earth's mantle. The origin of this signature had been previously attributed to the accretion of an unsampled type of meteorite material.

In the following study thermodynamic models are used to determine the partition coefficients of light elements between the mantle and core at lower mantle conditions. These conditions are experimentally very challenging and such models, that combine numerous types of thermodynamic data, are important for resolving conflicting experimental results. The final study dealing with the early Earth looks at the effect of pressure on the oxidation state of iron in silicate melts. An early magma ocean on the Earth would likely have been in equilibrium with core forming iron metal at its base and if the magma ocean were shallow this would constrain the ferric iron content of the magma to be very low. The small ratio of ferric (Fe_2O_3) to ferrous (FeO) iron in the magma would have established a general low oxidation state within the mantle. If the magma ocean extended into the deeper mantle, however, it is possible that higher magma ferric iron contents would be in equilibrium with the metal, as is the case for several high-pressure mineral phases. The experiments in this study indicate that a magma ocean extending to approximately 500 km would not contain raised ferric iron levels, however. Further experiments will be required to check if this is still the case at greater depths.

The next two studies are designed to understand the formation and capture of garnet inclusions in diamonds from the deep mantle. The first presents a calibration that relates the composition of garnet inclusions to both the depth of entrapment and the composition of the rocks in which the inclusions and diamonds were formed. The results show that diamonds do not form within typical mantle rocks at depths greater than 200 km. Instead they formed within heterogeneities caused either by the deep subduction of oceanic crust or through reactions between partial melts of subducted crust and the surrounding mantle. The following study attempts to reproduce these melting reactions and examine the compositions of garnets produced. In an intriguing experimental observation the melting reaction is found to create a mineral zone that is impermeable to further melt infiltration. This could potentially lead to the formation and preservation of pockets of silica-rich melt deep in the Earth's upper mantle. The final project dealing with the deep Earth's mantle employs in situ x-ray diffraction, performed at a synchrotron facility, to test the pressures calculated using mineral equilibria within particular rock assemblages. The partitioning of some elements between mineral phases is pressure dependent and can be used to estimate equilibration pressures of mantle rocks. The results show some discrepancies in pressures determined for equilibria commonly used for typical mantle rocks and imply that some recalibration is necessary.

The next study deals with the cycling of volatiles along subduction zones. By using a three-layer model for the subducting slab and thermodynamic data to predict phase equilibria in each of these layers to 7 GPa and 1000 °C a quantitative model for the release of H_2O and CO_2 at different subduction depth is derived. The results suggest that along common P-T trajectories to 200 km depth only the serpentinized harzburgite layer completely devolatilizes, whereas both the oceanic crust and overlying sediments carry volatiles to greater depth, primarily through the stability of phengite.

A rather controversial topic is investigated in the following contribution. There is a theory saying that some of the hydrocarbons occurring in the Earth's crust are of abiogenic rather than biogenic origin, and that these hydrocarbons formed within the mantle through reaction of methane. Experiments were conducted in diamond anvil cells at up to 4.5 GPa and 1500 °C to see whether oil reacts with the mineral assemblage of mantle rocks, and to what extent this affects the stability of complex hydrocarbons.

The next two studies focus on the behavior of volatiles and metals in upper crustal magma chambers. The first one is an experimental study to determine the composition of fluids exsolving from mafic magmas that intrude into the base of composite magma chambers and quench against overlying felsic magmas. The results suggest that S, Cl, Cu, Se, Te, Br and Cd are those elements that are most efficiently transferred from mafic magmas to overlying felsic magmas, and thus are best suited to monitor volatile fluxing. The other study focuses on one of the world's largest porphyry Cu-Mo-Au deposits, pursuing the question why this particular magma system became so heavily mineralized. By investigating melt inclusions and sulfide inclusions trapped within phenocrysts, the contents of metals and volatiles in the ore-forming latite magma is reconstructed and compared with corresponding data obtained from

unmineralized arc magma systems. It turns out that the mineralizing magmas at Bingham Canyon and two other porphyry Cu-Mo-Au deposits were neither enriched in metals nor in volatiles compared to their barren counterparts, leading to the conclusion that key to produce economic ore deposits are unusually large magma chambers rather than specialized magmas.

The last contribution of this section is an extension of a previous investigation on the partitioning of vanadium between magnetite and silicic silicate melts (cf. BGI annual report 2011) with the aim to develop an oxybarometer that can be applied also to slowly cooled rocks such as granites. The key for the latter application is that aliquotes of silicate melt and magnetite commonly occur as inclusion within quartz phenocrysts, hence if ablated as entities by LA-ICP-MS they provide original V concentrations and thus allow calculation of V partition coefficients. The experiment data reveal that the partitioning of V between magnetite and melt (DVmgt/melt) depends most strongly on fO_2, followed by melt composition and temperature, whereas pressure and magnetite composition have comparatively little influence.

a. *Origin of EL3 enstatite chondrites (A. El Goresy, Ph. Gillet/Lausanne, Y. Lin/Beijing, M. Miyahara/Hiroshima and E. Ohtani/Sendai)*

Enstatite chondrites (EC) comprise a distinct small group of undifferentiated meteorites characterized by formation at highly reducing conditions and the dominance of stoichiometric troilite as the major sulfide mineral thus attesting their formation at very low fO_2 and also very low fS_2. The low dual fO_2 and fS_2 is constrained by pristine natural buffers in the meteorites, on the one hand through the occurrence of native carbon and on the other hand by the buffered assemblage stoichiometric troilite + kamacite in which the activity of FeS in troilite is close to unity. It was controversially debated whether the highly reduced state of these metorites is indicative of a single common parental asteroid or emerged from specific evolutionary episodes shared among several individual asteroids. The dual buffered fugacity dependence was unfortunately not recognized in several publications over the last three decades. The origin of the primitive members EH3 and EL3 is highly controversial. Achieving a meaningful scheme reflecting the formational conditions, growth sequence of constituents of unequilibrated E-chondrites and origin can only rely on comprehensive documentation of the mineral inventories, their intergrowth and replacement textures, chemical compositions, isotopic signatures, evaluating their stabilities and presentation of detailed intergrowth textures fingerprinting nucleation and growth in the regions where they formed. It is disputed whether the unequilibrated E-chondrite members are solar condensates, resulted from impact melting of already accreted parental proto-asteroids, or emerged from unknown pre-accretionary melts. There are significant discrepancies between thermodynamically predicted gas-solid reactions (specifically theoretically predicted condensation sequences of the earliest solar condensates) and natural mineral assemblages encountered in both unequilibrated EH3 and EL3 chondrites. In contrast, the impact melting scenario is discrepant with the textural relations and nature of the assemblages encountered in both EH3 and EL3 members, their P-T stability fields and their trace element inventories.

Here we report our results on EL3 fragments MS-17 and MS-177 from the polymict asteroid Almahata Sitta, TC_3 that exploded above the Nubian Desert in North Sudan south of Wadi Halfa in October 2008. Both MS-17 and MS-177 contain, in addition to a crowded chondrule-lithology, heterogeneous FeNi metal nodules. FeNi metal nodules consist of a conglomerate of individual concentrically zoned oblong or round metal micro-pebbles thus indicating cold accretion of solid micro-pebbles (Figs. 3.2-1). Metal micro-pebbles vary in size between 15 and 40 µm. Cohenite and schreibersite grains also occur in the metal conglomerate along with feathery fan-shaped graphite and idiomorphic crystals or fragmented sinoite (Si_2N_2O) and fluffy grains of alabandite and troilite (Fig. 3.2-1). This texture of metal

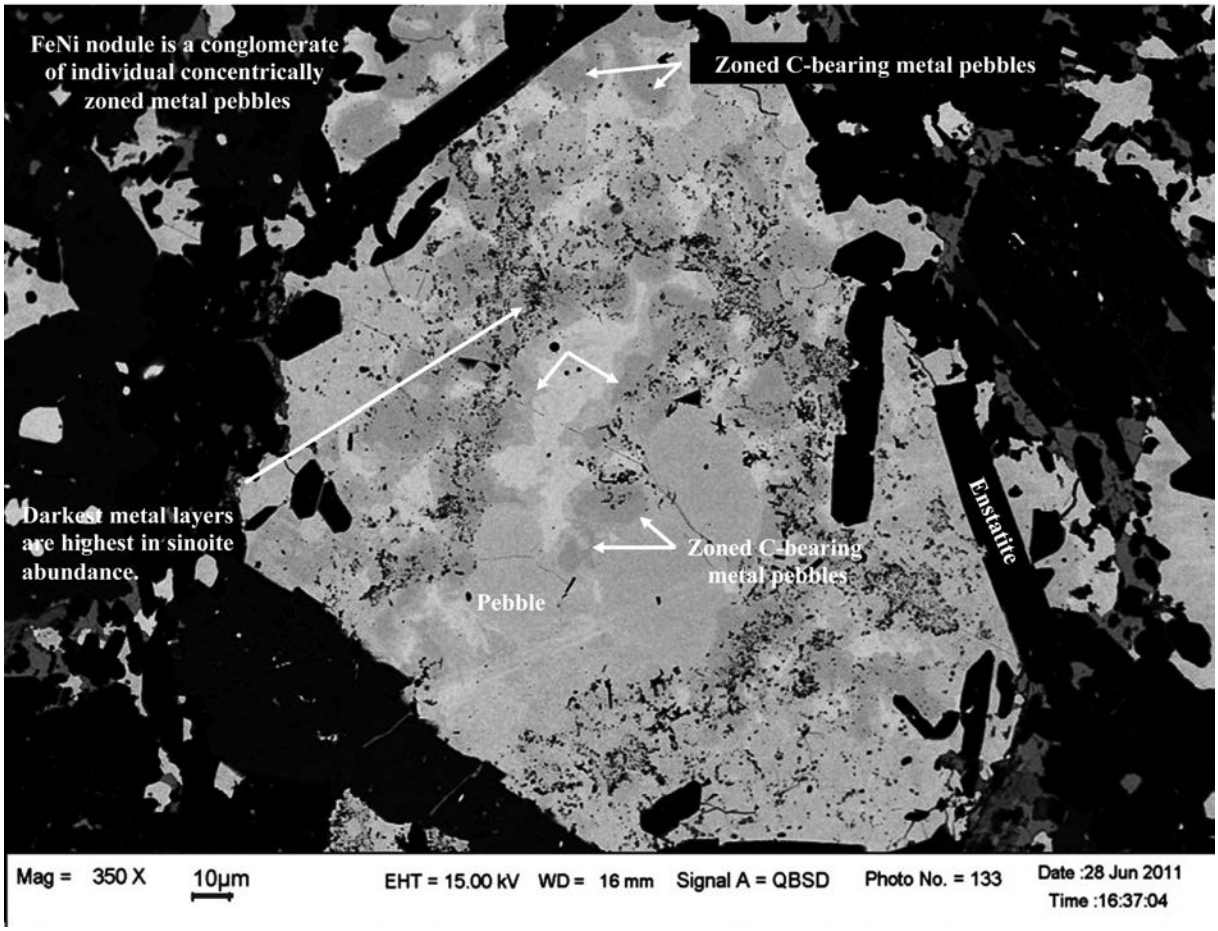

Fig. 3.2-1: BSE-SEM photograph of a metal nodule from the EL3 fragment MS-17 demonstrating the heterogeneous nature and the high abundance of concentrically zones C-bearing metal pebbles (white arrows) and high abundance of micro-crystallites of sinoite mainly in the areas with low contrast.

nodules in E-chondrites is novel and was never encountered in previously investigated Antarctic EL3 chondrites or recognized in Almahata Sitta EL3 chondrites. The metal phase reveals very small variation in its Ni and Si-contents (6.33- 7.30 wt. % Ni and 0.88-1.65 wt. % Si, respectively) with compositional totals below 98.7 wt. % suggestive of occurrence of a

light element. These minor variations in Ni- and Si-contents cannot account for the stark brightness variations observed (Figs. 3.2-1). Cores of the micro-pebbles depict lower brightness in BSE-SEM images than their rhythmically succeeding surrounding metal layers and rims, strongly suggesting the presence of some light elements presumably carbon (Fig. 3.2-1). The presence of shapeless cohenite patches strongly suggests the occurrence of carbon in solid-solution in the metal phase, in agreement with the Fe-C phase relations at ambient pressure. Ion mapping by nanoSIMS 50L revealed qualitative evidence for the presence of heterogeneously distributed ^{12}C in solid solution in the metal that needs to be quantified through use of reliable Fe-C alloy standards by nanoSIMS. Several nodules contain successive metal layers each decorated with sinoite crystallites (Fig. 3.2-2). The majority of the micro-pebbles are also decorated with µm-sized sinoite crystallites. Carbon isotopic investigations of graphite morphologies reveal clear evidence for dichotomy of $\delta^{13}C$ graphite feathers in the metal nodules ($\delta^{13}C$ = -6 to -26‰) and graphite books in the chondritic lithology ($\delta^{13}C$ = -2 to -8‰). Sinoite idiomorphic crystals or their fragments are tightly overgrown by feathery graphite, suggesting increase in the C/O ratio after nucleation and growth of sinoite. This novel finding attests to a variable C/O ratio in the medium in which the metal nodules grew.

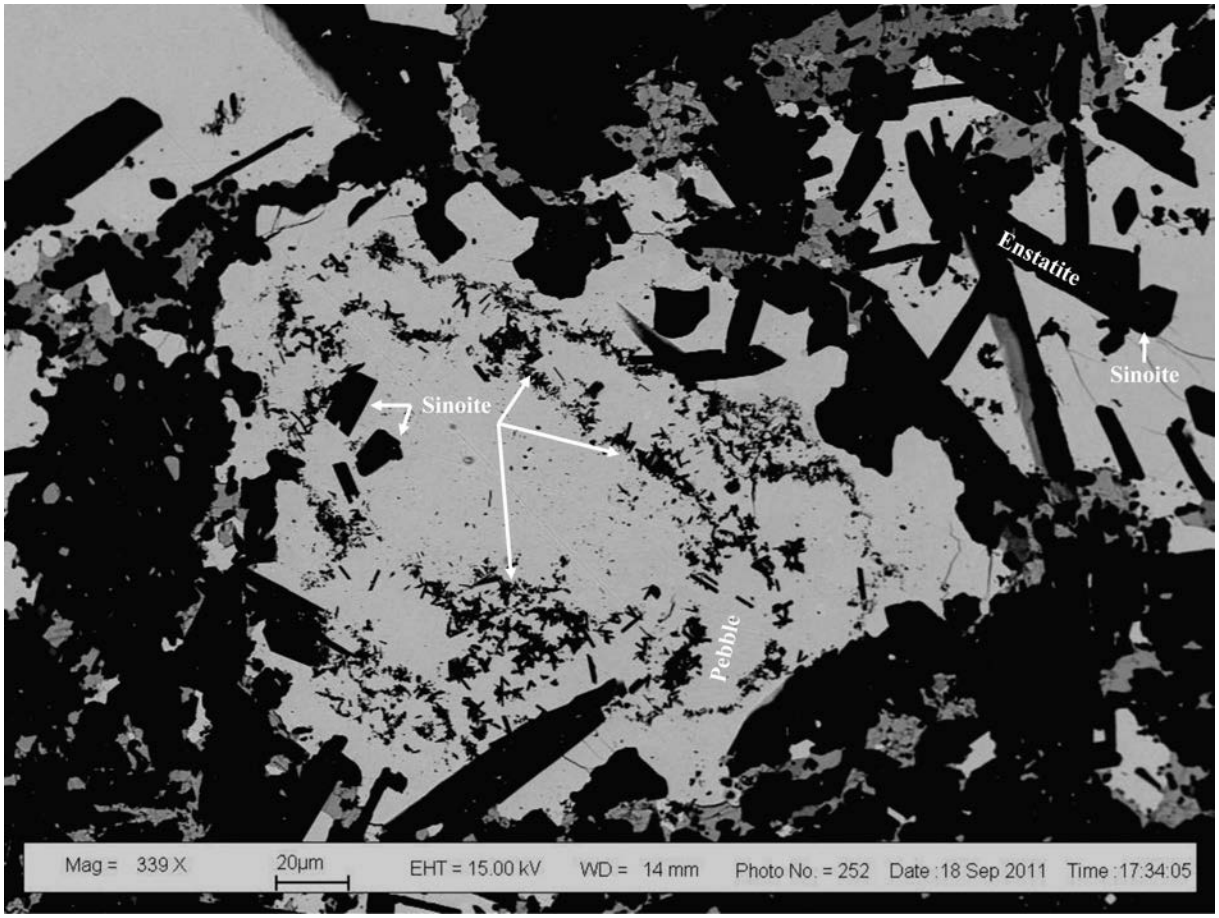

Fig. 3.2-2: A BSE-SEM photograph of a metal nodule from MS-177 clearly showing the individual metal pebbles and distinct layers in the nodule. Each metal object is decorated by sinoite crystallites.

The petrographically disclosed conglomerate of micro-pebbles, their decoration by sinoite crystallites and specifically the heterogeneity of the C-isotopic compositions of feathery graphite even in the same metal nodule is conducive of a lack of isotopic equilibration. We consider these results as stark evidence against any melting episode pre- or post-accretionary. We identified the following four metal-rich nodule types, all of which contain FeNi metal alloys as the major constituent:

(1) Nodules dominated in their interior by large stubby crystals (up to 60 μm) and prisms of sinoite (Si_2N_2O) and minor enstatite prisms. This type is more abundant in MS-177 than MS-17, (2) Metal nodules with inclusions of idiomorphic prismatic sinoite crystals that in turn entirely enclose rounded oldhamite fragments, (3) Metal nodules with a variety of mineral constituents consisting of individual wickerwork of idiomorphic, loosely touching sinoite prisms. These nodules also contain lawrencite ($FeCl_2$) and fanning feathery graphite. These graphite fans aren't in contact with any taenite thus negating their formation during the taenite-kamacite inversion. (4) Nodules enclosing crystallographically-controlled epitactic or topotactic intergrowth of oldhamite and sinoite encapsulated in enstatite and/or diopside. All the metal nodules in MS-17 and MS-177 are not homogeneous individual kamacite per se. They either consist of a heterogeneous conglomerate of individual small metal pebbles of variable sizes between 10 and 25 μm whereby each pebble depicts multi-zoned concentric metal layers with different brightness in BSE suggestive of variable concentrations in light elements in the different layers, or show an interior metal nucleus occasionally decorated by micron-sized sinoite crystals that is surrounded by metal shells many of which are decorated by sinoite crystallites. Remarkably, the interiors of many metal pebbles show lower brightness in BSE than the surrounding layers, strongly suggesting higher concentration of a light element presumably carbon. The individual metal nodules occasionally enclose nests of gently touching prismatic sinoite crystallites. Many blebs are also decorated on their exterior surfaces with micron-sized sinoite grains. A large number of metal nodules enclose fractured cohenite, feathery fan-shaped graphite, and submicron-sized sinoite but no kamacite-cohenite eutectic intergrowth, thus negating melting and quenching of C-bearing metal melts. Every nodule is surrounded by a fluffy sulfide-metal belt consisting of major idiomorphic troilite single crystallites, minor alabandite and FeNi metal fragments. We encounter in separate metal nodules two distinct and novel nucleation and growth sequences involving oldhamite, sinoite, enstatite, diopside and graphite: (1) The sequence **oldhamite ⇨sinoite ⇨enstatite ⇨diopside** and (2) **oldhamite ⇨sinoite ⇨graphite ⇨enstatite ⇨diopside.** These two sequences were never encountered in the same metal nodule. The delicate textures involved in the sequences and the lack of deformation of graphite or its inversion to diamond indicate that they are not impact-related but nucleated, accreted, and were then overgrown by the metal which were sequestered in different FeNi metal nodules, followed in the final stage by accretion of the nodules together with chondrules in the EL3 conglomerate. This hints to an abrupt increase in the C/O ratio of the medium from which the second sequence emerged.

b. *The significance of sulphur for the highly siderophile element budget of the Earth's mantle (V. Laurenz, D.C. Rubie, D.J. Frost, S.A. Jacobson and A.K. Vogel, in collaboration with A. Morbidelli/Nice and H. Palme/Frankfurt)*

The highly siderophile elements (HSEs - Re, Os, Ir, Ru, Pt, Pd, Rh, Au) are important tracers of processes involving metal-silicate equilibria such as the formation of Earth's core. It is generally considered that the HSEs were depleted from the Earth's mantle by core-forming metal and were subsequently replenished by a chondritic late veneer. However, the observed HSE mantle abundances, especially the suprachondritic Pd/Ir and Ru/Ir ratios, cannot be reproduced by any known meteorite group, bringing into questioning how the HSE abundances were established. A possible solution could be the presence of light elements in the core-forming metal, since light elements such as O, Si and S entering the core may have affected the partitioning behaviour of trace elements. For the behaviour of the HSEs sulphur potentially plays an important role, as they are also strongly chalcophile elements. Sulphur may influence the behaviour of the HSEs during core formation in two ways: Either as S dissolved in the core-forming metal, or through the formation of an immiscible FeS sulphide melt, which segregated to the core.

In order to investigate the effect of S on the behaviour of the HSEs during core formation, we performed two different sets of high *P-T* experiments. We studied the effect of S on HSE metal-silicate partitioning by equilibrating a peridotite melt with a range of compositions along the Fe-FeS binary phase diagram at constant *P* (11GPa) and *T* (2200 °C). Furthermore, the *P-T* dependence of HSE sulphide-silicate partitioning was investigated by equilibrating FeS sulphide melt with molten peridotite at pressures from 7 to 21 GPa and temperatures between 2100 °C and 2400 °C. All experiments were performed in a multianvil apparatus using single crystal MgO capsules. Major element compositions of the run products were analysed by electron microprobe, whereas HSE and S abundances in the silicates were determined using LA-ICP-MS.

Results from metal-silicate partitioning experiments show that the HSEs become less siderophile with increasing S-concentration in the metal. This effect is strongest for Ir, while the influence of S on Pd metal-silicate partitioning is moderate. If S is present, the core-forming metal will be less efficient in removing the HSEs from the Earth's mantle. Our second set of experiments confirms that the HSEs are strongly chalcophile at high *P* and *T*. $K_D^{\text{sulfide-silicate}}$ for all HSEs decrease with increasing *T* although the effect on Pd is weak. With increasing *P* $K_D^{\text{sulfide-silicate}}$ of Ru, Pd and Ir decrease while that of Pt increases (Fig. 3.2-3). The overall result is that at high *P-T* conditions Ru and Pd are less chalcophile than Pt and Ir. From these sulphide-silicate partitioning experiments, we have also determined the sulphur content at sulphide saturation (SCSS) for the peridotite melt composition that we used. As expected from previous studies, S-solubility in peridotite melt decreases strongly with increasing pressure. However, the SCSS in peridotite melt is higher than in basaltic and chondritic (CV3) melt, most likely due to a relatively strong effect of melt composition.

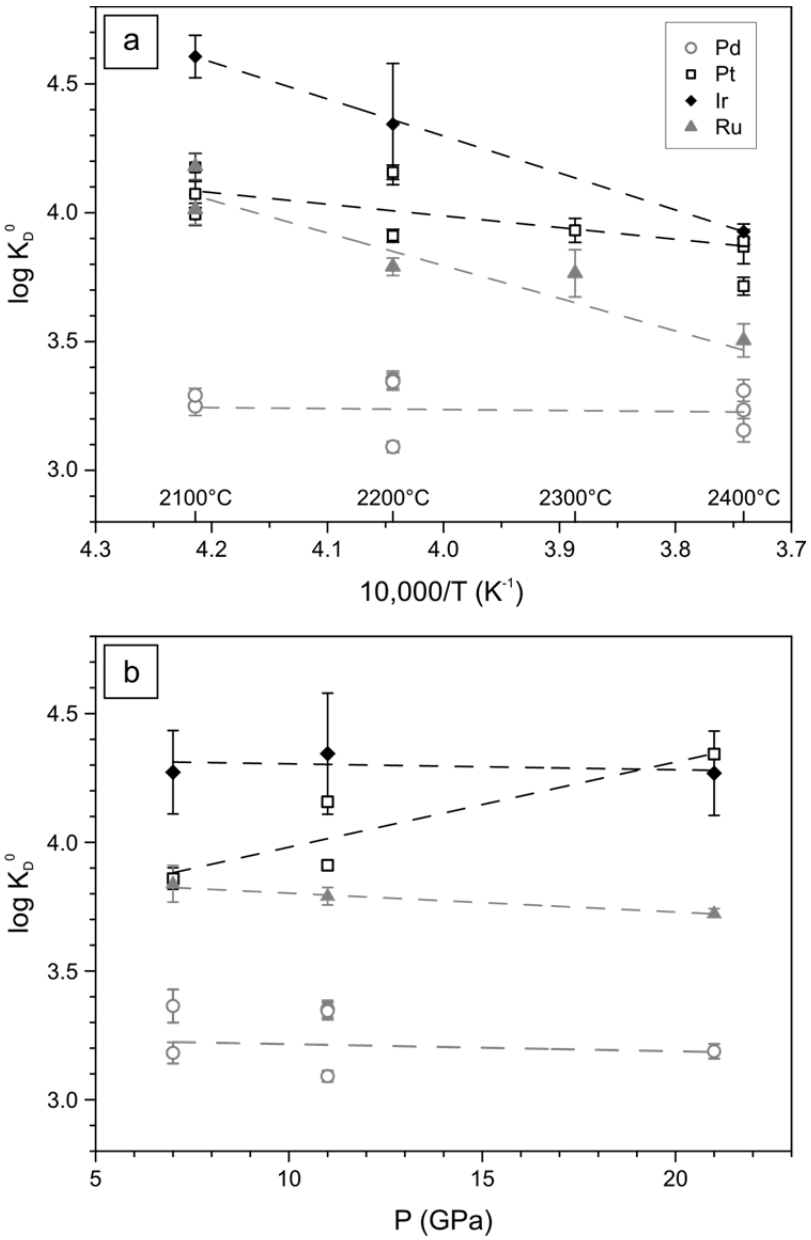

Fig. 3.2-3: Partitioning of HSEs between sulphide and peridotite liquids. Logarithmic values of the exchange coefficient K_D^0 of the HSEs are plotted as a function of inverse temperature (**a**) and pressure (**b**). Overall, at high pressures and temperatures Pd and Ru are less chalcophile than Pt and Ir.

In order to evaluate the effect of S on the abundances of the HSEs in Earth's mantle, we have modelled the partitioning of the HSEs and S in a combined accretion and core formation model using our newly determined metal-silicate and sulphide-silicate exchange coefficients, as well as the determined SCSS (cf. previous contribution by Rubie *et al.*). Results of this model demonstrate that HSE abundances in the Earth's mantle and its suprachondritic Pd/Ir and Ru/Ir ratios can be reproduced, if an immiscible sulphide melt segregated to the core, because Ru and Pd are less chalcophile than Pt and Ir.

c. *The evolution of highly siderophile element concentrations during accretion of the Earth (D.C. Rubie, V. Laurenz, D.J. Frost, S.A. Jacobson and A.K. Vogel, in collaboration with A. Morbidelli/Nice and H. Palme/Frankfurt)*

Moderately siderophile elements, such as Ni, Co, W and Mo, are variably depleted in Earth's mantle, relative to chondritic meteorite abundances, as a consequence of metal-silicate equilibration and segregation during formation of Earth's core. This is because the metal-silicate partition coefficients are different for each element. In contrast, highly siderophile elements (HSEs: Re, Os, Ir, Ru, Rh, Pt, Pd and Au) are present in Earth's mantle in near-chondritic relative abundances. The conventional explanation is that the HSEs were stripped from the mantle by metal-silicate segregation during core formation but were added back to near-chondritic proportions by the late accretion of chondritic material after core formation had ceased.

We have previously modelled the evolution of moderately siderophile element concentrations in Earth's mantle and core by combining a geochemical model of multistage core formation with the results of astrophysical N-body models of planetary accretion. The latter models start with around a hundred embryos (~ Mars-size) embedded in a protoplanetary disc consisting of a few thousand much smaller planetesimals that extends from 0.7 to 10 astronomical units (AU). The compositions of all starting bodies are defined by assuming chondritic relative abundances of non-volatile elements and a variable oxygen content that causes bodies to be more oxidized with increasing distance from the Sun. The planets accrete through embryo-embryo and embryo-planetesimal collisions. Each collision is considered to result in extensive melting, magma ocean formation and an episode of core formation that involves chemical equilibration between liquid metal and silicate. The compositions of the latter are determined by mass balance combined with element partitioning models for Si, Ni and FeO. Several parameters are refined in order to produce a model Earth-like planet with a final mantle composition close to that of Earth's mantle.

We have now extended the accretion/core formation model to include the four highly siderophile elements Pt, Pd, Ru and Ir, based on new element partitioning data (see contribution b. by Laurenz *et al.* in this chapter). The volatile element sulphur has a significant effect on metal-silicate partitioning of HSEs, by making them less siderophile, and is therefore included in the bulk compositions of starting bodies, with bulk S concentrations increasing with distance from the Sun. We consider first the effects of metal-silicate equilibration and segregation on the evolution of Pt, Ru, Pd and Ir in Earth's mantle. We assume that most impacting bodies had undergone early core-mantle differentiation as a result of heating caused by the rapid decay of ^{26}Al. HSE partition coefficients are extremely high (10^6-10^{11}) at the low *P*-*T* conditions of planetesimal differentiation (typically $\leq$0.3 GPa and $\leq$1900 K), which means that the HSEs partitioned almost entirely into their metallic cores during differentiation. The evolution of HSE concentrations in Earth's mantle as a function of time is shown in Fig. 3.2-4. Concentrations become high at an early stage of accretion and increase to exceed Earth mantle values by an order of magnitude by the end of accretion. Contrary to conventional wisdom, accreted metal actually *adds* HSEs to the mantle rather than removing them. The increases result mainly from the accretion of differentiated

planetesimals: at the high *P-T* conditions of metal-silicate equilibration in Earth, partition coefficients are lower (by 2-5 orders of magnitude) than under the conditions of planetesimal differentiation and HSEs are therefore transferred from the metal of impactors' cores to Earth's mantle. In addition, the HSE concentrations are highly fractionated because each has a different metal-silicate partition coefficient, so that final relative abundances are strongly non-chondritic. In addition, based on metal-silicate segregation alone, final mantle sulphur contents also exceed the mantle concentration by a factor of 5-6 (Fig. 3.2-4b).

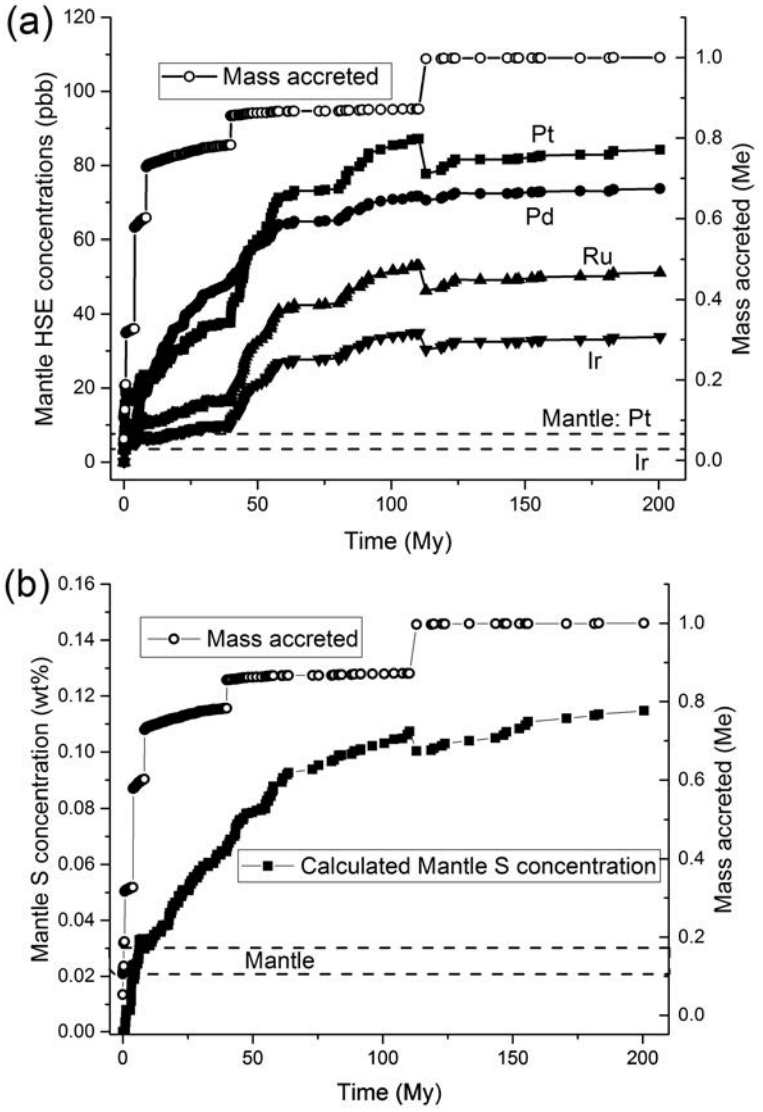

Fig. 3.2-4: Evolution of mantle abundances of HSEs (**a**) and sulphur (**b**) with time, based on metal-silicate equilibration and segregation, during accretion of the Earth-like planet in an N-body accretion simulation. Each symbol represents an impact and "mass accreted" is the accumulated mass after each impact normalized to Earth's current mass (M_e). The final giant impact, at 113 My, increases Earth's mass from $0.872M_e$ to $0.997\ M_e$. Mantle HSE and S abundances are shown by horizontal dashed lines.

The sulphur concentrations shown in Fig. 3.2-4b greatly exceed sulphur solubilities in magma oceans at high pressures. Therefore, exsolution of FeS liquid must have occurred in the magma ocean during Earth's accretion with segregation to the Earth's core. We model this as a pervasive process that also strips HSEs from the magma ocean because the latter elements are chalcophile as well as highly siderophile. Using our new HSE sulphide-silicate liquid partitioning data, Pt and Ir concentrations are reduced to < 1 ppb by this process whereas concentrations of Pd and Ru are 5-10 ppb because these elements are less chalcophile than Pt

and Ir. Finally, when a late veneer is added, with a mass 0.3 % of Earth's current mass, the final HSE concentrations are close to those of Earth's mantle. In particular, calculated Pd/Ir and Ru/Ir are suprachondritic in accordance with mantle values (Fig. 3.2-5). Previous explanations for these suprachondritic ratios have relied mainly on postulating the accretion of meteoritic material that is not present in existing meteorite collections. Here we show that a planetary differentiation process was responsible.

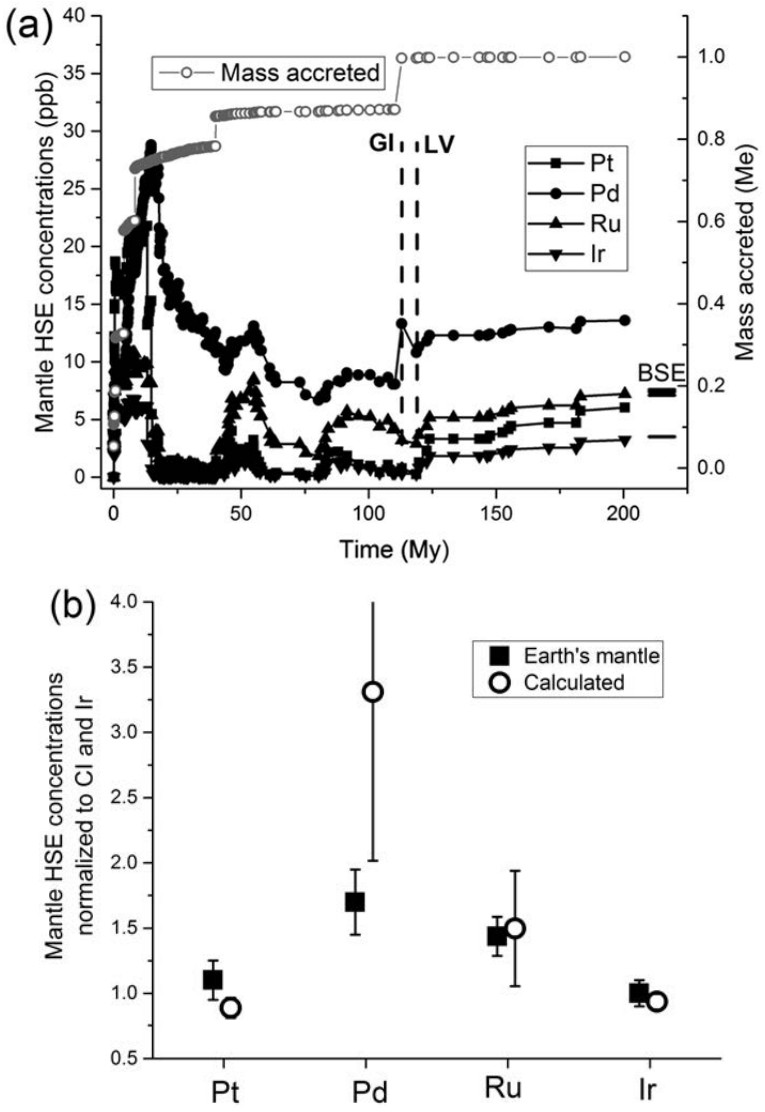

Fig. 3.2-5: (**a**) Evolution of mantle concentrations of HSEs with time based on both metal-silicate and sulphide segregation. The accretion history is also shown. The vertical dashed lines show the time of the final giant impact (GI) at 113 My (that increases Earth's mass by ~ 10 %) and the start of late veneer accretion (LV) at 119 My after sulphide segregation has ceased. (**b**) Final calculated mantle HSE concentrations normalized to Ir and CI compared with the actual values for the Earth's mantle.

d. *Thermodynamic models of light elements in metals and metallic melts (R. Myhill, D.C. Rubie and D.J. Frost)*

The cores of the terrestrial planets are composed of iron-nickel alloys which contain several weight percent of one or more unknown light elements. Likely candidates include Si, O, S, C (and perhaps H). The formation of planetary cores involved iron segregation through silicate magma oceans and solid mantle as a result of impacts between planetesimals and planetary

embryos. The partitioning of light elements into the core affected the volatile abundances in the Earth's mantle, thus controlling the species outgassed during early volcanism, and therefore influencing the composition of the early atmosphere. The presence of light elements in the core today is known from the density-deficit of the core, but the abundances of the light elements are unknown. There is some evidence from seismology that the liquid outer core may be compositionally stratified, but again, the nature and cause of this stratification is unknown.

In this study, we aim to produce the first thermodynamic model for iron-rich metallic alloys and melts containing light elements, which is valid throughout the Earth's mantle and into the core. Previous models have involved various ad-hoc assumptions and extrapolations, which tend to result in unreasonable or even non-physical results at high pressures and temperatures (including fully oxidised cores and negative heat capacities). Here, we first create a database of endmember minerals (Fe, FeO, FeSi, FeS and intermediate compounds) with available experimental data, including order-disorder, magnetic and electronic contributions to the free energy. We then construct liquid models which satisfy 1 bar entropy and volume data and melting curves. Many melting curves are poorly constrained, so where possible we have also employed constraints provided by the entropy and volume of fusion for end-member components. Subregular solution models for iron-light element melts are then constructed from solvus and eutectic data, allowing for changes in the excess properties of mixing with pressure and temperature. The models are then tested using partitioning data from the literature (Fig. 3.2-6).

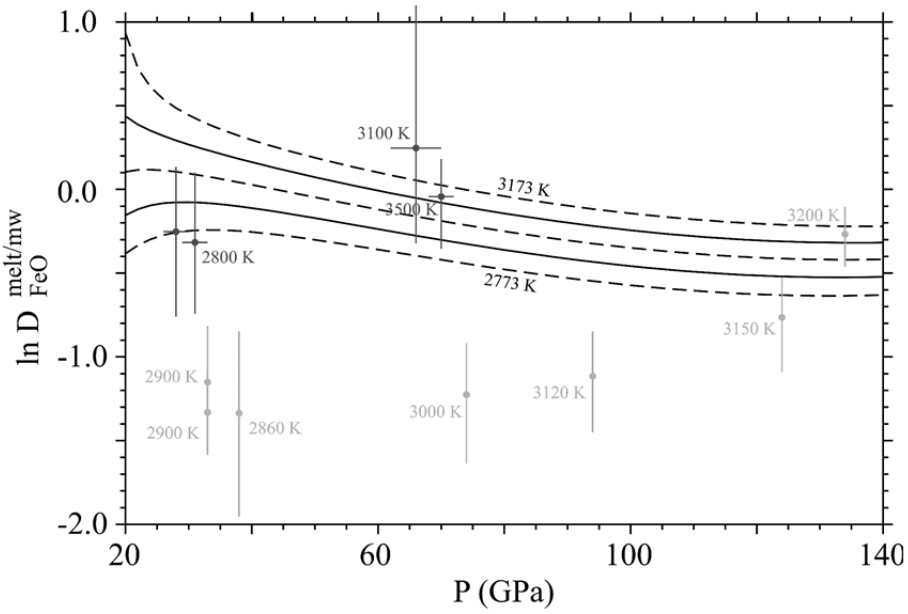

Fig. 3.2-6: Model results for the FeO partition coefficient between liquid iron and $Mg_{0.8}Fe_{0.2}O$ as a function of pressure and temperature, compared with two published experimental studies (black and grey symbols) from the literature.

Figure 3.2-6 shows model calculations for the FeO partition coefficient between iron liquid and magnesiowustite containing 10 mol. % FeO. Although the model is in good agreement with some experimental data, there are large variations between different experimental studies. Models based on well constrained thermodynamic data are, therefore, very important for evaluating these studies. Ultimately these models are important for predicting the chemical evolution of the Earth and other planetary bodies during core-mantle differentiation and can also provide constraints on seismic velocities and densities in planetary cores.

e. *Iron oxidation state in silicate melts at high pressure and the redox evolution of the early mantle (K. Armstrong, D.J. Frost, C.A. McCammon, D.C. Rubie and T. Boffa Ballaran)*

It is well established that during the late stages of accretion, planetesimals would have impacted the early Earth with sufficient energy to create a global magma ocean, within which core forming metal would have separated. If the magma ocean were chemically homogenous throughout its depth, the magmatic ratio of $Fe^{3+}/\sum$ Fe would have been set by metal-silicate equilibrium. Metal would sink through the magma ocean and final equilibration would have occurred at the base. At shallow pressures silicate melts in equilibrium with liquid metal contain practically no Fe^{3+}. However, it is possible that silicate melts, like many silicate minerals start to favour the formation of Fe^{3+} over Fe^{2+} at high pressure. This could potentially allow much higher $Fe^{3+}/\sum$Fe ratios be stable in equilibrium with iron metal at the base of the magma ocean. This would cause higher melt Fe_2O_3 levels to become increasingly stable at lower oxygen fugacities with increasing pressure. If a relatively high melt $Fe^{3+}/\sum$Fe ratio was in equilibrium with iron at the base of a deep magma ocean then a redox gradient would result where the top of the magma ocean would be at a much higher relative oxygen fugacity compared to the base. Crystallisation of this magma ocean would render a mantle oxygen fugacity gradient similar to that in the Earth today. This scenario is in contradiction, however, with existing experimental results, which indicate that at a fixed fO_2, the $Fe^{3+}/\sum$ Fe ratio of a silicate melt decreases with pressure, at least up to 3 GPa. In this study experiments have been performed to examine whether this trend reverses at a sufficiently high pressure for a redox gradient to exist in a magma ocean.

The starting material was an andesitic melt composition, chosen to promote the formation of glass on quenching, which was prepared by sintering in air such that most of the iron remained as Fe_2O_3. The powder was sealed in Pt capsules with the fO_2 buffered by the addition of ~ 20 wt. % Ru + RuO_2 (mixed 1:1 by weight). Experiments were performed in the 5000 tonne multianvil press at 10 and 17 GPa and 1900 and 2100 °C respectively for approximately one hour. Recovered capsules were analysed using the electron microprobe, XRD and Mössbauer spectroscopy. Both samples melted completely during the experiment but crystallized on quenching. XRD analyses revealed that the dominant phase in both samples is clinopyroxene. Mössbauer spectra showed a dominant Fe^{3+} doublet with a less intense Fe^{2+} doublet and a Fe^{3+} magnetic sextet. The quantitative determination of the bulk $Fe^{3+}/\sum$Fe ratio of both samples measured is 0.60 ± 0.05.

Figure 3.2-7 summarises the results of this study and previous work all performed with the same melt bulk composition and at an oxygen fugacity fixed by the Ru-RuO_2 buffer. Previous unpublished work performed in a multianvil at the BGI at 6 and 8 GPa is shown. Up to 8 GPa it was possible to quench the silicate liquid to a glass, however, by 10 GPa the liquid crystallises during quenching. The question remains as to how faithfully the $Fe^{3+}/\sum Fe$ ratio of the crystalline material reflects that of the initial melt. XRD analyses indicate that clinopyroxene is the only iron bearing phase. Although Mössbauer spectra show that a magnetic phase is also present, the proportion of Fe^{3+} in this phase is small and has also been included in the bulk measurement. Similarity between results at 8 and 10 GPa on glass and crystallised samples respectively, seems to indicate that crystallisation makes little difference to the results. Although the $Fe^{3+}/\sum Fe$ ratio does not continue to decrease at pressures between 8 and 17 GPa, there is no evidence that it increases. Over this pressure range, at least, there appears to be no tendency for silicate melt $Fe^{3+}/\sum Fe$ ratios to increase at a constant relative oxygen fugacity. Significantly higher pressures may be required to induce a reversal in this trend.

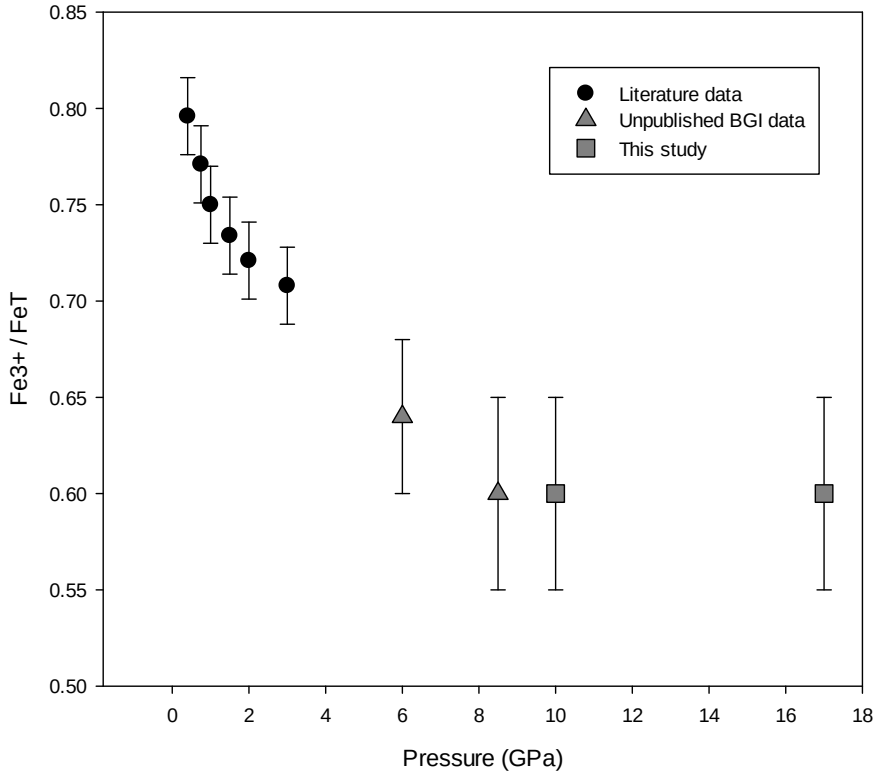

Fig. 3.2-7: The $Fe^{3+}/\sum Fe$ ratio of andesitic melt as a function of pressure at an oxygen fugacity buffered by Ru and RuO_2. Literature data and previous BGI experimental results are shown. While these previous Mössbauer measurements were performed on quenched glasses, the current study analysed crystallised quench materials. No reversal in the trend of decreasing melt Fe_2O_3 content with increasing pressure is observed but the flattening out of the trend raises the possibility that a reversal may occur at higher pressures.

f. *The depth of sub-lithospheric diamond formation and the redistribution of carbon in the deep mantle (C. Beyer and D.J. Frost)*

The existence of garnet inclusions within diamonds that are silica rich due to the presence of a majorite component provides one of the only robust indicators that these samples had a sub-lithospheric origin. Measurable proportions of the $M_3(MSi)Si_3O_{12}$ majorite component, where M is a divalent cation, the $Na_2M(Si_2)Si_3O_{12}$ sodium-majorite component, and the $Na_2M(Ti_2)Si_3O_{12}$ sodium-titanium-majorite component only occur in garnets equilibrated at depths > 150 km. We have calibrated the composition of majoritic garnets for use as a barometer across a range of basaltic, pyroxenitic and peridotitic bulk compositions. Up to 5 individual starting powders were loaded into spark-eroded multi-chamber AuPd capsules. Experiments were run in a multianvil apparatus between 6 and 16 GPa, 1000-1400 °C. A total of 38 garnet analyses were collected across the different bulk compositions. Using analyses from previous experiments on basalt (n=16) and peridotite (n=38) compositions, a final data set was assembled of 92 experiments in the range 6-20 GPa, 900-2200 °C. The barometer reproduces the experimental pressures with a standard deviation of 0.86 GPa, which could not be improved by accounting for the concentrations of any other cation.

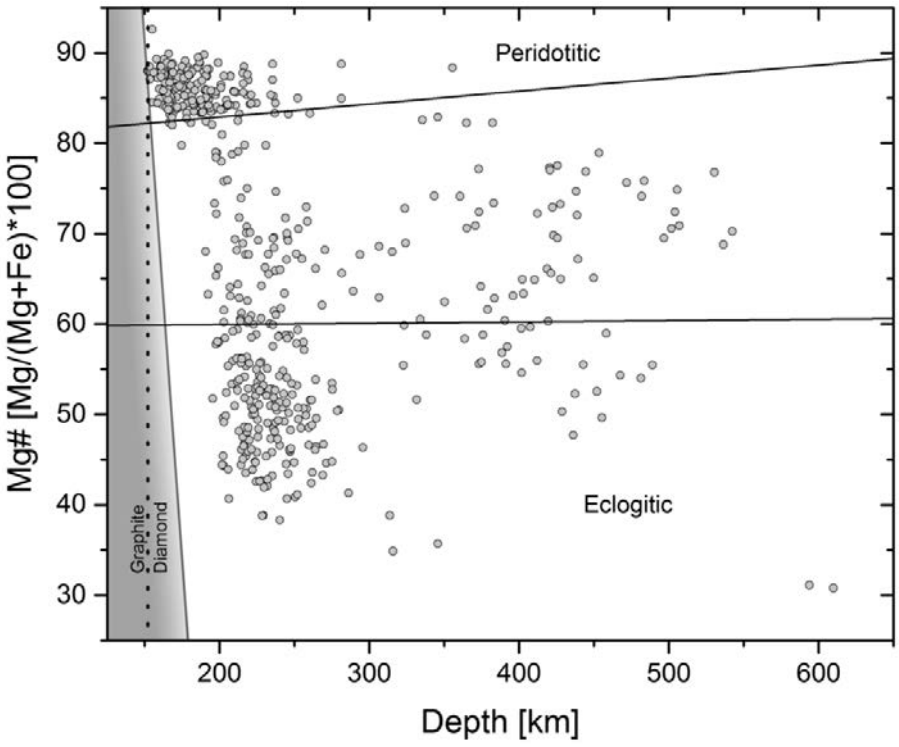

Fig. 3.2-8: The Mg# (Mg/[Mg+Fe]*100) of natural majoritic garnet inclusions in diamonds as a function of depth determined using the barometer calibration. The upper solid line defines the field of peridotites, whereas the lower solid line defines the field of eclogites. Between these fields lies a range of transitional compositions. The edge of the shaded zone indicates the minimum pressure at which the barometer can be employed.

The barometer was used to determine the formation pressures for 554 majoritic garnet inclusions found in diamonds worldwide. In figure 3.2-8 the formation depth of these inclusions is plotted as a function of Mg# (Mg/[Mg+Fe]*100) in order to differentiate between the types of rocks with which the inclusions would have been in equilibrium. The key finding is that inclusions with eclogitic and transitional affinities appear to originate from depths > 200 km, whereas, the majority of peridotitic inclusions originate from depths shallow than this.

g. *The compositions of garnets formed through the interaction of eclogitic partial melts with peridotite assemblages (Zs. Pintér, A. Rosenthal, D.J. Frost and C.A. McCammon)*

Garnet inclusions in diamonds are key to understanding the origin of diamond forming processes in the deep Earth's mantle. Previous studies have proposed that the majority of such inclusions form within two main lithologies that have either eclogitic or peridotitic affinities. Eclogitic garnets are more calcic, Cr-poor, and exhibit an higher Mg#, Mg/(Mg+Fe), than peridotitic garnets. In addition, experiments show that with increasing pressure the majorite substitution mechanism, $M^{2+} + Al^{3+} = Na^{+} + Si^{4+}$, where M^{2+} = Mg, Fe, Ca or Mn, dominates in garnets formed in eclogitic compositions, while the $2Al^{3+} = Si^{4+} + M^{2+}$ mechanism dominates in peridotitic garnets. Both substitutions occur as pyroxene components dissolve into garnet with increasing mantle depths. A number of natural garnet inclusions in diamonds, however, have compositions that are transitional between eclogitic and peridotitc end members. Although the origin of these garnets is unclear, it has been proposed that they may result from hybridization reactions as eclogitic partial melts react with surrounding peridotite rocks. These reactions result principally in the formation of orthopyroxene from olivine and form layers that can be generally described as pyroxenitic.

To determine whether such hybridization reactions can produce transitional garnets a series of experiments containing fertile peridotite and adjacent eclogitic layers have been performed. Layers were also doped with Ir metal to act as a redox sensor. Experiments were performed between 3 and 8 GPa and 1100-1660 °C, using a multianvil apparatus. The compositions of the resulting minerals and melts were analyzed using an electron microprobe.

Similar to previous studies, the eclogite unit starts to melt at lower temperatures than the peridotite such that small degree siliceous eclogitic partial melts infiltrate the sub solidus peridotite. This creates a reaction zone where orthopyroxene forms as the melt reacts with olivine in the peridotite. This forms a hybrid lithology rich in orthopyroxene but containing minor garnet and clinopyroxene, which is referred to as an orthopyroxene-rich reaction zone (Fig. 3.2-9). Between 3 and 5 GPa, however, only a very narrow reaction zone was found to form, as this layer acted as a very effective melt sealant that prevented any further reactive infiltration of melt with the peridotite. As shown in Fig. 3.2-9 significant degrees of partial melt are retained behind a very thin layer of orthopyroxene and prevented from further

reaction with olivine. Such sealing was effective in experiments performed for several days. The sealed off eclogitic melt fractions are, however, no longer in equilibrium with the original eclogite assemblage as they have reacted with olivine to form orthopyroxene. The residual eclogite, therefore, reequilibrates with this melt, forming what is referred to here as an eclogite-dominated reaction zone with a distinctive mineral chemistry. A large degree of chemical variation occurs within this eclogitic reaction layer. Figure 3.2-10 shows garnet analyses from different layers in experiments performed between 5 and 8 GPa. The majorite substitution trends expected in peridotitic and eclogitic assemblages are indicated. Hybrid garnet compositions are produced as a result of melt interaction and plot in the transitional region between the major trends as observed in natural inclusions in diamonds. However, the transitional hybrid garnets form within the eclogite-dominated reaction layer and not within the orthopyroxene rich layer, which follows the peridotitic substitution trend.

Melt reequilibration of the eclogite only occurred in these experiments because the orthopyroxene layer sealed in the melt. If this mechanism occurred in the mantle large degrees of melt could be trapped behind orthopyroxene layers as mantle containing mafic heterogeneities up-welled. Although this melt sealing mechanism persisted in the current experiments for many days, it is possible that in the mantle deformation processes would lead to more effective melt infiltration.

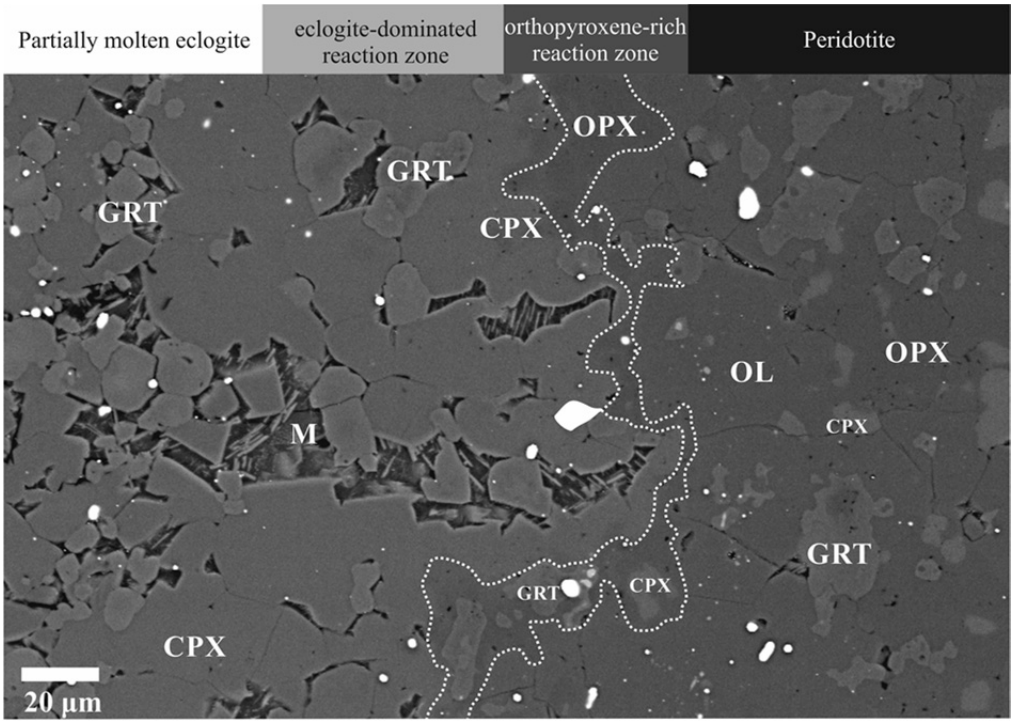

Fig. 3.2-9: SEM image of an experiment from 5 GPa, 1250 °C, containing partially molten eclogite (left), an eclogite-dominated reaction zone, an orthopyroxene-rich reaction zone and a subsolidus garnet peridotite (right). The orthopyroxene-rich zone acts as an effective melt seal. OL: olivine, OPX: orthopyroxene, CPX: clinopyroxene, GRT: garnet, M: melt.

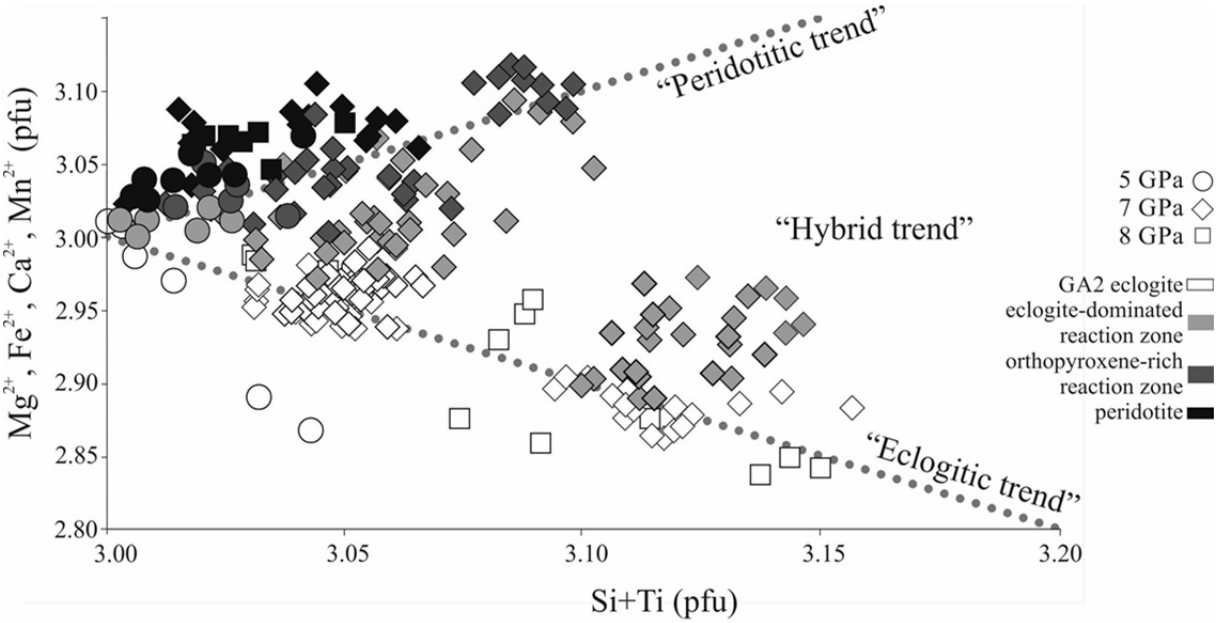

Fig. 3.2-10: Majorite garnet substitution trends for garnets produced within peridotite-eclogite layered experiments. The experimentally produced garnets are differentiated based on the reaction zone in which they formed. Garnets formed in orthopyroxene rich reaction zones follow the substitution trend expected for peridotites, only garnets from the eclogite dominated reaction zone have transitional hybrid compositions that lie between the two trends, as found as inclusions in some diamonds.

h. *Use of* in situ *X-ray diffraction for the pressure calibration of geobarometer equilibria (C. Beyer, A. Rosenthal, R. Myhill and D.J. Frost, in collaboration with W. Crichton/Grenoble, T. Yu and Y. Wang/Chicago)*

Geobarometers are essential in Earth sciences for determining the last equilibration depth of mantle derived rocks, and are important for determining the Earths heat flux and the depth at which metasomatic processes operate such as those that lead to diamond growth. Some barometers are routinely used at pressures up to 6 GPa, where pressure cannot be calculated directly in high-pressure devices due to frictional losses, but must be calibrated against known phase transitions. These known phase transitions have, in turn, been generally calibrated against volume equations of state of standard materials using *in situ* X-ray diffraction. A more rigorous approach, however, would be to calibrate barometer equilibria directly using X-ray diffraction analyses of calibrant materials.

In this study a number of petrological geobarometer equilibria have been tested against pressures determined directly using unit cell parameters of calibrant materials (Au, NaCl, MgO, h-BN). By equilibrating a series of geobarometer equilibria while simultaneously measuring pressure through *in situ* X-ray diffraction methods, a number of barometers

employed for both peridotitic and eclogitic rocks have been tested. Multi-chamber rhenium capsules were employed so that a number of geobarometers could be studied in the same experiment. Experiments were performed at the synchrotron facilities APS in Chicago and the ESRF in Grenoble. A modified 14 mm octahedral assembly was used to equilibrate samples between 3 and 13 GPa for 5 hours at 1400 °C. After the experiment the samples were sectioned and analysed using an electron microprobe. Mineral compositions from peridotite and eclogite assemblages were used to determine pressures using several geobarometer equilibria. For both assemblages these barometers employ the Al content of clinopyroxene. Figure 3.2-11 shows pressures determined using *in situ* pressure calibrations compared with those determined using the geobarometers. While the agreement for the eclogitic barometer is very good, pressures calculated for the peridotite assemblage using the mineral analyses are up to 0.75 GPa higher than the *in situ* measurements.

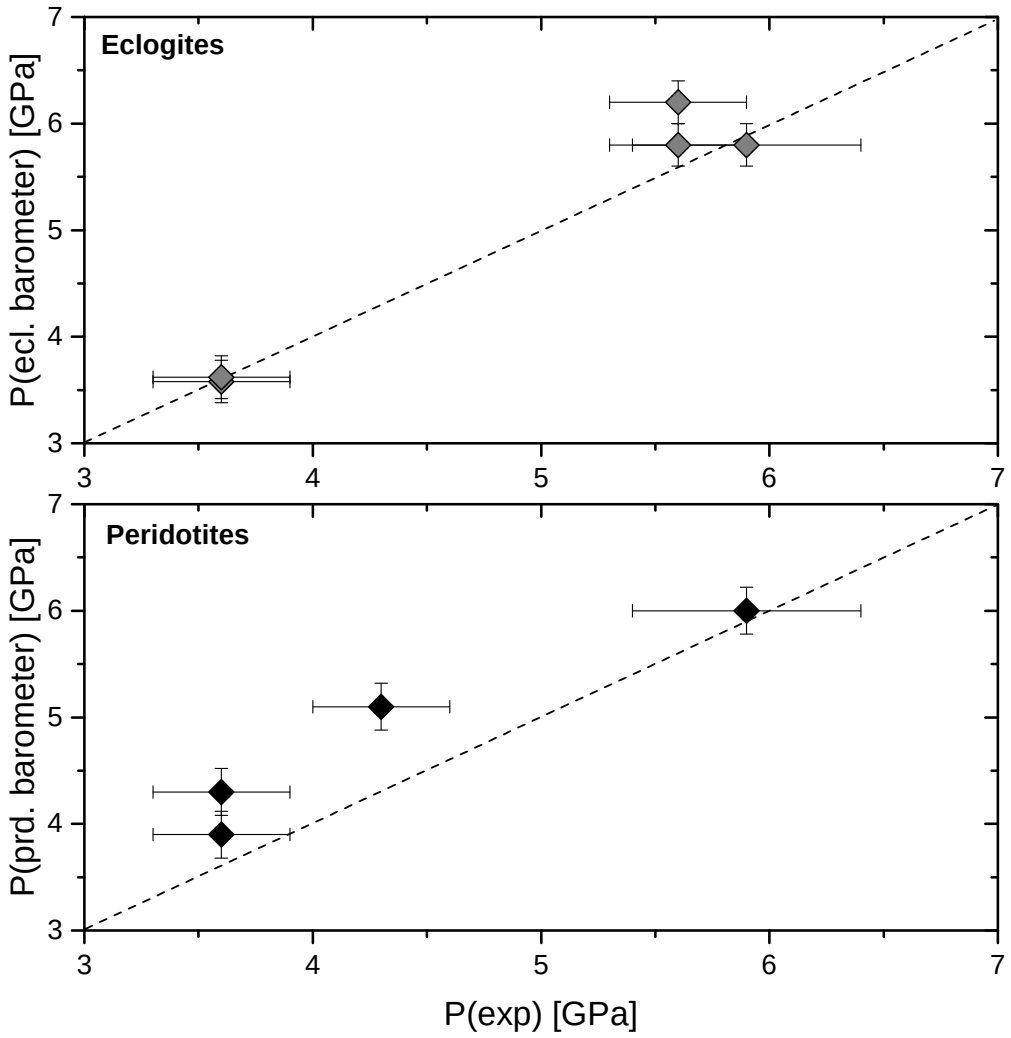

Fig. 3.2-11: A comparison between pressures measured using *in situ* X-ray diffraction (exp) and those determined using mineral equilibria, *i.e.*, geobarometers, for both eclogitic and peridotitic assemblages.

i. *Volatile content of subducting slabs (Z. Chemia/Copenhagen, D. Dolejš/Prague and G. Steinle-Neumann)*

Cycling of volatiles from the surface into the Earth's interior is channeled in subduction zones where the oceanic lithosphere transports a considerable amount of H_2O and CO_2 into the mantle, incorporated in hydrous minerals. Dehydration reactions lead to water cycling into the overlying mantle wedge, partial melting and magmatic activity in oceanic and continental arcs. The extent to which volatiles are also transported to greater depths remains not well characterized, and different lithologies within the slab play varying roles. Here, we use a model of oceanic lithosphere (Fig. 3.2-12) that is divided into three different layers with varying degree of hydration and carbonation. For the 1 km-thick sediments we use a previously established model for global subducting sediments (GLOSS) with ~ 7.7 wt. % H_2O and 3.0 wt. % CO_2. The sediments are the most important source of water that is released at relatively shallow depths. The oceanic crust consists of mid-ocean ridge basalts, gabbros and cumulates extending to a depth of 7 km. Their average composition is represented by primary melt in equilibrium with mantle peridotite that has not undergone subsequent fractionation. To estimate the composition of the bulk oceanic crust (BOC) we have re-evaluated major-element compositions of mid-ocean ridge glasses for incompatible elements and use only the most primitive compositions that are in equilibrium with Fo_{88-91} to be representative of primary melts. The volatile content of BOC is 2.7 wt. % of H_2O and ~ 3.0 wt. % of CO_2, measured in dredged sea floor samples. The dry component of the harzburgitic depleted mantle is computed from a mass balance relation between BOC and the pyrolite primitive mantle with a degree of partial melting of 0.206. The degree of serpentinization is highly variable due to differences in fracturing patterns and channeling of hydrothermal fluids, and we use a uniform value of 6.8 wt. % of H_2O for serpentinized harzburgite (SHB), *i.e.*, one half of the maximum hydration to average a linear decrease from full serpentization to 0 wt. % with depth.

Phase equilibria up to 7 GPa (corresponding to a depth of ~ 200 km) and 1000 °C are calculated for three different lithologies by Gibbs energy minimization using the Perple_X package and dehydration and decarbonation reactions are recorded. GLOSS is initially very close to fluid saturation, and devolatilization rapidly starts by breakdown of zeolites, reaching 5.6-6.1 wt. % H_2O+CO_2 in a blueschist assemblage (Fig. 3.2-13). Along a pressure-temperature subduction path representative for the top of the slab in the Nicaraguan subduction zone further dehydration occurs through chlorite, muscovite and amphibole breakdown. With the nearly univariant breakdown of lawsonite (along a line from 3 GPa and 660 °C to 7 GPa and 880 °C) dehydration stops, as phengite – the only potassium host with constant abundance in the assemblage – carries volatiles to greater depth. By contrast, dehydration in BOC commences with chlorite breakdown to a garnet-amphibolite assemblage over a temperature range of 520-660 °C (Fig. 3.2-13), at a pressure of slightly below 2 GPa along the subduction path at top of the basalt layer. Amphibole breakdown at 710-850 °C represents complete dehydration, but these conditions are not achieved during subduction.

Similar to GLOSS, devolatilization of BOC along characteristic subduction pressure-temperature paths is predicted to remain incomplete, with 2.1-2.2 wt. % and 3.0-3.2 wt. % CO_2 in lawsonite-, phengite-, and carbonate-bearing eclogites.

The partially serpentinized harzburgite (SHB) initially consists of a peridotite assemblage (olivine and clinopyroxene) that is incompletely transformed to chlorite, antigorite, and brucite (Fig. 3.2-13). The phase diagram is characterized by three quasi-univariant dehydration reactions, related to brucite, antigorite and chlorite breakdown. However, along the subduction path dehydration only starts at ~ 4 GPa. The SHB component is the only lithology in the subducting lithosphere that experiences complete dehydration above 5 GPa.

In summary, a separate consideration of different lithologies in the subducting slab emphasizes their different role in volatile release. Only the subducting sediments release a significant amount of H_2O at the onset of subduction while devolatilization of the oceanic crust and harzburgite initiates only at 2.5 GPa, 450 °C and 3.5 GPa and 600 °C, respectively. During subduction to ~ 200 km depth only the harzburgite experiences complete dehydration, while the sediments and basalt carry volatiles to greater depth, primarily through the stability of phengite.

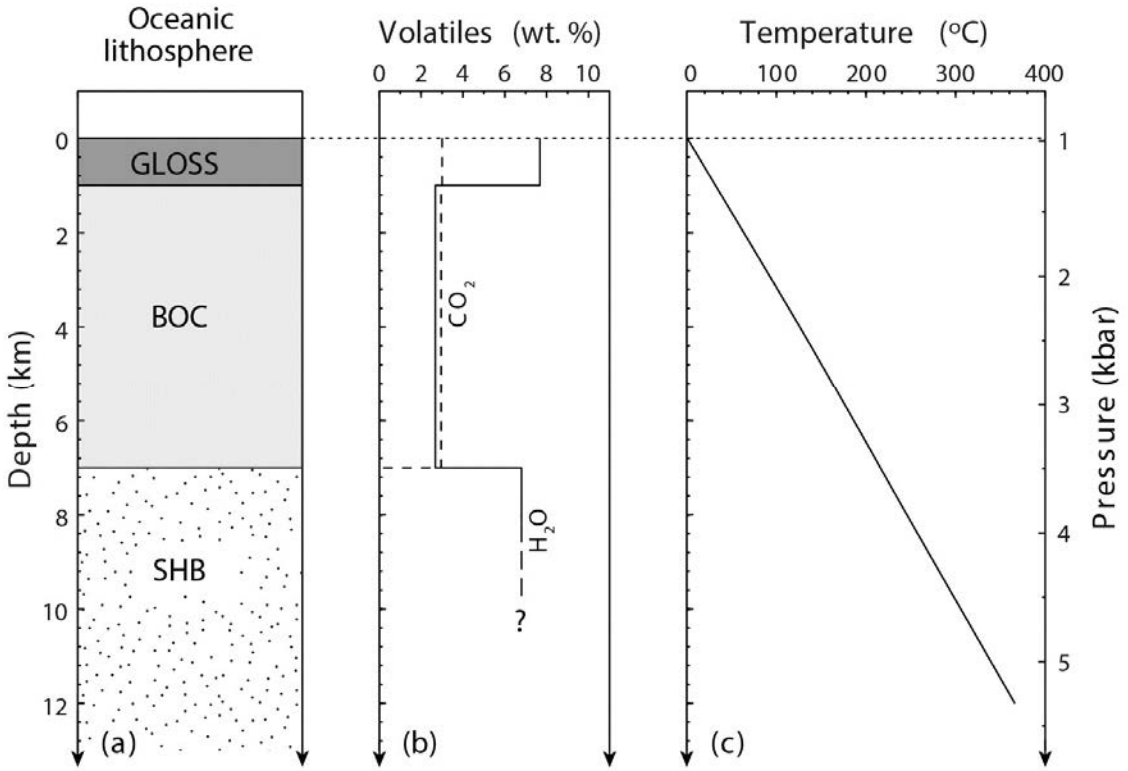

Fig. 3.2-12: Schematic cross section through the oceanic lithosphere indicating (a) the thickness of individual slab layers (GLOSS – global subducting sediments; BOC – bulk oceanic crust; SHB – serpentinized harzburgite), (b) the initial volatile budget, and (c) the initial steady state temperature profile for the Nicaraguan slab at the onset of subduction.

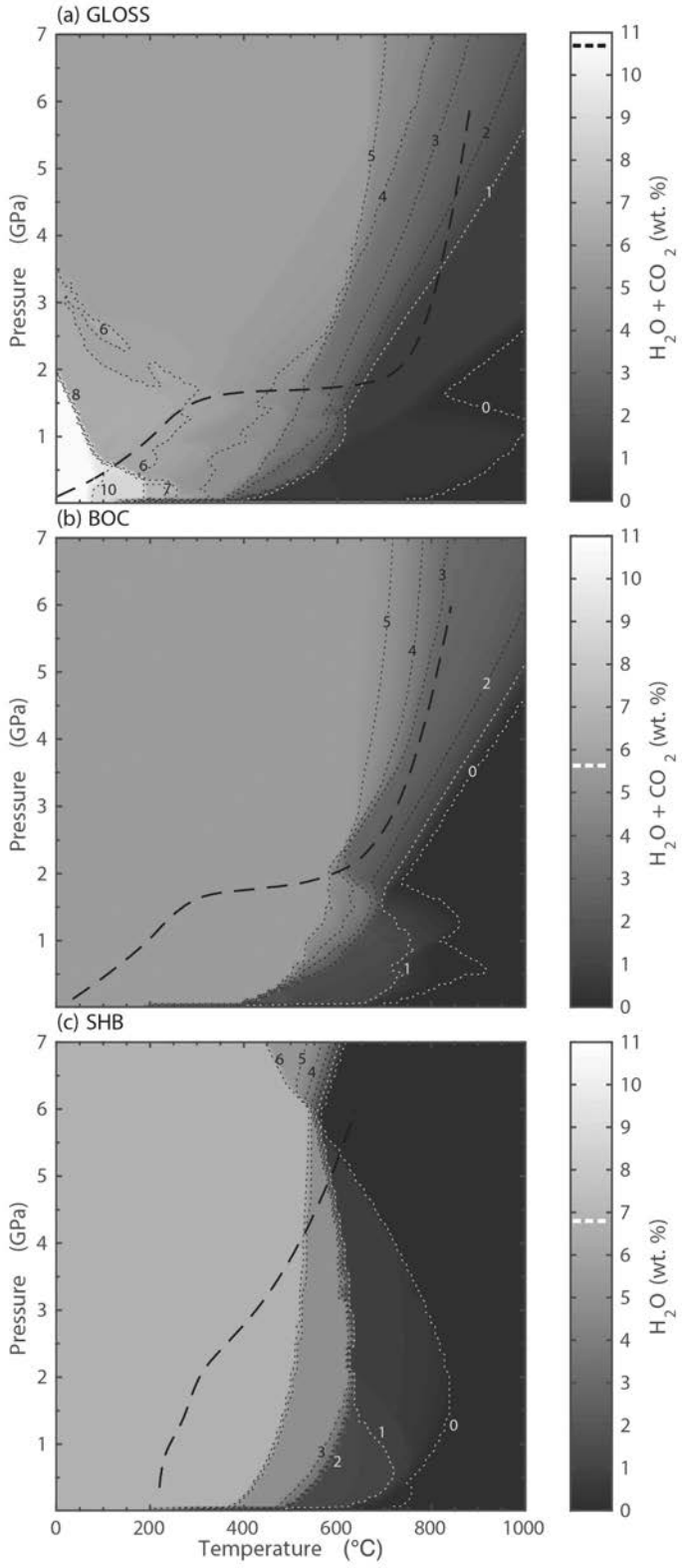

Fig. 3.2-13: Pressure-temperature diagrams illustrating the volatile budget (H_2O+CO_2) of the slab lithologies: (a) global oceanic subducting sediments (GLOSS), (b) bulk oceanic crust (BOC), and (c) serpentinized harzburgite (SHB). The initial volatile budget is indicated on the scale bar with white solid lines. P-T subduction paths at the top of respective lithological layers in the Nicaraguan subduction zone are superimposed as dashed lines.

j. *Experimental investigations of abiogenic synthesis of hydrocarbons at high P and T (E.M. Mukhina/Stockholm, A.Yu. Serovaysky/Moscow, I. Kupenko/Grenoble, L.S. Dubrovinsky and V.G. Kutcherov/Stockholm)*

Experimental studies of hydrocarbons at high pressure and temperature are extremely important with respect to the theory of abiogenic origins of hydrocarbons, especially due to a deficiency of such data. Recently a few aspects of the behaviour of complex hydrocarbon systems were discussed in the literature, such as the possibility of their synthesis under PT conditions of the Earth's interior, formation of heavier hydrocarbons from methane, models of fluid migration from the site of formation to the crust. This project aims at investigating reactions of complex hydrocarbons with Fe-bearing silicates (potential rock-forming reservoirs) at pressures and temperatures relevant to that of subcrustal zones.

Experiments were conducted in diamond anvil cells, and conventional Mössbauer spectroscopy at the BGI and SMS at ESRF (ID18) were employed as analytical methods. Mixtures of paraffin oil and silicate glass of $Mg_{0.91}Fe_{0.09}Si_{0.91}Al_{0.09}O_3$ starting composition (^{57}Fe-enriched) were studied at five different P-T points. At 0.8 GPa the sample was investigated at 1050 K, at 2.6 GPa at 1500 K, at 4.5 GPa at both 1400 K and 1800 K. Mössbauer spectra of the initial mixture shows a single doublet that is characteristic of pyroxene. After each experiment we have observed changes in the spectra. In addition to the doublet of pyroxene the following new component(s) appear: a sextet of α-Fe (0.8 GPa, 1050 K) (Fig. 3.2-14), a sextet of iron hydride (2.6 GPa, 1500 K) (Fig. 3.2-15), a sextet of iron hydride (4.5 GPa 1800 K). At 4.5 GPa and 1400 K no reaction was observed.

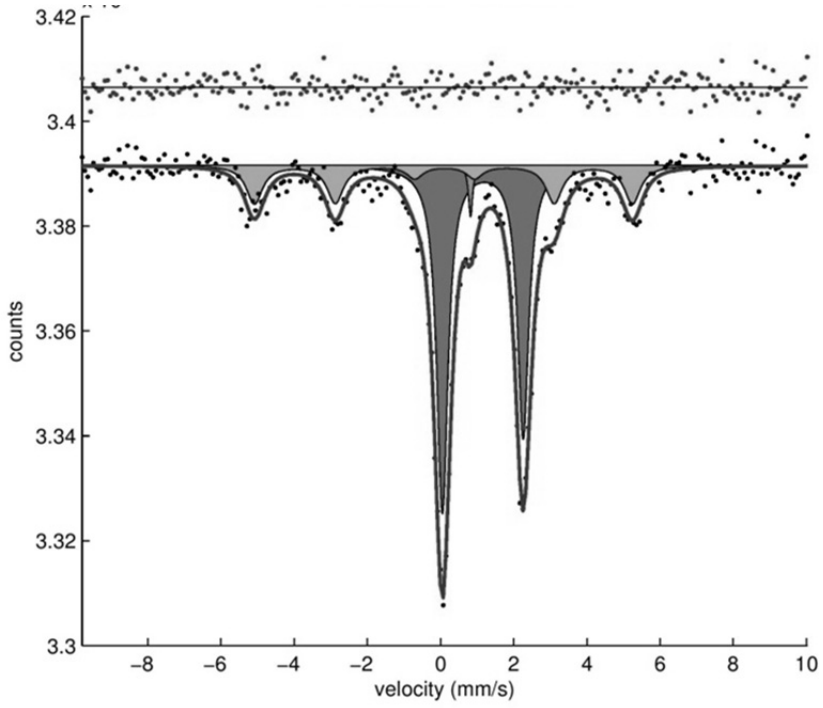

Fig. 3.2-14: Mössbauer spectrum of the experiment at 0.8 GPa and 1050 K: a doublet of pyroxene (*CS 1.155, QS 2.208*), a sextet of α-Fe (*CS 0.097, QS −0.035, BHF 32.021*) (the displacement of the central shift can be explained by the presence of dissolved hydrogen) and a singlet that belongs to a currently unidentified Fe^{2+} component (*CS 0.823*) (BGI).

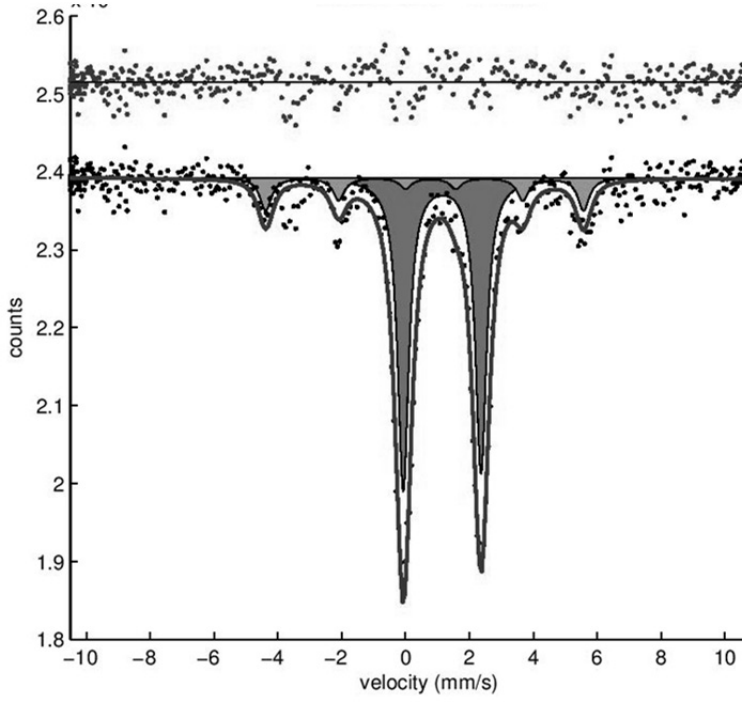

Fig. 3.2-15: Mössbauer spectrum of the experiment at 2.6 GPa and 1500 K: a doublet of pyroxene (*CS 1.145, QS 2.436*) and a sextet of iron hydride (*CS 0.693, QS −0.193, BHF 30.871*) (SMS).

These new results complement our previous experiments on mixtures of ferropericlase and crude oil in which no chemical reaction occurred at 6.9 GPa and 1300 K and 9.5 GPa and 1300 K, two sextets of iron hydride and a sextet iron of α-Fe were observed at 6.9 GPa and 1800 K, and sextets of iron hydride and iron carbide were detected at 9.5 GPa and 1800 K.
Our observations suggest that oil in subducted slabs may behave differently depending on temperature and lithology of the rocks.

k. *Transfer of volatiles and metals from mafic to felsic magmas in composite magma chambers (H. Guo and A. Audétat)*

Upper-crustal magma chambers commonly show evidence for compositional zonation and magma mush re-activation by ascending mafic magma. Fluids that are released from hot, mafic magma quenched against overlying felsic magma are thought to transport sulfur and other elements (*e.g.*, CO_2, Cl, metals) into the upper parts of the magma chamber. However, there is no experimental evidence to test this process. The aim of this study is to experimentally evaluate the major and trace element composition of fluids that exsolve from mafic alkaline magmas and to determine the geochemical signature imparted by such fluids to overlying, more felsic magmas.

In a first step, volatile- and metal-bearing mafic glasses were prepared by melting natural basaltic trachyandesite powders spiked with volatile- and metal-bearing fluids at 1200 °C / 10 kbar in piston cylinder presses. The hydrous glasses were then equilibrated in a second experiment at 850 °C / 2 kbar in cold-seal pressure vessels, which caused 80-90 % of the melt to crystallize (Figs. 3.2-16a, d). After 0.5-2.0 days of equilibration, aliquots of the exsolved fluid were trapped by means of *in situ* fracturing as synthetic fluid inclusions in quartz (Fig.

3.2-16c). Both the mafic rock residue and the fluid inclusions were subsequently analyzed by laser-ablation ICP-MS for major and trace elements. Partition coefficients ($D_{fluid/rock}=C_{fluid}/C_{rock}$) of elements between fluid and mafic rock residue were calculated from their concentrations in the fluid inclusions and the mafic residue (Fig. 3.2-17). Reverse experiments were conducted by equilibrating metal-bearing aqueous solutions with rock powder and then initiating the formation of fluid inclusions. Comparison of element concentrations in fluid inclusions between forward and reverse runs demonstrates that equilibrium was attained after 2 days.

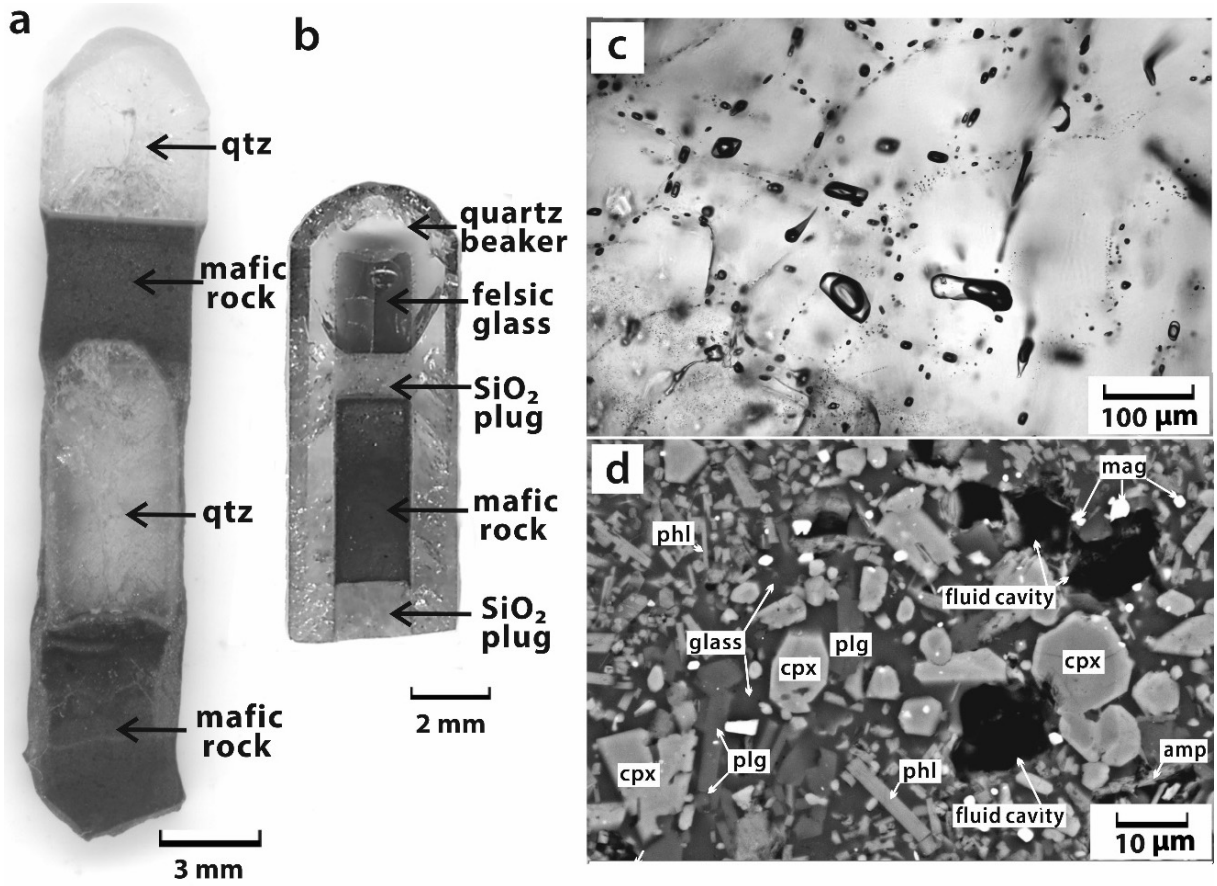

Fig. 3.2-16: Photographs of recovered samples. (a) Polished section through sample HG33 in which fluid was trapped in the form of synthetic fluid inclusions in the central quartz piece. (b) Polished section through sample HG42 in which fluids exsolving from the crystallizing mafic magma were able to diffuse into an overlying pool of felsic melt. (c) Fluid inclusions in the quartz piece recovered from sample HG32, which experiment was of the same type as that of HG33. (d) Back-scattered electron (BSE) image of the mafic run product in sample HG32 after 9 days at 850 °C and 2 kbar.
Abbreviations: cpx - clinopyroxene; plg - plagioclase; phl - phlogopite; amp - amphibole; qtz - quartz; mag - magnetite.

In two additional runs relative element mobilities were determined by allowing fluids that exsolved from the crystallizing mafic magma to react with overlying silicic melts. This approach has the advantage that it is more sensitive and thus allows also rather fluid-immobile

elements such as Ti and Zr to be studied, but it has the disadvantage that it does not allow to quantify the fluid composition.

The combined results suggest that S, Cl, Cu, Se, Te, Br, and Cd are most volatile ($D_{fluid/rock}$ > 10), followed by Li, B, Zn, Mo, Ag, As, Sb, Cs, W, Tl, Pb and Bi ($D_{fluid/rock}$ =1-10). Less volatile are Na, Mg, K, Al, Ca, Mn, Fe and Rb ($D_{fluid/rock}$ <1), and the least fluid-mobile elements are Ti, Zr, Sr, Ba and Ce ($D_{fluid/rock}$ <<1). This trend is broadly consistent with relative element volatilities determined on natural high-temperature fumarole gases (Fig. 3.2-18). The results of this study suggest that former periods of volatile fluxing in natural magma systems may be best recognized based on elevated concentrations of S, Cl, and Cu (plus CO_2) in silicate melts and -minerals, and/or high levels of Cu, Se, Te and Cd in magmatic sulfides.

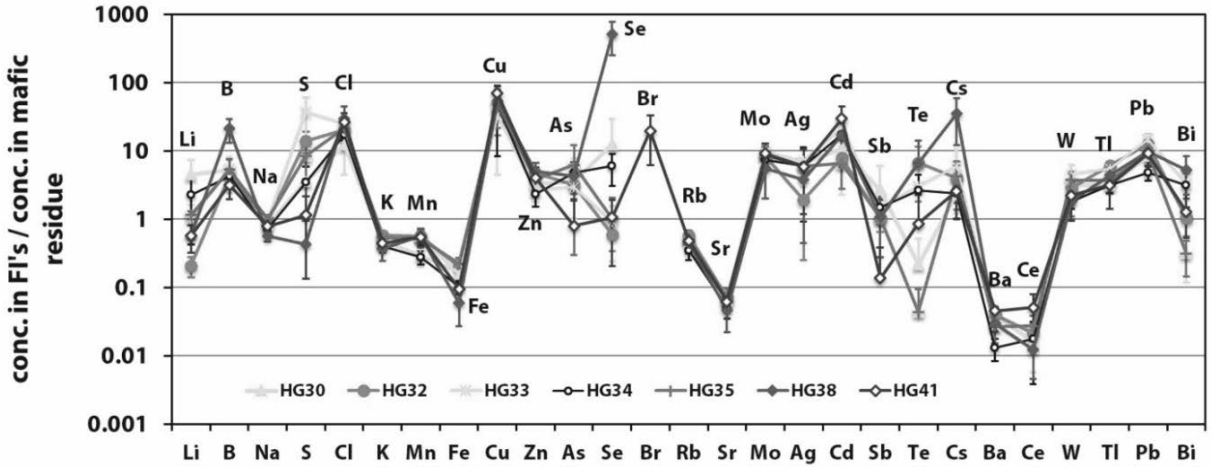

Fig. 3.2-17: Element concentrations in fluid inclusions (FI's) relative to the mafic residue.

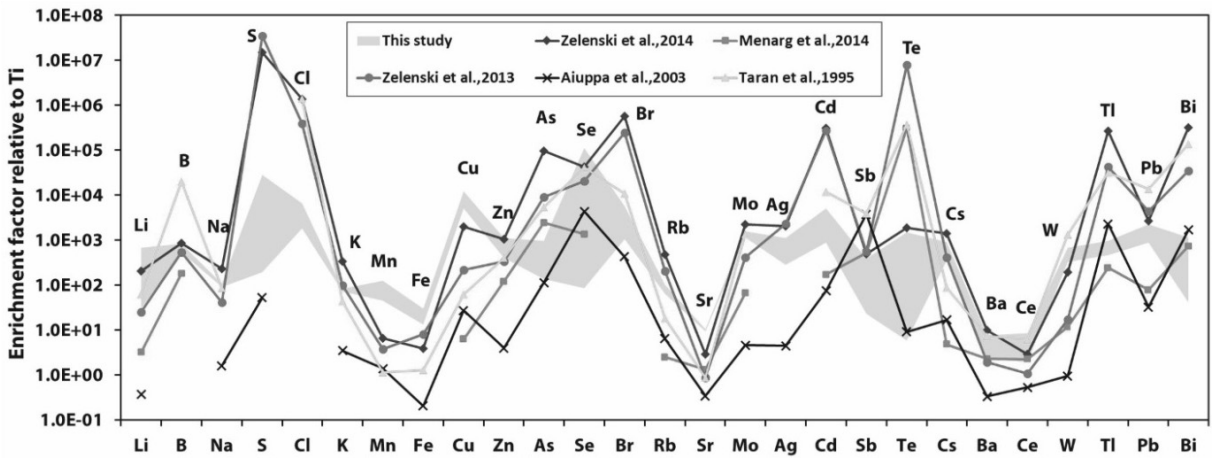

Fig. 3.2-18: Enrichment of elements in the fluid phase compared to their abundance in the mafic source rock/magma, normalized to the corresponding Ti concentrations. Data obtained from our experiments involving synthetic fluid inclusions (gray array) are compared with published data obtained from the analysis of fumarolic gases/aerosols and whole-rocks from five arc volcanoes worldwide.

l. *What caused the formation of the giant Bingham Canyon porphyry Cu-Mo-Au deposit? Insights from melt inclusions and magmatic sulfide inclusions (D.H. Zhang and A. Audétat)*

Porphyry Cu-forming magmas are commonly considered to have been enriched in sulfur and/or metals compared to non-fertile magmas. To test this hypothesis we reconstructed the metal content of the ore-forming latite magma at Bingham Canyon and compared it with estimated metal contents of intermediate magmas in several barren arc magma systems.

The ore-forming latite magma at Bingham Canyon appears to have formed by mixing of ~ 40 % mafic magma that was compositionally similar to melanephelinite (the most mafic rock preserved at Bingham Canyon; containing ~ 44 wt. % SiO_2) with ~ 60 % felsic magma of rhyolitic composition (~ 71 wt. % SiO_2). Based on the modal abundance of sulfides in this rock and LA-ICP-MS analyses of unaltered sulfide inclusions within hornblende and plagioclase phenocrysts the latite contained 60-90 ppm Cu, 0.8-2.0 ppb Au, 2-3 ppm Mo and 0.12-0.14 wt. % S, which elements were derived mainly from the mafic magma endmember. Magma mixing caused extensive precipitation of magmatic sulfides that sequestered ~ 65 % of the Au and ≥ 85 % of the Cu, Ag and PGE's present in the magma. However, the magmatic sufides ultimately became unstable and released sulfur and metals to the ore-forming fluids, as is indicated by similar metal ratios in sulfides vs. bulk ore vs. fluid inclusions.

Since many intermediate-composition arc magmas formed by magma mixing, and both sulfur and chalcophile elements were supplied mainly by the mafic endmember, the sulfur and metal content of mixed, intermediate magmas can be estimated from the sulfur and metal content of the mafic endmember plus the mixing ratio with felsic magma. Applying this approach to two other porphyry Cu-mineralized systems (Santa Rita and Alumbrera) and ≥10 presumably barren modern arc magma systems suggest that the magmas in mineralized systems were neither particularly metal-rich (Fig. 3.2-19) nor particularly volatile-rich (Fig. 3.2-20) compared to their barren counterparts. Specifically, the mafic endmember at Bingham Canyon contained 100-250 ppm Cu (Fig. 3.2-19) and 1000-2000 ppm S (Fig. 3.2-20a), which values are within the range of ordinary mafic arc magmas. The mafic endmember at Bingham Canyon was moderately enriched in Cl (2000-2500 ppm; Fig. 3.2-20b) and strongly enriched in F (3000-6000 ppm) compared to normal arc basalts, reflecting its origin by low-degree partial melting of metasomatized lithospheric mantle. Besides, it was also rich in H_2O, but probably not more than unmineralized arc basalts.

The most distinctive feature of porphyry Cu-mineralized magma systems seems to be the formation of a very large upper crustal magma chamber located at 5-15 km depth, containing ≥ 100 km^3 of intermediate-composition magma in the case of medium-sized deposits, and ≥ 1000 km^3 in the case of giant deposits. Therefore, the results of the present study suggest that the size of the upper crustal magma chamber, rather than magmatic metal and volatile contents, exerts the main control on mineralization potential.

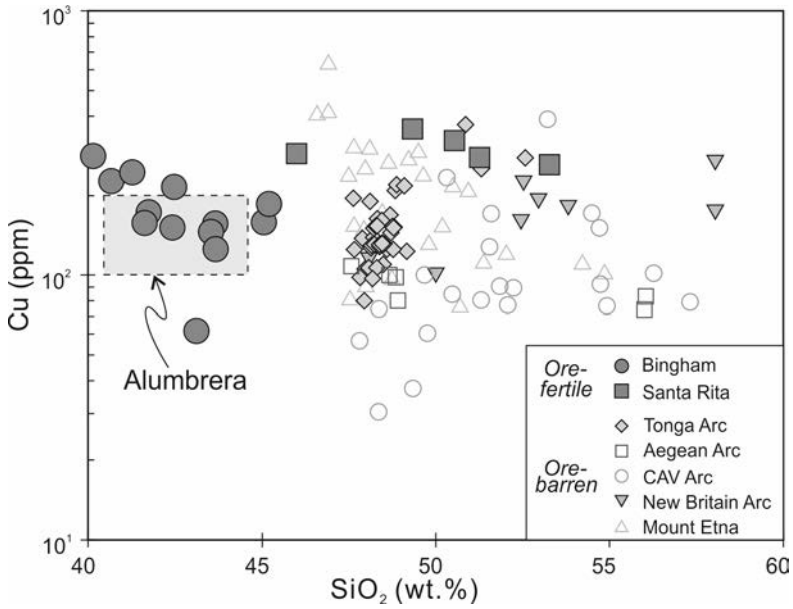

Fig. 3.2-19: Comparison of Cu concentrations in mafic melt inclusions from fertile versus barren arc magma systems.

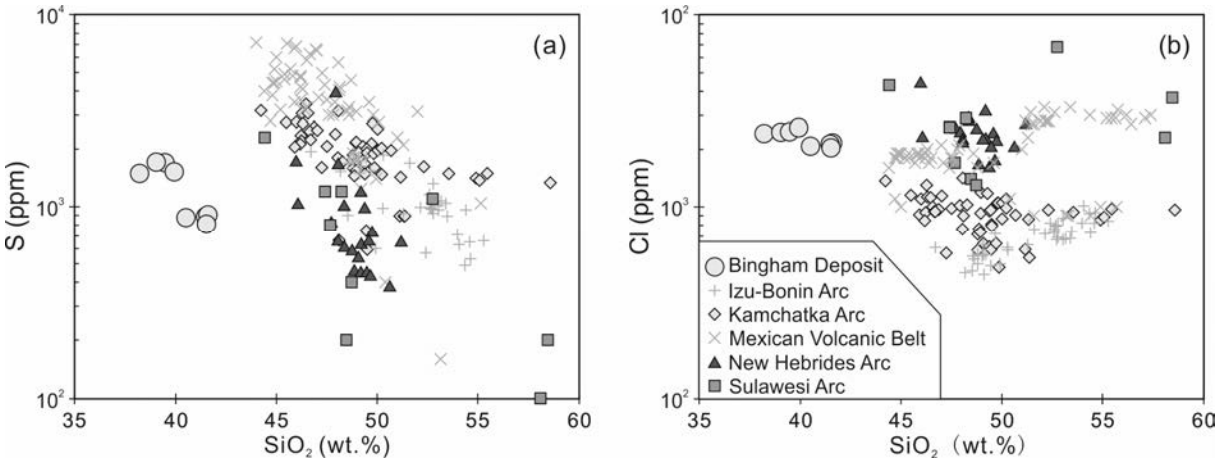

Fig. 3.2-20: Comparison of volatile contents of mafic melt inclusion from Bingham Canyon versus other primitive arc magmas.

m. *Experimental calibration of a new oxybarometer for Si-rich magmas based on the partitioning of vanadium between magnetite and silicate melt (R. Arato and A. Audétat)*

Oxygen fugacity is an important parameter in magmatic systems because it controls the stability and composition of certain minerals, the solubility of fluids in the magma, as well as the fluid–melt and mineral–melt partition coefficients of various elements. For these reasons it also affects the mineralizing potential of magmatic intrusions such as granites, for example. However, there is no well-established method to reconstruct the oxygen fugacity in such slowly cooled magmas because the existing oxybarometers (*e.g.*, magnetite-ilmenite method)

are primarily developed for rapidly quenched volcanics. Thus, they are susceptible to re-equilibration processes during slow cooling and lead to erroneous results when estimating fO_2 of granitic rocks. Using a new approach, we aim at developing an oxybarometer that is based on partition coefficients of vanadium (a redox-sensitive element) between magnetite and silicate melt, determined by LA-ICP-MS analysis of small, entire inclusions of magnetite and silicate melt trapped within quartz phenocrysts, thus having been protected from subsolidus alteration. In this contribution, only the experimental calibration of this method is presented.

We investigated the effects of temperature, pressure, oxygen fugacity, magnetite- and melt composition on the partition coefficient of vanadium between magnetite and melt ($D_V^{mgt\text{-}melt}$). The experiments were carried out in cold-seal pressure vessels over the p-T range of 1-2 kbar and 800-950 °C, while the oxygen fugacity was buffered at Ni-NiO, Re-ReO or MnO-Mn_3O_4 (*i.e.*, 0.7, 2.5 and 4 log units above FMQ, respectively). The starting material was a mixture of V-doped synthetic or natural obsidian powder with variable aluminium saturation index (ASI), and synthetic, V-free magnetite of 10-20 µm grain size. All experiments were conducted at fluid-saturated conditions. The duration of the experiments varied between 2 and 7 days and the attainment of equilibrium was proved by reverse experiments, using V-free glass and V-doped magnetite. $D_V^{mgt\text{-}melt}$ was determined by measuring the concentration of V in glass–magnetite pairs by LA-ICP-MS.

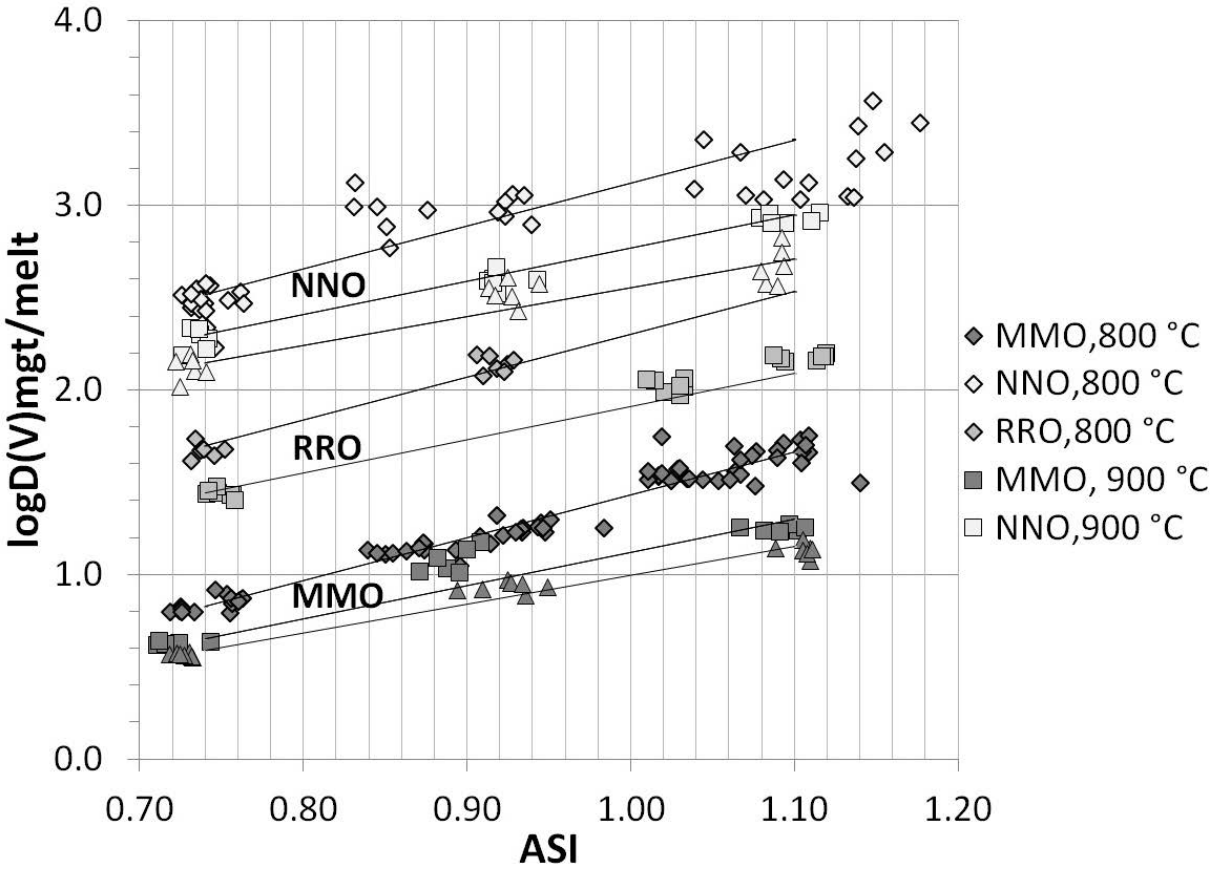

Fig. 3.2-21: Dependence of log $D_V^{mgt\text{-}melt}$ on ASI, temperature and oxygen fugacity. MMO – MnO-Mn_3O_4 buffer; RRO – Re-ReO buffer; NNO – Ni-NiO buffer.

The vanadium partition coefficient was found to depend strongly on oxygen fugacity, and to lesser (but still considerable) degrees on melt composition and temperature (Fig. 3.2-21). The more than 1.5 log unit decrease in $D_V^{mgt\text{-}melt}$ values with increasing oxygen fugacity over the investiaged fO_2 range can be explained by a change of the dominant valence state of V in the silicate melt from V^{3+} toV^{4+}, with the latter being more difficult to incorporate into the magnetite structure. For a given oxygen fugacity buffer $D_V^{mgt\text{-}melt}$ decreases with increasing temperature, but this reflects mostly the change in absolute fO_2 values while the net temperature effect is in fact positive. Changing pressure from 1 to 2 kbar has no effect at oxidizing conditions (MMO), whereas at NNO it appears to cause a 0.3 log unit increase in D. The small pressure effect is probably related to the Fe speciation in the melt, which itself is related to the water solubility. $D_V^{mgt\text{-}melt}$ depends significantly on the melt composition, with increasing aluminium saturation index (ASI) resulting in higher D-values. This appears to be a consequence of less favorable incorporation of V in peraluminous melts compared to depolymerized, peralkaline melts. The Ti-content of magnetite turned out to have negligible effect on the V partitioning.

In summary, the dependence of $D_V^{mgt\text{-}melt}$ on temperature, ASI and oxygen fugacity can be described by the following regression equation:

$$\log D(V)\mathrm{mgt/melt} = -1.22 + 0.31\frac{10^5}{T(°K)} + +1.73 * \mathrm{ASI} - 0.49 * \Delta\mathrm{FMQ}$$

3.3 Mineralogy, Crystal Chemistry and Phase Transformations

The link between microscopic properties and macroscopic observables continues to play a crucial role in our quest to understand the Earth's interior and the processes that control its dynamics and evolution. Experimental determinations of structures and stabilities span a wide range of variables that include not only pressure and temperature but also compositional parameters such as oxygen fugacity and water saturation, and theoretical approaches extend the parameter space even further. This chapter describes some of the most recent results from these studies.

Bridgmanite, the Earth's most abundant mineral, continues to attract attention. New results show that the distribution of iron between cation sites as well as the abundance of vacancies varies with both temperature and oxygen fugacity, and that the incorporation of argon can affect its equation of state and thermodynamic stability. The discovery of new iron oxides continues to reveal new hosts for ferric iron, and studies of spin transitions involving ferric iron demonstrate surprising regularities that link to its electronic structure. The crystal structure and morphology of minerals also provide information on the environment in which they formed, for example the unit cell of olivine acts as a geobarometer during entrapment in diamonds and spinel exsolution from ferropericlase in diamond targets pre-existing dislocations. The substitution of seemingly minor elements in wadsleyite such as transition metals affects charge balance and the incorporation of volatiles such as hydrogen and thereby influences deep volatile cycles. Similarly, polymorphs of silicon dioxide can incorporate hydrogen through coupled substitution with trivalent cations and studies of the phase transition sequence in silicon dioxide provide insight to the history of extra-terrestrial materials.

Phase transformations further link microscopic properties to macroscopic observables to provide constraints on seismic discontinuities. The thickness of the 660 km discontinuity is related to the extent of the three-phase field ringwoodite + bridgmanite + ferropericlase and new developments involving *in situ* X-ray diffraction promise a precise determination of the stability field. Carbonate phase transformations can place constraints on the deep carbon cycle if they can be resolved in seismic data, and new results on cobalt and manganese carbonates provide insight to the systematics of transformations involving the more common carbonates expected in the deep mantle. At more extreme conditions, theoretical calculations enable phase transformations in MgO to be determined that are relevant for the cores of giant planets or rocky exoplanets. Theory also expands possibilities to calculate phase relations and seismic properties of solid solutions that incorporate excess thermodynamic properties. Predictions of solid solution stability can be made based on endmember properties, which have been confirmed experimentally for the rutile structure between dioxides of silicon and germanium.

a. *Strong affinity of Al-containing bridgmanite for ferric iron (C.A. McCammon, J. van Driel, T. Kawazoe, R. Myhill and L.S. Dubrovinsky)*

It is well established that bridgmanite has a strong affinity for ferric iron in the presence of Al, and that the amount of ferric iron relative to total iron can strongly influence both physical and chemical properties of the phase, and in turn the entire lower mantle since bridgmanite is its dominant mineral. Recently, however, literature studies have suggested that under certain conditions, Al-containing bridgmanite will contain substantially less ferric iron than previously supposed. One possibility is that particular compositions may stabilise ferrous iron relative to ferric iron, for example an almandine composition where Al substitutes equally on both sites of the perovskite structure, thereby balancing divalent iron and tetravalent silicon. To explore this possibility as well as perform a more comprehensive investigation of the effect of temperature and oxygen fugacity on ferric iron concentration in Al-containing bridgmanite, we carried out a study combining multianvil experiments with Mössbauer spectroscopy.

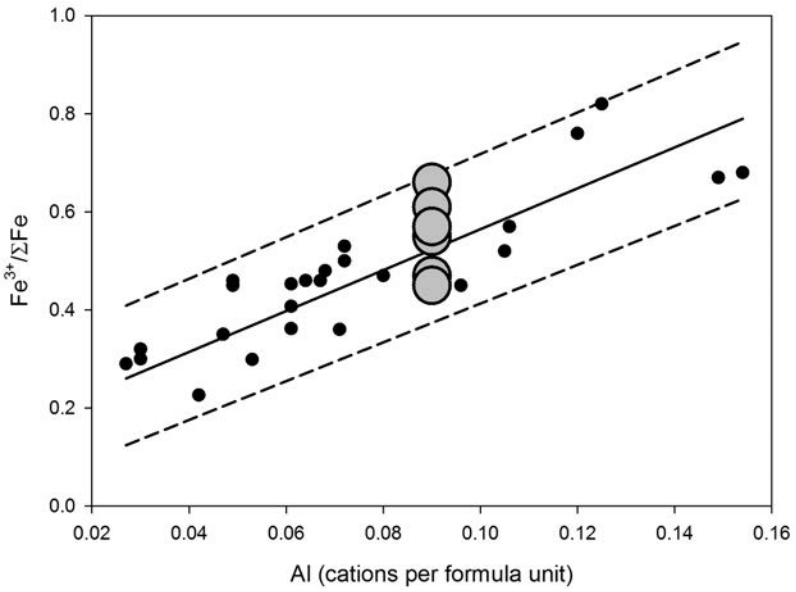

Fig. 3.3-1: Relative Fe^{3+} concentration versus Al concentration in $(Mg,Fe)(Si,Al)O_3$ bridgmanite synthesised in a multianvil press. The large circles represent new data while the small black dots are from the literature [McCammon *et al.* 2004, *Earth Planet. Sci. Lett.* 222: 435-449 and references therein]. The solid line represents the best fit to the literature data while the dashed lines are the 90 % prediction limits.

We synthesised a glass with nominal composition 0.9 $MgSiO_3$ (enstatite) + 0.1 $(Fe_{0.75}Al_{0.25})(Si_{0.75}Al_{0.25})O_3$ (almandine). Starting materials for the multianvil experiments were (1) the glass as synthesised in air ($Fe^{3+}/\Sigma Fe = 0.5$), and (2) the glass after reduction in a CO/CO_2 gas furnace ($Fe^{3+}/\Sigma Fe = 0$). All multianvil experiments were performed at 26 GPa using a Kawai-type apparatus with different combinations of starting material (oxidised or

reduced glass), temperature (1600 °C or 2000 °C) and capsule material (Fe or Re). A final experiment was performed at 1600 °C and then the run product was re-equilibrated in a new multianvil experiment at 2000 °C. All run products were examined using scanning electron microscopy and Mössbauer spectroscopy.

All multianvil experiments produced bridgmanite with $Fe^{3+}/\Sigma Fe$ values between 45 % and 66 %, consistent with previous results (Fig. 3.3-1). While there was no obvious influence of oxygen fugacity or temperature on $Fe^{3+}/\Sigma Fe$, we did observe changes in the shape of the Mössbauer spectra, consistent with an influence on the distribution of iron between cation sites. Since this distribution also affects physical and chemical properties, for example spin transitions, further analysis is underway to quantify the effect, as well as parallel experiments using a laser-heated diamond anvil cell.

b. *High-pressure X-ray diffraction studies of Ar-bearing bridgmanite (S. Shcheka, E. Bykova, M. Bykov, T. Boffa Ballaran, L.S. Dubrovinsky and H. Keppler)*

Recently, we observed high solubilities of Ar and Kr (0.3-1 wt. %) in bridgmanite, which is the main constituent of Earth's lower mantle. However, the mechanism of noble gas dissolution in the $MgSiO_3$-bridgmanite lattice remains unclear. One possible explanation relies on structural considerations. It is widely assumed that neutral noble gases reside in various defects in crystal lattices and bridgmanite may contain abundant oxygen vacancies. These oxygen vacancies may occur with charge balanced by Si vacancies at low silica activity, such as in equilibrium with the ferropericlase (Mg,Fe)O phase in the lower mantle. The substitution of Al^{3+} for Si^{4+} may also produce oxygen vacancies. In this case, the observed difference in solubilities between Ar, Kr and Xe is likely due to the size mismatch between the noble gas atoms and the oxygen vacancies. While Ar and Kr atomic radii are relatively close to the size of an oxygen vacancy (1.26-1.4 Å), xenon has an atomic radius of 1.96 Å which is likely too large to fit into the oxygen position in the lattice, consistent with its low solubility in bridgmanite. The recently measured argon solubilities in bridgmanite are so high that they could potentially change the equation of state and even shift the thermodynamic stability range of perovskite. This possibility is particularly interesting, because measurements of the equation of state of $MgSiO_3$ bridgmanite, with or without Al, have given a range of different results and many of these measurements have been carried out in diamond cells using noble gases as pressure medium.

High-quality single crystals of pure gas-free bridgmanite and argon-bearing bridgmanite were synthesized at high-pressure high-temperature conditions in Bayerisches Geoinstitut. Single crystal X-ray diffraction measurements were performed on the high-pressure beamline ID09A at ESRF (Grenoble). Both crystals were put together in a BX90 diamond anvil cell with Boehler-Almax diamond anvils (250 μm diameter culets). Neon was used as a pressure-transmitting medium. Diffraction data were collected at ambient temperature and up to pressures of ~ 55 GPa.

Measurements of an Ar-bearing bridgmanite crystal using synchrotron radiation have shown that at ambient pressure reflections are very broad indicating internal strain in the structure due to the presence of Ar (Fig. 3.3-2a). At 55 GPa, however, reflections of the same crystal become sharp (Fig. 3.3-2b). After decompression below 5 GPa, the peaks of the Ar-bearing crystal broadened again. This effect has never been observed in Ar-free bridgmanite and may indicate a change of the lattice site of argon in the crystal upon decompression.

Presently, the diffraction data are being analyzed to reveal the structural variations between pure and Ar-rich $MgSiO_3$-bridgmanite as well as the atomic position of Ar in the bridgmanite structure to quantify the effect of the Ar saturation on bond distances, bond angles, polyhedral compression and elasticity of bridgmanite.

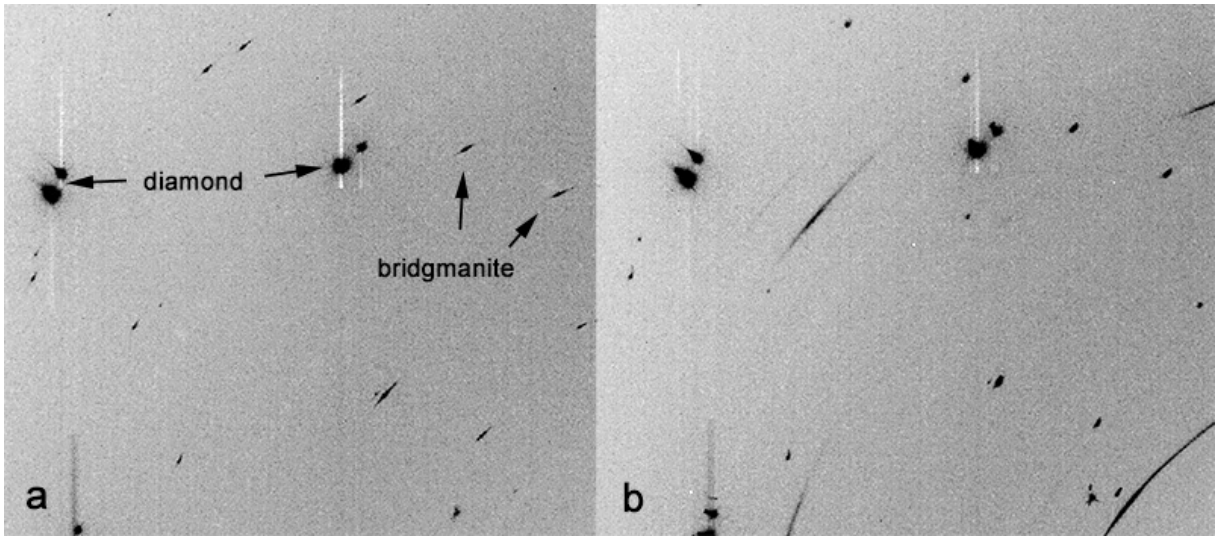

Fig. 3.3-2: Synchrotron 2D X-ray diffraction image of bridgmanite single crystals collected under continuous ω rotation from -20 to +20°: Ar-bearing bridgmanite at 3 GPa (a) and at 55 GPa (b).

c. *The stability of Fe_5O_6 at high pressures and temperatures (A. Woodland and L. Uenver-Thiele/Frankfurt; T. Boffa Ballaran and D.J. Frost)*

Since the recent discovery of Fe_4O_5 as a high-pressure phase, there has been interest in determining whether there are other Fe-oxide phases that could potentially be stable at the conditions of the Earth's deep upper mantle and transition zone. To this end, a series of multianvil experiments are being carried out over a range of pressures and temperatures to investigate whether Fe_5O_6 and Fe_6O_7 are stable phases and to determine their phase relations.

Experiments employing stoichiometric mixtures of magnetite and metallic iron reveal that Fe_5O_6 is a stable phase at least between 10 and 18 GPa at around 1200 °C. X-ray powder diffraction refinements and single crystal diffraction indicate that this phase has a *Cmcm*

space group and is isostructural with $CaFe_4O_6$, which is analogous to Fe_4O_5 being isostructural with $CaFe_3O_5$.

In several experiments, Fe_5O_6 is observed to coexist with either Fe_4O_5 or wustite. The refined cell parameters give a composition of $Fe_{0.925}O$ for the coexisting wustite. Thus, the redox stability of Fe_5O_6 is constrained by the following two equilibria:

$$4\ Fe_5O_6\ +\ 0.5\ O_2\ =\ 5\ Fe_4O_5 \text{ and } Fe_5O_6\ =\ 5.4\ Fe_{0.925}O\ +\ 0.3\ O_2$$

The coexistence of Fe_5O_6 and wustite also precludes the stability of further Fe-oxide phases with $Fe^{3+}/\sum Fe < 0.4$, such as Fe_6O_7, at least within the pressure and temperature range investigated so far.

In several experiments, an additional phase appeared along with Fe_5O_6 that has a diffraction pattern like that of wustite, but with a much smaller cell parameter than that previously reported from high-pressure experiments. An extrapolation using published cell parameter-composition systematics indicates that this wustite has a composition of about $Fe_{0.86}O$. This composition is very close to that of Fe_5O_6 ($Fe_{0.83}O$), which suggests that this additional phase may have formed during quenching or decompression and was probably not stable at high pressures and temperatures.

Combining this work with previous observations indicates that there are three stable assemblages in the Fe–O system at pressures above the stability of magnetite:
$Fe_2O_3 + Fe_4O_5$, $Fe_4O_5 + Fe_5O_6$ and $Fe_5O_6 + Fe_{0.925}O$.

d. *TEM investigation of Fe_5O_6 (N. Miyajima; A. Woodland and L. Uenver-Thiele/Frankfurt; T. Boffa Ballaran)*

Current systematic studies of high-pressure iron oxide phases of Fe_4O_5 and Fe_5O_6 using a multianvil press at BGI imply that a nonstoichiometric wustite forms during decompression from ~ 10 GPa. In fact, the powder diffraction pattern of a synthesis run recovered from an experiment at 10 GPa indicates that it is mostly Fe_5O_6 with additional diffraction peaks consistent with Fe_xO (X ~ 0.85). Selected area electron diffraction patterns from this sample revealed a phase analogous to the $Mg_5Fe_2O_8$ compound described in the next report. The SAED pattern from this phase can be indexed with a double rock salt unit cell (S.G. 225, *Fm3m*, a = ~ 0.85 nm). The dark-field TEM image with $\boldsymbol{g}$ = 311 displays a mottled contrast, which suggests the coexistence of a fine mixture of Fe_xO and Fe_3O_4 (magnetite) (Fig. 3.3-3). However, the Fe_xO phase would also be consistent with a rock salt-structured $Fe^{2+}{}_4Fe^{3+}{}_2O_7$ or $Fe^{2+}{}_5Fe^{3+}{}_2O_8$ compound. Since no magnetite was observed in the powder diffraction patterns, it appears that this new phase formed along with magnetite during TEM analysis and suggests that Fe_5O_6, like Fe_4O_5, is very sensitive to heating under ambient pressure conditions and quenching from high pressure and temperature.

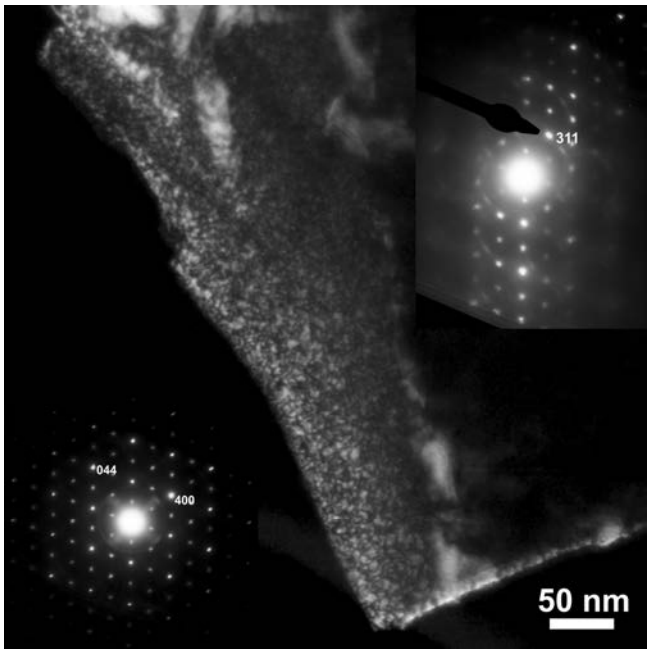

Fig. 3.3-3: Dark-field TEM image with $\boldsymbol{g}$ = 311 displays a mottled contrast in the iron oxide compound. The lower left and upper right insets are SAED patterns of the nearest zone axis and the corresponding diffraction pattern of the DF image, respectively.

e. *Does $Mg^{2+}{}_5Fe^{3+}{}_2O_8$ have a rock salt structure at high pressure? A TEM study (N. Miyajima; L. Uenver-Thiele and A. Woodland/Frankfurt; T. Boffa Ballaran)*

Current systematic studies of Mg-Fe oxide phases at high pressures and temperatures suggest that several different stoichiometries might be stable. Here we report TEM results of a recovered sample that had a $Mg_2Fe_2O_5$ bulk composition. This experiment was intended to test the low-pressure stability of $Mg_2Fe_2O_5$, which is already known to be stable at ~ 15 GPa and 1550 °C. The recovered sample was found to be a mixture of Fe_2O_3 (hematite) and a compound with $Mg_5Fe_2O_8$ stoichiometry as measured by electron microprobe. Powder X-ray diffraction confirms the presence of hematite, but other diffraction peaks are very broad and difficult to interpret. The selected area electron diffraction (SAED) pattern from the "$Mg_5Fe_2O_8$" compound can be indexed with a double rock salt unit cell (S.G. 225, Fm3m, a = ~ 0.85 nm), but the dark-field TEM image with $\boldsymbol{g}$ = 113 displays mottled white contrast (Fig. 3.3-4), which can be chemically identified as a fine mixture of MgO (periclase) and $MgFe_2O_4$ (magnesioferrite) by using chemical mapping in a scanning transmission electron microscope (STEM) equipped with an energy-dispersive X-ray (EDX) spectrometer (Inset of Fig. 3.3-4). Given the topotactic relationship between MgO and magnesioferrite diffraction patterns and the high-resolution TEM (Fig. 3.3-5), we suggest that the precursor phase of this compound at high pressure and temperature may be an oxide having the $Mg_5Fe_2O_8$ composition and a rock salt-like structure. These TEM results suggest that the $Mg_5Fe^{3+}{}_2O_8$ phase could be stable as a rock salt-like structure at high pressure and temperature; however, it decomposed into a nanometer-sized mixture of the two oxides during decompression or post-mortem TEM

analysis. The refinement of the crystal structure and its stability field in pressure-temperature-oxygen fugacity space need to be performed using *in situ* XRD diffraction at high pressure and temperature.

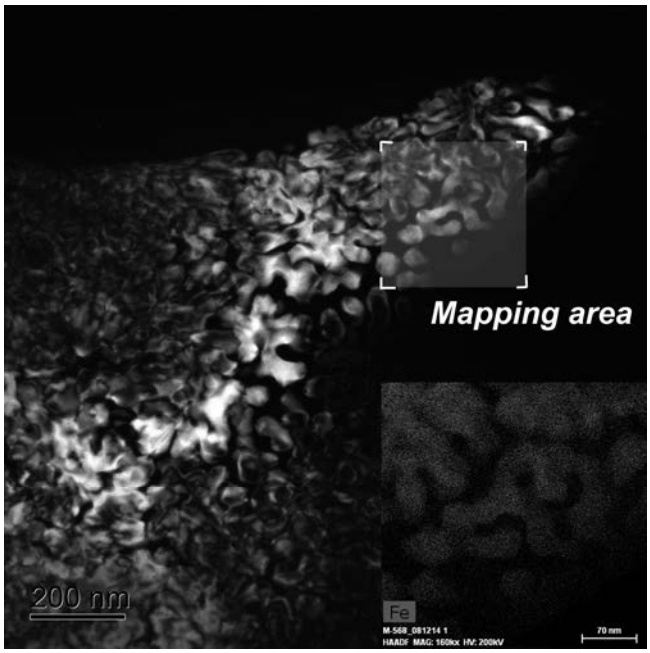

Fig. 3.3-4: Dark-field TEM image with ***g*** = 113 displays mottled white contrasts in the $Mg_5Fe_2O_8$ compound. The domains with white contrast correspond to Fe-enriched magnesioferrite. The inset is an iron elemental map of the square area, obtained using STEM-EDX spectroscopy.

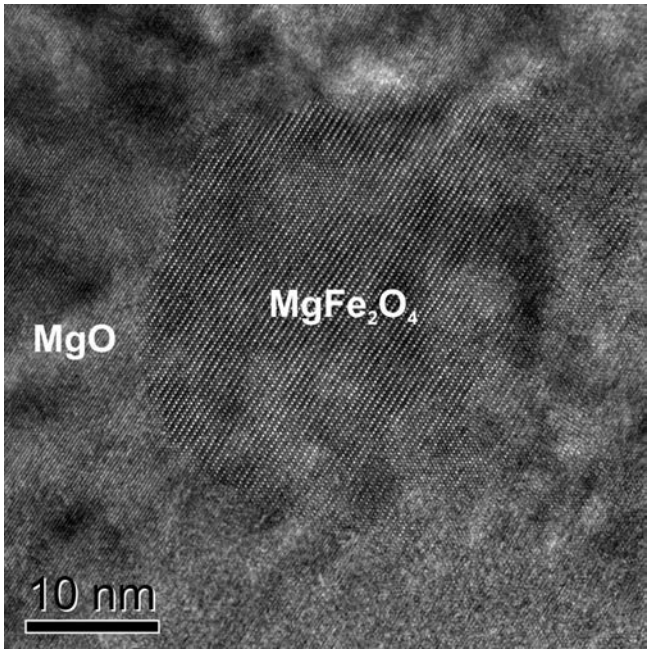

Fig. 3.3-5: A high resolution TEM image of a fine mixture of MgO (periclase) and $MgFe_2O_4$ (magnesioferrite), indicating a topotatic relationship.

f. *Pressure-induced spin pairing transition in trivalent iron octahedrally coordinated by oxygen (D. Vasiukov/Bayreuth, E. Bykova, I. Kupenko/Grenoble, L. Ismailova/Bayreuth, V. Cerantola, G. Aprilis/Bayreuth, C.A. McCammon, A.I. Chumakov/Grenoble, E. Greenberg/ Tel Aviv, C. Prescher and V.B. Prakapenka/Chicago, L.S. Dubrovinsky, N.A. Dubrovinskaia/ Bayreuth)*

The spin pairing transition in transition metals (also known as spin crossover) is an important phenomenon that can cause drastic changes in the physical properties of materials, including volume, compressibility and electrical conductivity. Upon high spin (HS) to low spin (LS) crossover the ionic radii change dramatically (for example, in Fe^{2+} it changes from 78 to 64.5 pm and in Fe^{3+} from 62 to 55 pm) that leads to a reduction of chemical bond lengths and may cause structural changes. The alteration in ionic radii means that LS iron can substitute for other cations without significantly changing the crystal structure, which is important for chemistry and especially for geochemistry. Magnetic properties may also change, for example, ferrous iron in the LS state is diamagnetic.

One way to observe spin transitions in compounds with low crystal-field splitting (Δ) is to increase Δ by applying external pressure, for example the spin transition in ferropericlase at lower mantle conditions. Recent advances in high-pressure crystallography (synchrotron facilities using fast 2D detectors and diamond anvil cells with high opening angle) enable careful investigation of the geometry of the FeO_6 octahedron before and after a spin transition through single-crystal X-ray diffraction, and Mössbauer spectroscopy provides information on correlations between the crystal chemistry and electronic structure through the hyperfine parameters.

We conducted a comparative study of compounds containing ferric iron octahedrally coordinated by oxygen. All experiments were performed on high quality single-crystal samples. Iron borate was studied using single-crystal synchrotron X-ray diffraction at 13-ID-D, Advanced Photon Source (Argonne, USA) and *in house* Mössbauer spectroscopy at BGI. Transmission Mössbauer spectra for hematite and skiagite were measured using a synchrotron Mössbauer source at the Nuclear Resonance Beamline ID18, European Synchrotron Radiation Facility (Grenoble, France).

The analysis of our new data combined with results from the literature showed the following: (*i*) despite the different values of the crystal field splitting parameter and the Racah parameter B shown by the different compounds at ambient conditions, all undergo a HS-LS spin transition within a narrow range of pressures (45-60 GPa); (*ii*) in all compounds studied the transition starts at octahedron volumes between 9.0 and 9.3 $Å^3$; (*iii*) the significant spread of quadrupole splitting values (0.7 to 2.5 mm/s) for LS Fe^{3+} may be related to the presence of a cooperative Jahn-Teller effect in some compounds.

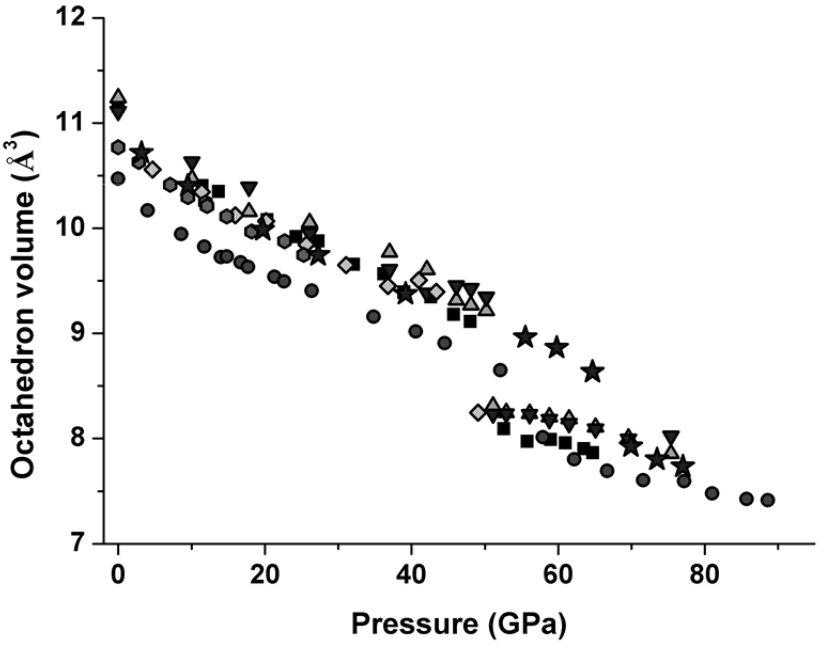

Fig. 3.3-6: Volume of $Fe^{3+}O_6$ octahedra as a function of pressure for different compounds. Squares correspond to iron borate, circles to skiagite, triangles to two different structural positions in calcium ferrite, diamonds to goethite, hexagons to hematite and stars to andradite. Despite the wide range of different crystal field splitting parameters at ambient conditions, it is notable that the spin transitions start within a narrow range of octahedron volumes, with the exception of skiagite which is due to mixed $(Fe,Si)O_6$ octahedra.

g. *Formation and evolution of diamonds constrained through the study of their inclusions (M.D. Wenz and T. Boffa Ballaran, in collaboration with S.D. Jacobsen/Evanston)*

Mineral inclusions in diamonds offer a glimpse into the Earth's interior which otherwise is mostly inaccessible. These inclusions are protected by the diamond host from alteration and therefore can be used to elucidate important details on diamond formation processes and formation depths, providing constraints for example on mantle oxygen fugacity (fO_2) and water content. Extracting information from the diamond inclusions, however, requires the use of non-destructive and non-extractive techniques and therefore experiments are usually performed at synchrotron facilities. Recently it has been shown that a conventional X-ray single-crystal diffraction source can be used to provide information on the minimum pressure at which inclusions may have been encapsulated during diamond formation.

Here we report a single-crystal diffraction study of four olivine inclusions in a macle-twin diamond performed using an in-house diffractometer with the aim of understanding the formation history of this diamond as well as an understanding of what can reliably be learned from these inclusions. A major effort has been made in obtaining accurate unit-cell parameters, as well as structural models for these olivines, since they are important

parameters for calculating isomekes, *i.e.*, lines of possible entrapment pressures and temperatures which the diamond and inclusion pair may have followed during their ascent to the Earth's surface. To this end five natural and synthetic olivine crystals having different iron content have been used to calibrate the CCD detector of the Xcalibur diffractometer used in this study. The unit-cell volumes of these five olivine samples have been compared to data in the literature to assess the accuracy of the data obtained (Fig. 3.3-7). As seen in the plot, our samples show a similar scatter to the literature data and therefore a second order polynomial was fit through all data in the region of iron content, X_{Fa}, between 0.0 and 0.5.

Intensity data collections also have been performed for the four diamond olivine inclusions and their iron content has been extracted from the results of structural refinements in which the occupancies of Fe and Mg at the olivine octahedral sites have been set as variables. The internal pressures still experienced by the inclusions (P_{inc}) due to the stiffer behaviour of diamond with respect to olivine have then been calculated using the difference between the measured unit-cell volumes and the volumes such inclusions would have at room pressure as calculated from the fit reported in Fig. 3.3-7. The inclusion pressures observed range between 0.1 and 0.7 GPa, suggesting that the minimum entrapment pressures occurred at ~ 4.3 GPa and at temperatures of ~ 1200 K.

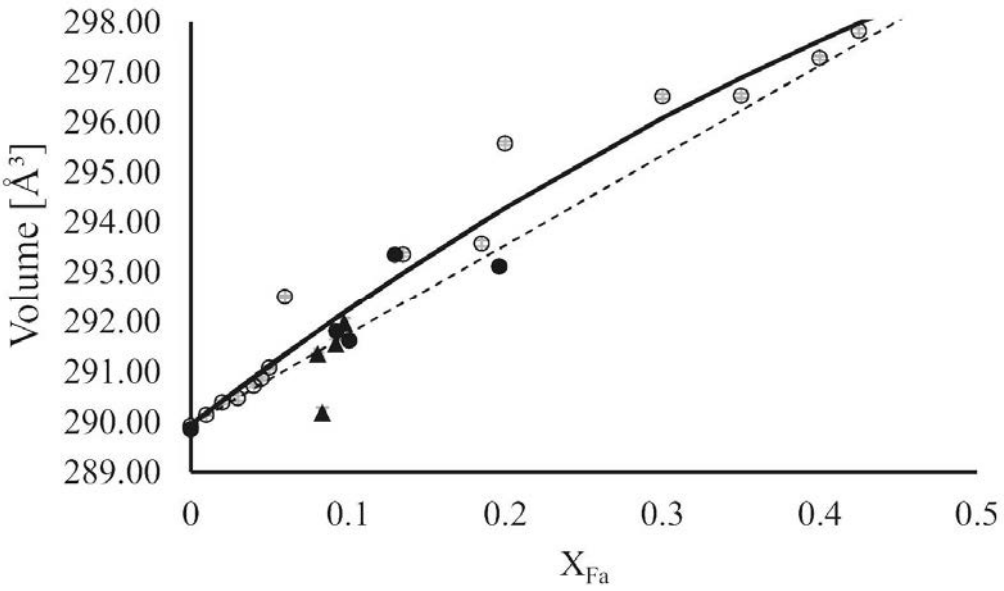

Fig. 3.3-7: Variation of the unit-cell volumes of synthetic and natural olivines as a function of their iron content, X_{Fa}. Open circles are literature data. Filled circles are data for the five natural and synthetic olivines used for the detector calibration in this study. Filled triangles are data obtained for the olivine inclusions. Note that these last data plot below the solid curve which represents a second order polynomial fit through the literature data indicating the room pressure volume variation with iron content. This suggests that the inclusions are still under pressure, due to the stiffer behaviour of the diamond.

h. *Spinel exsolution from a lower-mantle (Mg,Fe)O ferropericlase inclusion in diamond (K. Marquardt, S.D. Jacobsen/Evanston, N. Miyajima, M. Palot/Saint-Étienne, G. Pearson/ Edmonton and J. Harris/Glasgow)*

(Mg,Fe)O is of geophysical importance as the second most abundant phase of the Earth's lower mantle. Previous studies show that periclase (MgO) incorporates significant amounts of alumina at high temperature; below the solvus (~ 2000 °C) $MgAl_2O_4$ spinel exsolves and is usually dispersed within periclase grains or along grain boundaries. In nature, incorporation of various trivalent cations (generally M^{3+} for Al^{3+}, Fe^{3+}, Cr^{3+}) in ferropericlase can lead to exsolution of *e.g.*, magnesioferrite spinel, $(Mg,Fe^{2+})(M^{3+})_2O_4$, with implications for the oxidation state of the mantle. The presence of magnesioferrite exsolved from (Mg,Fe)O affects the physical properties of the bulk material, *e.g.*, strength. The change of interfaces between exsolved spinel and MgO from coherent to incoherent upon growth exhibits similarities to thin-film-substrate interfaces, where the extent of interfacial stress is compensated by regularly spaced interface dislocations. We studied magnesioferrite precipitates from a natural ferropericlase $(Mg_{0.83}Fe_{0.17})O$ that was included in a natural diamond by transmission electron microscopy on an electron transparent lamella prepared by focused ion beam (FIB) machining. We observe that areas free of linear defects are generally characterized by 20 nm-sized spinel octahedra, evenly distributed in the ferropericlase matrix (Fig. 3.3-8). However, in the presence of dislocation-like features, the magnesioferrite

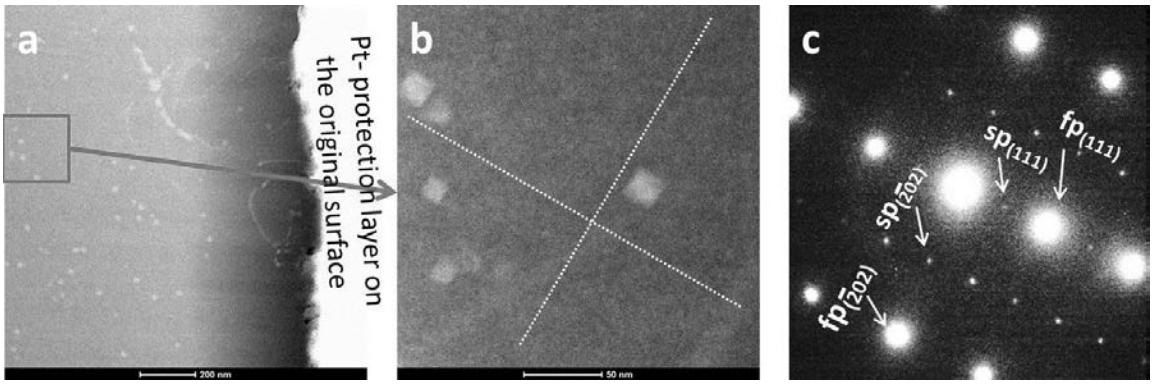

Fig. 3.3-8: Spatial relation between matrix precipitates of spinel and elongated precipitates of magnesioferrite in ferropericlase. a, b) Scanning transmission electron (STEM) image tuned to give Z-contrast. b) Enlargement of the boxed region in a. The broken lines indicate principal crystallographic planes of the matrix spinel, {111} and {202}. c) Selected area electron diffraction highlighting the intergrowth relation between ferropericlase and magnesioferrite.

preferentially nucleates along these features. It appears that the final shape of the resulting single-crystal spinels is controlled by pre-existing dislocations, in agreement with observations in another natural sample. Linear dislocation features as thin as 10 nm are filled with spinel (Fig. 3.3-9a-d). These linear features are spatially associated with surface features attributed to deformation. Our observations may explain previously observed exsolution

microstructures of needle-like spinels in ferropericlase that form a “tweed” pattern which we suggest also formed along pre-existing dislocations. We conclude from the habit and shape of spinel in this (Mg,Fe)O that exsolution nucleation sites are defect controlled, as opposed to lattice strain controlled in the defect-free regions or other known exsolution systems, *e.g.*, spinodal decomposition in feldspars. The higher density of these elongated precipitate clusters at the interface between inclusion and host hints at former differential stresses between these two phases, triggering the formation of dislocations that later act as nucleation sites for spinel exsolution.

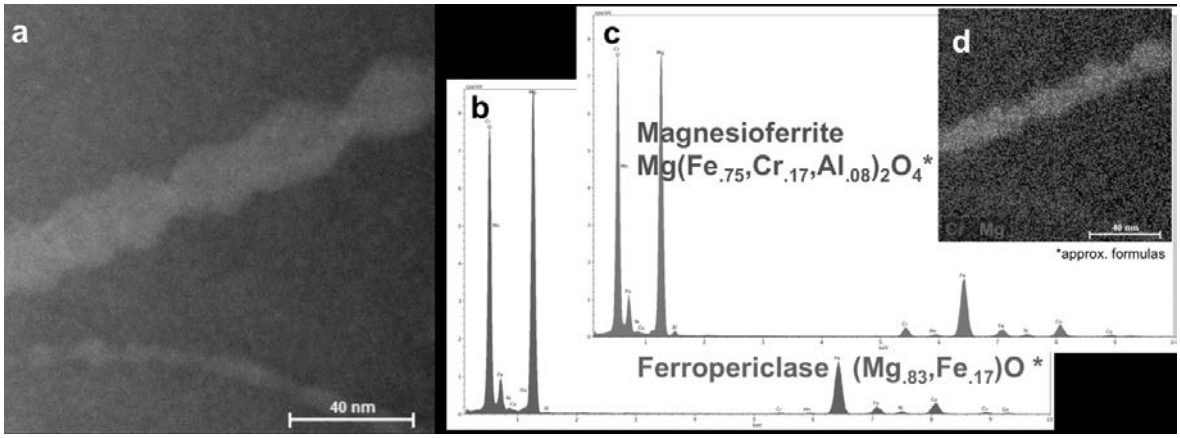

Fig. 3.3-9: a) STEM image using Z-contrast conditions. The spinel linearly aligned along a ‘dislocation like’ feature. b) Energy-dispersive X-ray (EDX)-spectra of the ferropericlase matrix with the indicated approximate composition. c) EDX-spectra of the exsolved magnesioferrite (spinel structure) with the indicated approximate composition. d) EDX-map highlighting the regional distribution of elevated Cr-content (white) with the complementary distribution of Mg (black).

i. *Transition metals in the transition zone: Crystal chemistry of minor element substitution in wadsleyite (L. Zhang, J.R. Smyth, J. Allaz, and E. Ellison/Boulder; T. Kawazoe; S.D. Jacobsen/Evanston)*

Wadsleyite (β-Mg_2SiO_4) is considered to be the fourth most abundant silicate phase in the Earth. Unlike olivine, wadsleyite can also incorporate significant amounts of trivalent cations at both tetrahedral and octahedral sites. Therefore, minor element substitution in wadsleyite may have played a significant role in the chemical evolution of the bulk silicate Earth. Because wadsleyite is a phase of very broad geochemical significance in which minor element ordering and substitution is poorly understood, we have explored the substitution and ordering of various transition metals in this mineral.

We have synthesized wadsleyite coexisting with pyroxene with 2 to 3 wt. % of either TiO_2, Cr_2O_3, V_2O_3, CoO, NiO, or ZnO under hydrous conditions in separate experiments at 1300ºC and 15 GPa. We have refined the crystal structures of these wadsleyites by single-crystal X-ray diffraction and analyzed the compositions by electron microprobe. According to crystal

structure refinements, trivalent cations Cr^{3+} and V^{3+} show a strong preference for M3 over M1 and M2 and significant substitution up to 2.7 % at the tetrahedral site. Divalent cations Ni^{2+}, Co^{2+} and Zn^{2+} show site preferences similar to those of Fe^{2+} with M1≈ M3 > M2 > T. The tetravalent cation Ti^{4+} tends to substitute into the M3 octahedron, and the site occupancy is significantly greater than that at M1, M2 and T sites (Fig. 3.3-10).

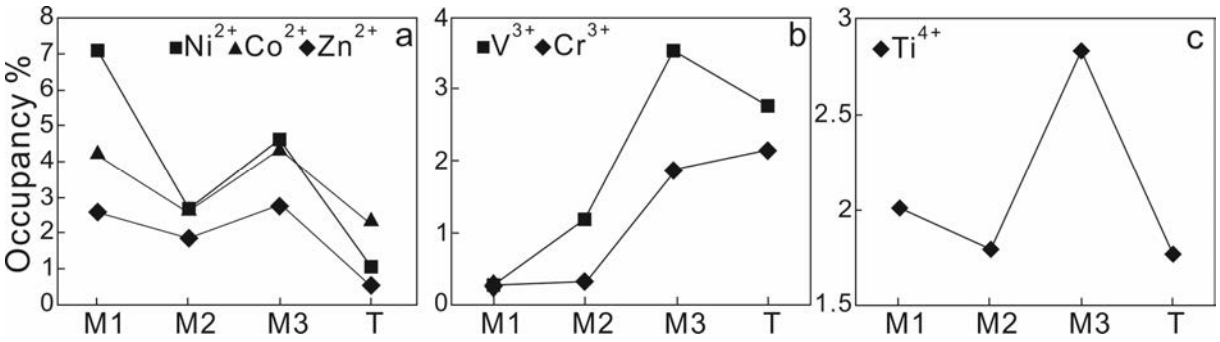

Fig. 3.3-10: Occupancies of transition metal cations at M1, M2, M3 and tetrahedral sites. (**a**) Ni^{2+}, Co^{2+} and Zn^{2+}. (**b**) V^{3+} and Cr^{3+}. (**c**) Ti^{4+}.

The observed ordering of the divalent metal cations Ni^{2+}, Co^{2+} and Zn^{2+} does not appear to be consistent with cation radius. Crystal field effects can be the most likely explanation. The calculated CFSE of Ni^{2+}, Co^{2+}, Fe^{2+} and Zn^{2+} has an approximately positive correlation with occupancy ratios (M2/(M1+M3)) at the octahedral sites, indicating that the avoidance of M2 is more apparent for cations that have lower CFSE (Fig. 3.3-11a).

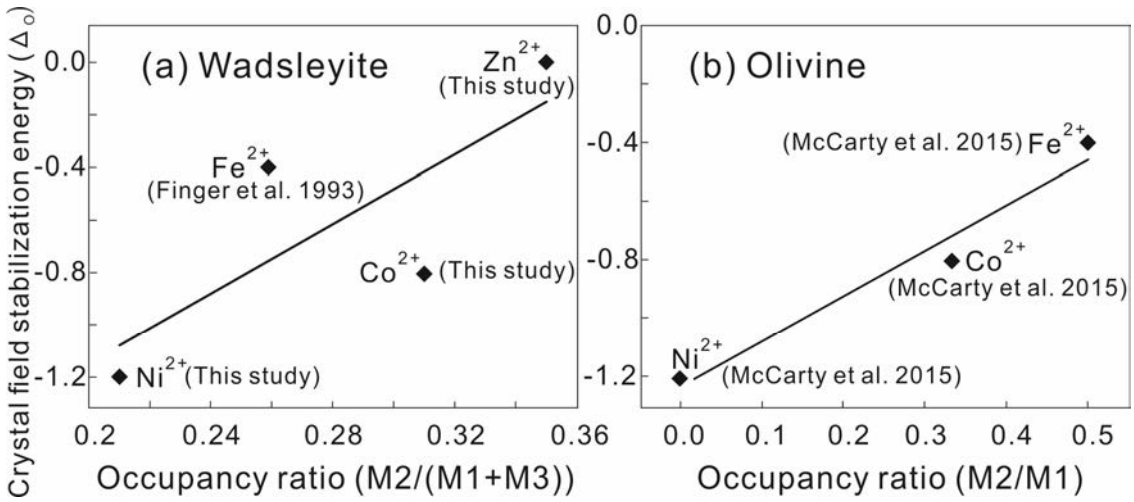

Fig. 3.3-11: (**a**) The positive correlation between occupancy ratios (M2/(M1+M3)) and crystal field stabilization energy of divalent cations in octahedra for Ni^{2+}, Co^{2+}, Fe^{2+} and Zn^{2+} in wadsleyite. Occupancy ratios of Fe^{2+} in wadsleyite ($(Mg_{0.6}Fe_{0.4})_2SiO_4$) reported by Finger *et al.* (Phys. Chem. Miner. 19, 361-368, 1993). (**b**) The positive correlation between reported occupancy ratios (M2/M1) and crystal field stabilization energy of divalent cations in octahedra for Ni^{2+}, Co^{2+} and Fe^{2+} in olivine. Occupancy ratios of Ni^{2+}, Co^{2+} and Fe^{2+} in olivine reported by McCarty *et al.* (Am. Mineral. 100, 1265-1276, 2015).

In olivine, M2 has a relatively larger octahedral volume, whereas it is less symmetric than M1. A previous study demonstrated that Ni^{2+} occupies only M1, Fe^{2+} occupies M1 and M2 roughly equally, and Co^{2+} occupies both M1 and M2 in an approximately 3:1 ratio (see McCarty *et al.* 2015), revealing a similar positive correlation between calculated CFSEs of Ni^{2+}, Co^{2+}, Fe^{2+} and occupancy ratios M2/M1 (Fig. 3.3-11b). This correlation implies that the crystal field effect is an important factor that controls the cation ordering at octahedral sites in both wadsleyite and olivine.

Microprobe analysis reveals that the tetravalent cation Ti^{4+} and trivalent cations Cr^{3+} and V^{3+} have greater solubility in wadsleyite than in olivine. Therefore our experiments indicate that Ti^{4+}, Cr^{3+} and V^{3+} may be enriched in a melt or an accessory phase if hydrous melting occurs during upward convection across the wadsleyite-olivine boundary.

j. *Coupled substitution of Fe^{3+} and H^{+} for Si in wadsleyite (T. Kawazoe, A. Chaudhari, J.R. Smyth/Boulder and C.A. McCammon)*

Wadsleyite is the most abundant mineral in the upper part of the mantle transition zone (MTZ). Incorporation of water (or hydrogen) in wadsleyite significantly influences its physical properties. Therefore, determination of substitution mechanisms of hydrogen in wadsleyite is fundamentally important to address the effects of water on the properties of the upper MTZ.

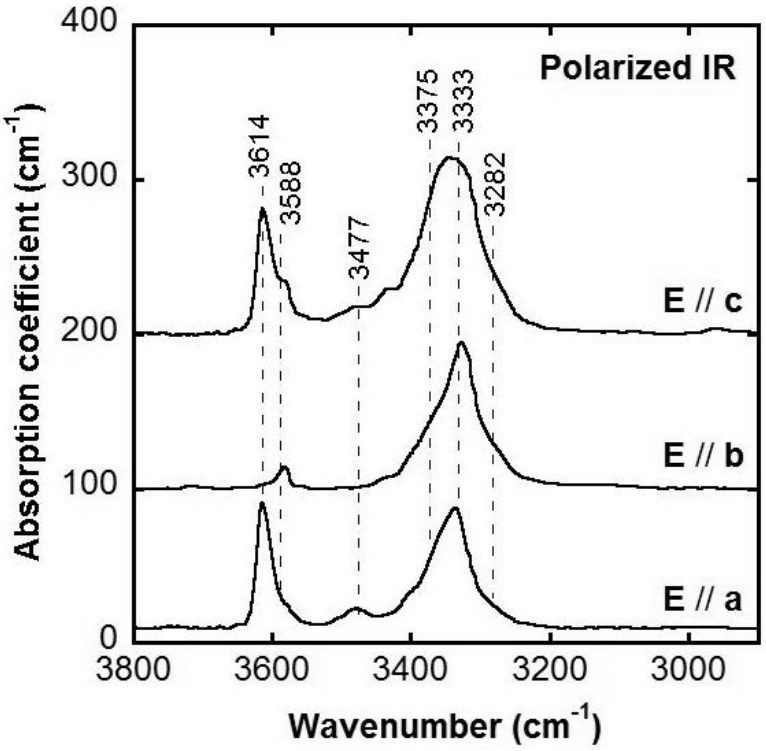

Fig. 3.3-12: Polarized infrared absorption spectra of single crystals of Fe-bearing wadsleyite with the electric vector (**E**) parallel to the crystallographic axes.

Coupled substitution of Fe^{3+} and H^+ for Si in wadsleyite was studied on single crystals of $(Mg_{0.9},Fe_{0.1})_2SiO_4$ wadsleyite containing 0.2 wt. % H_2O. The presence of Fe^{3+} at the tetrahedral site in the sample was confirmed by single-crystal X-ray diffraction and Mössbauer spectroscopy. The pleochroic behaviour of the infrared absorption band at 3477 cm^{-1} can be interpreted as protonation of silicate oxygen O3 in Fe-bearing hydrous wadsleyite (Fig. 3.3-12). The protonation of O3 together with the presence of Fe^{3+} at the tetrahedral site confirms the coupled substitution of Fe^{3+} and H^+ for Si in Fe-bearing hydrous wadsleyite.

k. *High-pressure behaviour of α-cristobalite: Bridging the gap towards the "seifertite enigma" (A. Černok, K. Marquardt, R. Caracas/Lyon, E. Bykova, G. Habler/Vienna, H.-P. Liermann/Hamburg, M. Hanfland/Grenoble and L.S. Dubrovinsky)*

In contrast to its subordinate and rather exotic terrestrial occurrence among silica phases, α-cristobalite is observed as the predominant SiO_2 polymorph in various planetary materials: from dust particles in proto-planetary disks surrounding T-Tauri stars, over lunar basalts to chondrules and the matrix of chondritic meteorites. Cristobalite was documented alongside all natural occurrences of the high-pressure, post-stishovite silica polymorph seifertite, related to heavily shocked meteorites. The response of α-cristobalite to high pressure has been a subject of numerous experimental and theoretical studies for more than two decades. The results indicated prolific polymorphism under high pressures, but no consensus has yet emerged on the sequence of these pressure-induced transformations. In particular, the structure of the high-pressure polymorph that appears above ~ 10 GPa (hereafter cristobalite X-I), which is believed to be a direct link between the low-pressure (silicon in SiO_4 tetrahedra) and the high-pressure (SiO_6 octahedra) forms of silica remained elusive. This study examined the response of α-cristobalite when compressed at different levels of hydrostaticity, with the special focus on formation and stability of cristobalite X-I.

The structural behaviour of cristobalite under pressure was investigated up to ~ 80 GPa and at ambient temperature. We investigated the behaviour of single crystals and powders, in either (quasi)-hydrostatic or non-hydrostatic environments. The high-pressure transformation path and structural behaviour were studied *in situ* by means of Raman spectroscopy and synchrotron X-ray diffraction (XRD). The experimentally determined structure was then applied in *ab initio* calculations to obtain the unit cell parameters and the Raman active modes up to 100 GPa. The samples recovered after pressure release were additionally investigated by transmission electron microscopy (TEM).

Single crystals of α-cristobalite respond differently to high pressure depending on the degree of the hydrostaticity. The highest attainable hydrostaticity preserves the initial structure of cristobalite at least up to ~ 15 GPa. When the crystal experiences even slight stresses during an experiment, the transformation sequence leads to cristobalite X-I – a monoclinic

polymorph with silicon in octahedral coordination. This polymorph belongs to the family of the high-pressure silica phases that are comprised of a distorted close-packed array of oxygen ions in which silicon atoms fully or partially occupy octahedral sites (Fig. 3.3-13). The reflections collected on a single crystal at ~ 11 GPa can be indexed by a monoclinic unit cell a = 6.658(9) Å, b = 4.1077(6) Å, c = 6.8947(11) Å, β = 98.31(4)°, V = 186.6(3) Å^3 (Z = 8 and ρ = 4.28 g/cm^3). The structure was solved in the $P2_1/n$ space group and refined at this pressure with final R_1 indices of 9 % for 209 unique reflections. This polymorph has a bulk modulus (K_{T0}=230(7) GPa) slightly smaller than that of other octahedral-based silica polymorphs (Fig. 3.3-13). Although the increase in coordination number of silicon from four to six does not

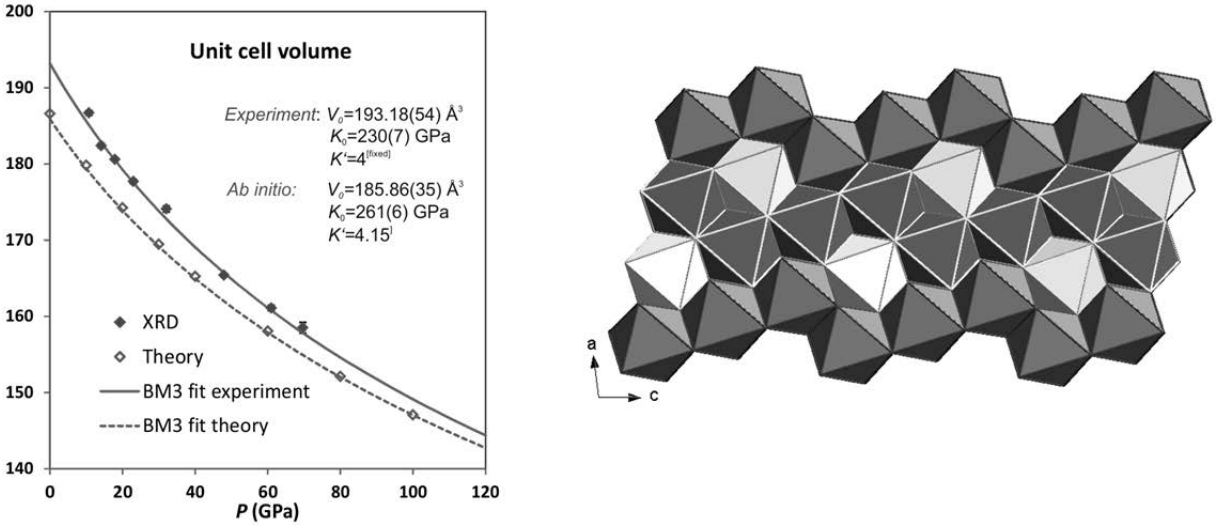

Fig. 3.3-13: Structure and compressibility of cristobalite X-I. Birch-Murnaghan Equation of State fitted to the *P*-*V* data (left) obtained in experiment (top curve) and by *ab initio* calculations (bottom curve). The structure of cristobalite X-I (right): dark gray are fully occupied octahedra (Si1 and Si2), light gray are half-occupied positions (Si3) and white-edged octahedra represent the "3x2 skeleton".

require any thermal activation, the high-pressure polymorph cannot be preserved at ambient conditions. No other silica polymorph was found to transform to an octahedra-based structure on cold compression at such low pressures (~ 11 GPa). This structure could be accommodated in a (quasi)-hydrostatic environment where temperature is not sufficient to form stishovite. Powder samples have revealed that in non-hydrostatic conditions cristobalite eventually transforms to seifertite-like SiO_2, which is quenchable (Fig. 3.3-14). The presence of seifertite might not always require the minimum shock pressures equal to that of thermodynamic equilibrium (~ 80 GPa) as it can be clearly formed at much lower pressures in an environment of uniaxial compression (*e.g.*, dynamic event). By clarifying the stability field of cristobalite X-I and revealing its structure we gained an insight into the long disputed transition mechanism α-cristobalite>II-cristobalite >X-I-cristobalite >α-PbO_2 structured SiO_2.

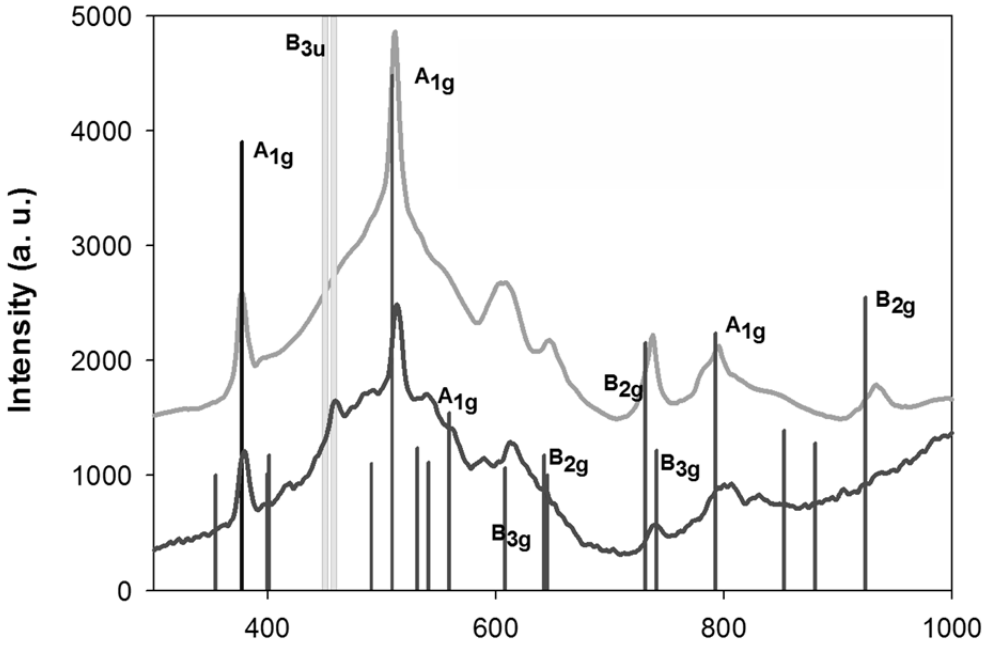

Fig. 3.3-14: Raman spectrum of recovered seifertite (bottom spectrum), collected outside diamond anvil cell. Ar^+ laser beam conditions: excitation wavelength 514 nm; power 0.7 W, acquisition 3x120 seconds. For comparison, a Raman spectrum from the literature of seifertite obtained experimentally (top spectrum) and theoretically (symmetry labeled lines) from the WURM database are given.

l. *Quenchable post-stishovite and implications for water in the lower mantle (R. Myhill, T. Boffa Ballaran, D.J. Frost and N. Miyajima, in collaboration with H. Bureau and C. Raepsaet/Paris)*

The high-pressure polymorph of quartz, stishovite, has a tetragonal structure similar to that of rutile with Si in octahedral coordination. Above 50 GPa stishovite transforms to an orthorhombic $CaCl_2$-type structure indicated as post-stishovite. This transition is reversible and therefore it is not possible to recover the post-stishovite phase at room conditions. Due to the softening of the shear modulus of stishovite at the transition pressure, the transformation to post-stishovite should produce zones of low shear wave velocities which act as scatterers in the deep mantle and it is therefore of interest to seismologists. The incorporation of Al_2O_3 in stishovite has a profound effect on the stability of the post-stishovite phase. Al_2O_3 can be incorporated into stishovite by the substitution of Si by Al with the formation of oxygen vacancies. It has been argued that the addition of 4 wt. % Al_2O_3 in the absence of any other components causes the transition pressure to shift from 50 to 23 GPa at room temperature. Incorporation of Al into the stishovite structure also can occur according to the coupled substitution of Al and H for Si, which may have an even more drastic effect on the tetragonal to orthorhombic transition. However, H_2O contents in tetragonal stishovite measured using infrared spectroscopy are less than 20 % of that expected from an AlOOH substitution.

This study was designed to investigate water solubility in Al-rich stishovite by synthesising crystals at relatively high temperature. Large crystals were grown at 1900 °C for 15 minutes from two compositions corresponding to 90:10 and 85:15 mole ratios SiO_2:$Al(OH)_3$. The more aluminium-rich composition grew small amounts of aluminous phase D in addition to stishovite.

The recovered capsule with 90:10 SiO_2:$Al(OH)_3$ bulk composition was mounted in epoxy and polished to expose the synthetized material. The mount was first analysed using a Bruker micro-diffractometer equipped with a microfocus source with Co radiation focused to 50 μm by means of a polycapillary mini-lens and a Vantec500 2D detector. Some reflections of the measured diffraction pattern (Fig. 3.3-15) present a clear splitting suggesting that the orthorhombic post-stishovite structure has been retained during quenching or it is stable at all pressures.

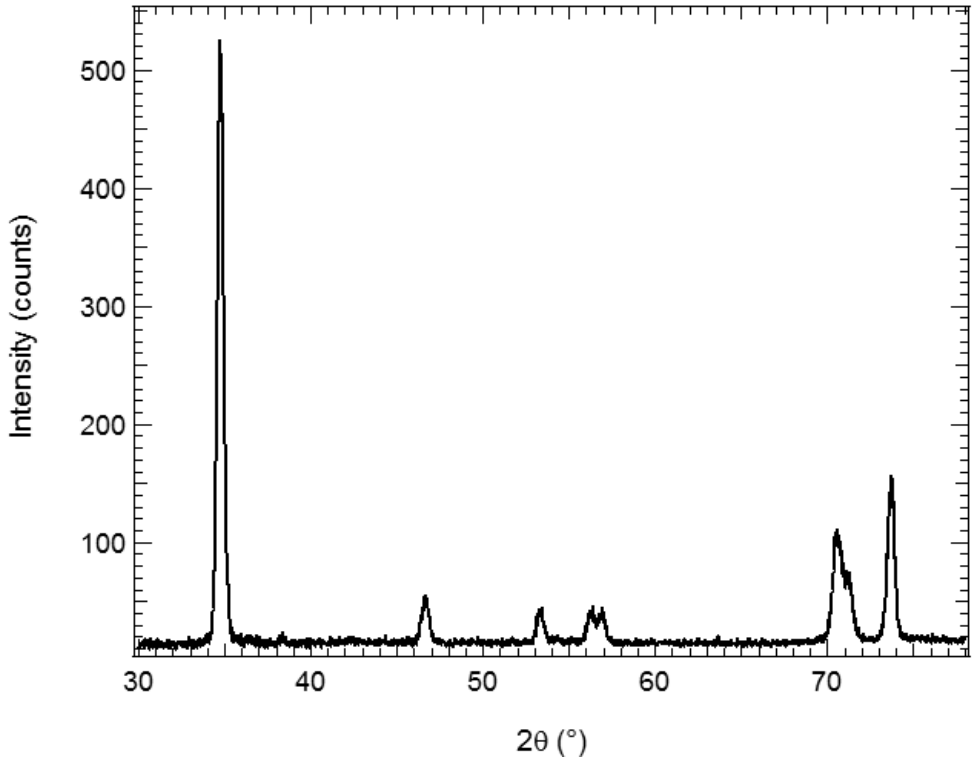

Fig. 3.3-15: Diffraction pattern of sample H4095 collected for 1000 seconds using the Bruker micro-diffractometer. Stishovite is the only phase present in the run product.

Microprobe analysis of the same sample yielded 9:1 SiO_2:$AlO_{1.5}$ molar ratios, consistent with the starting composition. Water concentrations were analysed by elastic recoil detection analysis (ERDA) at Saclay, Paris, and found to be ~ 20000 ppm, which is identical (within 13 % analytical uncertainty) to a 1:1 molar ratio of Al:H.

m. *Precise determination of the ringwoodite-periclase-bridgmanite field of the post-spinel transition in MgO-FeO-SiO_2 (R. Huang, D. Druzhbin, T. Yamamoto/Hiroshima, N. Tsujino/ Okayama, L. Wang, H. Fei, T. Ishii, E. Kulik/Hamburg, Y. Tange/Hyogo, Y. Higo/Hyogo and T. Katsura)*

The 660-km discontinuity, which provides a key for understanding the structure and dynamics of the deep mantle of the Earth, is primarily explained by the dissociation of $(Mg,Fe)_2SiO_4$ ringwoodite (Rw) to $(Mg,Fe)SiO_3$ bridgmanite (Brg) and (Mg,Fe)O ferropericlase (fPc). Several seismological studies suggested that its thickness is extremely small, namely only 2-4 km. If the 660-km discontinuity is attributed to the Rw dissociation, the pressure interval of the coexistence of Rw+Brg+fPc will be only 0.10-0.15 GPa. Because of experimental difficulties, it is not clear whether the pressure interval of the Rw+Brg+fPc coexistence satisfies the above requirement. In this project, we will determine the regions of the Rw+Brg+fPc coexistence in the system $(Mg,Fe)_2SiO_4$ at a temperature of 1700 or 1800 K with precision better than 0.05 GPa by means of *in situ* X-ray diffraction.

High *P-T in situ* X-ray diffraction experiments were conducted using a Kawai-type multianvil apparatus with a DIA-type guide block system in the white X-ray beam line BL04B1 at the third generation synchrotron radiation facility, SPring-8. Energy-dispersive X-ray diffraction was conducted using a Ge solid-state detector with a horizontal goniometer with a 0.05-mm wide horizontal incident slit. The horizontal width of the dispersion and receiving slits were 0.05 and 0.2 mm, respectively. Exposure times were usually 300-600 s. The 2-theta angle was about 8°.

The edge length of the octahedral pressure medium was 8.3 mm, which was compressed with eight tungsten carbide anvils with 3 mm truncation. A TiB_2 cylinder was used as a heater, and also provided a reduced sample environment and X-ray transparency. A D-type thermocouple was inserted into the heater through Al_2O_3 tubes of electric insulator, whose junction was placed between the sample and pressure marker of sintered MgO.

We prepared two kinds of starting materials. One starting material is a mixture of Mg_2SiO_4 forsterite, $MgSiO_3$ enstatite and MgO periclase with a molar ratio of 1:1:1, which was sintered at a temperature of 873 K and a pressure of 3 GPa. The other starting material consisted of $(Mg_{1.41}Fe_{0.59})SiO_4$ olivine, $(Mg_{0.89}Fe_{0.11})SiO_3$ orthopyroxene and $(Mg_{0.59}Fe_{0.41})O$ ferropericlase also with the same molar ratio, and was sintered at the same conditions as the other starting material. The bulk composition of this starting material was $(Mg_{0.7}Fe_{0.3})_2SiO_4$.

We pressurized the samples to 27.2 ~ 27.5 GPa at ambient temperature, and heated them firstly to temperatures of 1000 ~ 1200 K, then finally to 1700 or 1800 K at a constant press load. Two examples showing changes in diffraction patterns with heating are shown in Fig. 3.3-16 and Fig. 3.3-17. In the first example, the starting material was of the Mg_2SiO_4 bulk composition, showing diffraction peaks of Fo, En and Pc. It was pressurized to 27.2 GPa at ambient temperature, and then heated to 1000 K, at which Rw peaks appeared at 22.6 GPa.

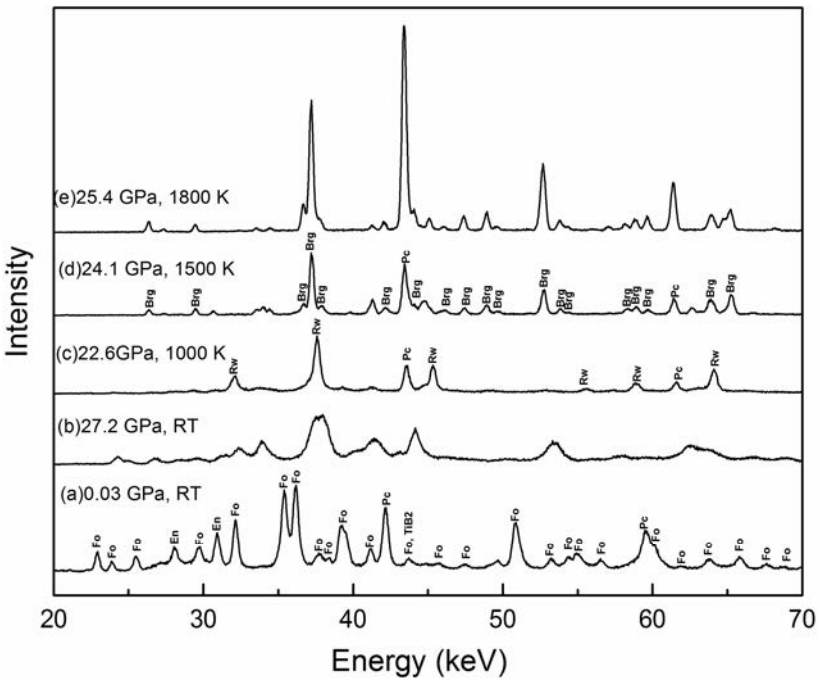

Fig. 3.3-16: XRD patterns at different pressure and temperature conditions of Mg_2SiO_4 bulk composition. Fo: forsterite; En: enstatite; Pc: periclase; Rw: ringwoodite; Brg: bridgmanite.

By further heating to 1500 K, Brg peaks appeared and Rw peaks disappeared at 24.1 GPa, and then Brg peaks remained at 1800 K and 25.4 GPa, suggesting the Brg stability field. In the other example, the starting material was of the $(Mg_{0.7}Fe_{0.3})_2SiO_4$ bulk composition, showing only Ol and fPc peaks, but not Opx ones. By pressurizing and then heating to 1200 K, the Ol peaks disappeared and Rw and akimotoite (Ak) peaks appeared at 23.4 GPa. By further heating to 1700 K, Ak peaks disappeared and Rw peaks remained without appearance of Brg peaks at pressures from 22.1 to 22.5 GPa, suggesting the Rw stability field.

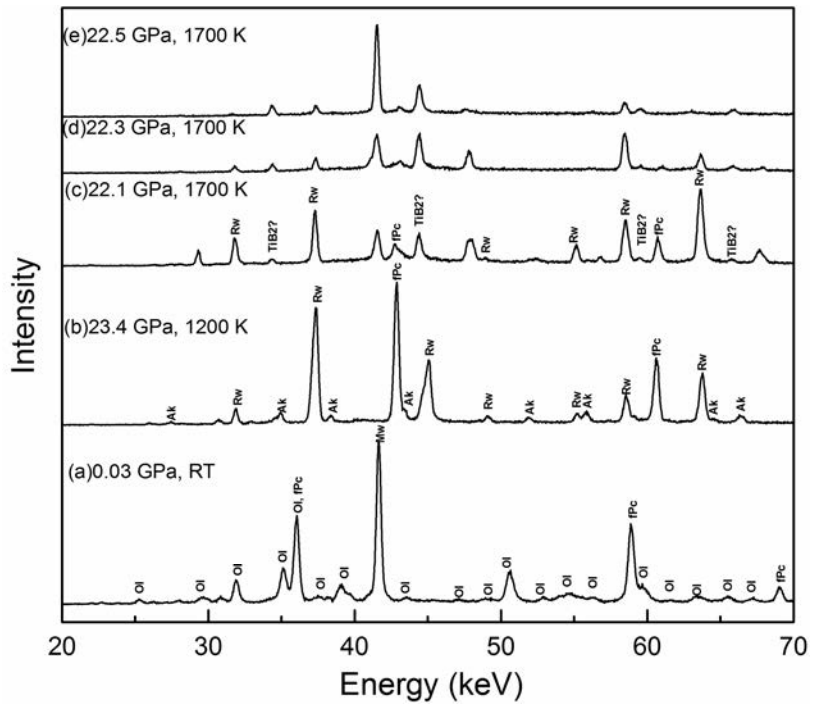

Fig. 3.3-17: XRD patterns at different pressure and temperature conditions of $(Mg_{0.7}Fe_{0.3})_2SiO_4$ bulk composition. (b) (c), (d), (e) are kept at constant press load of 6.5 MN and 1700 K for 5 min, 15 min and 25 min, respectively. Ol: olivine; fPc: ferropericlase; Ak: akimotoite; Rw: ringwoodite.

Thus, we established an appropriate procedure to determine the region of Rw-Brg-fPc coexistence. We are going to determine the phase relations by means of this procedure in 2016.

n. *The high-pressure behaviour of spherocobaltite ($CoCO_3$): A Raman spectroscopy and XRD study (S. Chariton, V. Cerantola, L. Ismailova/Bayreuth, E. Bykova, M. Bykov, I. Kupenko/ Grenoble, L.S. Dubrovinsky, C.A. McCammon, T. Boffa Ballaran and A. Kurnosov)*

Carbonate-bearing rocks can play a prominent role in the deep carbon cycle. Recently, it has been of great interest to study carbonates at the pressure and temperature conditions of the Earth's mantle. While the most abundant carbonate minerals, namely calcite ($CaCO_3$), magnesite ($MgCO_3$) and siderite ($FeCO_3$), have been the focus of previous studies, the behaviour of rarer carbonates is less well known. Studying transition metal carbonates can be useful when searching for systematics in their high-pressure behaviour in terms of structure and spin transitions with respect to the size of their cationic radius. Therefore, in the present work we studied the high-pressure behaviour of spherocobaltite ($CoCO_3$), a mineral which contains a transition metal element with a cationic radius comparable to that of Fe^{2+}.

Pure $CoCO_3$ single crystals were synthesized, loaded into diamond anvil cells, and then subjected to high pressures. Raman spectra and X-ray diffraction (XRD) patterns were collected at pressures up to ~ 55 GPa. The synthesis of the samples and the Raman spectroscopy measurements were performed at BGI, while single crystal XRD data were collected at a synchrotron (ESRF). One of the crystals was laser heated to ~ 2000 K at ~ 57 GPa.

Raman spectra in combination with XRD data of spherocobaltite ($CoCO_3$) show that no structure transformation and no spin crossover takes place upon compression to at least ~ 55 GPa at room temperature. The frequencies of four Raman bands progressively shift to higher values with increasing pressure (Fig. 3.3-18a,b). No splitting of the Raman peaks or new peaks appear. We fitted the equation of state (EoS) for $CoCO_3$ using a 3rd order Birch-Murnaghan EoS and no irregularities or volume collapse were observed (Fig. 3.3-18c). The bulk modulus is 130.1(1) GPa (K'=4.34) and thus $CoCO_3$ is less compressible than $FeCO_3$ and $MnCO_3$, where the bulk moduli are 110(2) and 106.9(11) GPa, respectively. The evolution of the carbon-oxygen (C-O) bond lengths with increasing pressure suggests that the CO_3 units remain nearly rigid. On the other hand, the cobalt-oxygen (Co-O) bond length decreases faster, suggesting more compressible CoO_6 octahedra (Fig. 3.3-18d)

The magnesite-type ($R\bar{3}c$) structure is stable up to 54 GPa at room temperature and after heating to ~ 1200 K. After heating at ~ 2000 K at the same pressure we observed decomposition of the compound, where one of the dissociation products is Co_3O_4 according to Raman spectroscopy and XRD data. By comparison with other carbonates we suggest that

with decreasing cationic radius the respective carbonate mineral becomes less compressible, forms less distorted octahedra, and is stable in a magnesite-type structure over a wider pressure range. However, there are still many open questions, such as the relation between cationic radii and spin crossover pressure in transition metal carbonates at the pressures over which the magnesite ($R\bar{3}c$) structure remains stable. Understanding the high-pressure structures and properties of transition metal carbonates provides some insight into systematics in their crystal chemistry.

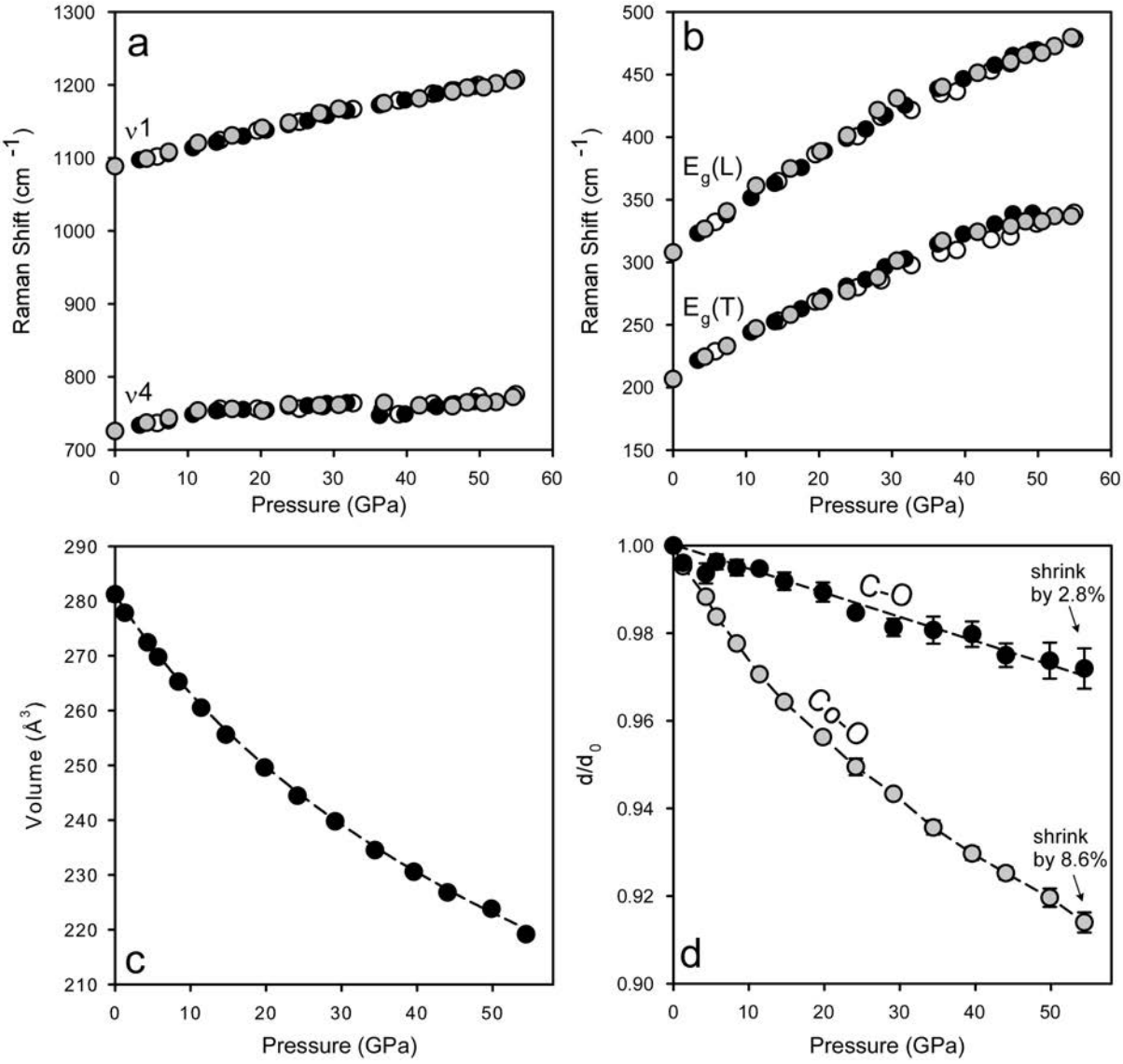

Fig. 3.3-18: (a) Pressure dependence of the frequency shifts of ν1 and ν4 Raman modes for two experiments, DAC1 on compression (open circles) and DAC2 on compression (black circles) and decompression (grey circles), (b) Pressure dependence of the frequency shifts of E_g(L) and E_g(T) Raman modes where symbols are the same as for the previous plot, (c) Equation of state for $CoCO_3$, (d) Evolution of the C-O and Co-O bond lengths with increasing pressure. Error bars are shown in all plots and in some cases they are smaller than the symbols.

o. *The high-pressure transformations of rhodochrosite ($MnCO_3$) (S. Chariton, E. Bykova, M. Bykov, V. Cerantola, L. Ismailova/Bayreuth, I. Kupenko/Grenoble, G. Aprilis/Bayreuth, L.S. Dubrovinsky and C.A. McCammon)*

There is compelling evidence that carbon and carbonates are present inside the Earth's mantle. Magnesite ($MgCO_3$), ankerite ($(Mg,Ca,Fe)CO_3$) and dolomite ($(Mg,Ca)CO_3$) (or their high-pressure forms) have been shown to be the most likely stable carbon-bearing phases, together with diamonds and fluid components, existing in mantle mineral assemblages. Thus, the discovery of crystal-chemical regularities in the behaviour of carbonates at high-pressure and high-temperature conditions is an important task of mineral physics. It is well known that at low pressures, the crystallization of carbonates into calcite or aragonite-type structure is controlled by the cation radius. Moreover, changes in the electronic state of transition metal cations (like Fe^{2+}, Mn^{2+}, etc.) may further affect the high-pressure behaviour of carbonates. Apart from siderite ($FeCO_3$), rhodochrosite, a Mn-bearing carbonate with $3d^5$ electrons, is one of the most obvious candidates to be studied.

We synthesized pure $MnCO_3$ single crystals at 18 GPa and 1600 K using a Sumitomo multianvil press at BGI. Diamond anvil cells were employed for high-pressure experiments and Ne gas, which was loaded at 1.4 kbar, was used as a pressure-transmitting medium to ensure hydrostaticity. Raman measurements up to ~ 55 GPa were carried out using a Dilor XY spectrometer (Ar^+ excitation laser, 2 cm^{-1} spectral resolution, 514 nm line). Single crystal X-ray diffraction measurements up to ~ 66 GPa were conducted at the ID09A beamline at ESRF.

The frequency shifts of four Raman bands (E_g(T), E_g(L), ν4, ν1) of $MnCO_3$ were monitored with increasing pressure (Fig. 3.3-19). All four peaks gradually shift to higher frequencies up to ~ 40 GPa. However, at higher pressures 12 new Raman peaks appear in the spectrum, one of which (ν1') appears at higher frequencies than the ν1 mode. This dramatic change in the Raman spectrum is associated with a structural transformation that takes place. Analysis of the XRD data reveals that the magnesite-type structure ($R\bar{3}c$) of rhodochrosite transforms to the triclinic structure ($P\bar{1}$) of $MnCO_3$-II, which is similar to that of $CaCO_3$-VI. This observation is in good agreement with a recent report in the literature. Second order Birch Murnaghan equations of state were fitted to the magnesite-type $MnCO_3$ (K_0 = 107(1) GPa) and the triclinic $MnCO_3$-II (K_0 = 93(1) GPa) compression data (Fig. 3.3-20). The structural transition in $MnCO_3$-II is accompanied by a ~ 5 % volume collapse (Fig. 3.3-20). This may be a sign of a high to low spin transition in Mn^{2+}. The new peak that appeared in the Raman spectra upon the structural transition, which is close to the ν1 mode (ν1'), also supports this hypothesis. However, it is worth mentioning that we did not observe any color change of the crystals above 43 GPa and thus the exact nature of this phase transition requires further study.

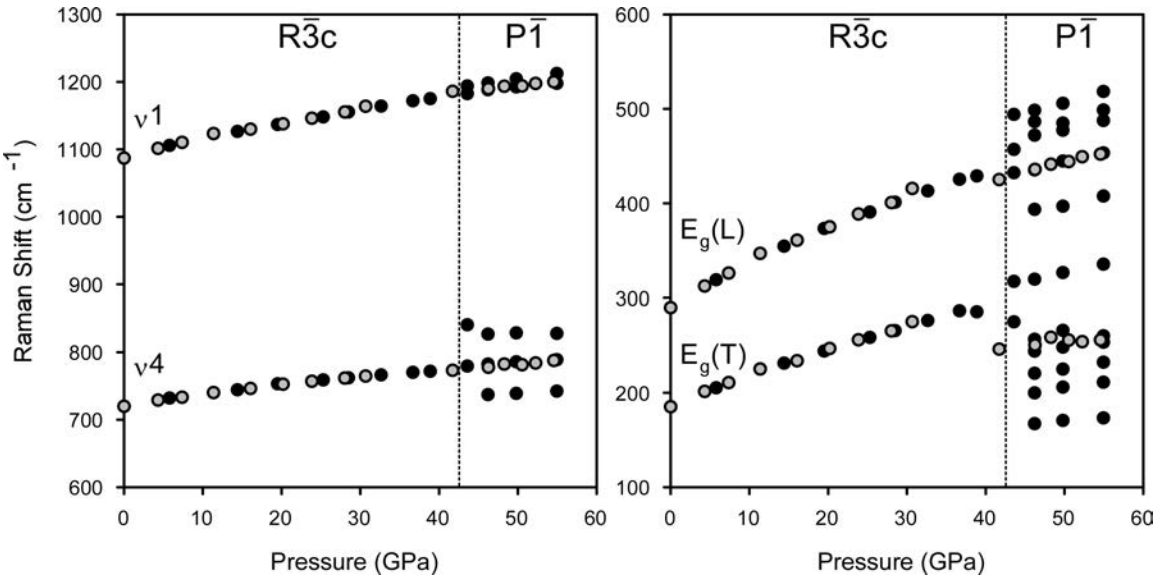

Fig. 3.3-19: Pressure dependence of the frequency shifts of four Raman modes of $MnCO_3$ upon compression (black circles) and decompression (grey circles).

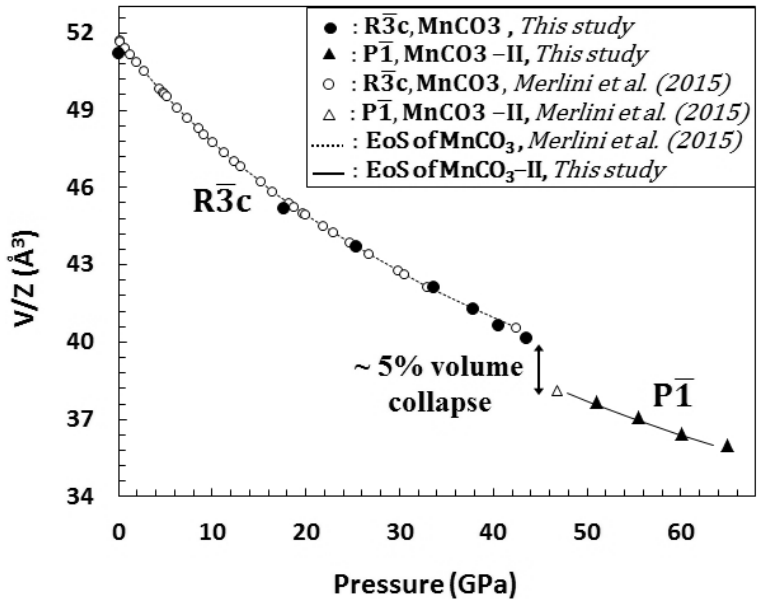

Fig. 3.3-20: Volume data of rhodochrosite with increasing pressure and the equation of state for magnesite-type $MnCO_3$ and triclinic $MnCO_3$-II showing data from this study and the literature [Merlini *et al.*, 2015, Am. Mineral., 100, 2625-2629]. Error bars are shown in both plots and in some cases they are smaller than the symbols.

p. *The B1-B2 phase transition in MgO from self-consistent phonon calculations (M. Wenz and G. Steinle-Neumann)*

Magnesium oxide (MgO) is geophysically significant as it is an important mineral phase in the Earth's lower mantle, and it is expected to play an important role in the interior of larger

planets. MgO is rather unique among minerals because of its extreme phase stability under pressure (P) and temperature (T). This is due in part to its high melting T and wide electronic band gap. The phase diagram of MgO consists of three phases: at ambient conditions, it is stable in the B1 structure, at $T = 3{,}100$ K it melts and at high P it transforms to the B2 structure. Within the Earth's mantle only the B1 structure exists, but the B1-B2 transition may play a role in the cores of giant planets (*i.e.*, Jupiter) or the mantle of super-earths with $P > 1$ TPa. As it is extremely challenging to reach conditions of the B1-B2 transition in experiments, there is a need for computational research to describe the behaviour of MgO at and past this transition. Therefore, *ab initio* simulations have become a key tool in exploring the MgO phase diagram and properties. At static conditions computational studies have found the B1-B2 transition to occur in the range 400-500 GPa, and high T methods (molecular and lattice dynamics) found a negative Clausius-Clapeyron slope for the transition.

Simulations of the behaviour of crystals at relatively low T often employ lattice dynamics (LD), which restricts the atomic displacements to crystallographically defined directions (eigendirections) with small amplitudes, yielding results in the quasi-harmonic (QH) limit that are valid below the Debye temperature (743 K for MgO at ambient pressure). Beyond the QH limit, phonon-phonon interactions are no longer negligible, and the Self-Consistent *Ab Initio* Lattice Dynamics (SCAILD) approach has been developed to consider these contributions. In the SCAILD approach frequencies change with temperature and thus calculations are performed for each temperature separately. Here we compute both QH and self-consistent phonons to explore to what extent phonon-phonon interactions influence the B1-B2 phase transition in MgO, using the Hellmann-Feynman forces computed within density functional theory-based electronic structure methods. From the phonon frequencies, the thermal contribution to Helmholtz energy (F_{th}) is computed and added to the total energy E_0 of the static lattice to compute a total Helmholtz energy F_{tot}. The stable phase at each unit cell volume and temperature is the one that is energetically favored as long as all phonon modes have real frequencies, *i.e.*, the structure is dynamically stable.

Neglecting thermal contributions (static conditions), the B2 phase becomes energetically favored over B1 at cell volumes $V \leq 9.05$ Å^3 p.f.u. (*i.e.*, a compression of $V/V_0 = 0.47$, corresponding to a P of ~ 495 GPa), in line with previous computations. Taking zero point motion from the QH-LD simulations into account the transition is shifted to $V = 9.15$ Å^3 p.f.u., or ~ 485 GPa (Fig. 3.3-21). The Clapeyron slope found in the QH-LD is negative, consistent with previous results. As we do not have a sufficient number of results to fit a series of isothermal equations-of-state from SCAILD computations, we are unable to convert F_{tot}-V-T triplets to P, and have to consider the B1-B2 transition in V-T space (Fig. 3.3-21). We find that the slope of the phase transition shifts to larger values compared to the QH-LD results, with the B2 phase stable at smaller V at high T (Fig. 3.3-21). Further simulations are required to confirm the transition location and to fit reliable equations-of-states to the SCAILD results. Isothermal equations-of-state and ideally closed expressions for F_{tot}-V-T equations-of-state in the form of a Mie-Debye-Grüneisen Birch-Murnaghan model will help

to convert the phase transition location to P-T space and compute thermodynamic properties such as density and compressibility, appropriate for applications in planetary structure.

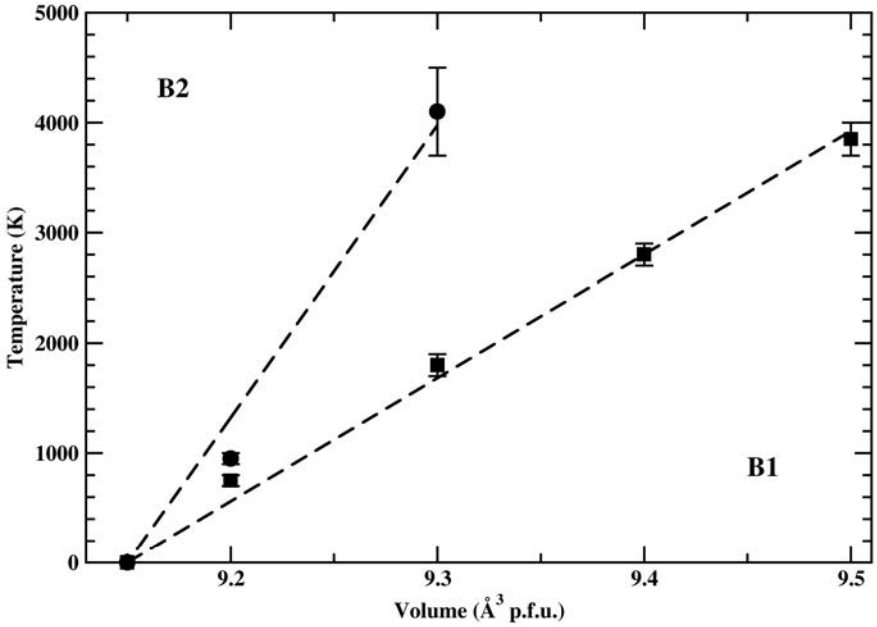

Fig. 3.3-21: Location of the B1-B2 phase transition in V-T space as predicted in the QH-LD approximation (squares) and with the SCAILD method (spheres). Dashed lines show linear interpolations of the results.

q. *Excess properties of thermodynamic solution models: Applications to high-pressure phase relations and seismology (R. Myhill)*

Thermodynamic models of solid and liquid solutions are increasingly used to calculate phase relations and seismic properties over large pressure and temperature ranges. Research into mantle phase relations, subduction and differentiation of the early Earth frequently involves calculations spanning thousands of Kelvin and tens or even hundreds of gigapascals. Despite modelling properties over such huge ranges, existing thermodynamic models tend to assume that excess entropies and volumes remain constant. This assumption is both thermodynamically inconsistent and deviates significantly from experimental results when large temperature and pressure ranges are investigated.

This study introduces an extension to the subregular Margules mixing model which employs intermediate compounds to define the excess thermodynamic properties of solid solutions. Mathematical derivations are provided for excess thermodynamic properties (enthalpy, entropy, volume) and their pressure and temperature derivatives (bulk modulus, thermal expansion etc.). Heuristics are suggested for intermediate compounds where individual thermodynamic properties are poorly constrained.

The extended solution model scheme has been applied to pyroxene, garnet and melt solutions (see Fig. 3.3-22 for example). Accurate modelling of phase relations and seismic velocities require excess volumes of mixing to decrease as a function of pressure. The formulation proposed here allows for a wealth of experimental data to be incorporated into solution models, and is expected to be important for geochemical and geophysical models of the Earth and other planetary bodies.

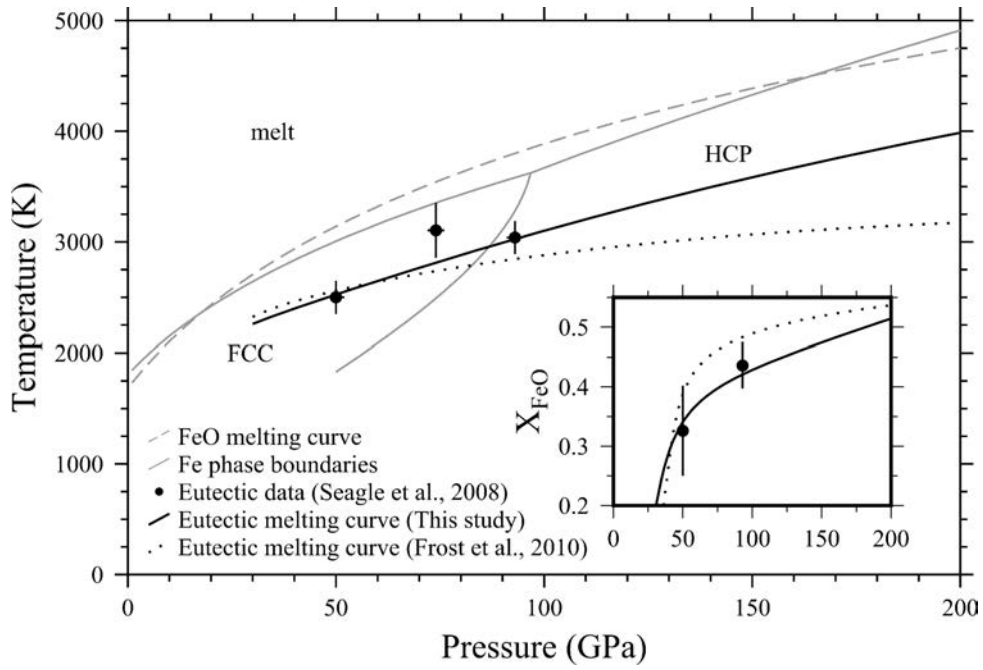

Fig. 3.3-22: Melting temperature in the Fe-O system as a function of pressure. Inset: eutectic composition in the Fe-O system. Previous models employ constant volume and entropy terms derived from data obtained at < 25 GPa. Such models deviate significantly from experimental constraints at pressures corresponding to the Earth's core.

r. *Synthesis of rutile-type complete solid solution in the SiO_2-GeO_2 system at 12 GPa and 1600 °C (E. Kulik, N. Nishiyama/Hamburg, A. Masuno/Tokyo, Ya. Zubavichus/Moscow, H. Ohfuji/Matsuyama and T. Katsura)*

Silicon dioxide (silica) is a fundamental oxide component for Earth and materials sciences. Pressure-induced phase transitions in silica have been heavily studied and it is known that at pressures above 9 GPa silica undergoes phase transitions with the coordination number of Si increasing from 4 to 6. This high-pressure polymorph modification of SiO_2 with the rutile-type structure, stishovite, is stable between 9 and 50 GPa and further transforms into the $CaCl_2$-type structure. Pressure-induced phase transitions in germanium dioxide (germania) have also been widely studied because this material is regarded as a structural analogue of silica. Rutile-type germania is stable at ambient conditions and transforms to the $CaCl_2$-type

structure at a pressure ~ 35 GPa. The phase diagrams of silica and germania show that the rutile structure for both components is stable in a pressure interval between 9 and 35 GPa. Based on theoretical predictions that these two end members are completely miscible, we hypothesized that a rutile-structured phase becomes stable as $(Si_{1-x},Ge_x)O_2$ (x = 0-1) solid solution in a pressure range from 9 to 35 GPa.

At ambient conditions, stishovite is known to be the hardest oxide and it is also elastically stiff. The reported bulk modulus and Vickers hardness is 300 GPa and 30 GPa, respectively. Rutile-type germanium dioxide is also a potential hard material, since the hardness of ionic and covalent materials increases with bulk modulus. For germania, the reported bulk modulus is 259 GPa, which is slightly larger than that of Al_2O_3 corundum (254 GPa). For these reasons, the solid solution between SiO_2 and GeO_2 with rutile structure also have potential as hard ceramics with tunable elastic and mechanical properties of stishovite by substituting Ge into the Si sites.

In previous experimental studies, the solubility of SiO_2 and GeO_2 into the rutile phase was investigated at 9-11 GPa and 400 °C-1200 °C. Those results indicated limited mutual solubility of these two components in the rutile structure. In this study, we report the synthesis of solid solutions with rutile-type structure in the SiO_2-GeO_2 system at 12 GPa and 1600 °C using SiO_2-GeO_2 glasses prepared by a container-less processing method. Our experimental data indicate that rutile structures in this system form a complete series of solid solutions at these conditions.

In this study we used three different types of starting materials. Homogeneous glasses with composition (Si_{1-x},Ge_x) (x = 0.1, 0.2, 0.5, 0.7) were fabricated by container-less processing using an aerodynamic levitation furnace (ALF) installed at the Institute of Industrial science, Tokyo. For both end-members we used commercially available silica glass and germania quartz powder. These powders were also used for mechanical mixtures with two different bulk compositions (x = 0.5, x = 0.7). The last type of starting material was SiO_2-GeO_2 glasses, prepared using a normal lamp furnace (NF).

For high-pressure and high-temperature synthesis, we used a 1000-ton Kawai-type apparatus installed at the Deutsches Elektronen Synchrotron (DESY). In all synthesis runs, samples were compressed at room temperature up to the target pressure (7, 9 and 12 GPa), and after compression, temperature was increased with the heating rate ~ 100 °C /min. The synthesis temperature (1200 °C, 1400 °C and 1600 °C) was maintained for 2 hours. After temperature quenching, decompression was performed at room temperature. For the characterization of the recovered samples, we used a combination of X-ray diffraction measurements and Raman spectroscopy. For powdered samples XRD measurements were performed at K1.3b (structure materials science beamline) at the Kurchatov synchrotron radiation source, where X-rays were monochromatized by a channel-cut monochromator with Si(111) crystal to 17.998 keV. We also observed the microstructure of sample with composition $(Si_{0.5},Ge_{0.5})O_2$, synthesized at 1600 °C using a field emission scanning electron microscope.

Figure 3.3-23 shows powder X-ray diffraction patterns of the samples recovered from 12 GPa and 1600 °C. We used ALF-glasses as starting materials for the intermediate compositions. Each XRD pattern can be explained by the presence of a single phase with a rutile structure. With increasing GeO_2 content of the staring composition, all of the peak positions shift towards lower diffraction angle. We also can clearly observe that the lattice constants increase linearly with the germanium content (x) (Fig. 3.3-24), which indicates the formation of a complete solid solution with the rutile structure at these conditions. Our results from low-temperature experiments with different starting materials demonstrate that thermodynamic equilibrium state is achieved in this system at 12 GPa and 1600 °C. A temperature of 1200 °C and a heating duration of 2 hours (the same conditions as in previous studies) are insufficient to achieve thermodynamic equilibrium to study the mutual substitution between SiO_2 stishovite and GeO_2 argutite. At lower pressure (7 and 9 GPa) and 1600 °C we observed decomposition of $(Si_{0.5},Ge_{0.5})O_2$ into SiO_2-rich coesite and GeO_2-rich rutile phase. In summary, a complete solid solution with a rutile-type structure was synthesized at 12 GPa and 1600 °C in theSiO_2-GeO_2 system. Therefore, the elastic and mechanical properties of SiO_2 stishovite, which is the hardest oxide at ambient conditions, are tunable with substitution of Ge into the Si site.

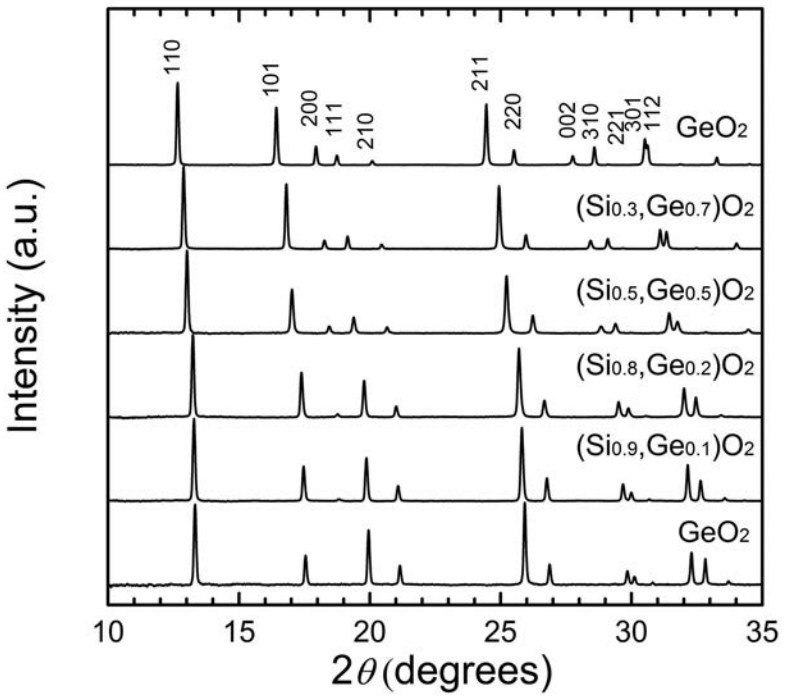

Fig. 3.3-23: Powder X-ray diffraction patterns of (Si_{1-x},Ge_x) (x = 0, 0.1, 0.2, 0.5, 0.7 and 1) rutile-phase synthesized at 12 GPa and 1600 °C. All patterns were collected at the K1.3 b beamline, Kurchatov institute, Russia. X-ray energy was 17.998 keV.

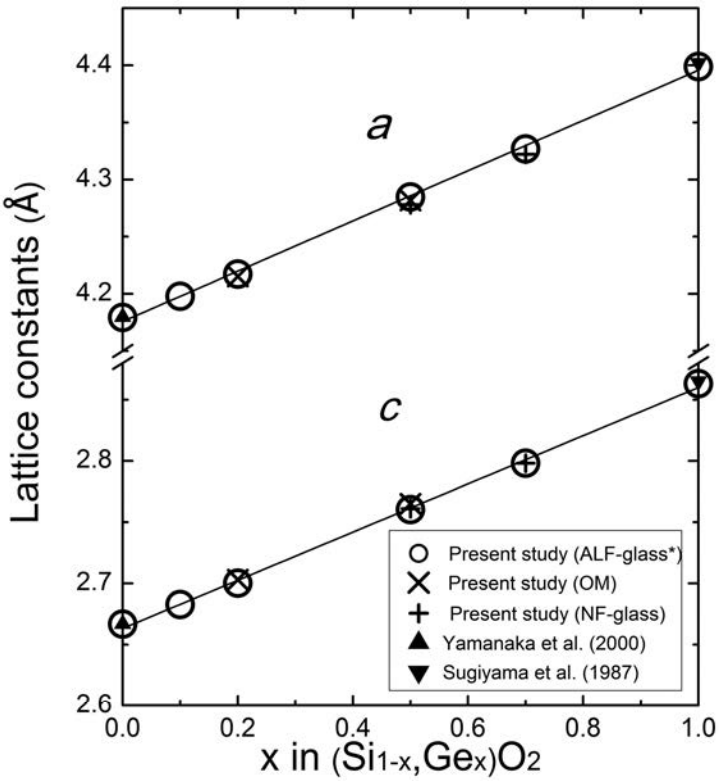

Fig. 3.3-24: Relationship between lattice constants (*a* and *c*) of (Si_{1-x},Ge_x) (x = 0, 0.1, 0.2, 0.5, 0.7 and 1) rutile phase and the Ge content (x). The lattice constants are expressed as linear functions: a = 4.176(2) + 0. 220(4) x; c = 2.663(2) + 0.197(4) x.

3.4 Physical Properties of Minerals

A quantitative knowledge of the physical properties of minerals is essential to link geophysical observables to the structure and composition of the Earth's interior and to reliably model the dynamics of our planet.

This year particular effort has been undertaken in obtaining accurate elastic properties of different minerals as described in four contributions of this section. The Earth's transition zone, located between 410 and 660 km depths, is of major importance for Earth's inner dynamics and may be a huge reservoir for water and volatile elements. The first two contributions focus on improving our understanding of the elastic properties of the olivine polymorphs wadsleyite and ringwoodite which dominate the transition zone by volume. Experiments have been performed in diamond-anvil cells (DAC) using a combination of X-ray diffraction (XRD) and Brillouin spectroscopy. A particularity of these studies is the loading in the same DAC of several single crystals having customized sizes and shapes obtained through focused ion beam (FIB) preparation. In this way, direct information on the effects of Fe- and OH-content on the elasticity of wadsleyite and ringwoodite can be obtained at high pressures and at high temperatures without having to rely on secondary standards. The third contribution also combines FIB-sample preparation with simultaneous XRD and Brillouin spectroscopy to obtain a self-consistent elasticity data set on Al-Fe-bearing bridgmanite at pressures of the Earth's lower mantle. Al-Fe-bearing bridgmanite is by far the most abundant mineral phase below the 660 km seismic discontinuity, and the reported data are needed to link observations of seismic heterogeneities in the lower mantle to possible chemical variations of this mineral. The fourth contribution reports elasticity measurements carried out on polycrystalline SiO_2 stishovite, another potentially important lower mantle mineral phase. Experiments were performed using synchrotron X-ray diffraction (XRD) at Petra III (DESY) to 60 GPa, whereas Brillouin spectra are currently being collected in order to measure the acoustic shear wave velocity of this material across the tetragonal to orthorhombic transition occurring above 50 GPa.

FIB sample preparation was also used in the fifth contribution for three glass samples of different chemical compositions (SiO_2, $MgSiO_3$, $(Mg,Fe)SiO_3$). These have been loaded into the same DAC to allow a direct comparison among their compression behaviour, and how it is affected by using different pressure transmitting media.

The following three contributions report results from high-pressure XRD experiments on mantle phases aiming at a systematic understanding of the relations between structure, composition, spin states and compression behaviour. Contribution (**f**) reports the compression behaviour and associated structural changes of a novel oxide $Mg_2Fe_2O_5$ which forms as breakdown product of the spinel magnesioferrite, $MgFe_2O_4$, at high-pressures. A major observation in this study is a highly anisotropic axial compression, with the *c*-axis being the softest direction. Contribution (**g**) reports high-pressure single-crystal XRD and synchrotron Mössbauer measurements of Fe-bearing silicate garnet in order to constrain the effects of Fe-oxidation and spin state on the garnet structure within the solid solution series between

skiagite ($Fe^{2+}_3Fe^{3+}_2Si_3O_{12}$) and majorite ($Fe_4Si_3O_{12}$). The four different garnet compositions, surprisingly, show very similar compressibilities and exhibit a volume reduction at pressures between 50 and 60 GPa associated with a spin transition of Fe^{3+} present at the octahedral site of the garnet structure. In the following contribution, these synthetic skiagite-majorite garnets were laser-heated in a diamond-anvil cell at pressures above 45 GPa. One of their break-down products was an orthorhombic perovskite phase with composition $(Fe^{2+}_{0.64}Fe^{3+}_{0.24})SiO_3$. The compressibility of this phase has been measured up to 130 GPa by synchrotron XRD diffraction and compared to that of $MgSiO_3$ and of $(Mg,Fe)(Si,Al)O_3$ bridgmanites in order to constrain the effects of chemistry, valance state, and spin state on the compression behaviour of this mineral.

Transport properties are of major importance to model the dynamic state of the Earth's interior, and these are addressed in contributions (**i**) and (**j**). Zn-Co diffusion experiments performed in a multi-anvil press on single-crystals of $NaCoF_3$ post-perovskite, which serves as a low-pressure analogue for silicate post-perovskite, are described in contribution (**i**). The results show that the chemical diffusivity is three orders of magnitude faster along <100> than along <010>/<001>. The results from *in situ* electrical conductivity measurements of partially molten olivine aggregates containing various proportions of basaltic melt (0 to 100%) at upper mantle conditions are reported in contribution (**j**). The melt appears fully interconnected already at a volume fraction as low as 0.5%, suggesting that deformation is not necessary to enhance the electrical conductivity of partially molten mantle rocks.

In the final contribution of this section, different formulations of heat capacity are critically discussed and their accuracy compared in order to give a better understanding of the approaches used in different thermodynamic models.

a. *Internally consistent high-pressure high-temperature single-crystal elasticity of wadsleyite, β-$(Mg_{0.9}Fe_{0.1})_2SiO_4$ (J. Buchen, H. Marquardt, T. Kawazoe, A. Kurnosov, S. Speziale/ Potsdam and T. Boffa Ballaran)*

The transition zone of the Earth's mantle where the phase assemblage of upper mantle rocks progressively transforms into minerals with denser structures, appears to control deep Earth dynamics by, for instance, affecting the fate of subducted slabs. Interpretations of seismological observations like seismic anisotropy and of seismic tomographic profiles in terms of the mineralogy, structure, and dynamics of the transition zone rely on our knowledge of the elastic behaviour and densities of the materials present at depths between 410 km and 660 km. In this region, the elastic properties of the high-pressure polymorphs of olivine, wadsleyite and ringwoodite, which account for more than 50 vol. % of a pyrolitic mantle rock, probably dictate the bulk seismic properties. Delimiting the transition zone at the 410-km seismic discontinuity, wadsleyite, β-$(Mg,Fe)_2SiO_4$, classifies as an anchor phase for the appraisal of chemical and thermal heterogeneities down to about 520 km depth. Owing to its extensive hydrogen storage capacity, wadsleyite is furthermore expected to govern the hydration state of the upper transition zone.

The most accurate and versatile description of the elastic behaviour of minerals is through single-crystal elasticity tensors measured at relevant pressure and temperature conditions, which can then be used to calculate the bulk rock properties. We are determining single-crystal elastic constants for wadsleyite at high pressures (H*P*) and high temperatures (H*P*) by means of Brillouin spectroscopy and X-ray diffraction on single-crystal specimens contained in resistively heated diamond anvil cells (DAC). Large (~ 500 µm), gem-quality wadsleyite crystals were synthesized from San Carlos olivine powder in a multianvil press and characterized by electron microprobe analysis (Fe/(Mg+Fe) = 0.112(2)) and Fourier-transform infrared spectroscopy (0.2 wt. % H_2O). Half disks were cut from X-ray oriented single-crystal thin sections with a focused ion beam (FIB). The orientations of the platelets were chosen to optimize the spatial distribution of propagation directions for the sound waves to be probed by Brillouin spectroscopy. For orthorhombic crystals like wadsleyite, a suitable selection of sound wave vectors is crucial for the accurate determination of all 9 independent elastic constants. The customized dimensions of the FIB-cut specimens allow us to load platelets of two complementary oriented single-crystals together into the pressure chamber of the same DAC (inset in Fig. 3.4-1b). In this way, uncertainties in *P*-*T* conditions inherent to multiple loadings for different crystal orientations can be reduced while providing at the same time enough spatial variability in sound wave vectors. Especially for experiments at combined H*P*-H*T*, we believe this multi-sample approach to be the only one which ensures consistent

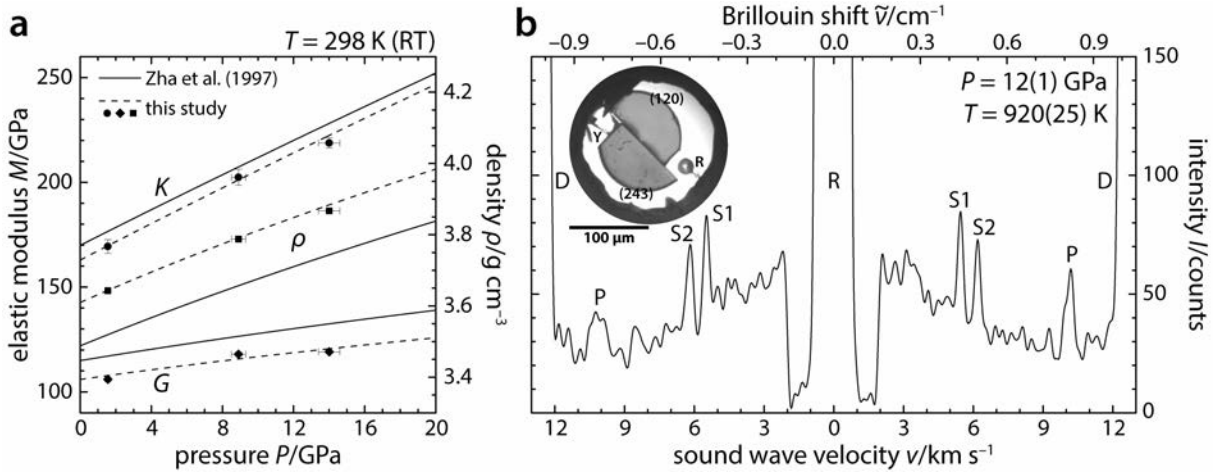

Fig. 3.4-1: (a) Elastic moduli and density of wadsleyite as a function of pressure at room temperature (RT); the trends from Zha *et al.*, *Earth Planet. Sci. Lett.* 147, E9-E15 (1997) for iron-free wadsleyite are drawn for comparison; (b) Brillouin spectrum of wadsleyite at 12(1) GPa and 920(25) K with the following features: elastic Rayleigh line (R), acoustic waves of the diamond anvils (D), shear (S1, S2) and compressional (P) sound waves of wadsleyite. The inset shows a view into the DAC loaded with two wadsleyite crystals with indicated orientations, a crystal of $Y_3Al_5O_{12}$ doped with Sm (Sm:YAG, Y), and a ruby sphere (R).

measurement conditions and thus facilitates the determination of internally consistent elasticity tensors. The experimental combination of Brillouin spectroscopy with X-ray

diffraction yields data pairs of bulk moduli and unit-cell volumes as functions of pressure and temperature which enable us to compute absolute pressures. Calibrated shifts of fluorescence lines of reference materials serve as cross-checks on the *P*-*T* conditions and allow estimates of the temperature inside the DAC. As shown in Fig. 3.4-1a, we traced the evolution of density and elastic properties of wadsleyite up to about 14 GPa at room temperature and are currently extending this pressure range. The substitution of iron for magnesium results in a reduction of the elastic moduli while increasing the density. First results have also been obtained at combined H*P*-H*T* conditions (Fig. 3.4-1b). The emerging description of the H*P*-H*T* single-crystal elastic behaviour of wadsleyite with a typical mantle composition will enhance our ability to interpret seismic observables and improve our current image of the transition zone as an important layer for Earth's inner dynamics.

b. *Comparative single-crystal elasticity measurements of ringwoodite at simultaneous high pressure and high temperature (K. Schulze, H. Marquardt, A. Kurnosov, T. Kawazoe and T. Boffa Ballaran, in collaboration with M. Koch-Müller/Potsdam)*

Radial and lateral variations in seismic observations are likely caused by variations in chemistry and/or temperature in the Earth's mantle. A quantitative evaluation of the seismic observations in the transition zone, therefore, requires knowledge of the effect of iron content and hydration state on the elastic tensor of ringwoodite under high-pressure/high-temperature conditions, given the abundance of this mineral at this depth.

The effect of iron and hydration variations on the elastic constants is small with respect to changes due to pressure and temperature. To quantify these small effects, we designed a study were four single-crystals of ringwoodite were loaded together in the pressure chamber of one diamond anvil cell (DAC). The loaded crystals, which have different chemical compositions, can thus be measured at identical temperature and pressure conditions. For the experiment, three samples with an iron to magnesium ratio of 0.1 and varying water content between 0.4 and 2.2 wt. % were chosen. In addition a Mg-endmember ringwoodite crystal with low water content (0.6 wt. %) was loaded together with the iron-bearing samples. All crystals were synthesised in a multi anvil apparatus and characterised by infrared spectroscopy (FTIR), X-ray diffraction (XRD), and electron microprobe. Crystals of sufficient size (> 100 µm) and quality were oriented and double-side polished to a thickness of 17 µm. To facilitate the loading of four samples into one DAC pressure chamber, the polished crystals were cut into quarter circles with a FEI Scios focused ion beam machine (FIB). The crystals were loaded in the pressure chamber of a BX90 DAC (Fig. 3.4-2) equipped with a resistive heater, using neon as a pressure-transmitting medium. Ruby spheres were added as pressure calibrants. The crystals can be differentiated using both their colour and their unit-cell volume measured by means of XRD (Fig. 3.4-2). The unit-cell volume of ringwoodite, in fact, increases as a function of both iron and water content, moreover, in the presence of iron, water darkens the blue colour of ringwoodite. We are measuring the elastic properties of these four crystals by combined Brillouin spectroscopy and XRD at high pressure, and we are planning to increase temperature once pressures of the Earth's transition zone are reached. The result will be an

internally consistent experimental dataset that allows for quantifying the effects of both Fe- and OH-incorporation on the elastic tensor of ringwoodite at transition zone conditions.

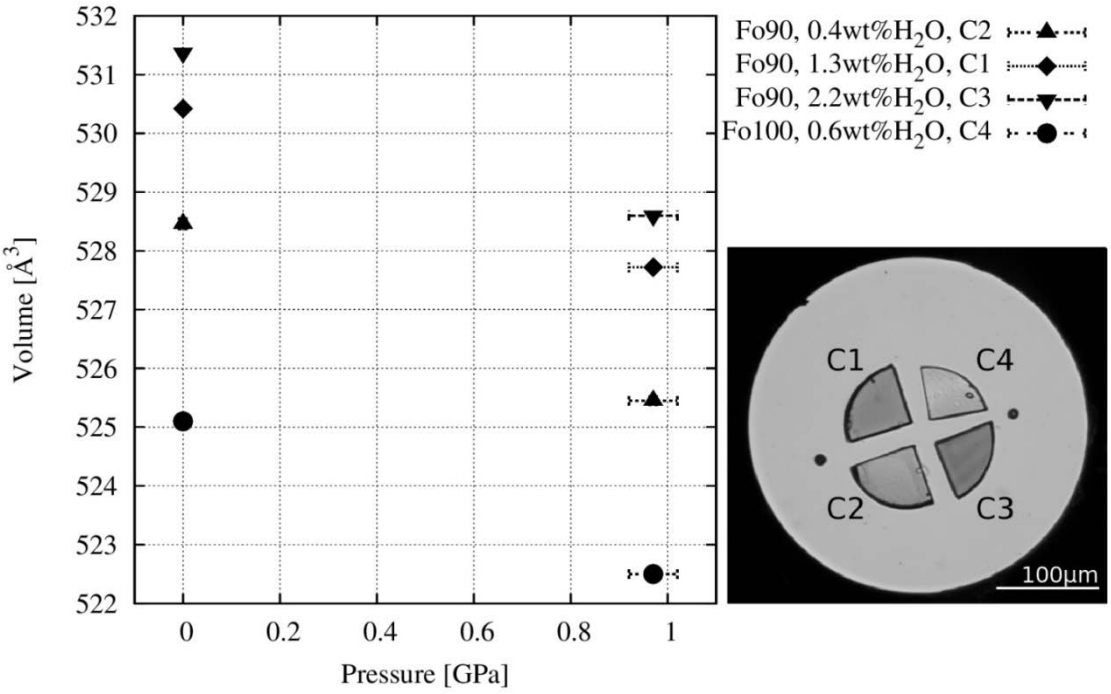

Fig. 3.4-2: Unit-cell volumes at ambient pressure and 0.97 GPa of the four single-crystals of ringwoodite (depicted on the right) having different chemical compositions.

c. *Elasticity of Al-, Fe-bridgmanite at pressures up to 26 GPa (A. Kurnosov, H. Marquardt, T. Boffa Ballaran and D.J. Frost)*

$MgSiO_3$ bridgmanite constitutes about 70 % by volume of the Earth's lower mantle and likely governs the physical behaviour of this region. Chemical substitutions in $MgSiO_3$ bridgmanite involving Al and Fe may explain seismic velocity anomalies observed in the Earth's lower mantle. However, the effects of these substitutions on the anisotropic elastic properties of bridgmanite at high pressure and temperature are still experimentally unconstrained.

Here we report compressional and shear sound velocities of $Mg_{0.88}Fe_{0.12}Si_{0.09}Al_{0.11}O_3$ bridgmanite as a function of pressure. Two differently oriented single-crystals of bridgmanite have been double-side polished and cut as semi-disks using a FEI Scios Focused Ion Beam (FIB) machine and subsequently loaded together in the pressure chamber of a diamond anvil cell with helium as pressure-transmitting medium (Fig. 3.4-3). Simultaneous measurements of density and sound velocities have been made on both crystals at high pressures using single-crystal X-ray diffraction and Brillouin spectroscopy in order to obtain self-consistent data, which do not depend on a secondary pressure scale. The Brillouin data at each pressure were fitted for both crystals simultaneously in order to reduce correlations among the elastic constants, C_{ij}. We will use our results for Al-Fe-bearing bridgmanite to discuss the effects of

chemical substitution on the high-pressure elasticity of bridgmanite and to interpret the seismic heterogeneities in the Earth's lower mantle.

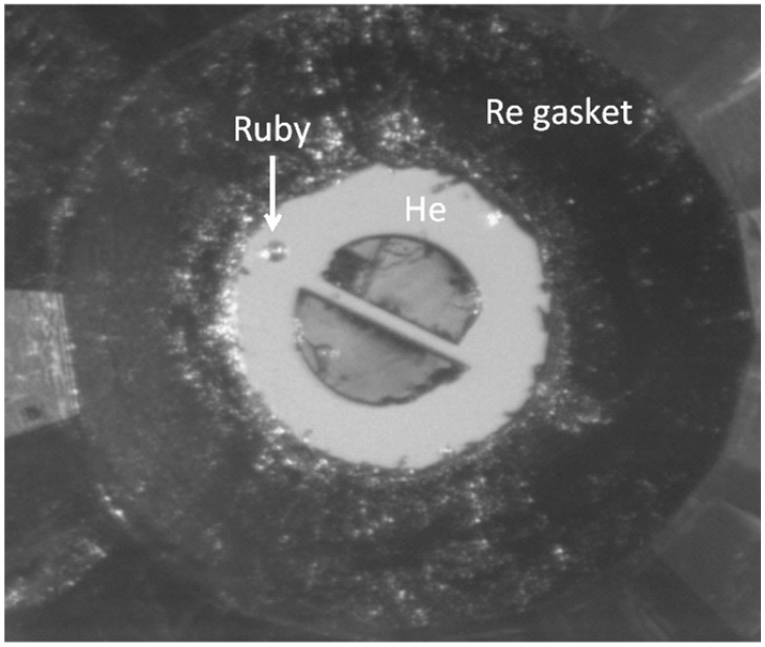

Fig. 3.4-3: Two differently oriented samples in a DAC with He pressure medium at P=6.1 GPa.

d. *Elasticity of fine-grained polycrystalline stishovite to high pressures (A. Chaudhari, H. Marquardt, A. Kurnosov, in collaboration with S. Speziale/Potsdam and N. Nishiyama/ Hamburg)*

Stishovite, a high-pressure polymorph of SiO_2, is a potential constituent of the Earth's mantle and may thereby affect seismic observations. Softening of the elastic shear modulus of stishovite has been reported to occur at 20-30 GPa under non-hydrostatic compressions in diamond anvil cells (DAC). This softening is associated with the tetragonal (rutile-structure) to orthorhombic ($CaCl_2$-structure) phase transition that takes place above 50 GPa under hydrostatic conditions. The significant variations in transition pressures indicate a pronounced effect of the stress distribution on the physical behaviour across the phase transition. So far, no direct measurements of acoustic velocities and/or elastic shear properties of Al-free stishovite across the phase transition have been reported under hydrostatic conditions. Here, we report the experimental results obtained by X-ray diffraction (XRD) and Brillouin scattering on polycrystalline stishovite loaded in a diamond anvil cell with neon as pressure-transmitting medium to ensure quasi-hydrostatic conditions. In this way, the shear modulus can be derived from the measured average shear velocities (Brillouin scattering) and densities (XRD), whereas the bulk modulus can be derived from the compression curve measured by XRD (isothermal bulk modulus).

The polycrystalline stishovite sample was synthesized in a multianvil press at 15.6 GPa and 1300 °C from silica powder at DESY, Hamburg. The sintered sample has an average crystallite size of about 200 nm. The mm-sized sample was mechanically double-side

polished to a thickness of 13 µm, and circular discs with diameters between 60 and 100 µm were cut from the mm-sized sample using a Focused Ion Beam (FIB) machine. High-pressure Brillouin spectra have been collected so far up to 30 GPa at the Bayerisches Geoinstitut. To verify the elastic isotropy of the polycrystalline sample, measurements were taken in different orientations at some pressure steps. XRD patterns were collected on another disk of the stishovite sample up to 62 GPa at the beamline P02.2 (Extreme Conditions Beamline) of PETRA III in Hamburg. A 42.8 keV X-ray beam was focused on a spot size of 2µm x 2µm. The diffraction images were acquired on a Perkin Elmer XRD 1261 flat panel detector with a collection time of 30s. Ruby fluorescence was used as an internal pressure standard. We observe the transition from the rutile type structure to $CaCl_2$ structure at around 50-55 GPa based on the X-ray diffraction analysis (Fig. 3.4-4). A preliminary fit of our data below 50 GPa to a third order Birch-Murnaghan equation of state leads to values of V_0 = 47.07 (±0.11) Å; K_{0T} = 296.2 (±23.5) GPa; K_{0T}'= 4.88 (±1). The acoustic velocities obtained so far are in

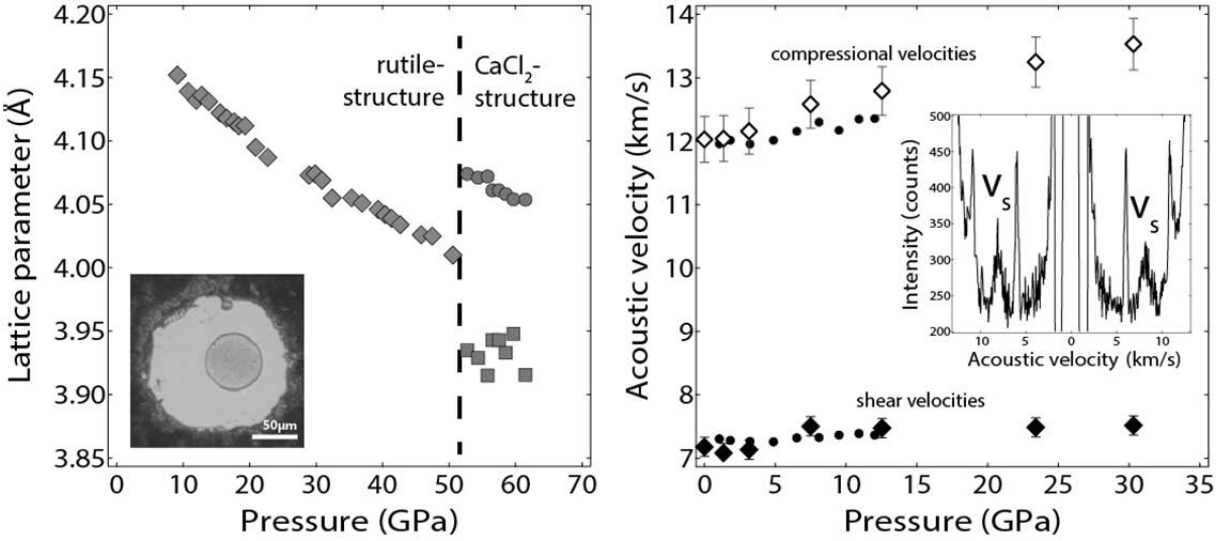

Fig. 3.4-4: (left) Unit-cell *a* lattice parameter of stishovite as a function of pressure obtained from synchrotron XRD data. Splitting of the *a* lattice parameter is observed at around 52 GPa due to the tetragonal to orthorhombic transition occurring in stishovite. The inset shows the FIB-cut sample loaded in the DAC pressure chamber. (right) Pressure-dependent acoustic wave velocities of stishovite (diamonds). Shear wave velocities were directly measured by Brillouin spectroscopy, whereas compressional velocities were derived from the combined analysis of Brillouin velocities and high-pressure XRD. The inset depicts a typical Brillouin spectrum collected at 22 GPa. The small circles are from a single-crystal elasticity study of stishovite (Jiang *et al.*, 2009, PEPI, 172, 235-240).

good agreement with a previous Brillouin scattering study on stishovite single crystals performed up to 12 GPa. We do not observe any softening of the acoustic shear velocity up to 30 GPa in contrast to the results obtained in the study performed under non-hydrostatic

conditions. Computational studies predict a drop in shear wave velocity at around 50 GPa consistent with the pressure at which we observe the phase transition in our XRD data. We therefore plan to extend the pressure range covered by our Brillouin scattering measurements.

e. *Comparative sound wave velocity measurements of SiO_2, $MgSiO_3$, and $(Mg,Fe)SiO_3$ glasses at high pressures and the effect of the pressure-transmitting medium (J. Emilien, H. Marquardt, S. Petitgirard, A. Kurnosov and J. Buchen)*

High-pressure experiments performed on SiO_2 glasses have shown that helium used as pressure-transmitting medium penetrates into the glass network and thereby reduces its apparent compressibility. This conclusion is based on observations of sample size by optical microscopy and synchrotron X-ray diffraction showing that the reduction of molar volume with pressure is much smaller in experiments carried out in helium pressure-transmitting medium (PTM) compared to presumably non-penetrating media, such as methanol-ethanol. A follow-up study verified these findings by analyzing high-pressure acoustic wave velocities - which are sensitive to both compressibility and density - collected by means of Brillouin spectroscopy, however, the measurements were limited to pressures up to 6 GPa.

Here, we aim at extending the covered pressure range to investigate the effect of glass densification expected at pressures above ~ 10 GPa on helium incorporation. In addition, we aim to determine the effect of different PTM on glasses with different chemical compositions and consequently different network structures. To this end, we designed a set up in which three glasses with different chemical compositions are loaded together in the pressure chamber of one diamond anvil cell (DAC). This approach allows for a direct comparison of the sound wave velocities and compression behaviour of these glasses. Moreover the small diamond culet size chosen (*i.e.*, 400 μm) will allow for covering a larger pressure range.

Glasses with chemical compositions $MgSiO_3$, $(Mg,Fe)SiO_3$, and SiO_2 were synthesized using the levitation method from stoichiometric mixtures of oxides. They were mechanically double-side polished to a thickness of about 20-30 μm and cut in pieces by using a FEI Scios focused ion beam machine (FIB). Three glass pieces were then loaded into the pressure chamber of a BX90-type DAC with helium as PTM. The DAC was equipped with Boehler-Almax seats and diamonds to allow for a large optical opening. Our measurements of acoustic wave velocities on SiO_2 glass in helium PTM are in excellent agreement with the previously published data to 6 GPa (Fig. 3.4-5). Our velocity measurements on $(Mg,Fe)SiO_3$ glass are similar to those reported for a sample with similar chemical composition using neon as PTM. In contrast, the acoustic wave velocities measured for the $MgSiO_3$ glass in helium show smaller acoustic velocities than the literature reference values at low pressures and a strong pressure dependence above 2 GPa (Fig. 3.4-5). Further measurements on the same samples using neon as PTM will allow to determine the effect of cation network modifiers on the incorporation of helium in the structure of depolymerized glasses and the role of the PTM on the compressbility and structural changes of such glasses.

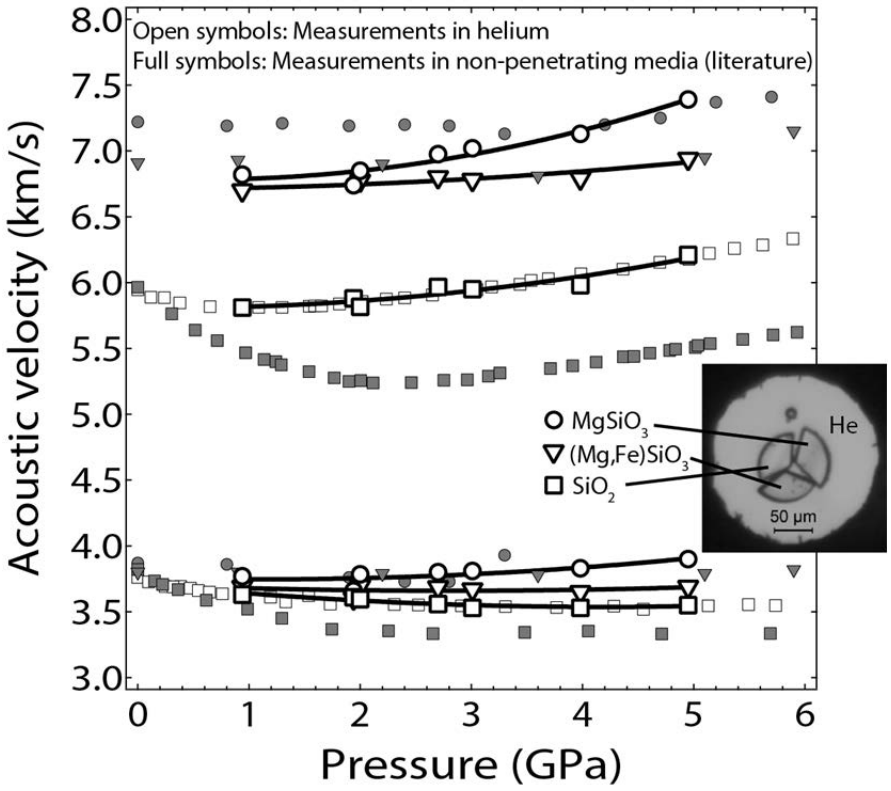

Fig. 3.4-5: Acoustic wave velocities of different glasses as a function of pressure. Large open symbols and solid curves: measurements carried out in this study using helium as pressure-transmitting medium. Small squares: literature data on SiO_2 glass measured in helium (open symbols) and methanol-ethanol (full symbols) up to 6 GPa (Weigel *et al.*, 2012, Physical Review Letters, 109, 245504). Full circles and inverse triangles: Brillouin measurements on $MgSiO_3$ and $(Mg,Fe)SiO_3$ glass performed in neon (Liu and Lin, 2014, Geophysical Research Letters, 41, 8832).

f. *High-pressure behaviour of the novel oxide $Mg_2Fe_2O_5$ (N. Siersch and T. Boffa Ballaran, in collaboration with L. Uenver-Thiele and A. Woodland/Frankfurt)*

Novel oxides with M_4O_5 stoichiometry have been observed recently as breakdown products at high pressures and temperatures of several spinel-type structures, like magnetite (Fe_3O_4), chromite ($FeCr_2O_4$), and magnesium-ferrite ($MgFe_2O_4$). These phases can be considered, therefore, a new addition to the phase relations of a number of simple oxide systems, hence knowledge of their compressibility and phase stability is required to construct thermodynamic models to assess their possible presence in the Earth's mantle. The aim of this study is to obtain the compressional and high-pressure structural behaviour of one of these oxides, namely $Mg_2Fe_2O_5$.

A single-crystal of $Mg_2Fe_2O_5$ was selected from a synthesis-run performed using a multianvil press at 1550 °C and 15 GPa and was polished to a thickness of ~ 15 µm for the high-pressure single-crystal diffraction study. The crystal was loaded in a diamond anvil cell with Ne as

pressure-transmitting medium and with a ruby chip for pressure calibration. Intensity data were collected at several pressures up to 17 GPa using an Xcalibur diffractometer with MoKα radiation operated at 50 kV and 40 mA, equipped with a CCD detector and a graphite monochromator. Unit-cell lattice parameters were obtained using up to 250 reflections. The bulk compressibility of $Mg_2Fe_2O_5$ has been described using a second-order Birch-Murnaghan equation of state (EoS), with room pressure volume V_0 = 352.4(5) Å^3 and room pressure bulk modulus K_0 = 171(5) GPa, with its first pressure derivative K' fixed to the value of 4 (Fig. 3.4-6). The axial compressibility of $Mg_2Fe_2O_5$ was found to be highly anisotropic with the *a*- and *b*-axes having similar compressibilities and the *c*-axis being the most compressible one (Fig. 3.4-6).

Refinements of the $Mg_2Fe_2O_5$ structure were also performed in the *Cmcm* space group at all pressures. The structure consists of edge-sharing octahedra alternating with layers of trigonal prisms (Fig. 3.4-6). With increasing pressure the M1 octahedra and M3 prism become more regular, whereas the M2 octahedra show an anisotropic compression behaviour with the shorter bond M2-O1 being one of the most compressible bonds. This bond lies almost parallel to the *c*-axis and therefore may be the cause of its larger compressibility. Another reason for the larger compressibility of the *c*-axis is represented by the tilting of the angle M2-O1-M2 that increases with pressure. Above 4 GPa, however, this angle appears to stiffen very rapidly, likely due to the repulsion of the O3 atoms of the two adjacent M2 octahedra.

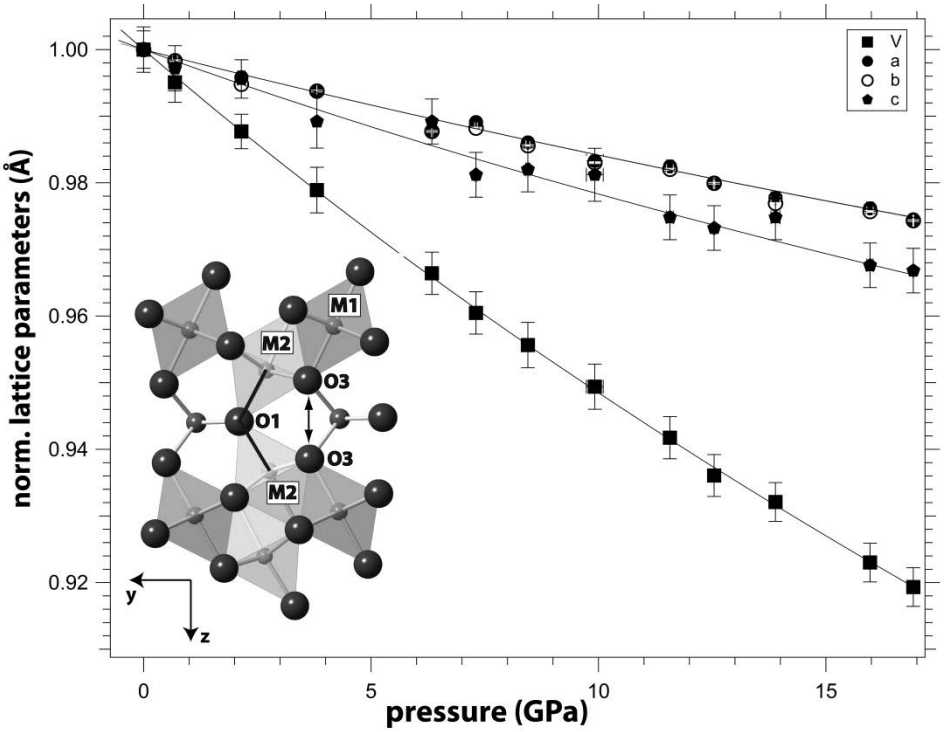

Fig. 3.4-6: Volume and axial compressibility of $Mg_2Fe_2O_5$. The *c*-axis is the softest direction whereas the *a* and *b*-axes have similar compressibilities. The crystal structure of $Mg_2Fe_2O_5$ at ambient conditions is depicted in the inset. The larger compressibility of the *c*-axis may be caused by the tilting mechanism described by the M2-O1-M2 angle.

g. *High-pressure behaviour of Fe-bearing silicate garnets up to 90 GPa (L. Ismailova, A. Bobrov/Moscow, M. Bykov, E. Bykova, V. Cerantola, I. Kupenko/Grenoble, D. Vasiukov/ Bayreuth, C.A. McCammon, N.A. Dubrovinskaia/Bayreuth and L.S. Dubrovinsky)*

Natural silicate garnets can accommodate a variety of divalent and trivalent cations in their crystal structure and form many solid solutions. While most major cations in garnet occur in only a single oxidation state (Al^{3+}, Ca^{2+}, Mg^{2+}, Si^{4+}), iron occurs as both Fe^{2+} and Fe^{3+}. An example is the skiagite garnet ($Fe^{2+}{}_3Fe^{3+}{}_2Si_3O_{12}$) which contains iron in both oxidation states and which, as a component of peridotitic garnets, can be used as a redox sensor to determine the mantle oxygen fugacity (fO_2) from the $Fe^{3+}/\sum Fe$ ratio. With increasing pressure skiagite garnet is expected to accommodate an excess of Si, forming a solid solution with the iron majorite endmember ($Fe_4Si_4O_{12}$). Studying the high-pressure behaviour and redox relations of Fe-bearing silicate garnet can therefore provide important insight into the chemical composition and physical properties of the Earth's mantle.

Skiagite-majorite ($Fe^{2+}{}_3Fe^{3+}{}_2Si_3O_{12}$ - $Fe_4Si_4O_{12}$) garnets with compositions $Ski_{76.6}Maj_{23.4,}$ $Ski_{69}Maj_{31,}$ $Ski_{54}Maj_{46,}$ and $Ski_{24}Maj_{76}$ were synthesized at 7.5-9.5 GPa and 1100-1300 °C in a multianvil apparatus at the Bayerisches Geoinstitut (Bayreuth, Germany). Crystals for single crystal X-ray diffraction studies were pre-selected based on the absence of twinning and on the quality of their diffraction peaks. The best quality crystals were loaded in diamond anvil cells (DACs) with Ne as pressure-transmitting medium and ruby chips as pressure markers. Diamond anvil cells equipped with Boehler-Almax beveled diamonds with 250 μm culets were used for measurements up to 50 GPa, while diamonds with 120 μm culets were used for pressures up to 90 GPa. Single-crystal X-ray diffraction experiments were performed at the beamline ID09a at ESRF, Grenoble, France (λ= 0.4151 Å) and at the Extreme Conditions Beamline P02.2 at PETRA III, Hamburg, Germany (λ= 0.2903 Å). Synchrotron Mössbauer source spectra were recorded at the Nuclear Resonance Beamline ID18 at ESRF. *P-V* data were collected at pressures ranging from ambient to 90 GPa for all four garnets. No structural transitions have been detected and even at the highest pressures reached skiagite-majorite garnets remained cubic (space group *Ia-3d*). However, we observed an anomalous volume drop (~ 4 %) in the pressure range between 50 and 60 GPa. Structural refinements indicate that a volume collapse of the FeO_6 octahedra occurs at such pressures, whereas the bond distances of the SiO_4 tetrahedra and FeO_8 dodecahedra do not show any discontinuous change (Fig. 3.4-7). Synchrotron Mössbauer source spectra at ambient pressure show two doublets assigned to dodecahedral Fe^{2+} and octahedral Fe^{3+} that remain essentially unchanged up to 50 GPa. However at ~ 52 GPa the hyperfine parameters of Fe^{3+} change due to an inferred spin-pairing transition. Combining diffraction and Mössbauer data, we can conclude that the reduction of the unit-cell volume of these skiagite-majorite garnets is associated with the spin transition of Fe^{3+} and results from the volume collapse of the $Fe^{3+}O_6$ octahedral site. Remarkably, the pressure range at which the spin transition occurs as well as the compressibility of these garnets does not depend on their Fe^{3+} content across the skiagite-majorite solid solution.

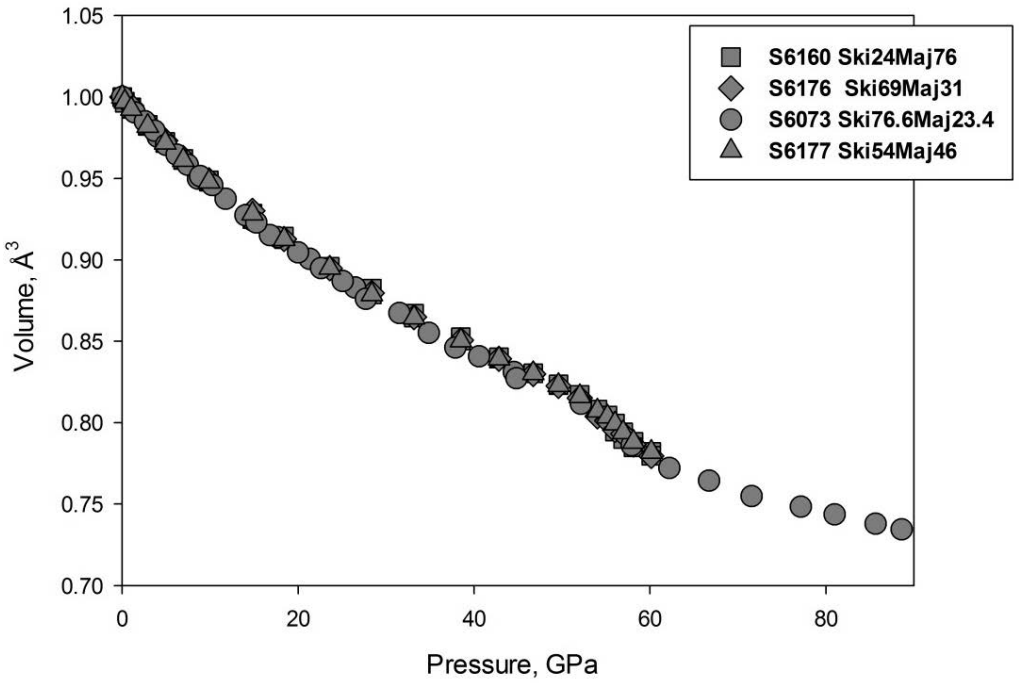

Fig. 3.4-7: Variation with pressure of the unit-cell volumes of the skiagite-majorite garnets investigated in this study normalized with respect to their room pressure values.

h. *Synthesis and equation of state of iron silicate bridgmanite, $FeSiO_3$ (L. Ismailova, E. Bykova, V. Cerantola, M. Bykov, L.S. Dubrovinsky and N.A. Dubrovinskaia/Bayreuth, in collaboration with V. Prakapenka/Argonne and M. Hanfland/Grenoble)*

The oxidation and spin state(s) of Fe in mantle phases have important implications for the chemistry and physical properties of the mantle. The behaviour of iron in the lower mantle dominant phase, bridgmanite, is complex because Fe may be present with different valence states (Fe^{2+} and Fe^{3+}) and spin states (high, low and intermediate spin), thus differently affecting the compressibility of this material. Although several studies have investigated the effect of small Fe substitutions in bridgmanite, with or without Al, a silicate perovskite phase has never been so far synthesized with an iron-pure composition, *i.e.*, having the chemical formula $FeSiO_3$.

Here we report the results from a synthesis and compressibility study of $FeSiO_3$ bridgmanite synthesized from a synthetic skiagite-majorite garnet with composition $Fe^{2+}{}_3(Fe^{2+}{}_{0.234(2)}Fe^{3+}{}_{1.532(1)}Si^{4+}{}_{0.234(2)})(SiO_4)_3$. The garnet crystal was loaded in a diamond anvil cell and single-crystal X-ray diffraction experiments were performed at the beamline 13 ID-D (GSECARS) at APS, Argonne, USA and at the beamline ID09a at ESRF, Grenoble, France. At pressures above ~ 45 GPa upon heating, we observed the dissociation of the garnet sample to a mixture comprising an orthorhombic perovskite, stishovite (SiO_2) and the high-pressure orthorhombic *h*-Fe_3O_4 phase. At 51 GPa and 2100(100) K the diffraction lines of stishovite

are absent and the intensities of the reflections of *h*-Fe_3O_4 decrease, hence the diffraction pattern is dominated by the perovskite phase. The same orthorhombic perovskite phase can be synthesized up to over 100 GPa and once formed, it can be recovered down to ~ 13 GPa. The crystal structure refinements of several perovskite crystals synthesized at different pressures and temperatures converge always to a composition of $(Fe^{2+}_{0.64(2)}Fe^{3+}_{0.24(2)})Si_{1.00(3)}O_3$ suggesting the presence of vacancies at the A site.

Fitting of the room-temperature *P-V* data of this perovskite using a second-order Birch-Murnaghan equation of state yields an ambient unit-cell volume V_0 = 178.98(6) $Å^3$ and an isothermal bulk modulus K_T = 190(4) GPa with *K*'=4. (Fig. 3.4-8)

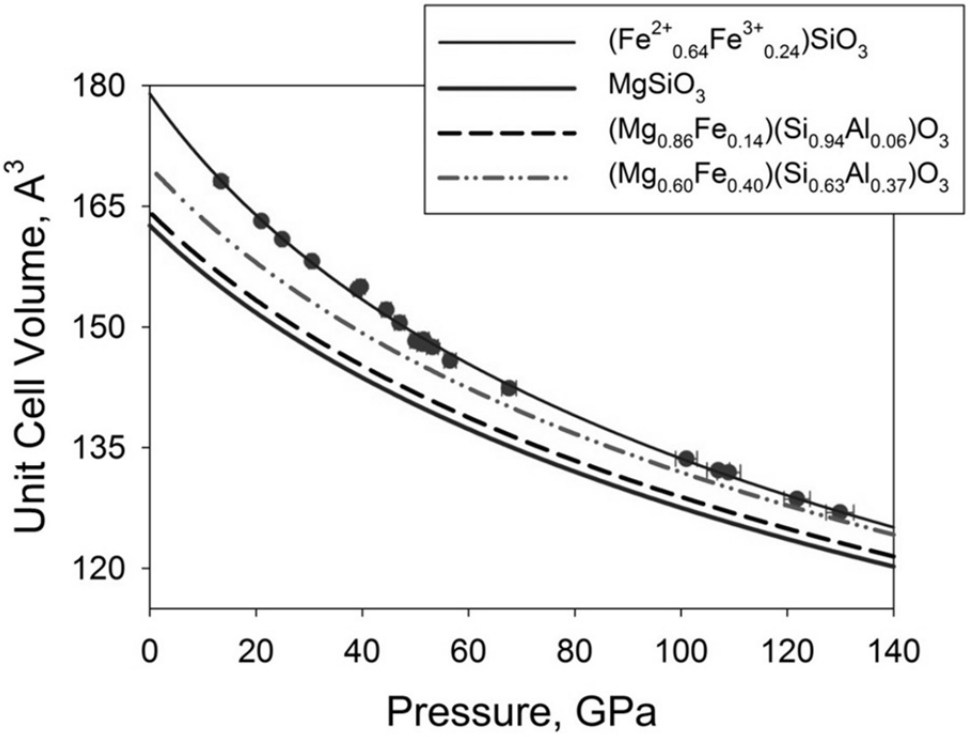

Fig. 3.4-8: Compressibility data for $(Fe^{2+}_{0.64}Fe^{3+}_{0.24})SiO_3$ perovskite synthesized in this study (filled circles) compared with data published in the literature for bridgmanites having different compositions. The curves represent the Birch–Murnaghan equation of state fits.

i. *Anisotropic chemical diffusion in fluoride post-perovskite (D.P. Dobson, A. Lindsay-Scott, E. Bailey, I. Wood and J. Brodholt/London)*

The post-perovskite phase ($CaIrO_3$-type) of (Mg,Fe)(Si,Al)O_3 is stable at pressures above 120 GPa, corresponding to the D" region of Earth's lowermost mantle. It shows strong elastic and rheological anisotropy, related to the way in which SiO_6 octahedra are arranged as sheets separated by Mg-O polyhedral units. In addition to the elastic anisotropy, ab initio simulations

suggest that post-perovskite $MgSiO_3$ has extremely anisotropic chemical diffusivity, with 8 orders of magnitude difference between the fast and slow diffusion directions. This would be the largest diffusion anisotropy in any material, to the best of our knowledge, and if correct it might have significant implications for the dynamics of the core-mantle boundary region. Single-crystal diffusion studies at 120 GPa are prohibitively difficult so we have been performing a combined simulations and experimental study of diffusion in $NaBF_3$ perovskite and post-perovskite samples with B = Zn, Co being the exchanging cations as analogues of the mantle phase.

Experiments were performed at the Bayerisches Geoinstitut by embedding single crystals of $NaCoF_3$ post perovskite in $NaZnF_3$ powder and annealing at 14 GPa in a multianvil press. Recovered samples were polished to expose the $NaCoF_3$ crystals and analysed using the LEO Gemini 1530 FEG SEM. The beam convolution was determined by measuring a profile across an interface which had been prepared to 0.1 micrometre roughness and had no diffusion across it. Zn vacancy diffusivities were calculated at UCL using Vineyard theory implemented in the VASP ab initio code as described elsewhere (Ammann *et al.*, Nature 465, 462-465, 2010). The diffusion profiles observed in the axial and radial directions in one crystal, corresponding to the *a* and *b*/*c* crystallographic directions are shown in Fig. 3.4-9. The fits to the observed profiles are shown as solid curves and the true diffusion profiles, with the beam convolution removed, are shown as dashed curves. While the absolute values of diffusivity in this experiment are not well determined (there was a significant contribution from the heating and cooling duration) diffusion in <100> is over 1000 times faster than in <010>/<001>, in good agreement with the simulations results which predict 4 orders of magnitude difference between <100> and <010>/<001>.

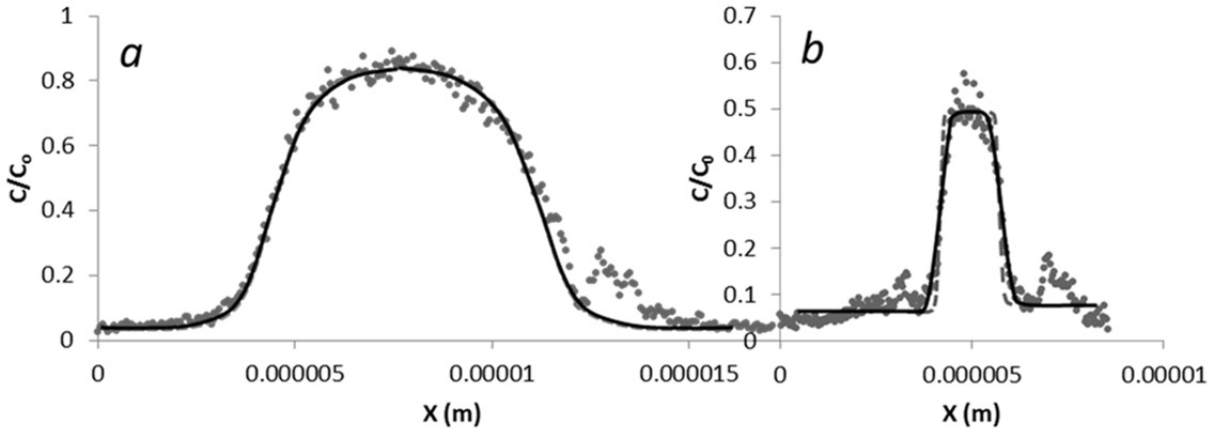

Fig. 3.4-9: Measured Zn-Co diffusion profiles in the axial (<100>) and radial directions in one $NaCoF_3$ post-perovskite single crystal. The beam convolution is a significant effect in the slow diffusion direction but is negligible in the fast direction. The anisotropy of chemical diffusivity is over 3 orders of magnitude in this system, in good agreement with the ab initio simulations results.

j. *Electrical conductivity of partially molten olivine aggregate and melt interconnectivity in the upper mantle (M. Laumonier, D.J. Frost, R. Farla, T. Katsura and K. Marquardt)*

Geophysical studies (magnetotelluric and seismic surveys) reveal the presence of electrical conductivity and seismic velocity 'anomalies' in the upper mantle such as at the lithosphere-asthenosphere boundary (LAB) beneath oceans. The most relevant explanation for these anomalies is based on the existence of small amounts of melt trapped at the grain boundaries of the solid peridotite. If these melts are interconnected, they can increase the electrical conductivity of the mantle in accordance with magnetotelluric observations. In order to assess the fraction of melt that may exist at these depths, mathematical models have been used to estimate how melts with known electrical conductivities would influence the bulk conductivity of the mantle as a function of melt fraction. These models calculate the bulk conductivity from the conductivities of the melt and mineral phases assuming different geometric relations. To date, however, there are very few experimental studies available through which to differentiate between potential model geometries. In this study, *in situ* electrical conductivity measurements have been performed on partially-molten olivine aggregates containing various proportions of basaltic melt (0 to 100 %) at upper mantle conditions in order to test such models.

The sample used in this study consisted of a homogeneous mechanical mixture of olivine (Fo92) obtained from a natural peridotite (Lanzarote, Canary Islands, Spain) and a glass with a MORB-like composition produced from an initial oxide mix. Compositions of both materials were chosen to closely reflect upper mantle assemblages and were mixed in differing proportions to obtain a range of melt fractions. Experiments were performed in the MAVO 6-ram press at a pressure of 1.5 GPa and temperatures up to 1400 °C. A gain phase analyser was used to acquire the electrical resistance of the partially molten sample.

As expected, the results show an increase in the electrical conductivity with temperature and with melt fraction. The conductivity of the partially molten aggregates fits a modified Archie's law with an exponent of 0.73 (at 1300 °C) over a large range of melt fractions (0.5 to 100 vol. %). However, at melt fractions of 0.25, 0.15 and 0.0 vol. %, the conductivity deviates from the trend previously defined, implying that the melt is no longer fully interconnected through the sample, as supported by chemical mapping. A melt fraction of 0.5 vol. % was also studied at 3.0 GPa in order to determine whether pressure has an effect on the electrical conductivity. This appears to be negligible. Therefore, we can apply our model to natural settings of the upper mantle for a large range of temperatures, pressures and melt fractions.

The individual conductivities of the olivine aggregate and the basaltic melt are consistent with values found in the literature. Since the melt remains fully interconnected down to relatively low melt fractions (0.5 vol. %), it would seem that deformation is not necessary to enhance the electrical conductivity of partially molten mantle rocks. As shown in Fig. 3.4-10, the model can be used to estimate the relationship between the temperature and melt fraction

required to explain mantle electrical conductivity observations. Anomalous conductivities (log σ in the range -0.6 to -0.8) observed for the lithosphere-asthenosphere boundary can be explained at typical mantle temperatures by a fraction of basaltic melt in the range 0.5-1 vol. %. The lower conductivities reported for normal mantle, however, can be explained by a melt-free assemblage.

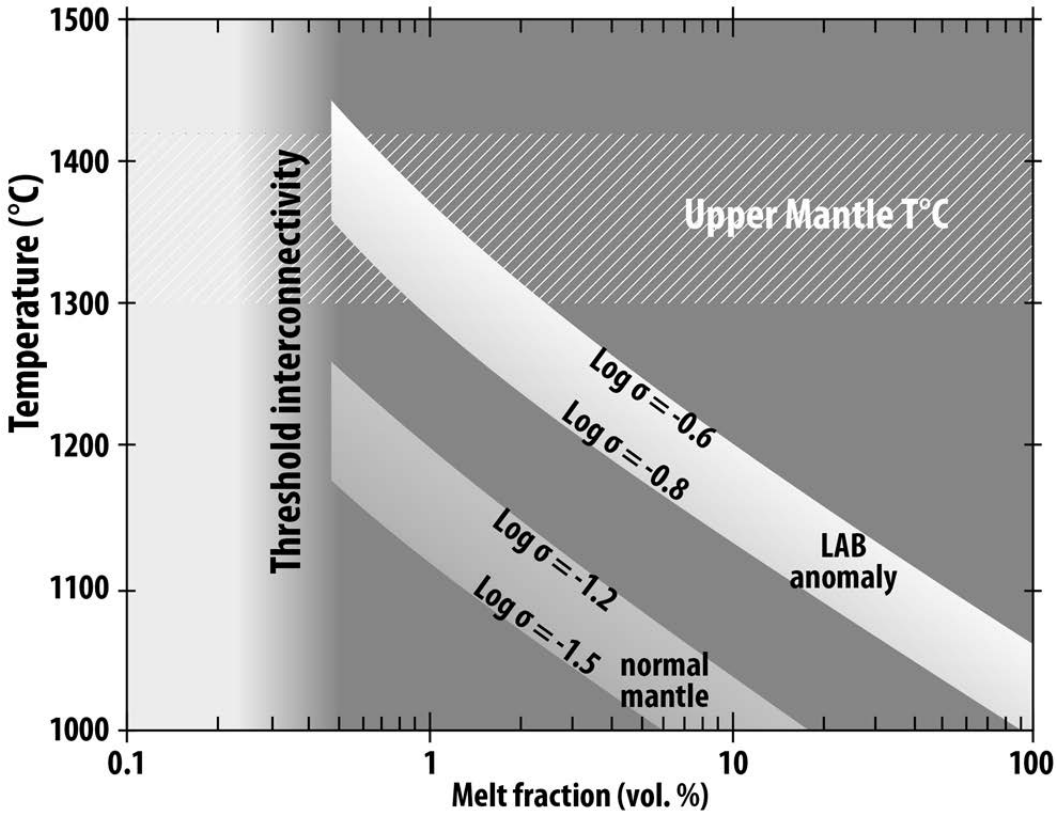

Fig. 3.4-10: The covariation of temperature and melt fraction that can explain the electrical conductivities (σ) of the "normal" mantle and anomalous values reported for the lithosphere-asthenosphere boundary (LAB). The conductivity ranges are estimated from magnetotelluric observations. The temperature range for the upper mantle is indicated. To explain the LAB conductivity anomaly at typical mantle temperatures requires 0.5 to 1 vol. % of partial melt to be present. As the electrical conductivity range of the "normal" mantle is significantly lower, the temperature-melt relation at typical mantle temperatures would predict melt fractions below the level of interconnectivity, where the melts would anyway not contribute to the conductivity. Melts are therefore not required to explain conductivities in the "normal" mantle.

k. *Formulation of heat capacity in thermodynamic models (T. Chust and G. Steinle-Neumann, in collaboration with D. Dolejš/Prague)*

Thermodynamic models of minerals play a significant role in the characterization of phase assemblages, their physical properties and stability ranges. Such models are used more and

more often in the quantitative interpretation of geological and geophysical observations, including structure of the Earth's interior. While model compositions of the Earth's mantle, for example, are a complex mixture of different oxides that leads to a mineral assemblage with solid solutions, the endmember properties within a solid solution ultimately determine the composition and properties of the minerals in the phase assemblage, and their characterization is therefore of critical importance in any thermodynamic consideration.

To determine the Gibbs energy of a mineral phase that defines its stability at a given pressure (P) and temperature (T), an integration from the reference state (typically ambient pressure $P_0 = 10^5$ Pa and room temperature $T_0 = 298$ K) is required. Conventionally, most models use additive energetic contributions, which are computed along two alternative integration paths: (i) isobaric heating to *T*, followed by isothermal compression (elastic) to *P*, or (ii) isothermal compression at T_0, followed by isochoric heating (at volume *V*) to *T*. While these integration paths can and do use similar formulations for the elastic segment, the thermal contribution is fundamentally different. For heating at ambient pressure in path (i), models are formulated in terms of the isobaric heat capacity $c_P$which is frequently described by empirical polynomials in *T*. Integration path (ii) is more appropriately described by Helmholtz energy, and Gibbs energy is subsequently computed by a Legendre transform. Here the isochoric thermal contribution is formulated by c_V which is well suited for an analytical treatment based on statistical mechanics such as the Einstein or Debye model. In contrast to a polynomial formulation of c_P such an approach can guarantee acceptable extrapolation behaviour and reproduction of the theoretical limits at low and high T (Dulong-Petit) and leads to a thermodynamically self-consistent description, while sacrificing the accurate reproduction of experimental observations slightly. These two formulations of heat capacity are related to one another by other thermodynamic parameters

$$c_P - c_V = V \cdot T \cdot \alpha^2 \cdot K_T, \qquad (1)$$

with V the molar volume, α the thermal expansivity, and K_T the isothermal bulk modulus. Here we compare these types of formulations explicitly using a polynomial model for c_P and a Debye model for c_V from models of *Holland et al.* (*J. Petrol.* **54**, 1901 (2013), abbreviated as HHPH13) and *Stixrude and Lithgow-Bertellloni* (*Geophys. J. Int.* **184**, 1180, (2011), abbreviated as SLB11), respectively. The distinct formulations of heat capacity also lead to significant differences in caloric properties (entropy, enthalpy, energy) at high *T*. The principal differences between the HHPH13 and SLB11 models in computed heat capacity c_P are a stronger increase at low *T*, but significantly reduced slopes at high T in the Debye model compared to the empirical polynomial formulation as illustrated for the Mg_2SiO_4 polymorphs (Fig. 3.4-11), a direct consequence of the physically correct limiting behaviour of the Debye model. This discrepancy is even more pronounced for the Fe_2SiO_4 polymorphs (Fig. 3.4-11), where the polynomial model has significantly larger values than the Debye model above 770 K. A comparison to experimental results for forsterite and fayalite (Fig. 3.4-11) shows that the polynomial model of HHPH13 represents the experimental data more closely than the Debye

model of SLB11. The nature of the Debye approximation prevents a more accurate heat capacity fit for many phases. The model assumes heat is stored entirely in the form of acoustic lattice vibrations that have a linear dispersion curve, and this leaves only a single parameter – the Debye temperature Θ_D – to describe the phonon spectrum.

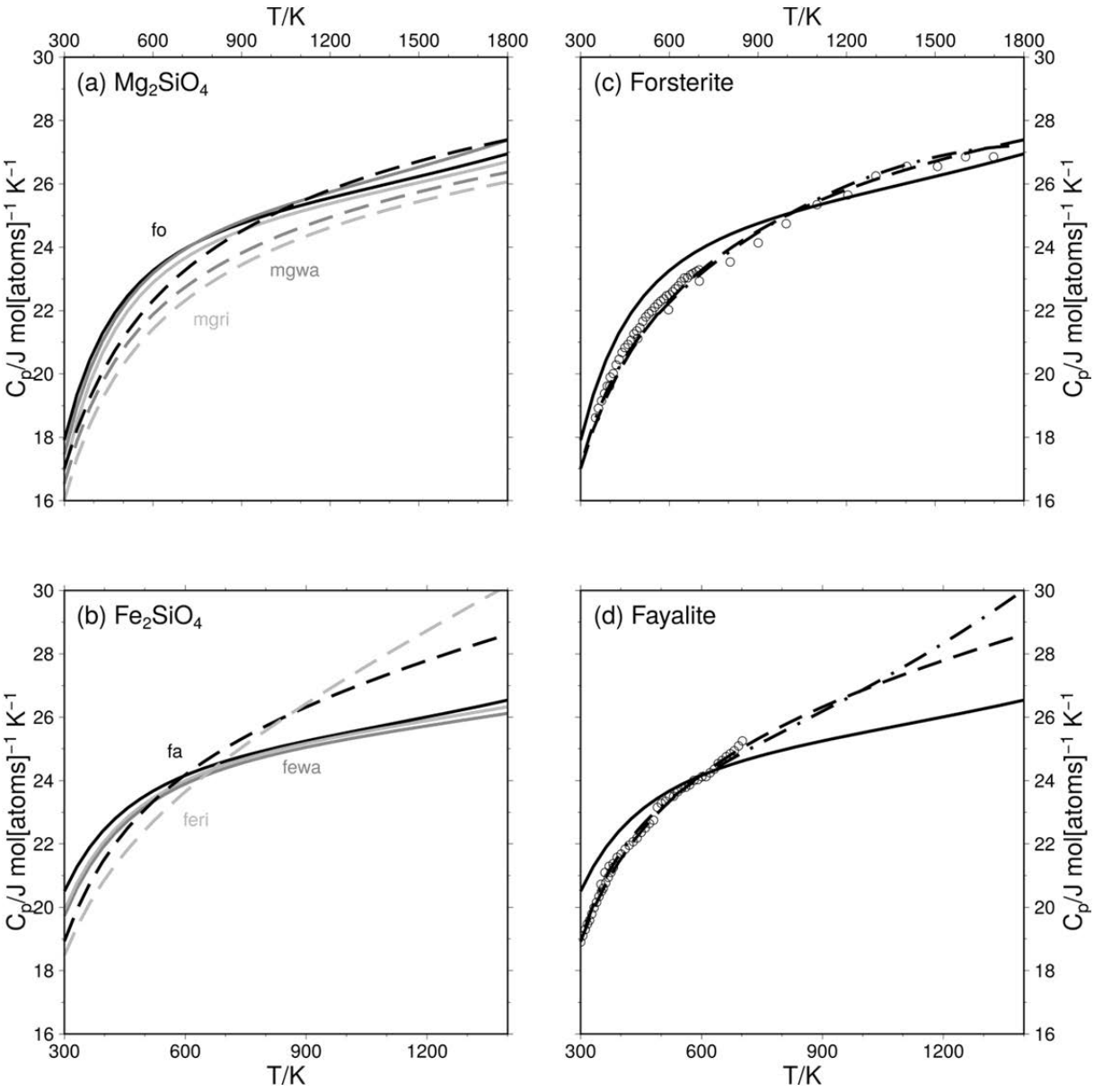

Fig. 3.4-11: Isobaric heat capacity at $P_0 = 10^5$ Pa for the (a) Mg_2SiO_4 (fo), wadsleyite (mgwa) and ringwoodite (mgri); and (b) Fe_2SiO_4 (fa), fe-wadsleyite (fewa) and fe-ringwoodite (feri) polymorphs computed with the Debye model and parameters from SLB11 (solid lines) and a polynomial model with parameters from HHPH13 (dashed lines). Comparison of the model results for (c) forsterite and (d) fayalite with a previous model by Robie and Hemingway (*U. S. Geol. Surv. Bull.* **2131**, 1 (1995), dashed-dotted lines) and experimental data (circles). Note that temperature scales for the Mg_2SiO_4 (upper row) and Fe_2SiO_4 (lower row) polymorphs are different to account for the different coverage of experimental data.

The deviations in the isobaric heat capacity for the Mg_2SiO_4 polymorphs are no longer significant when integrated to entropy (Fig. 3.4-12). By contrast, for the Fe_2SiO_4 polymorphs the entropy computed with the polynomial model remain significantly larger than that obtained from the Debye model (Fig. 3.4-12). This difference can only partly be attributed to the varying thermodynamic formulations, other factors such as missing data on the Fe-endmembers or their insufficient chemical characterization and purity can play a role as well.

Accuracy of a physical model over that of the Debye approximation could be improved by using more advanced formulations of lattice vibrations, such as the Kieffer model, which takes more complex dispersion characteristics and optical lattice modes into account. In such a formulation, the thermodynamic self-consistency of the Debye model, including the fulfilment of Maxwell's relations, is maintained.

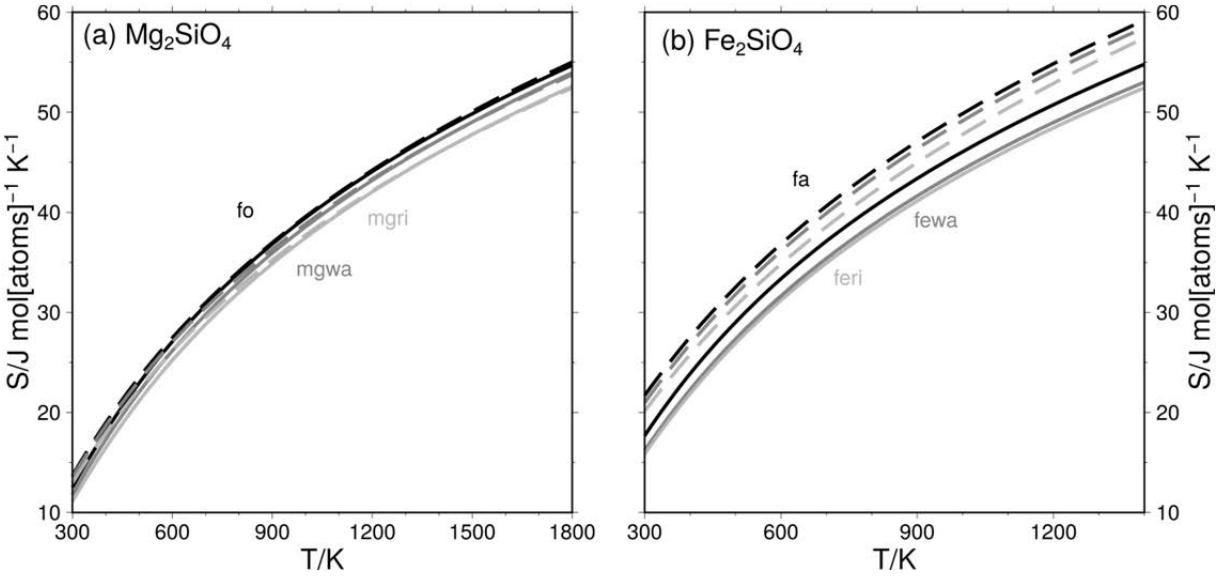

Fig. 3.4-12: Entropy for the (a) Mg_2SiO_4 (fo), wadsleyite (mgwa) and ringwoodite (mgri); and (b) Fe_2SiO_4 (fa), fe-wadsleyite (fewa) and fe-ringwoodite (feri) polymorphs computed with the Debye model and parameters from SLB11 (solid lines) and a polynomial model and parameters from HHPH13 (dashed lines). Temperature scales for the Mg_2SiO_4 (a) and Fe_2SiO_4 (b) polymorphs are different and consistent with those in Fig. 3.4-11.

3.5 Fluids, Melts and their Interaction with Minerals

In the 1990's, there was not much public discussion about global warming. The main reason for this was the 1991 eruption of Mt. Pinatubo volcano; the stratospheric sulfate aerosols created by this event backscattered sunlight and compensated for several years the effects of anthropogenic CO_2 emissions. Since these effects are related to the amount of sulfur injected into the stratosphere, constraining the sulfur yield of explosive volcanic eruptions is a problem not only of academic interest. A main difficulty here used to be that previous measurements yielded very different values for the fluid/melt partition coefficient of sulfur. A first contribution in this chapter describes a systematic study of fluid/melt partition coefficients of sulfur over a wide range of typical arc magma compositions. The data show that $D_S^{fluid/melt}$ very strongly depends on melt composition, while temperature appears to have no detectable effect. A new numerical model allows quantitative forecasts of the sulfur yield and therefore, of the climatic impact of eruptions.

All explosive volcanic eruptions are ultimately powered by the exsolution of gases – mostly water vapor - that were dissolved in the melt at high pressure. The kinetics of this exsolution process is largely controlled by the diffusion coefficient of water. While the diffusion coefficient of water in rhyolitic melts is well constrained, there are less data for basalts. The second contribution in this paper fills this gap; the diffusion coefficient is found to strongly increase with water content. The occurrence of volcanic eruptions on the surface does not only require some melt to be formed at depth; rather, this melt has to be able to segregate from the solid rock in which it formed. A critical parameter is here the dihedral angle of melt in melt pockets. This parameter has been studied in the forsterite-enstatite model system at 1 bar in another study reported here. Continental crust is mostly generated by magmas forming in subduction zone setting. Although these processes have been studied since decades, there are still controversies regarding the precise mechanism of melting in this tectonic environment. A systematic study of published melt inclusion data in the Georoc database shows that the concentrations of trace elements such as Sr, Rb, U, Ce, and La in the magmas strongly increase with the Cl/H_2O ratio recorded in undegassed melt inclusions. This can only be explained if these elements were transported from the dehydrating slab into the zone of melting in the mantle wedge by saline aqueous fluids. The salinity of these fluids enhanced the efficiency of the transport process by the formation of chloride complexes of the trace elements.

Research at Bayerisches Geoinstitut over several decades has shown that volatile elements, such as hydrogen or nitrogen, may be dissolved in some mantle minerals, which may represent a major reservoir for volatiles deep in Earth's interior. Another contribution in this chapter reports the first measurement of nitrogen solubility in $(Mg,Fe)_2SiO_4$ wadsleyite coexisting with olivine. Apparently, nitrogen is strongly enriched in wadsleyite as compared to olivine. This opens up the possibility that Earth's transition zone may not only be a major host for water, but also for nitrogen.

The last two contributions in this chapter shed light on processes that occurred in the very early history of the Earth, during core formation and the crystallization of the magma ocean. New X-ray absorption measurements on glasses under high pressure suggest that silicate melts in the lowermost mantle will always be denser than crystalline phases. Accordingly, a very deep magma ocean surrounding the core may still have persisted when the more shallow parts of the mantle were already solidified. The extent of metal silicate equilibrium during core formation is partially determined by the diffusion coefficients of elements such as Si, O, and Cr. A combination of experimental data and first-principle molecular dynamics simulations is used to show that these diffusion coefficients follow a simple relationship involving the melting temperature of iron.

a. *The sulfur budget in differentiated arc magmas (M. Masotta, H. Keppler and A. Chaudhari)*

Explosive volcanic eruptions may inject large amounts of sulfur into the stratosphere in a single event, inducing atmospheric perturbations that may eventually change the Earth's surface temperature. Once injected in the stratosphere, SO_2 is photochemically oxidized to sulfate aerosols that increase the Earth's albedo by backscattering the incoming solar radiation, while at the same time, they warm the stratosphere by absorbing the upwelling infrared radiation. The 1991 eruption of Mt. Pinatubo produced one of the largest climate perturbations of the 20th century, by injecting around 17-20 Tg of SO_2 into the stratosphere that were responsible of a global cooling of 0.5 °C.

The behaviour of sulfur during an eruption is mainly controlled by two factors: (1) the partitioning of sulfur between the silicate melt and the fluid phase, and (2) the solubility of sulfur-bearing minerals (mostly pyrrhotite FeS and anhydrite $CaSO_4$). At oxidizing conditions (fO_2 > NNO+1), sulfur is oxidized to S^{6+} and its concentration in the melt is controlled by the solubility of anhydrite. If the solubility of anhydrite is known, the concentration of sulfur in the fluid can be determined from the fluid-melt partition coefficient, and used to calculate the sulfur budget in arc magmas.

In this study, we experimentally determined the fluid-melt partitioning of sulfur ($D_S^{fluid/melt}$) under oxidizing conditions (Re-ReO_2 buffer), at temperature between 800 and 950 °C, and pressure of 200 MPa (Fig. 3.5-1). The $D_S^{fluid/melt}$ increases with increasing melt differentiation, ranging from 2 to 15 in the trachytic melt, from 20 to 100 in the dacitic and rhyodacitic melts and from 100 to 120 in the rhyolitic melt. The variation of the $D_S^{fluid/melt}$ is entirely controlled by the compositional variation of the silicate melt, with temperature having a minor effect within the investigated range. A model to predict the $D_S^{fluid/melt}$ was calibrated experimentally using structural and compositional parameters of the silicate melt:

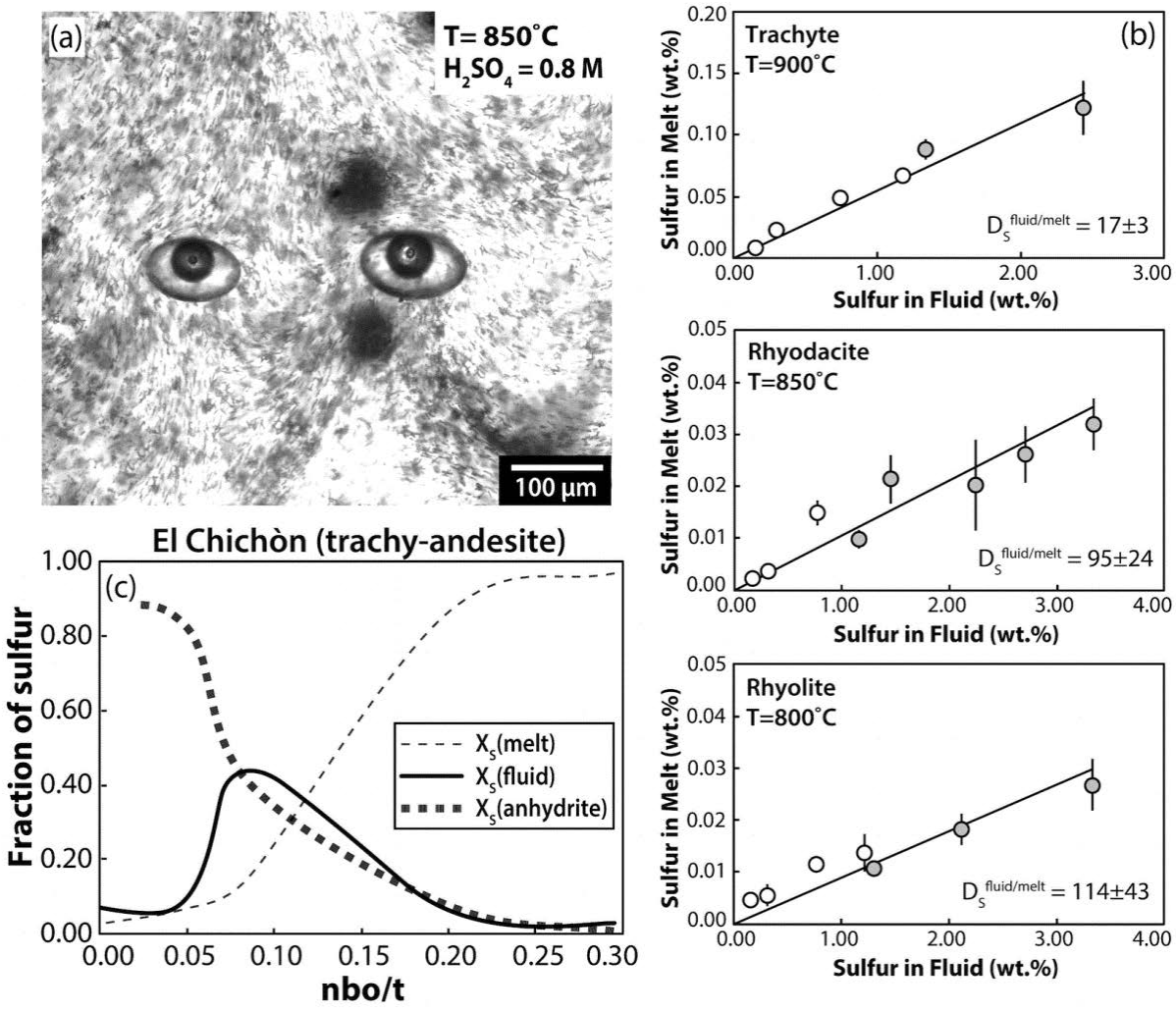

Fig. 3.5-1: (a) Microscopic image of a quenched glass containing crystals and two fluid inclusions. (b) Fluid/melt partition coefficients of sulfur as determined by weighted least square regression of data from experiments with trachyte, rhyodacite and rhyolite base composition (grey symbols refer to anhydrite-saturated experiments). (c) Variation of the sulfur distribution among melt (X_S^{melt}), fluid (X_S^{fluid}) and anhydrite ($X_S^{anhydrite}$) during differentiation of the trachy-andesite from the 1982 eruption of El Chichòn (Mexico).

$$\ln\left(D_S^{fluid/melt}\right) = 9.2 - 31.4 \cdot \frac{nbo}{t} - 1.8 \cdot ASI - 29.5 \cdot Al\# + 4.2 \cdot Ca\#$$

where *nbo/t* is the non-bridging oxygen atoms per tetrahedron, ASI is the alumina saturation index, Al# and Ca# are two compositional parameters calculated in molar units ($Al\# = \frac{X_{Al2O3}}{X_{SiO2}+X_{TiO2}+X_{Al2O3}}$ and $Ca\# = \frac{X_{CaO}}{X_{Na2O}+X_{K2O}}$)

The interplay between fluid-melt partitioning and anhydrite solubility determines the sulfur distribution among anhydrite, melt and fluid (Fig. 3.5-1 c). At increasing melt polymerization, the increase of the partition coefficient and the decrease of anhydrite solubility favour the

accumulation of sulfur either in the fluid phase or as anhydrite. On the other hand, the higher anhydrite solubility and lower partition coefficient for less polymerized melts favour the retention of sulfur in the melt. At equilibrium conditions, these effects yield a maximum of the sulfur fraction in the fluid phase for slightly depolymerized melts (= 0.05 to 0.15). Our data allow quantitative predictions of the sulfur yield of explosive volcanic eruptions over a wide range of magma compositions.

b. *Water diffusion in a basaltic melt (L. Zhang and H. Ni/Hefei)*

Water diffusion feeds bubble growth in silicate melts during volcanic eruptions. Compared to felsic systems, water diffusivity in basaltic melt has not been thoroughly studied with a satisfactory precision. Furthermore, the role played by OH relative to molecular H_2O in the transport of water is still not clear.

We synthesized a haplobasaltic glass with a composition similar to a typical arc basalt. Hydrous glasses with up to 1.3 wt. % H_2O were prepared by fusing anhydrous glass powder and water. Diffusion couple experiments (for samples with 0.028-1.28 wt. % H_2O) and hydration experiments (for the nominally anhydrous samples with 280-600 ppm H_2O) were carried out in a piston cylinder apparatus at 1.0 GPa in the temperature range of 1390-1560 °C. H_2O concentration profiles preserved in the quenched products were measured by FTIR micro-spectroscopy along the cylindrical axis.

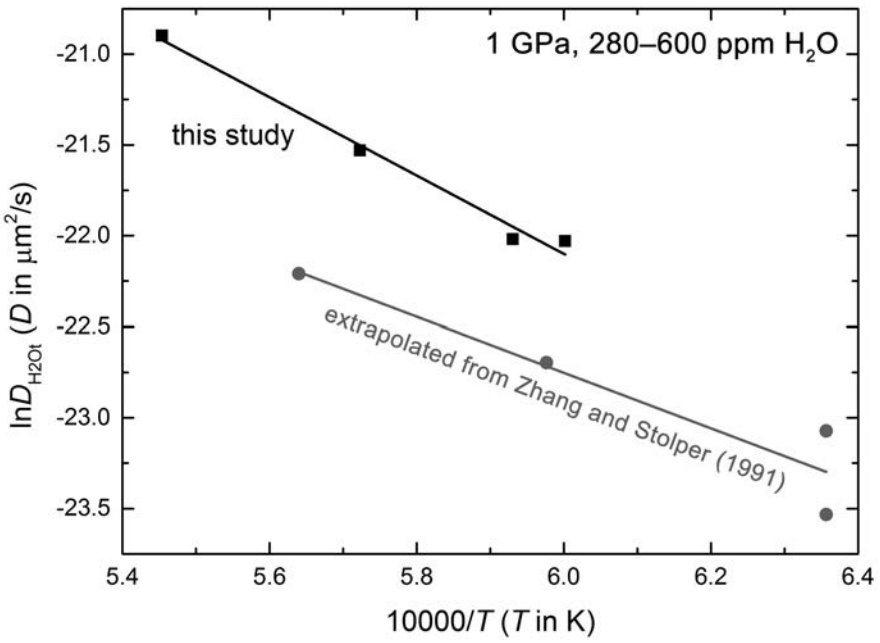

Fig. 3.5-2: Temperature dependence of water diffusivity at 1390-1560 °C, 1 GPa and 280-600 ppm H_2O, compared to an extrapolation of literature data for a MORB melt.

Preliminary results from the hydration experiments indicate that the diffusion profiles can be well fitted by error function curves. This implies that water diffusivity is independent of water content below 600 ppm and suggests that H_2O diffusivity and OH diffusivity are comparable in this concentration range. The total H_2O diffusivities extracted from modeling the measured profiles are greater than those for a MORB melt by a factor of 2-3. The data line up nicely in an Arrhenian plot and yield an activation energy of ~ 180 kJ/mol (Fig. 3.5-2). On the other hand, results from the diffusion couple experiments reveal a positive correlation between the average diffusivity and the average water content (Fig. 3.5-3), implying the dominance of molecular H_2O in water diffusion at high water contents (> 0.2 wt. %).

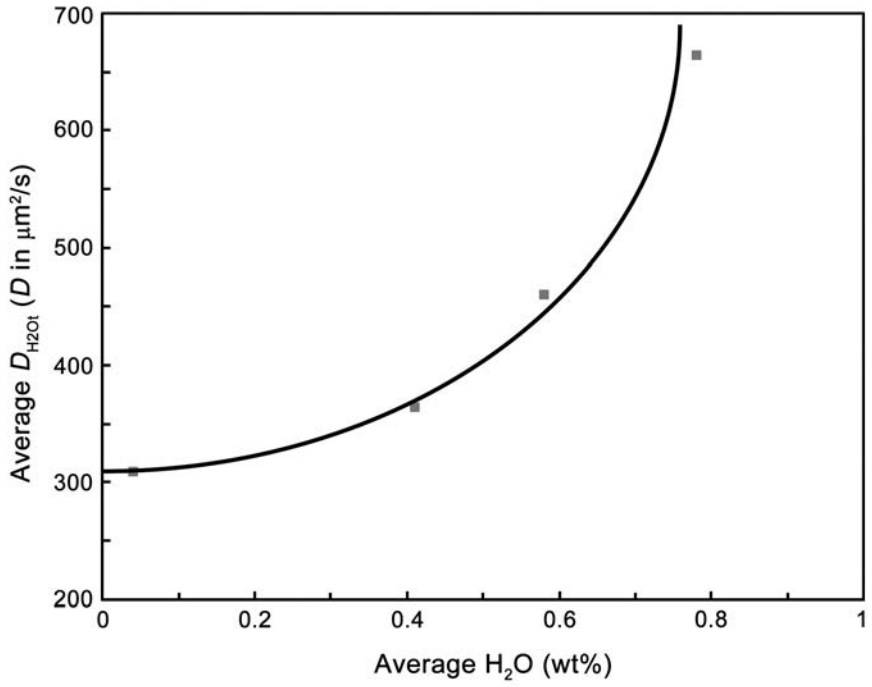

Fig. 3.5-3: Average water diffusivity from diffusion couple experiments increases with increasing average water content.

c. *Melt distribution in synthetic olivine-orthopyroxene rock (A. Adams, K. Marquardt and R. Myhill)*

The majority of Earth's upper mantle is solid containing a small fraction of a melt phase, which plays a significant role in many geologic processes, such as for example mantle metasomatism and plate tectonics. In order to better understand the physical properties of these partially molten rocks, it is necessary to characterize the melt and its distribution on the grain scale. Here, we performed analog experiments in a highly simplified system of a synthetic olivine-orthopyroxene rock (98 % Mg_2SiO_4 and 2 % $MgSiO_3$). The vacuum-sintered aggregate has an average grain size of 6 µm.

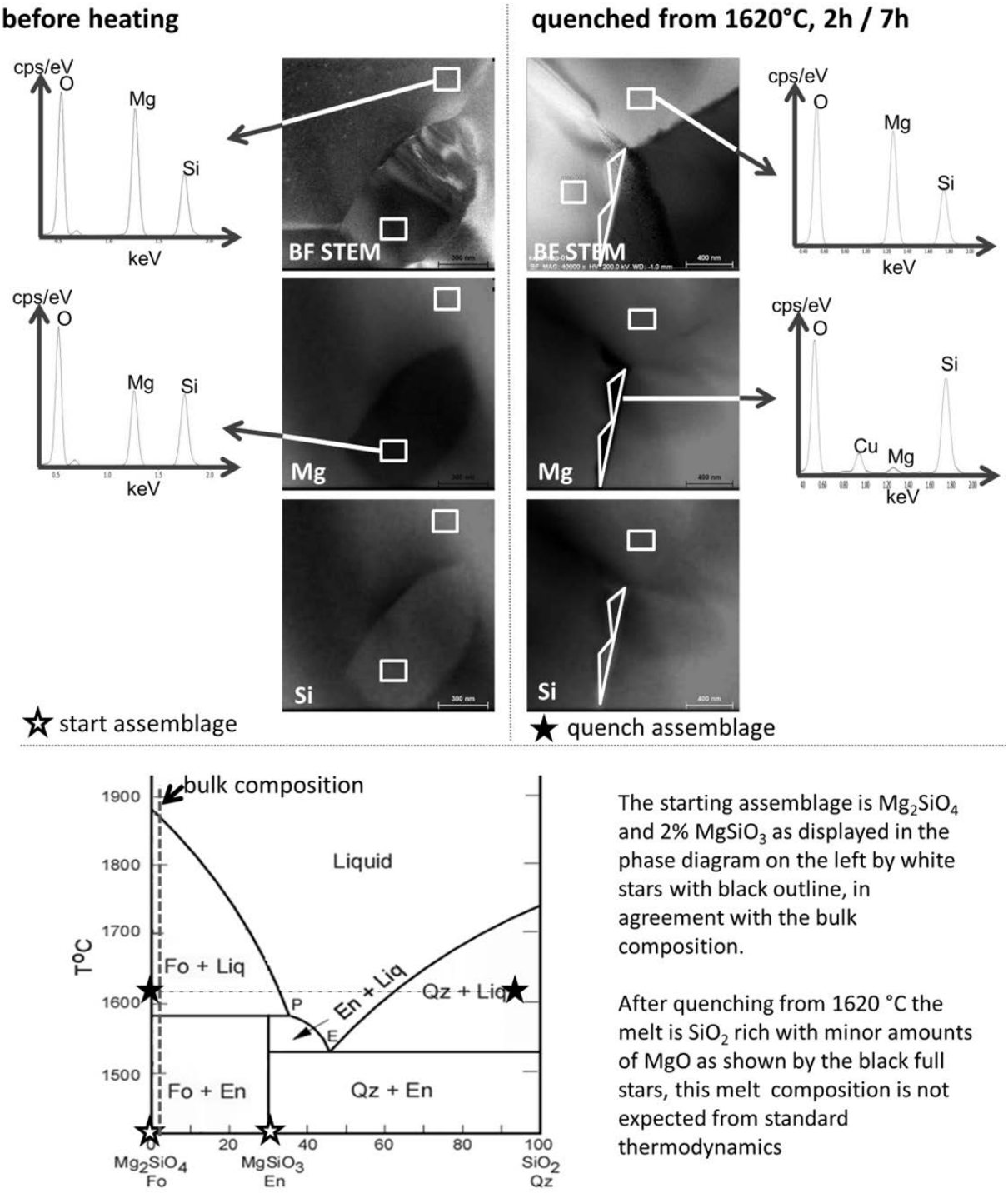

Fig. 3.5-4: Microstructure of a small fraction of melt in a synthetic olivine-orthopyroxene rock. Left side depicts the starting sample, the right side the sample after the heating experiment. The top row shows bright field scanning transmission electron images and energy dispersive X-ray (EDX) spectra of the forsterite in the indicated regions. The second row shows Mg-distribution EDX-maps and EDS spectra of the enstatite of the starting material to the left. On the right an EDX-spectra of the resulting melt-phase is shown. The third row shows a Si-distribution EDX-map. The phase diagram highlights the observed phase relation when surface energy dominates the system.

The sample was heated ambient pressure to 1619 °C near the FMQ buffer to produce an anticipated 2 % melt phase of enstatitic composition according to the phase diagram in depicted in Fig. 3.5-4. To characterize melt interconnectivity and wetting angles we used scanning and transmission electron microscopy (TEM). In contrast to previous studies, the median dihedral angle of the melt in isotropic triple junctions was found to be ~ 59°, which is considerably higher than expected for a melt of enstatitic melt composition (about 40°). Furthermore, the abundance of the melt phase was less than the expected 2 % and is estimated to be approximately 0.5 %. In addition to melt-filled triple junctions, we observed anisotropic melt pockets, including fully-wetted grain boundaries and large, multigrain melt pools that we interpret as transient features resulting from dynamic recrystallization. TEM analyses show, that in contrast to the thermodynamically expected equilibrium melt composition, we generated an extremely silica-rich melt phase that did not change composition with extended experimental duration. The SiO_2-rich composition of the melt explains the high dihedral melt geometries and lowers the total connectivity of the melt system.

d. *Trace elements in subduction zone fluids (H. Keppler)*

Together with mid-ocean ridges, volcanic arcs above subduction zones are the most important locations of magma production in the Earth. Arc magmas are the main source for the growth of the continental crust. Despite many decades of research, the precise mechanism of magma generation in subduction zones is still being debated. Very early models envisaged the direct melting of the subducted slab; however, this is likely only feasible under unusual circumstances, *e.g.*, during the subduction of very young and hot plates. The "standard model" of magma generation in subduction zones assumes that water is being released by the dehydration of amphibole, serpentine, and other hydrous phases in the subducted slab; this water infiltrates the mantle wedge above the slab and causes melting. The trace element abundances in subduction zone magmas likely contain the signature of fluid transport, with strong enrichments of "fluid mobile" trace elements, such as Ba, Pb, or Rb and strong depletions (*e.g.*, the "negative Nb-Ta-anomaly") for fluid immobile elements. However, the validity of this standard model has been increasingly questioned in recent years. Based on some experimental data, it has been suggested that aqueous fluids are "too dilute" to explain the observed trace element enrichments, particularly of the rare earth (REE) elements. Moreover, high Ce/H_2O ratios have been interpreted as a "slab geothermometer", implying temperatures on the surface of the slab that would be so high that melting should occur. Accordingly, a new class of models has emerged that considers melting of sediments on the slab surface as the main mechanism for material transfer from the slab to the zone of melting in the mantle wedge.

While pure aqueous fluids in equilibrium with the minerals of the subducted slab indeed contain many trace elements only in rather low abundances, the addition of chloride to the system should greatly increase the fluid/melt partition coefficients due to the formation of Cl

complexes in the fluid. While this effect had already been observed in some experimental studies, direct observational evidence from the composition of natural magmas is largely lacking. Since Cl and H_2O are volatile components, their relationship with trace element abundances can only be studied using data from undegassed melt inclusions. In recent years, an increasing number of such data has become available. We therefore carried out a systematic study of possible relationships between fluid salinity and trace element enrichments in arc magmas using the data in the Georoc database (georoc.mpch-mainz.gwdg.de).

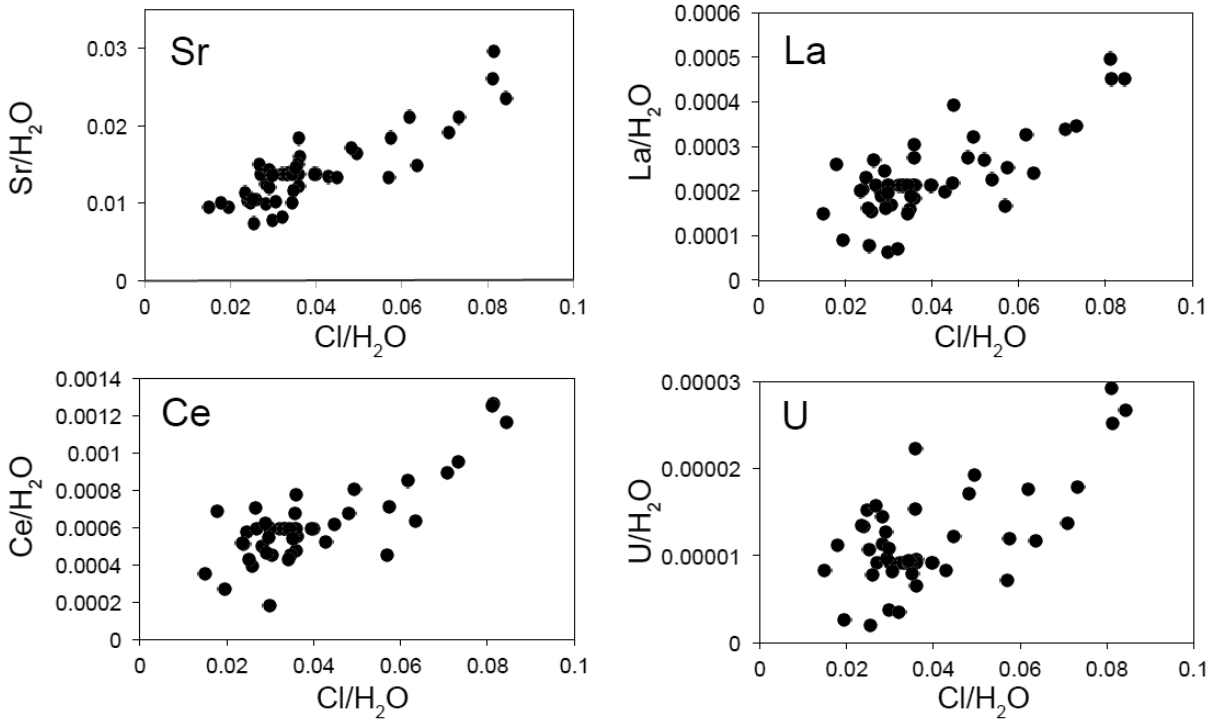

Fig. 3.5-5: Relationship between trace element abundances and the Cl/H_2O ratio in undegassed melt inclusions of primitive arc basalts from Kamchatka. Data from the Georoc database (georoc.mpch-mainz.gwdg.de).

If one considers that fluid transport made a major contribution to the trace element budget of a magma, then the trace element / H_2O ratio should be a proxy for the concentration of this element in the fluid, while the Cl/H_2O ratio gives the salinity of the fluid. The data in the Georoc database show systematic positive relationships between the Sr/H_2O, U/H_2O, Rb/H_2O, Ce/H_2O, La/H_2O ratios and fluid salinity, as represented by the Cl/H_2O ratio, for many data sets of undegassed melt inclusions from arc magmas worldwide. Figure 3.5-5 shows an example for a suite of primitive arc basalts from Kamchatka. It is very obvious that fluid salinity here is the main parameter controlling trace element abundances. This observation provides conclusive evidence for the transport of these elements by aqueous fluids from the slab to the mantle wedge. The relationships in Figure 3.5-5 cannot be explained by trace element transport via silicate melts, since the solubility of Cl in silicate melts is very low

(typically < 1 wt. %) and no effect of Cl on the solubility of these trace elements in silicate melts has ever been observed. Particularly interesting is the relationship between Ce/H_2O and Cl/H_2O, since Ce/H_2O is one of the "canonical" ratios that is constant in MORB and OIB, indicating that Ce and H_2O are not fractionated by partial melting or fractional crystallization. The observed relationship with Cl/H_2O strongly suggests that high Ce/H_2O ratios are not an indicator of high slab surface temperature; rather, they are caused by elevated fluid salinity.

e. *Nitrogen solubility in transition zone minerals (T. Yoshioka, M. Wiedenbeck/Potsdam, S. Shcheka and H. Keppler)*

Geochemical evidence suggests that there is presently much more nitrogen being recycled into the mantle in subduction zones than is degassed at mid-ocean ridges. This is only one of several lines of evidence that suggest that the deep nitrogen geochemical cycle has evolved over time. However, it is still not well known where and how nitrogen may be stored in the solid Earth. To complement some pioneering studies on nitrogen solubility in upper mantle minerals that had been carried out at BGI in recent years, we started to investigate nitrogen solubility in transition zone and lower mantle minerals.

Figure 3.5-6 shows a run product from a multianvil experiment at 16 GPa and 1500 °C. The run product contains coexisting $(Mg,Fe)_2SiO_4$ olivine and wadsleyite, together with metallic iron and quenched silicate melt. The minerals crystallized from an oxide starting mixture,

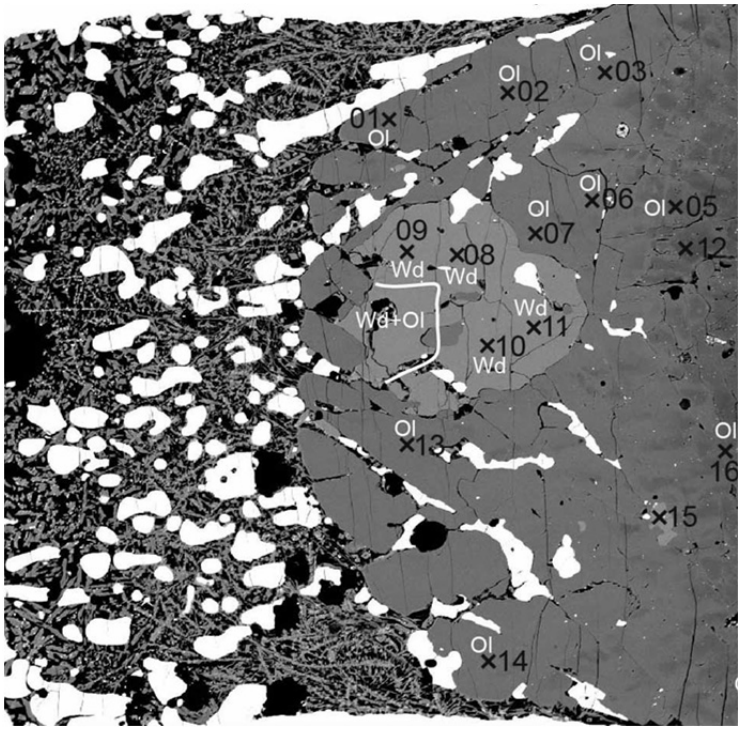

Fig. 3.5-6: SEM image of a run product from a multianvil experiment on the partitioning of nitrogen at 16 GPa and 1500 °C. Coexisting phases are olivine (Ol), wadsleyite (Wd), iron metal (bright spots), and quenched silicate melt (fine dendrites on left hand side of the image). Width of the image is about 0.8 mm; crosses are spots selected for SIMS analyses.

together with a nitrogen-source (^{15}N-doped NH_4NO_3). The metallic iron was added to buffer the oxygen fugacity close to the Fe-FeO buffer, consistent with the reducing conditions in the

deep mantle. SIMS analyses with the Cameca 1280-HR at GFZ Potsdam revealed that wadsleyite strongly concentrates nitrogen in equilibrium with olivine. In wadsleyite, about 150 ppm nitrogen by weight were detected, but only about 30 ppm in the coexisting olivine, suggesting a partition coefficient of $D_N^{wadsleyite/olivine}$ of about 5. These data suggest that the deep, reduced mantle may be a major host of nitrogen in the Earth and it is by no means certain that the majority of the nitrogen in our planet resides in the atmosphere. Depending on the evolution of the deep nitrogen cycle over geologic time, it is quite plausible that atmospheric pressure may have largely fluctuated during the evolution of the Earth.

f. *The fate of silicate melts at core-mantle boundary conditions (S. Petitgirard, W.J. Malfait/ Zurich, R. Sinmyo, I. Kupenko/Grenoble, D. Harries/Jena and D.C. Rubie)*

The early vision of the mantle crystallizing from the bottom upwards towards the surface has been disputed due to computational data on melt densities supporting crystallization at an intermediate depth and an accumulation of dense melts in the deep mantle. The controversy between the two models arises because the exact nature of the partitioning of iron between solid and liquid phases in the lower mantle remains unclear. In addition, no experimental studies have measured directly the density of melts at the conditions of the deep mantle, even though it is the key parameter controlling the entrainment and/or settling of matter in the deep mantle.

Using a novel approach, we measured the density of $MgSiO_3$ amorphous glass in the small sample environment of the diamond anvil cell up to the core-mantle boundary pressure. With a pencil synchrotron X-ray beam, we first measured the attenuation of the X-ray passing through a disc of $MgSiO_3$, pre-cut with the FIB, through a beryllium gasket. By rotating the diamond cell by 90°, we could measure the exact path length of $MgSiO_3$ exposed to the X-ray beam in the previous step. Finally, combining the attenuation with the path length, we retrieved the linear absorption of $MgSiO_3$ at any pressure. The latter is directly linked to the density by $\rho_{HP} / \mu_{HP} = \rho_0 / \mu_0$ with ρ_{HP} being the density at high pressure, μ_{HP} the linear absorption at high pressure, ρ_0 the density of $MgSiO_3$ at ambient conditions and μ_0 the linear absorption measured on the beamline at ambient conditions. We discovered that $MgSiO_3$ glass (300 K) and melt (4000 K) are as dense, within the uncertainties, as their crystalline $MgSiO_3$ bridgmanite counterpart phases in the lowermost mantle Fig. 3.5-7a. Our data on $MgSiO_3$ glass and melt provide the first experimental evidence for such high-density melts in the deep mantle.

Taking into account that iron will partition into the melt phase, we conclude that melting in the $MgSiO_3$-$FeSiO_3$ system will produce magmas that are denser than the residual solids, regardless of the exact nature of iron partitioning (Fig. 3.5-7b). This study therefore supports the theory of a deep basal magma ocean concomitant with the late accretion stage of the Earth. Such a magma ocean surrounding the core would be an ideal candidate for storing

incompatible elements, thermally insulating the iron-rich core, thus delaying the crystallization time of the inner core.

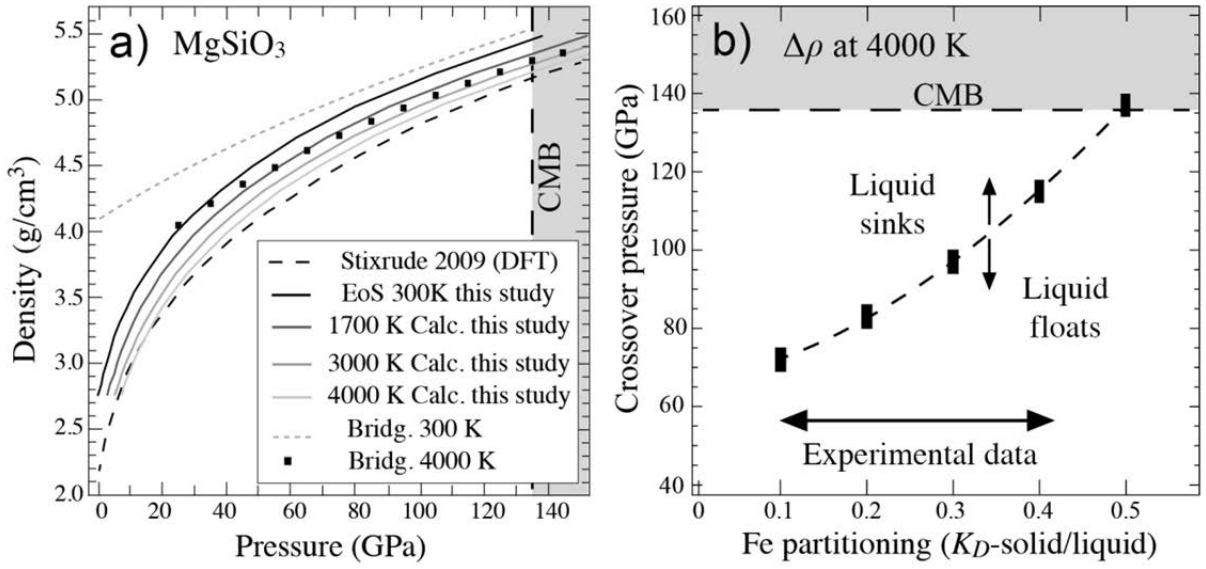

Fig. 3.5-7: a) Results obtained using the X-ray absorption method. The thick dark line is the 4th order Birch Murnaghan equation of sate (EoS) determined in this study at 300 K. The thick grey lines are EoS calculated at high temperature from the 300 K EoS. The dashed grey line is the EoS for bridgmanite at 300 K. Squares show the EoS for bridgmanite at 4000 K and the dashed dark line is the EoS for $MgSiO_3$ melt at 4000 K from Stixrude et al 2009. b) Evaluation of the density difference between melt and solid using our EoS at 4000 K. Regardless of the partitioning of iron, magmas will be denser in the deep Earth on top of the core.

g. *High P-T experiments and first principles calculations of the diffusion of Si, O, Cr in liquid iron (E.S. Posner, D.C. Rubie, D.J. Frost, V. Vlček, and G. Steinle-Neumann)*

Diffusion transport properties of molten iron and iron alloys at high pressures and temperatures are important for understanding large-scale geodynamic processes and the thermochemical evolution of planetary interiors, such as the time and length scales of metal-silicate equilibration during core formation and chemical exchange across core-mantle boundaries during cooling. The density of the Earth's outer core is ~ 10 percent too low to be composed of pure Fe-Ni and is assumed to contain significant concentrations of light elements, such as Si, S, O, and/or C, in addition to siderophile transition metals (V, Cr, Mn, W) which are depleted in the Earth's mantle relative to chondrites. The chemical diffusivity of light and siderophile elements in liquid iron under *P-T* conditions of the Earth's core and its formation are therefore required to constrain the composition and potential chemical stratification of planetary cores, in addition to the kinetics of chemical buoyancy from inner core crystallization that partially drives the geodynamo. In order to better understand the

effects of pressure and temperature on Si, O, and Cr diffusion in liquid iron, we have conducted (1) chemical diffusion-couple experiments combined with numerical modeling of diffusion profiles to account for non-isothermal annealing, and (2) first principles molecular dynamic (FP-MD) calculations from ambient pressure to 135 GPa and 2200-5500 K. To the best of our knowledge, this is the first study to jointly use and compare experimental and theoretical results, conducted under similar conditions, to measure the effect of pressure on diffusion in liquid iron and iron alloys.

Experimental diffusion couples comprised of highly polished cylindrical disks of 99.97 % Fe and metallic Fe alloy (all compositions) were contained within an MgO capsule and annealed within the *P-T* range 1873-2653 K and 1-18 GPa using a multianvil apparatus. A series of experiments are conducted at each pressure using variable heating rates, final quench temperatures (T_f), and time duration at T_f. To minimize the occurrence of diffusion prior to reaching the target temperature, a rapid heating rate of 25 or 50°C/sec was used to ramp the temperature to the required value. Experimental durations were very short (< 180 sec) and diffusion was terminated by quenching at ~ 500 K/sec by switching off the electrical power. Recovered capsules were cut and polished parallel to the axis of the cylindrical sample and measured using EMPA 10 μm-step line scans. To extend our dataset to *P-T* conditions of the Earth's core-mantle boundary, first principles molecular dynamics (FP-MD) simulations were performed based on density-functional theory and implemented using the VASP code. Fe supercells of 150 atoms are overheated to induce melting, compressed to volumes along several isobars (0.0001-135 GPa) according to densities from the liquid iron equation of state reported in the literature, and allowing for changes in chemistry (Si, O, Cr). Diffusion coefficients are computed from the atomic trajectories in the simulation cell via the Einstein relation.

Diffusion coefficients calculated from FP-MD simulations are in excellent agreement with experimental results, as shown in Fig. 3.5-8. Arrhenian activation terms of Si, O, and Cr chemical diffusion obtained by both methods are appreciably smaller and more consistent with empirical and theoretical data than previously reported experimental values for Fe and alloying element self-diffusion in liquid iron and iron alloys derived from much smaller data sets. Our findings corroborate theoretical estimates that diffusion coefficients are scalable to absolute melting temperature (T_m) yielding constant Si, O, and Cr diffusivities of approximately 5×10^{-9} m^2 s^{-1} along the melting curve from ambient to core pressures (Fig. 3.5-9). A simple homologous temperature relation with the parameter $T_h = T_m/T$ can therefore be used to predict diffusion rates relative to the melting curve, as shown in Fig. 3.5-10. The homologous temperature activation term determined from FP-MD calculations for Si diffusion is larger by a factor of 1.3 than the value determined from experiments, but diffusion coefficients at T_m are identical within error for both two methods. Verification of a homologous temperature relation for chemical diffusion in liquid iron implies that low-pressure experiments can be used as accurate analogues of mass transport properties of the Earth's outer core.

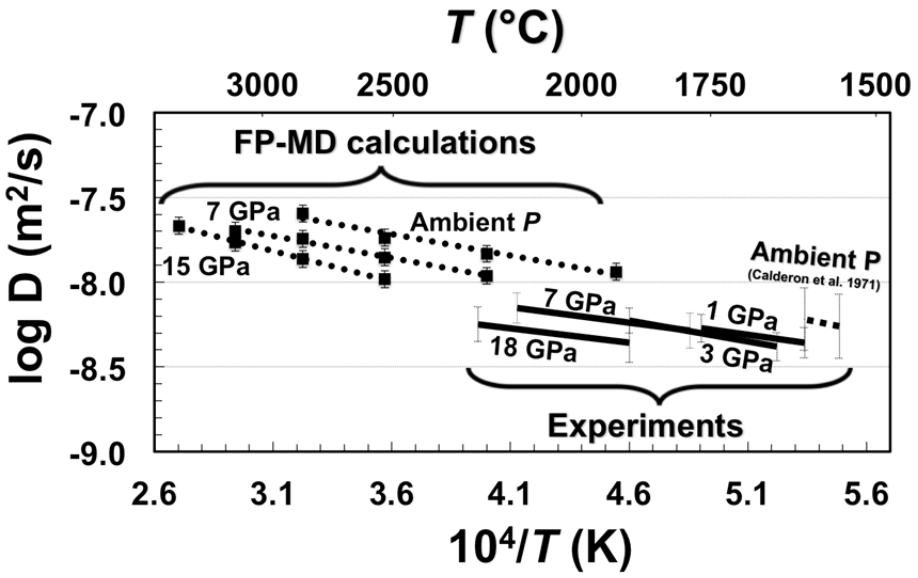

Fig. 3.5-8: Arrhenius plot for Si chemical diffusion in liquid iron determined by (1) diffusion-couple experiments under the *P*-*T* range of 1-18 GPa and 1873-2423 K and (2) FP-MD calculations using cell volumes derived from liquid iron densities to simulate a *P*-*T* range of ambient pressure to 15 GPa and 2200-3700 K. Experimental results yield slightly smaller activation terms (ΔH ~ 40 kJ/mol and ΔV ~ 0.4 cm^3/mol) than the computations (ΔH ~ 56 kJ/mol and ΔV ~ 0.9 cm^3/mol), but results from both methods are in good overall agreement. Error bars represent 1σ.

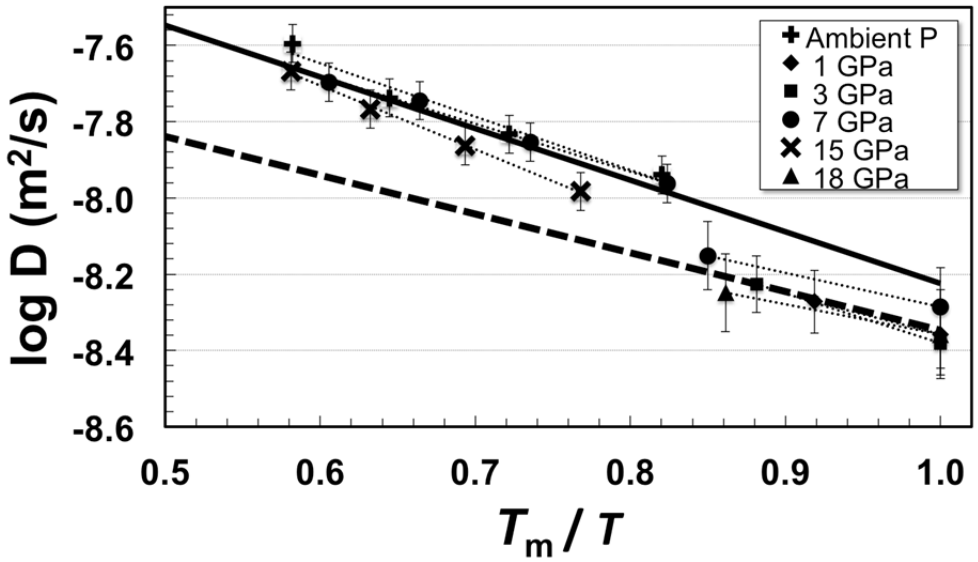

Fig. 3.5-9: Diffusion rates of Si, O, and Cr in liquid iron are constant at melting temperature (T_m) yielding $D_{Fe\text{-}Si}$ = (4.4 ± 2.0) × 10^{-9} m^2/s, $D_{Fe\text{-}Cr}$ = (3.8 ± 2.2) × 10^{-9} m^2/s, and $D_{Fe\text{-}O}$ = (5.6 ± 4.0) × 10^{-9} m^2/s. Melting temperatures were determined experimentally at each pressure and are consistent with previously reported melting curves in the literature. These are the first high-pressure experimental results (above ~ 11 bar) to corroborate previous theoretical estimates that diffusion rates in liquid metals are scalable to melting temperature.

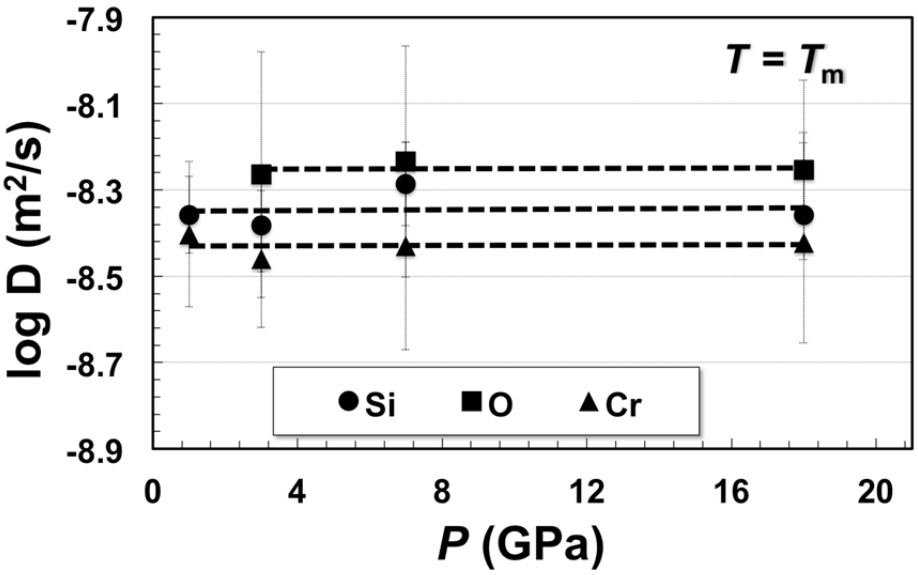

Fig. 3.5-10: Homologous temperature (T_h) relation for Si chemical diffusion in liquid iron as determined from all experimental data (dashed line) and all FP-MD results (solid line). Symbols among the experimental data (lower curve) represent the highest and lowest temperature diffusion coefficients obtained from the global least squares best fit to several (6-9) diffusion profiles at each pressure. The dependence on T_h, as determined from the computational results is a factor of ~ 1.3 higher than experimental data but both models yield the same diffusion coefficient at T_m, (4.4 ± 2.0) × 10^{-9} m^2/s. According to both model curves, a two-fold increase of the melting temperature (T_h = 0.5) results in an increase of diffusion rates by ~ 0.6 log units.

3.6 Rheology and Metamorphism

Various geological and geophysical phenomena such as volcanisms and earthquakes originate from the dynamic motion in the Earth's interior. The rheological properties of the constituent minerals and the resulting rocks of the Earth's interior govern its dynamic behavior. The most direct way to determine rheological properties is conducting deformation experiments under controlled environments where relations between the stress and strain rate are determined. The 6-axis multi-anvil apparatus operated at the Bayerisches Geoinstitut allows the generation of shear stresses by retracting or approaching one pair of rams relative to the others and thus deforming samples at high pressures of several GPa. Furthermore, the D-DIA apparatus allows deformation experiments at GPa pressures. The first contribution of this chapter is focused on the effects of deviatotic stresses and concurrent plastic deformation on formation of garnetite from eclogite. The production rate of garnet under shear stresses was found to increase by up to 40 % at 10 GPa compared to hydrostatic conditions. In the second contribution, the rheology of eclogite as a bimineralic mixture in its stability field is studied using measurements of the lattice micro-strains of each mineral by using a D-DIA apparatus in combination with *in situ* X-ray diffraction at ESRF. In addition to these deformation studies in the large-volume apparatus, deformation experiments have also been conducted in diamond anvil cells. In the third study single crystal X-ray diffraction was adopted to study ice VI at high pressures to understand the dynamic interiors of icy satellites. The fourth study is focused on possible changes in slip systems at 30-40 GPa in ferropericlase at high temperatures to examine a previously reported increase in its yield strength and understand seismic anisotropy in the lower mantle. For this purpose, powder X-ray diffraction of ferropericlase was carried out at pressures of 40-80 GPa and temperatures of 1100-1500 K at the Extreme Condition Beamline at PETRA III, DESY.

Although deformation experiments are the most direct way to study mineral rheology, researchers follow different strategies to examine results obtained by deformation experiments. Stress and strain rates in deformation apparatus are many orders of magnitude higher than those in nature, and therefore, Si self-diffusion is expected to be the most fundamental rate-limiting process in the creep-dominated deformation regime of silicates. A method to measure Si and O self-diffusion coefficients in single-crystal wadsleyite is being developed in the fourth study. The BGI scientists and coworkers found that the oxygen diffusion coefficient of forsterite has a positive pressure dependence, in contrast to other species such as silicon.

Diffusion coefficients yield only indirect information on dislocation creep, which should be the most essential creep mechanism in the mantle. Consequently, dislocation recovery experiments, where dislocation annihilation rates are measured under quasi-hydrostatic annealing, may give a more complete image. The dislocation mobility under low stress conditions shows a water-content dependence, while temperature dependence is consistent with that obtained by deformation experiments. A comparison of dislocation annihilation rates between bridgmanite and ringwoodite with various water contents demonstrates that dislocation mobility in bridgmanite is higher than that in dry ringwoodite but lower than the one in wet ringwoodite with 1 % of water. This explains the global variation of slab

stagnation and also suggests a wet mantle transition zone. Although dislocation recovery experiments usually provide information about dislocation climb mobility, a new analysis allows us to estimate glide and climb mobilities simultaneously. This analysis suggests that the dislocation mobility in deformation experiments is glide-controlled.

Micro-textural observation by TEM provides essential information about rheological properties of minerals. Careful observation by weak-beam dark-field images on wadsleyite deformed in the [001] direction on the (010) plane allowed the demonstration that the [001](010) slip occurs by glide of the dissociated dislocations of 1/2<101>. To understand the process of solid creep, the change in microstructure was studied by *in situ* deformation in the TEM. In the field of metallurgy, it is widely known that Cottrell atmosphere, segregation of impurities to dislocation cores, causes hardening and embrittlement in FCC and BCC metals. Preliminary experiments to produce Cottrell atmosphere through pipe diffusion in synthetic forsterite were made to examine the effects of Cottrell atmosphere in mantle minerals. The last contribution investigated phase transition mechanisms from olivine to ringwoodite and ahrensite in the Tissint meteorite based on careful observation by SEM, EPMA and FIB-TEM techniques.

a. *Experimental investigation of garnet formation in the CMNAS system at high pressure under deviatoric stress (F. Heidelbach)*

The formation of eclogite and its transition to garnetite at greater depth are crucial processes during subduction of crustal material in the geodynamic cycle. These transitions have been investigated closely in experiments under hydrostatic conditions. However, studies of naturally occurring eclogites indicate that deviatoric stresses and concurrent plastic deformation during the phase transition may influence microstructures of eclogite and also the rheology of garnetite. In the present project, we aim to investigate their influence on the transition of eclogite to garnetite with increasing pressures.

The starting material with a simplified dry CMNAS composition was synthesized from glass in piston cylinder experiments at 3 GPa and 1200 °C, yielding fine grained (~ 10-20 μm) mixtures of omphacite, garnet and quartz as well as some residual kyanite (Fig. 3.6-1a). Transformation experiments were then performed in a pressure range from 6.5 to 10 GPa at 1200 °C in a 6-axis multianvil press. Pure shear deformation of 30 % was achieved with strain rates ranging from 5×10^{-5} to 5×10^{-6} s^{-1}. For comparison, phase transition experiments were performed under quasi-hydrostatic conditions. The reaction of the crystalline starting materials was characterized by the interdiffusion of all chemical components between the garnet and omphacite; however, diffusion was too slow to reach equilibrium even after the longest experiment duration (1000 minutes) (Fig. 3.6-1b). With increasing pressure, garnet is more enriched in Na, Ca and Si and depleted in Mg and Al, producing majoritic garnet with up to 3.3 Si atoms pfu and small contents of Na (0.05 atoms pfu) at the highest pressure (10 GPa). Comparison of static and dynamic experiments showed no difference in final compositions of garnet and omphacite. However, concurrent deformation enhanced the overall production rate of garnet by 12 % at 6.5 GPa and up to 44 % at 10 GPa.

Deformation was accommodated by intracrystalline plasticity of omphacite as well as diffusion assisted grain boundary sliding. They produced crystallographic preferred orientations (CPOs), in which omphacite crystals were elongated in the [001] direction, and shortened in the [110] and [010] directions over the whole investigated pressure range. These textures are similar to omphacite textures in naturally deformed eclogite. Garnet also started to develop subgrain structures and internal dispersions of lattice orientation, which indicates intracrystalline plasticity during growth. Note that garnet did not show particular CPO patterns, which is also similar to those in naturally deformed eclogite.

A similar study of garnet formation in a peridotitic CMAS system (see last year's annual report) yielded an increase of 53 % in garnet growth rate, indicating a similar value for the influence of concurrent plastic deformation on the reaction progress. In this previous study, large differences in reaction rate could only be observed during the nucleation stage of the reaction, which is of lesser importance here, because garnet is already present in the starting material and diffusive transport is the main mechanism of garnet growth.

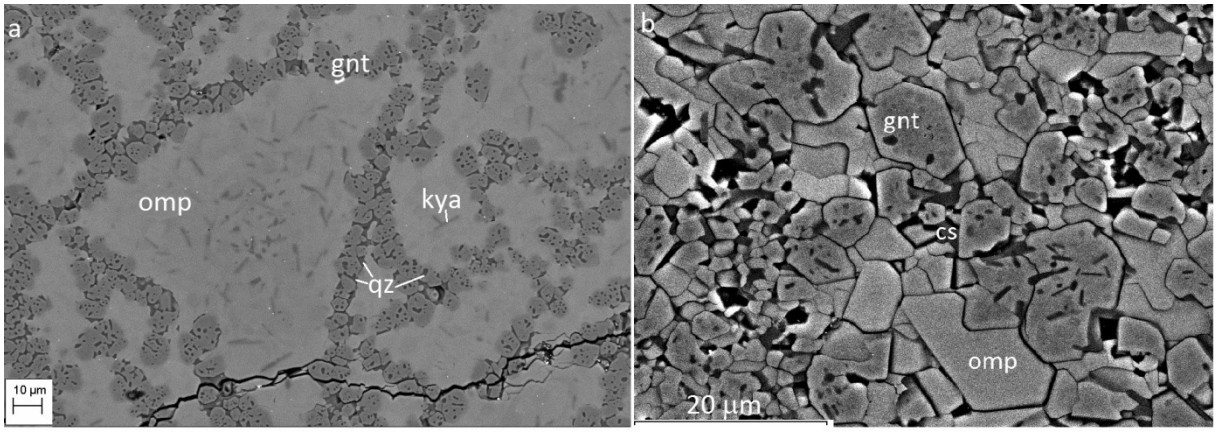

Fig. 3.6-1: SEM-BSE images. (a) starting material. (b) sample deformed at a pressure of 10 GPa and a temperature of 1200 °C for 200 minutes to 30 % of pure shear (compression and extension in the vertical and horizontal directions). Note bright rims of garnet crystals due to diffusion of Ca into the garnet phase as well as the partial euhedral shape of garnet grains due to crystal growth.

b. *Deformation of bimineralic eclogite and olivine polycrystals at high pressures and temperatures (R. Farla, A. Rosenthal, C. Bollinger, S. Petitgirard, J. Guignard/Grenoble, T. Kawazoe and D.J. Frost)*

The transformation of basaltic material as part of the oceanic crust to mafic eclogite during subduction into the deep Earth is a key process of plate tectonics. Eclogite is a bimineralic mixture composed mainly of garnet and clinopyroxene (omphacite), which will exist as a layer of a few-km thickness on subducted lithosphere and as dense mafic cumulates at the roots of orogenic belts. At these contact regions, bimineralic eclogite poses an upper bound on the shear strength in the Earth, and therefore may play an important role in material transport

of the peridotite-dominated mantle. However, few experimental deformation studies to date have been able to determine the strength of bimineralic eclogite due to the challenges of stress measurements at high pressures at which eclogite is stable. In this study, we carried out deformation experiments on bimineralic eclogite in a large volume press in combination with *in situ* X-ray diffraction at the beamline ID06 in ESRF to measure the lattice micro-strains of the minerals and estimate stresses as a function of strain (rate).

Eclogite composed of 50:50 garnet and clinopyroxene was pre-synthesized in a multianvil apparatus using a starting material with a model-altered MORB composition. Grain sizes of clinopyroxene and garnet in the synthesized eclogite were 10-60 and 1-60 µm, respectively. San Carlos olivine powder with similar grain sizes was synthesized at 1250 °C and 2 GPa in a piston cylinder apparatus. In each deformation experiment, an eclogite sample was placed on an olivine sample and was performed at step-wise increasing displacement/strain rates to total strains of 20-30 %.

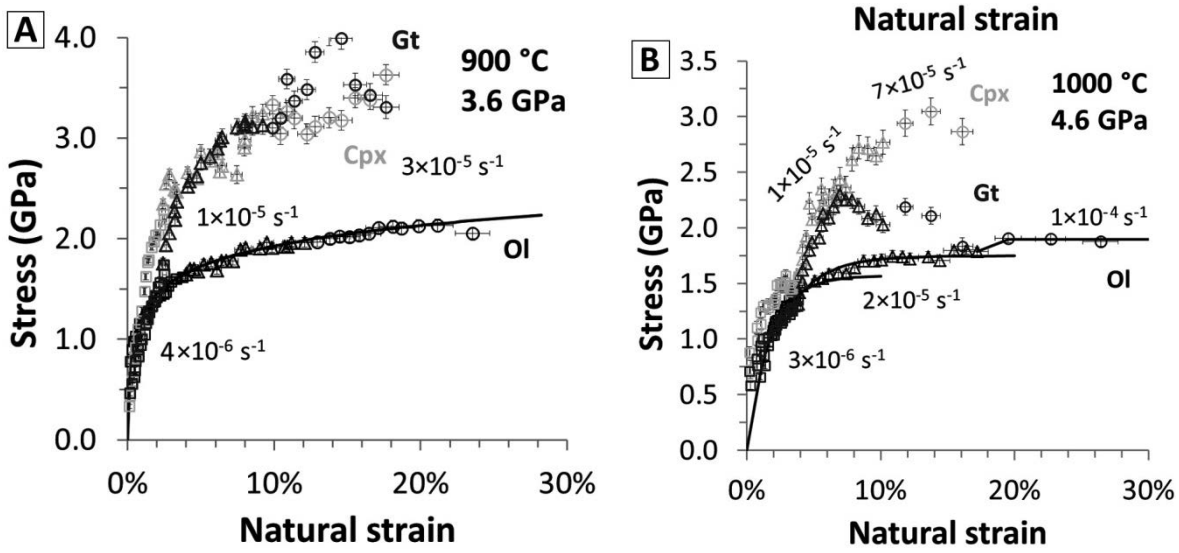

Fig. 3.6-2: Stress estimations (based on the elasticity tensor at given PT conditions) of olivine, garnet and clinopyroxene as a function of strain (rate).

In situ synchrotron X-ray diffraction measurements of the lattice micro-strains of the deforming phases suggest high mean stresses at 900 °C/3.6 GPa and at 1000 °C/4.6 GPa (Fig. 3.6-2 A, and B respectively). At low strain rates of 3×10^{-6} s^{-1}, stresses appear to be equal amongst garnet, clinopyroxene and olivine phases. However, at higher displacement/strain rates, olivine deformed twice as fast as eclogite. At equal strain rates in both samples, the mean stresses in garnet and clinopyroxene thus increased by more than a factor of 2, depending on the stress exponent, in contrast to olivine. In addition, all phases exhibit significant plastic anisotropy with a maximum range in stresses spanning 0.5 GPa for garnet and 1.3 GPa for olivine (not shown). Figure 3.6-3 A, B show typical microstructures of the bimineralic eclogite before and after deformation (to about 30 % strain). The most striking

observation is the formation of segregated garnet-clinopyroxene layers and flattening of clinopyroxene grains. No significant crystallographic preferred orientation (CPO) developed for garnet, however a strong CPO developed for clinopyroxene with [001] axes that form a girdle in the shear direction and [010] axes that form maxima in the plane normal to the shear direction (Fig. 3.6-3 C, D) However, (010)[001] slip is not typical. Based on previous TEM observations and modeling, the activation of multiple slip systems such as {110}[001] and {110}1/2⟨110⟩ can, however, reproduce the observed textures.

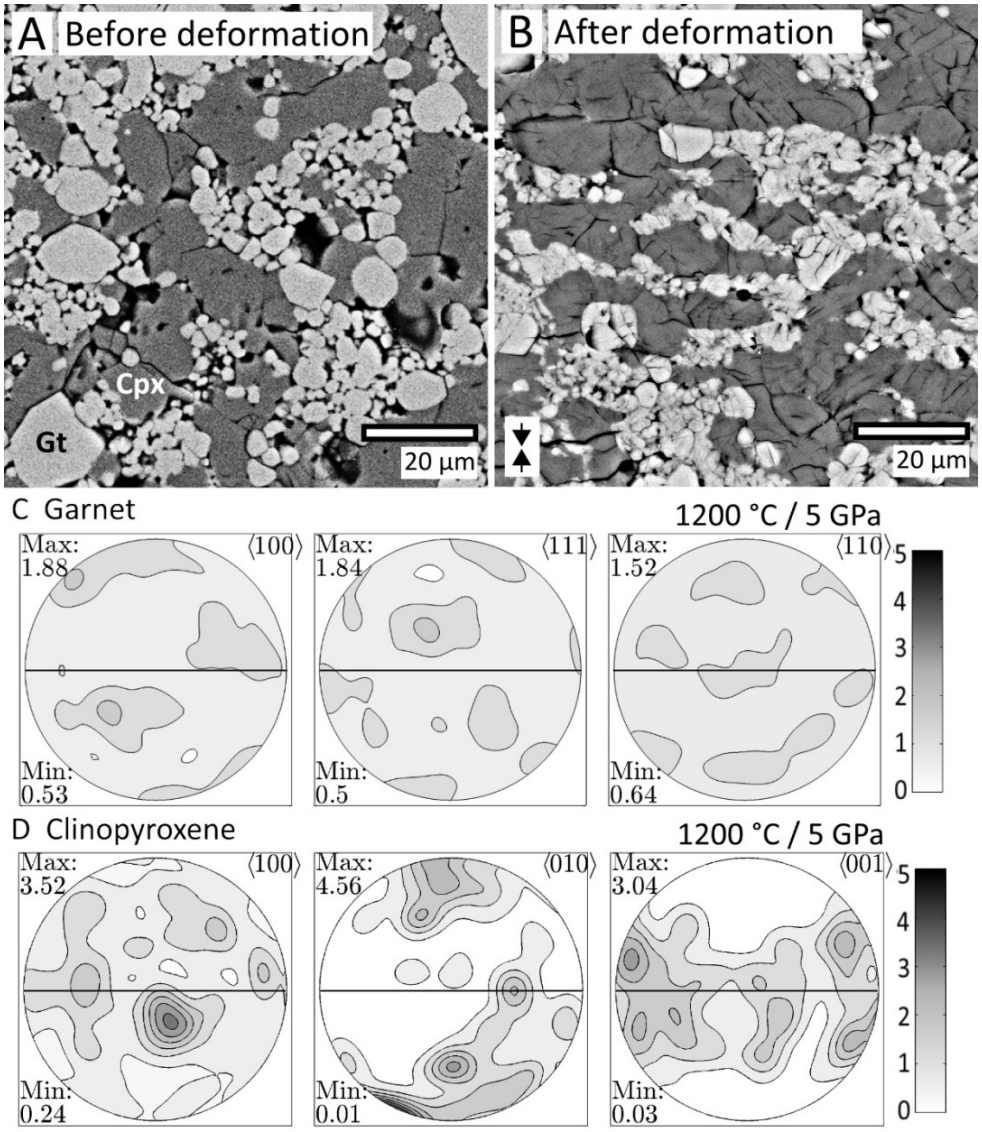

Fig. 3.6-3: Microstructural observations of eclogite. Panel A shows the distribution of garnet (light gray) and clinopyroxene (dark gray) grains in a hydrostatically sintered sample. Panel B shows the microstructure after axial compressive deformation to about 30 % strain. Panels C and D represent stereographic projections of grain orientations of garnet and clinopyroxene along important crystallographic directions. The north-south direction is the compression direction and the east-west direction is the shear direction. The legends on the right show the multiples of uniform distribution (where 1 denotes a uniform distribution), also given by Max and Min for each projection.

Based on existing flow laws for olivine, and microstructural observations, it is clear that olivine deformed under experimental conditions by dislocation glide (Peierls mechanism) with an estimated activation volume of ~ 16×10^{-6} m^3 mol^{-1}. The bimineralic eclogite likewise deformed by dislocation processes, and surprisingly clinopyroxene appears as strong as garnet. Lastly, several higher temperature experiments (1200 °C/ 5 GPa) on stacked olivine and eclogite samples carried out at BGI suggest a switch in flow strength, where the eclogite deformed 1.7 times faster than olivine. However, no stresses could be measured. Future, high temperature (1200-1300 °C) synchrotron experiments are planned to explore thermal and large strain softening in bimineralic eclogite, garnetite and clinopyroxenite compositions.

c. *Deformation of water ice VI: a single-crystal X-ray diffraction study (A.S. Pakhomova, T. Boffa Ballaran and A. Kurnosov)*

A significant portion of the icy satellites orbiting the giant planets consist of high-pressure polymorphs of ice. These satellites are of particular interest to planetary science, because they show a range of diverse geological features including the only extraterrestrial evidence for liquid oceans, active plate tectonics and volcanism. Each icy satellite seems to have experienced quite different processes of accretion, differentiation and early evolution. For example, the third Jupiter satellite, Ganymede is fully differentiated and has a metallic core, a rocky mantle and an overlaying icy mantle and crust, whereas the fourth satellite, Callisto has an undifferentiated interior. In order to explore early dynamic processes which have led to varying degrees of differentiation of the interiors of different satellites, information concerning the viscosity of ice is required. In this study, we conducted deformation of two single crystals of ice VI in a DAC. An advantage of this method is that it allows orientations of the single crystals to be determined with respect to the loading axis of the DAC as well as with respect to each other.

Two single crystals of ice VI were grown *in situ* inside a four-screw DAC at room temperature. Firstly water was loaded in the hole of a copper gasket indented to 100 μm thickness. Two ruby spheres were also loaded to measure pressure. The pressure was increased above 1 GPa to form several ice VI crystals. The DAC was then externally heated up to ~ 70 °C in order to melt all crystals except for two. The DAC was cooled down to room temperature for few hours to grow the two crystals (Fig. 3.6-4). The single-crystal X-ray diffraction was taken at 1.2 GPa and room temperature using a Huber 4-circle diffractometer to investigate broadening effects due to the applied pressure. Selected reflection profiles were repeatedly measured for a month in order to monitor their broadening with time.

After 20 hours, the appearance of an additional peak was observed from Crystal 1by ω scans to the (2 0 1) reflection. The difference in the positions of the two peaks of the ω profiles, $\Delta\omega$, increases with time (Fig. 3.6-5a). A different behaviour was observed for the (0 2 1) reflection which lies along the loading axis of the DAC. This reflection did not show any additional peak during the whole experiment (Fig. 3.6-5b). Planes normal to the (0 2 1) plane (*e.g.*, (400), (201)) showed additional peaks with large $\Delta\omega$, whereas planes with small angles to the (0 2 1) showed smaller $\Delta\omega$. The reflections from Crystal 2 did not show such additional peaks.

The uniaxial compression of the DAC leads to bending of the crystals resulting in broadening of the initial ω-profiles and indicates the formation of randomly distributed dislocations. The energy associated with the elastic bending of the crystal lattice is reduced in the case of crystal 1 by rearranging the dislocations into a vertical wall to form a symmetrical tilt boundary. This boundary can be described on the base of the diffraction data in terms of the rotation axis ~ [-2 0 1] and of a rotation angle of ~ 0.7°. The calculated rotation angle and the observed misorientation in the ω-profile of the (400) plane are in a good agreement. A further increase in pressure to 1.3 GPa led to significant broadening of the reflections of Crystal 2 similar to what was observed for crystal 1. Measurements are currently being performed at this pressure to better understand the slip system and deformation mechanism of ice VI.

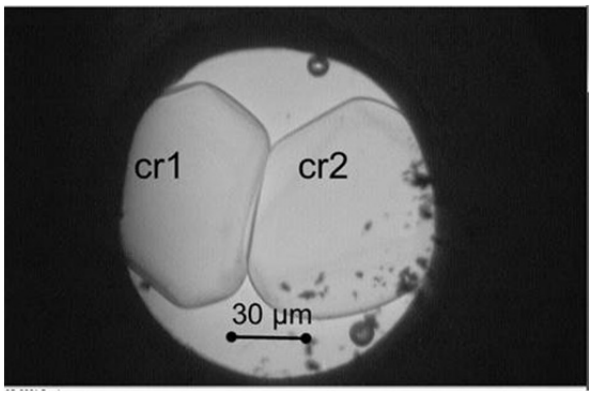

Fig. 3.6-4: Two single crystals of ice VI grown in the DAC.

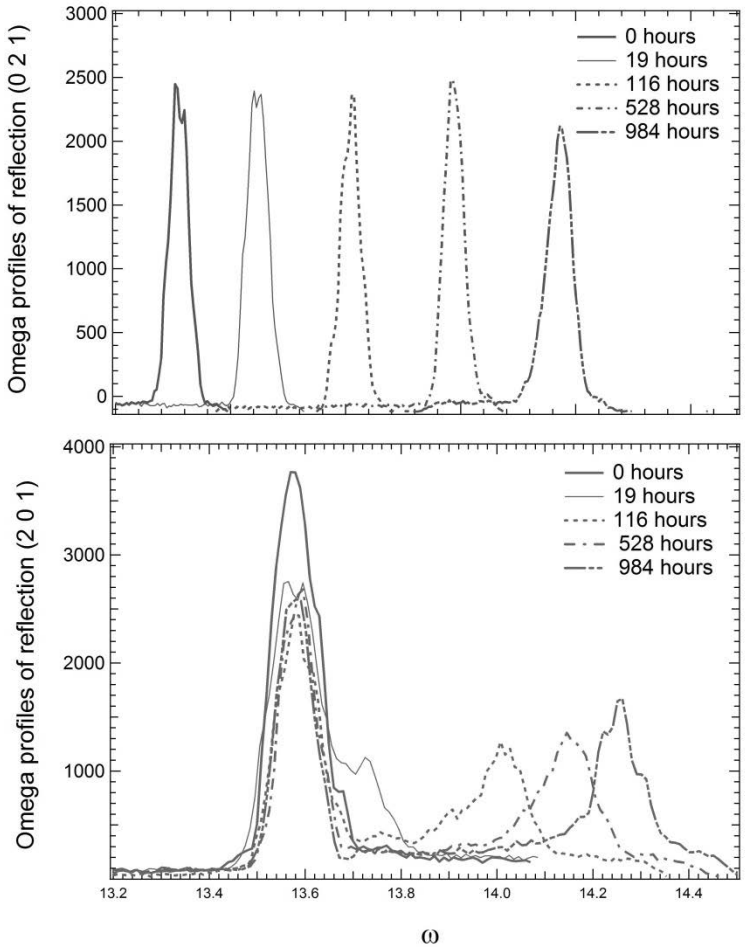

Fig. 3.6-5: Time evolution of (201) and (021) peaks of ice VI, synthesized and deformed in a DAC, using omega scans of the single crystal X-ray diffractometer.

d. *Experimental deformation of (Mg,Fe)O at conditions of the lower mantle (J. Immoor, H. Marquardt, L. Miyagi/Utah, S. Speziale/Potsdam and H.-P. Liermann/Hamburg)*

Ferropericlase is thought to be the second most abundant mineral in Earth's lower mantle. Due to its potentially weak rheological behaviour, it may play a key role in controlling rheology of the lower mantle and in generating seismic anisotropy. However, our understanding of the high-pressure deformation behaviour of ferropericlase is incomplete, particularly at high temperatures where no experimental data are published. Room temperature data from our previous study show that the yield strength of ferropericlase increases by a factor of 3 between 25 and 65 GPa. This behaviour may cause subducted slabs to stagnate in the shallow lower mantle, but high-temperature experiments are needed to understand if the observed effects take place at conditions relevant for the deep mantle. Furthermore, high-temperature data allow for the first experimental testing of a theoretically predicted change of slip-system activities at around 30-40 GPa in MgO, with implications for our understanding of seismic anisotropy observations in the lowermost mantle.

We have performed X-ray diffraction (XRD) experiments on ferropericlase compressed in a diamond anvil cell (DAC) at the Extreme Conditions Beamline (ECB) at PETRA III. Experiments were performed with the DAC aligned with the compressional axis at 90º to the incident X-ray beam (radial XRD). $(Mg_{0.8}Fe_{0.2})O$ powder was loaded in Mao-Bell-type DACs without any pressure-transmitting medium to enhance texture by differential stresses. Either cubic boron nitride (cBN) or amorphous boron gaskets were employed and a graphite resistive heater was used to achieve high temperatures. XRD spectra were collected using a fast flat-panel detector XRD1621 from Perkin Elmer at photon energy of ~ 26 keV. A gas membrane device was employed to remotely increase pressure and stress on the sample. We collected experimental data up to 79 GPa at 1150 K and 40 GPa at 1500 K (Fig. 3.6-6). The maximum experimental pressures were limited by diamond failure.

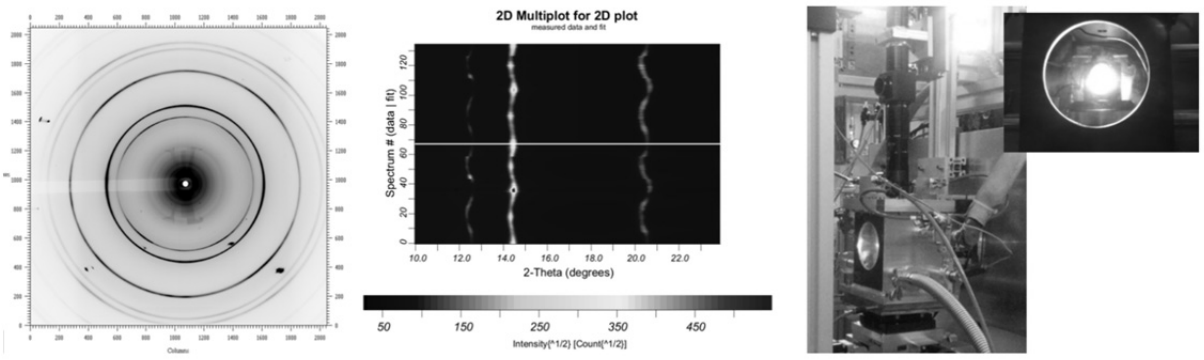

Fig. 3.6-6: (left) Radial XRD pattern of $(Mg_{0.8}Fe_{0.2})O$ at 79 GPa and 1150 K. Unrolled spectrum (center) showing differential strains (curvature of the diffraction "rings") and texture (intensity variations along the "rings") along with the best-fit model (upper half). All visible "rings" belong to ferropericlase. (Right) Image of experimental setup and sample chamber at 1500 K and 40 GPa.

The collected data allow for understanding the creep strength and texture of ferropericlase at conditions of the Earth's lower mantle, because texture and strain in the sample can be deduced from the variations of diffraction intensities as a function of the azimuthal angle. Preliminary data analysis indicates that the creep strength of ferropericlase increases with depth in the lower mantle in a similar way as previously found based on room-temperature measurements. We will combine the measured data with elastic viscoplastic self-consistent modeling to extract slip-system activities of (Mg,Fe)O, which will then be used to model seismic anisotropy in the lowermost mantle.

e. *Si self-diffusion coefficient in wadsleyite as a function of water and iron content (D. Druzhbin, T. Kawazoe, H. Fei, D.J. Frost and T. Katsura)*

Silicon is the slowest diffusing species in most mantle minerals and thus it controls the creep rate. Hence, measurement of Si self-diffusion coefficients has important implications when investigating mantle flow. Wadsleyite $(Mg,Fe)_2SiO_4$ (a high-pressure polymorph of olivine) is one of the most abundant minerals in the mantle transition zone. Experiments have shown that wadsleyite can accommodate significant amounts of water, which could affect the rate of silicon self-diffusion in this mineral.

Several deformation experiments concluded that an increase in water content in olivine considerably enhances the creep rate. Nevertheless, Si self-diffusion experiments in forsterite showed noticeably lower water dependence than that obtained by deformation experiments. The purpose of this work is to measure the Si self-diffusion coefficient (D_{Si}) of wadsleyite, as a function of water concentration in this mineral (C_{H_2O}). Forsterite and natural olivine have the same C_{H_2O} dependence, and therefore iron does not seem to affect the C_{H_2O} exponent of D_{Si} in olivine. However, even though iron does not affect D_{Si} in the case of olivine, it may have an affect in the case of wadsleyite. Therefore, the C_{H_2O} exponent will be also studied using Fe-bearing samples.

In order to avoid grain-boundary diffusivity which takes place in polycrystalline material, wadsleyite single crystals larger than 0.5 mm will be used for the diffusion studies, and were synthesized in the following way. For synthesis of Mg_2SiO_4 wadsleyite crystals, several runs were performed in a Kawai-type multianvil apparatus at different pressures (from 16 to 21 GPa with 0.5 GPa step) with forsterite powder as a starting material in a platinum capsule. The sample was first compressed to the target pressure at room temperature, then temperature was increased to 1770 °C at a rate of 100 K/min. This temperature was kept for 3 hours before fast quenching. Run products were checked by X-ray diffraction and Raman spectroscopy. Only at 21 GPa and 1770 °C we found transparent crystals that were identified by single-crystal diffractometer (Mo Kα) as a wadsleyite with *Imma* space group (Fig. 3.6-7a). The largest crystals were about 0.9 mm in size, but they had numerous cracks parallel to each other, which are probably caused by relatively fast decompression. However, crystals within 0.4-0.6 mm in size have no inclusions and cracks. Polarized FTIR spectra were taken from the double-side polished samples parallel to (0 1 0) in order to estimate water content, showing

about 500 wt. ppm of water. We synthesized dark green $(Mg,Fe)_2SiO_4$ crystals within 0.5-1 mm in size without any crack or inclusion (Fig. 3.6-7b). The water contents in these crystals were about 1800 wt. ppm.

In order to decrease water content in the crystals, the crystals were pre-annealed at the same *P-T* conditions as the synthesis experiments by using dense CsCl pellets without a capsule to avoid breakage of the crystals. Pre-annealing experiments with small iron grains mixed with buffer for a long duration (3-5h) led to water-content decreases down to < 100 wt. ppm.

Si diffusion rates should be low and therefore the diffusion distance should be very short even at high temperatures for a long duration of diffusion annealing. Secondary ion mass spectroscopy (SIMS) is usually used to measure such short diffusion profiles. Initial surface roughness and roughness after diffusion annealing strongly lower the SIMS profile resolution. For this reason, we mechanically polished crystal surfaces by ¼ μm diamond powder before producing a diffusion couple. The resultant surface roughness was measured by a confocal microscope. To produce the diffusion couple, the polished surfaces of the Fe-free wadsleyite crystals were deposited with thin films (300-400 nm thickness) with major element compositions of forsterite doped with ^{18}O and ^{29}Si by the pulsed laser deposition technique in the Institute of Geology, Mineralogy and Geophysics at Ruhr-Universität in Bochum. For Fe-bearing samples, the major element compositions of the thin film were the same as the wadsleyite crystals, and were enriched in ^{18}O and ^{29}Si. Since both O and Si ions were isotope-enriched, their diffusion rates will be measured simultaneously in the same samples.

We conducted pre-annealing experiments using the wadsleyite crystals with thin films to examine changes of the surface roughness during annealing, and found that the crystal surface roughness increased up to 600 nm. Such roughness is too large for the present purpose because expected diffusion lengths will be 100 nm. Therefore the assembly design for the diffusion annealing is being improved to prevent increase in the surface roughness.

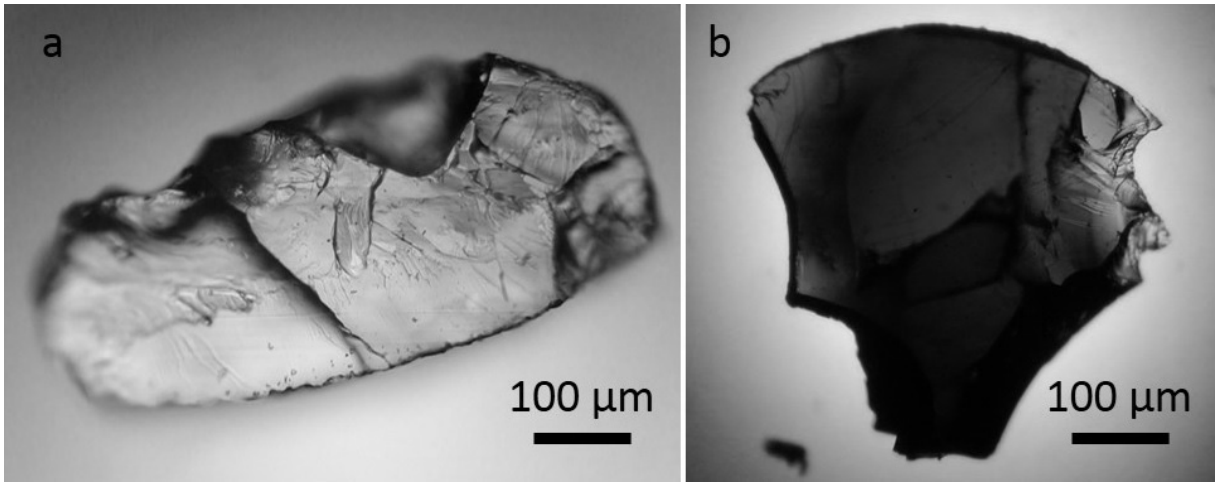

Fig. 3.6-7: Transmitted light optical photographs of Fe-free wadsleyite (a) and Fe-bearing wadsleyite (b) crystals.

f. *Pressure dependence of oxygen self-diffusion coefficient in forsterite (H. Fei, M. Wiedenbeck/Potsdam, N. Sakamoto/Hokkaido, H. Yurimoto/Hokkaido, T. Yoshino/Misasa, D. Yamazaki/Misasa and T. Katsura)*

Atomic diffusion controls the kinetic processes of minerals, such as grain growth, solid-state reaction, electrical conductivity, and creep. Olivine is thought to contribute 60 % in volume of the Earth's upper mantle. Measurement of the diffusion coefficients of elements in olivine is therefore critical to understand the dynamical processes in the Earth's interior. The Mg and Si diffusion coefficients (D_{Mg} and D_{Si}, respectively) have already been systematically measured as functions of pressure, temperature, and water content in both natural olivine and pure forsterite in previous studies. A series of studies about the temperature, water content, and oxygen fugacity dependences have been performed also for O diffusion. However, the pressure dependence, which is essential to investigate the kinetic problems in the Earth's interior because of its ultrahigh-pressure conditions, is still unclear. In this study, we determined the pressure dependence of the oxygen self-diffusion coefficient (D_O) in forsterite.

Dry synthetic forsterite single crystals, after polishing in colloidal silica solution, were deposited with 500 nm ^{18}O enriched Mg_2SiO_4 films annealed at 1600 K at pressures from 1 atm up to 13 GPa using an ambient-pressure furnace and Kawai-type multianvil apparatus. The diffusion profiles were obtained by secondary ion mass spectrometry and the D_O were determined by fitting the profiles to Fick's second law.

As shown in Fig. 3.6-8, D_O systematically increases with increasing pressure from 1 atm to 13 GPa. Namely, in contrast to Si or Mg diffusion, the oxygen diffusion in forsterite has a negative activation volume, which is found to be -3.9±0.4 cm^3 mol^{-1}. In the case of iron-bearing olivine, one study found that D_O at 2 GPa is about one order of magnitude higher than that at ambient pressure. Though they claimed such a difference is caused by water, our previous study found no effect of water on D_O. Therefore, the negative activation volume for D_O could be not only the case for pure forsterite, but also for iron-bearing olivine.

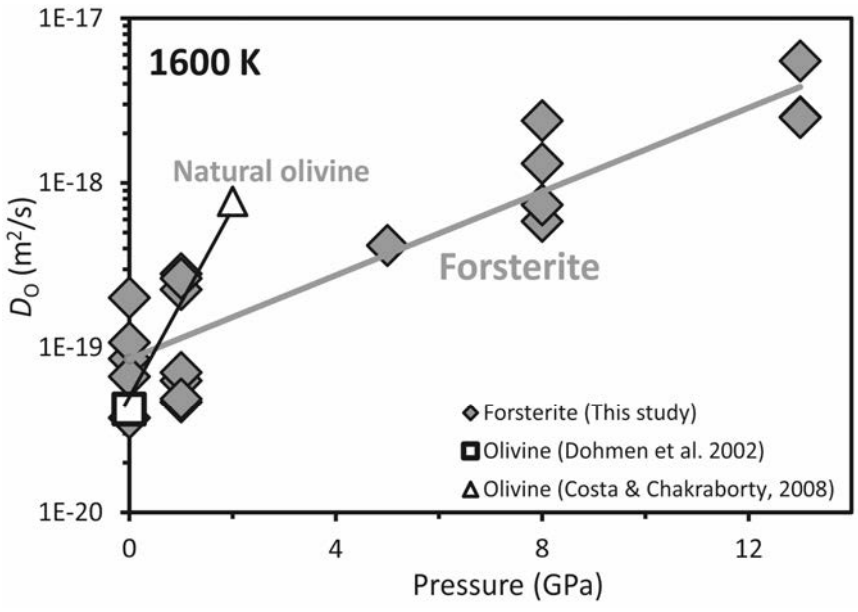

Fig. 3.6-8: Pressure dependence of D_O at 1600 K in forsterite obtained in this study and a comparison with that in natural olivine. The data points given by Costa and Chakraborty (PEPI 166, 11-29, 2008) were obtained in hydrous olivine with 30-50 wt. ppm of water.

Due to the negative and positive activation volumes for O and Mg diffusion, respectively, O becomes the fastest at pressures higher than ~ 10-11 GPa, although Mg is the fastest diffusion species in forsterite under low-pressure conditions (Fig. 3.6-9). Because the ionic conduction is dominated by diffusion of the faster species, the ionic electrical conductivity in the upper mantle will decrease with increasing depth in the asthenosphere down to 350-km depth, and then increase in the deeper part of the upper mantle. This variation with pressure explains the electrical conductivity profile beneath the Canadian Shield (Fig. 3.6-9).

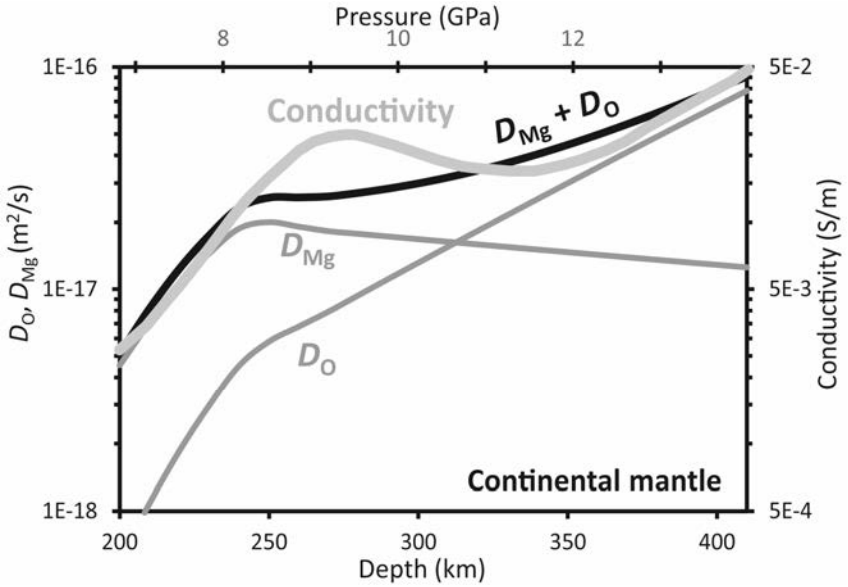

Fig. 3.6-9: $D_{O,}$ D_{Mg} and electrical conductivity in the continental mantle. D_O data is from Fei et al. (JGR 119, 7598-7606, 2014) with activation volume of -3.9 cm^3/mol determined in this study. The conductivity data are from the geophysical observation beneath the Canadian Shield.

g. *Water-content dependence of dislocation mobility of olivine in the[100](010) slip system (S. Blaha and T. Katsura)*

Processes related to viscous flow of solid rocks in the Earth's mantle fundamentally control a large variety of geodynamic processes and hence also on geological processes on the Earth's surface, such as volcanism, earthquakes and continental drift. In the upper mantle, dislocation creep, which is driven by motion of dislocations, is considered to be a dominant creep mechanism. Understanding dislocation mobility is therefore essential to investigate mantle dynamics. Olivine is the most abundant mineral and it is also considered to be the rheologically weakest phase in the upper mantle and should therefore control the rheology. Rheological properties of olivine were studied in numerous deformation experiments. One significant result from deformation experiments is the effect of water on the strain rate: the strain rate of hydrous olivine increases proportional to 1.2 power of water content.

Deformation experiments have certain drawbacks, because they are conducted on small samples (< 1 cm) and applicable time scales (~ 1 day), which are extrapolated by many orders

of magnitudes to correspond to geological processes (10-10^3 km, 10^5-10^6 years). Therefore, the results of deformation experiments should be examined by an independent technique. In this study, the water-content dependence of dislocation mobility in the [100](010) slip system is investigated by means of the dislocation-recovery technique, in which olivine crystals are deformed to form dislocations and then annealed under quasi-hydrostatic conditions.

The samples are hydrated and sheared using water dopant of brucite+talc at 1500 K and 2.75 GPa. Finally, the samples are annealed under the same pressure and temperature conditions as the hydration experiments. Dislocation densities of the samples were obtained by the oxidation decoration technique. The dislocation annihilation rate, k, was obtained from the dislocation densities before and after the annealing and duration of the annealing by the following equation: $1/\rho_{\mathrm{f}} - 1/\rho_{\mathrm{i}} = k\,t$, where ρ_{i} is the dislocation density before the annealing, ρ_{f} the dislocation density after the annealing, and t the duration of the annealing.

Figure 3.6-10 shows the water-content dependence of the annihilation rate for the [100](010) slip system, which is considered proportional to the dislocation mobility in this study. The annihilation rate is found to be proportional to the 1.06 power of water content. This value is in a good agreement to the results of deformation experiments.

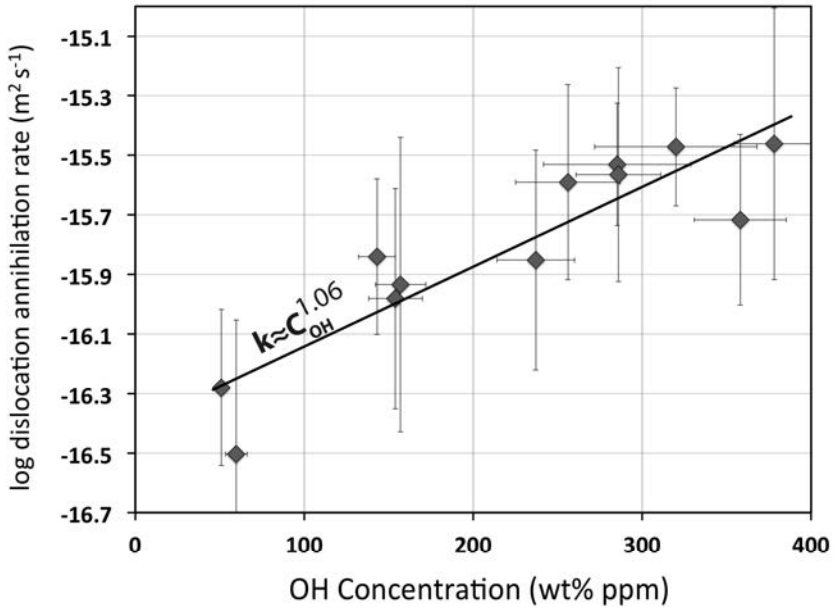

Fig. 3.6-10: Dependence of dislocation mobility on the water content of the [100](010) slip-system in olivine at 2.75 GPa and 1500 K.

It is assumed that dislocation climb is controlled by silicon diffusion. However, the determined correlation between water content and lattice diffusion coefficient of silicon is $D_{\mathrm{Si}} \propto {C_{\mathrm{H2O}}}^{1/3}$.This exponent is significantly lower than the value of deformation experiments which would suggest that the lattice diffusion does not control dislocation climb. Probably a combination of pipe-diffusion and volume diffusion is the controlling mechanism for dislocation creep in olivine.

h. *Dislocation recovery in ringwoodite and bridgmanite (H. Fei, D. Yamazaki/Misasa, T. Katsura, M. Sakurai/Tokyo, N. Miyajima, H. Ohfuji/Ehime and T. Yamamoto/Hiroshima)*

Ringwoodite and bridgmanite are the dominant minerals in the Earth's transition zone and lower mantle, respectively. Knowledge of the rheological properties of ringwoodite and bridgmanite are thus essential to investigate the geodynamical processes in the Earth's interior such as mantle convection, subduction and stagnation of slabs and postglacial rebound. Deformation experiments on minerals are a common way to study mantle rheology. However, such experiments are usually limited within the shallow part of transition zone conditions due to the experimental difficulties. In addition, the stress in deformation experiments is orders of magnitude higher than that in the real mantle, which may cause significant uncertainties when applying to the Earth's interior. Another approach to study mineral rheology is the dislocation recovery experiment, because dislocation creep of minerals is driven by dislocation motion which is related to the dislocation annihilation rate in a recovery process. In this study, we systematically measured the dislocation annihilation rates in ringwoodite and bridgmanite as functions of temperature and water content.

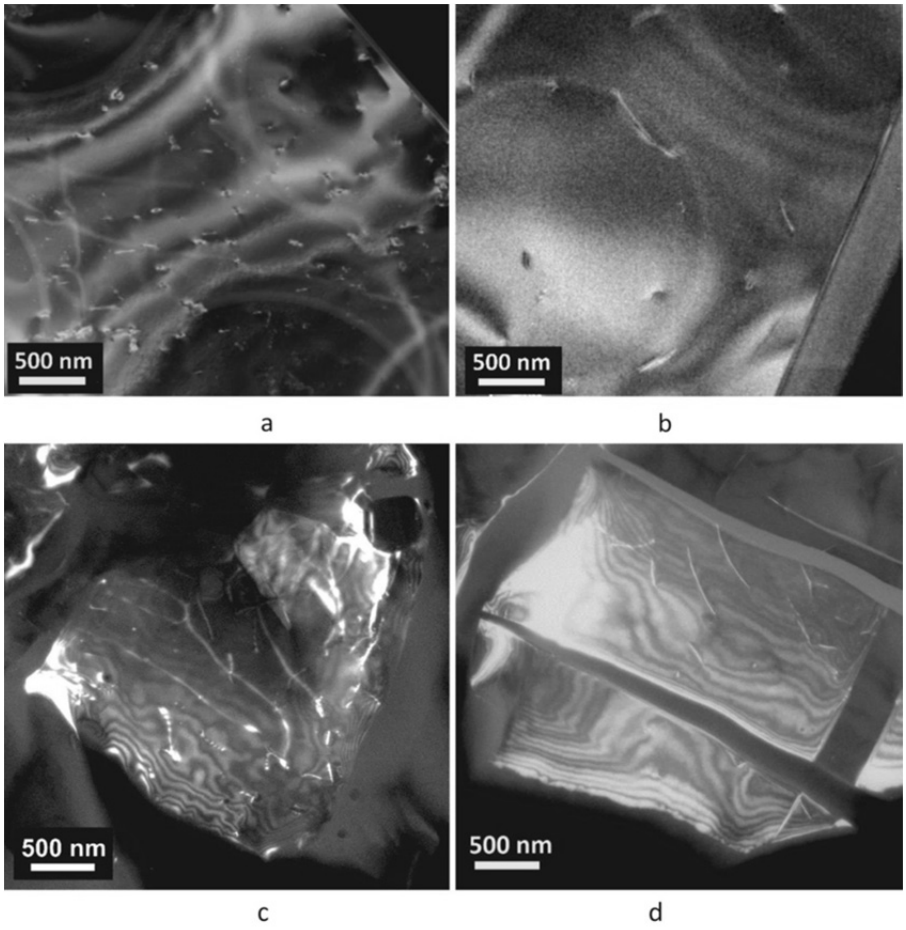

Fig. 3.6-11: Transmission electron microscope images of ringwoodite and bridgmanite before and after dislocation recovery experiments. (a) Ringwoodite before recovery (ρ_i = 11.0 μm^{-2}). (b) Ringwoodite after recovery (2000 K, 12 h, ρ_f = 0.87 μm^{-2}). (c) Bridgmanite before recovery (ρ_i = 8.43 μm^{-2}). (d) Bridgmanite after recovery (1600 K, 24 h, ρ_f = 4.32 μm^{-2}).

Ringwoodite single crystals and bridgmanite aggregates were synthesized at 1800 K, 22 and 25 GPa, respectively, in a Kawai-type multianvil apparatus and deformed by increasing press loads at high temperatures to create dislocations. The synthesized samples were surrounded by CsCl and annealed under quasi-hydrostatic conditions at temperatures of 1600-2200 K and pressures of 22 and 25 GPa for ringwoodite and bridgimanite, respectively. During annealed, dislocation annihilation happened when two dislocations with opposite signs meet and as a result dislocation density decreased. The dislocation densities before and after annealing were measured by transmission electron microscopy (Fig. 3.6-11) and the dislocation annihilation rates were calculated from the dislocation densities and annealing durations. The water contents in the samples were measured by FT-IR spectroscopy.

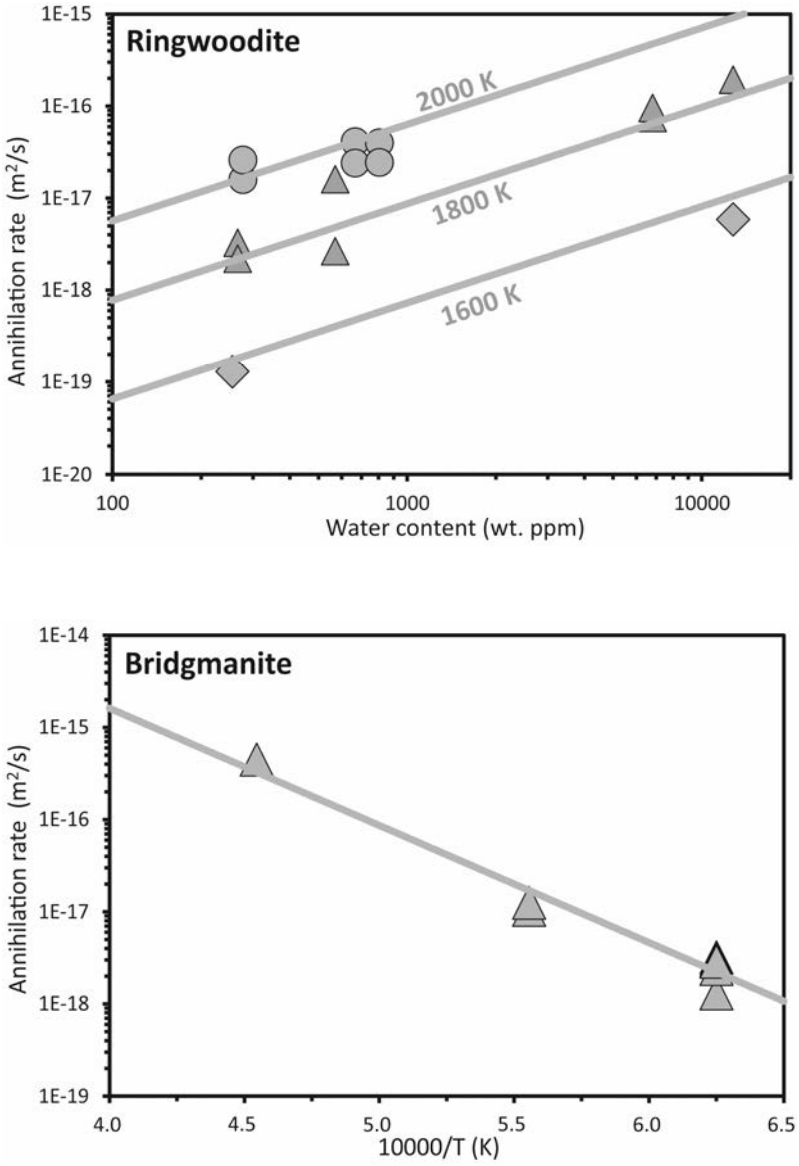

Fig. 3.6-12: Dislocation annihilation rates in ringwoodite and bridgmanite. (top) In ringwoodite as a function of temperature and water content. (bottom) In bridgmanite as a function of temperature.

As shown in Fig. 3.6-12, the dislocation annihilation rate in ringwoodite systematically increases with increasing water content with an exponent of 1.1±0.1. Namely, water has a large effect on dislocation mobility in ringwoodite as well as in olivine. Our results indicate that the dislocation annihilation rate in bridgmanite is much faster than dry ringwoodite, but slower than water-saturated ringwoodite (Fig. 3.6-13). Since the viscosity in the transition zone is lower than that in the lower mantle based on postglacial rebound and gravity observation, the mantle transition zone should be enriched in water.

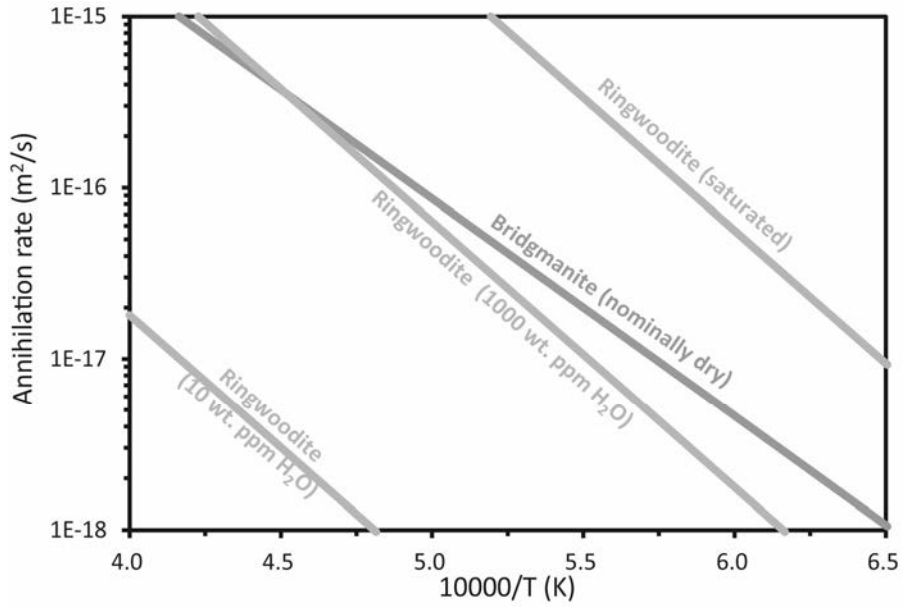

Fig. 3.6-13: A comparison of dislocation annihilation rates in ringwoodite and bridgmanite. The annihilation rate in bridgmanite is faster than that in dry ringwoodite, but slower than that in wet ringwoodite.

i. *Dislocation glide and climb velocity estimation from subgrain boundary formation and dislocation annihilation (L. Wang and T. Katsura)*

Olivine is the most abundant mineral in the upper mantle, and its rheological properties are fundamental to understand mantle dynamics. Dislocation creep, which is driven by the motion of dislocations, is considered as the dominant mechanism for olivine deformation in the upper mantle. Therefore, to understand how dislocations move under different conditions, it is essential to understand olivine rheological behaviour.

Glide and climb are two fundamental motions of dislocations. In olivine, it is usually assumed that the velocity of climb is much slower than that of glide at high temperature, and therefore, the rheology of olivine is controlled by dislocation climb, *i.e.*, diffusion process. However, there is no direct experimental proof to support this assumption because it is difficult to link the macroscopic variables, like stress and strain rate, to microscopic behaviour of dislocation movement in deformation experiments.

In this study, we tried to obtain the temperature dependence of mobility of dislocation glide and climb simultaneously by means of dislocation recovery. In this technique, a pre-deformed sample is annealed at target temperature to decrease its free dislocation density. Such decrease is due to i) forming arrays of dislocations with the same sign caused by dislocation glide and ii) annihilation by two dislocations with opposite signs caused by dislocation climb. Therefore, by measuring the rate of formation of dislocation arrays and of dislocation annihilation, the velocity of dislocation climb and glide can be compared.

Dislocations were introduced by deformation at a pressure of 3 GPa and a temperature of 1600 K under simple shear geometry and then several deformed single crystals with suitable high dislocation densities were recovered. The crystals were ideally oriented for activation of dislocation glide in the [100] direction on the (010) plane. Previous studies demonstrated that dominant dislocations activated in this setting are [100](010) edge dislocations. The deformed crystals were subsequently cut and annealed at temperatures between 1470 and 1770 K at ambient pressure with oxygen partial pressure at the Ni-NiO buffer for certain durations to determine the temperature dependence of the velocity of dislocation glide and climb. We also determined the pressure dependence of these two parameters by annealing samples at pressures of 2, 7 and 12 GPa at a temperature of 1650 K. Dislocations were highlighted using the oxidation-decoration technique reported in the literature. Free dislocation densities before and after annealing were imaged by backscattered electron images (BEI) and counted by Image-J software.

Then the following equations were formulated to express the change in dislocation density by formation of dislocation arrays.

$$\begin{cases} -\dfrac{d\rho_{\mathrm{free}}}{dt} = a{\rho_{\mathrm{free}}}^2 + b\rho_{\mathrm{free}}\rho_{\mathrm{sub}} & (1) \\ \dfrac{d\rho_{\mathrm{ar}}}{dt} = b\rho_{\mathrm{free}}\rho_{\mathrm{sub}} & (2) \end{cases}$$

where ρ_{free} and ρ_{sub} are free dislocation density and dislocation density in dislocation arrays, and a and b are climb and glide constants, respectively. The climb constant (a) is obtained from the areas where no dislocation arrays appear before and after annealing by the solving the equation

$$-\frac{d\rho_{\mathrm{free}}}{dt} = a\,{\rho_{\mathrm{free}}}^2 \qquad (3)$$

The decrease of dislocation density and formation of dislocation arrays can be seen in Fig. 3.6-14. The temperature and pressure dependence of glide and climb constants are shown in Fig. 3.6-15 and Fig. 3.6-16, respectively. We observe that the glide constant is higher than climb constant at high temperature and low pressure. By fitting to the Arrhenius equation, the

activation energies for the glide and climb constant are E_g= 590±90 and E_c = 400±30 kJ mol^{-1}. The activation volume for the two parameters are V_g = 7±2 and V_c = 2.7±0.2 cm^3 mol^{-1}.

The deformation experiments gave high activation energy of ~ 500 kJ mol^{-1}, whereas the Si self-diffusion experiment gave a small one of 400 kJ/mol^{-1}. The deformation experiments gave a higher activation volume than the Si self-diffusion measurement. These facts suggest that the creep in deformation experiments is mainly controlled by dislocation glide. If dislocation creep is controlled by climb motion in the Earth's mantle, the results given by deformation experiments could cause some misinterpretation.

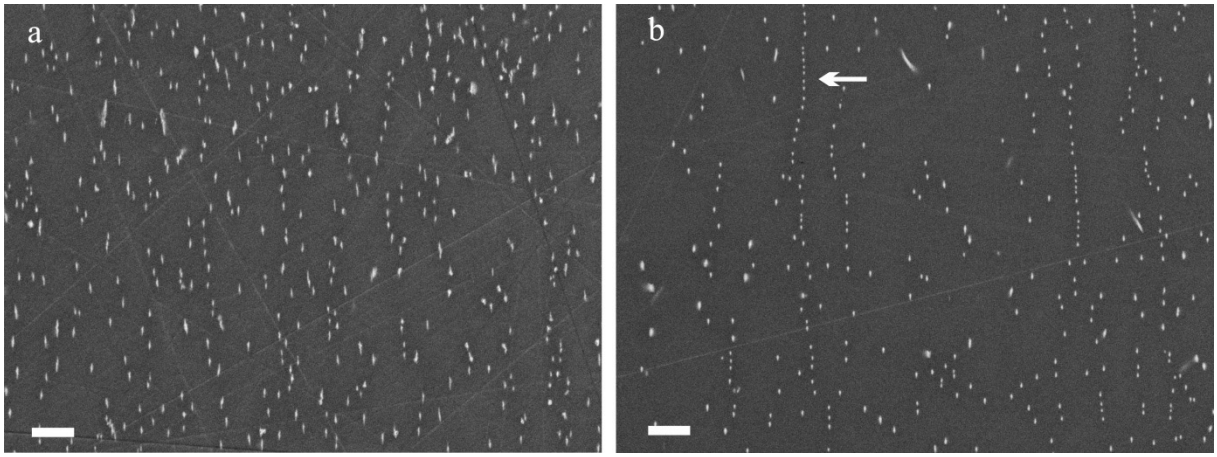

Fig. 3.6-14: Backscattered electron images of the oxidation-decorated olivine. The bright spots are expected to indicate presence of dislocations. The scale bars denote 2 μm. (a) Dislocation structure before annealing. (b) Dislocation structure after annealing. Dislocation density decreased and dislocations formed arrays (indicated by the arrow).

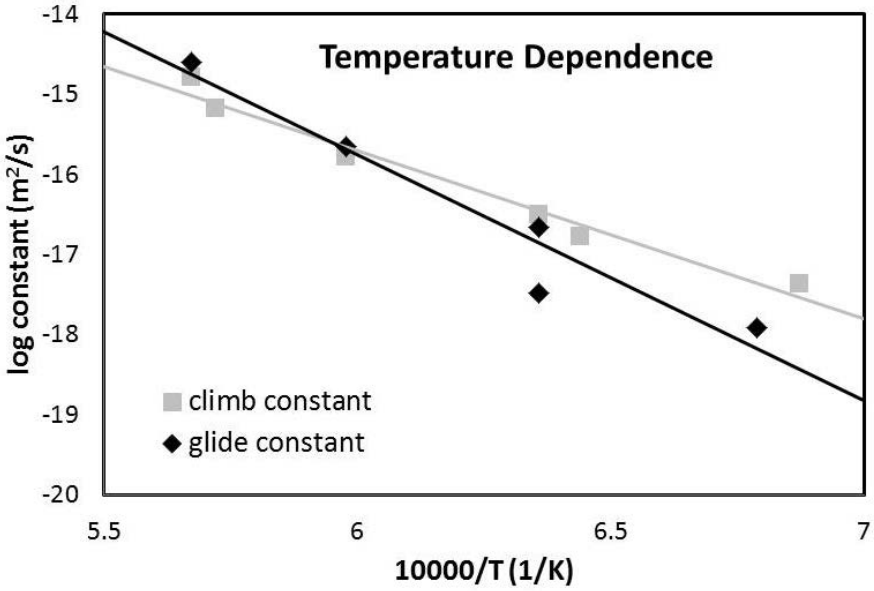

Fig. 3.6-15: Glide and climb constants of [100](010) dislocations versus reciprocal temperature. Dislocation glide has a larger value at high temperature.

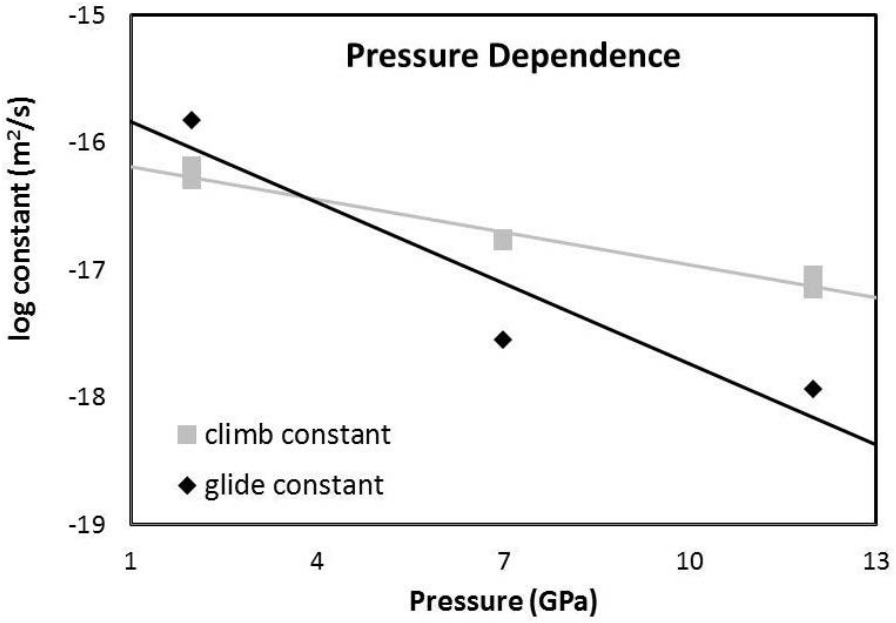

Fig. 3.6-16: Glide and climb constants of [100](010) dislocations versus pressure.

j. *Weak-beam dark-field TEM characterization of dislocations on the (010) plane in simple-shear-deformed wadsleyite (N. Miyajima and T. Kawazoe)*

Enigmatic [001] glide on the (010) plane; *i.e.*, the [001](010) slip system, in deformed wadsleyite has been recently deduced from crystallographic preferred orientation (CPO) patterns obtained by deformation experiments. In the previous studies, wadsleyite aggregate was deformed at pressure-temperature conditions characteristic of the mantle transition zone, and a [001](010)-textured CPO pattern was found from electron backscatter diffraction (EBSD) measurement on recovered samples. However, real activation of the [001](010) slip system has not yet been confirmed clearly by dislocation microstructures in conventional bright-field and dark-field transmission electron microscopy (TEM). Therefore, we re-examined a deformed wadsleyite with the [001](010) fabric by using weak-beam dark-field (WBDF) TEM imaging.

The typical dislocation structures are displayed in Fig. 3.6-17. The long screw segment of [100] dislocations are visible in a WBDF TEM image along the [001] zone axis direction, which is likely to indicate a strong lattice friction along the [100] zone axis and less mobility of the screw segment than the edge one. One of the most important characters to explain the (010)[001] fabric is that a high density of dislocations parallel to both the [101] and [$\bar{1}$01] directions are visible in WBDF images with $\boldsymbol{g}$ = 004 (Fig. 3.6-18), while one of those two dislocations is invisible systematically with $\boldsymbol{g}$ = 404 and $\bar{4}$04, respectively observed along the [010] zone axis. The dislocation lines are also most likely to be on the (010) plane, not on the {101} planes, because of their long projection lengths on the plane and because no oscillation

contrast exists along the lines which indicate that the dislocation lines are not strongly inclined in the [010]-oriented TEM foil (about 200 nm thickness on the middle of the image) but almost parallel to the foil. From the further systematic TEM analysis, we conclude that 1⁄2<101> partial dislocations on the (010) plane are characterized with [100] dislocations on the (001) plane and 1⁄2<111> dislocations forming {011} slip bands. The partial dislocations are extended on the (010) stacking fault as a glide configuration (*i.e.*, Shockley-type stacking faults with 1⁄2<101> displacement vector). The [001] slip on the (010) plane occurs by glide of the dissociated dislocations, which can play an important role in the generation of the CPO patterns reported in water-poor deformation conditions.

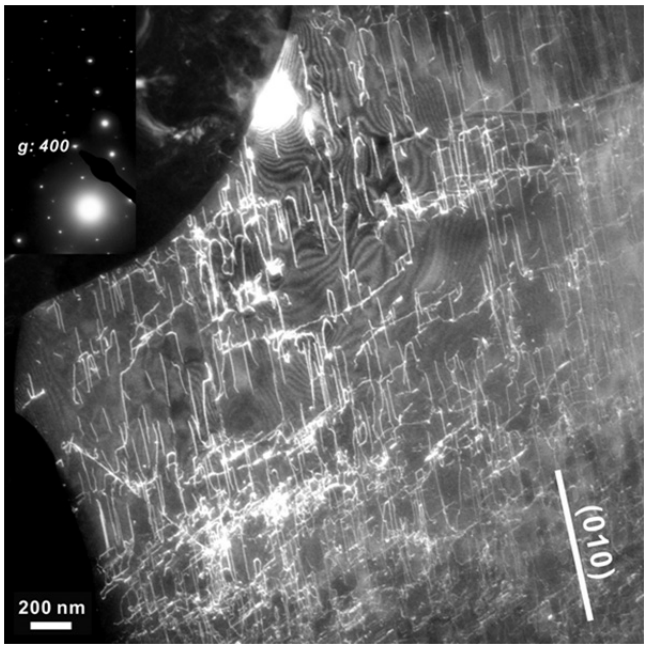

Fig. 3.6-17: A typical dislocation microstructure of the simple-shear deformed wadsleyite. Straight, long screw segments of [100] dislocations and a few of 1/2[111] dislocations are visible. The inset is the selected area electron diffractions pattern indicating the diffraction condition of the WBDF image with $\boldsymbol{g}$ = 400.

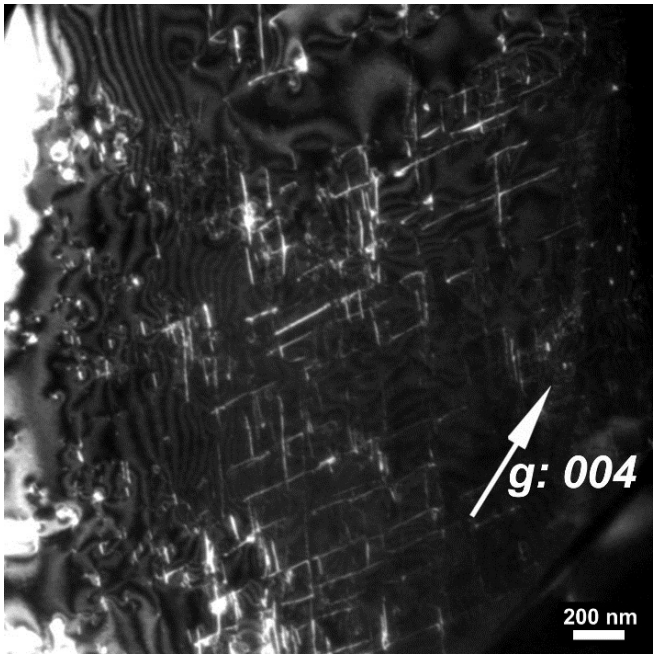

Fig. 3.6-18: The other typical dislocation microstructures of 1/2<101> partial dislocations. The dislocation lines, parallel to both the [101] and [$\bar{1}$01] directions are visible in the WBDF image with $\boldsymbol{g}$ = 004.

k. *Low-temperature plasticity of olivine revisited with* in situ *TEM nanomechanical testing (C. Bollinger, H. Idrissi/Antwerp, F. Boioli/Lyon, D. Schryvers/Antwerp and P. Cordier/Lille)*

The rheology of the lithospheric mantle is fundamental for understanding how mantle convection couples with plate tectonics. There is a growing consensus that the rheology of olivine at low temperatures relevant for the lithospheric mantle cannot be extrapolated from rheological laws established from experiments at high temperature (*ca.* > 1300 K). Deforming olivine in the laboratory becomes extremely difficult when temperatures approach 1000 K. Not only olivine becomes increasingly brittle, but also a steady-state becomes difficult to reach and instabilities often develop. Below 600 K, data are scarce. The earliest studies involved indention experiments, simple to use, but rather difficult to interpret since strain rate, pressure and microstructures are poorly constrained and very heterogeneous.

With high-pressure deformation apparatus like the D-DIA, the ductile field of olivine can be extended by applying larger confining pressures between 4 and 10 GPa, to prevent cracks to open and propagate and to enhance ductility. It appears that, in the low temperature range where dislocation mobility is low, olivine is strongly driven at laboratory strain-rates inducing strain-hardening due to large dislocation densities. Some recent experiments performed in the Griggs apparatus found olivine to be significantly weaker than previously suggested. However, the discrepancy between published studies is large since, for instance, data at room temperature span a 4 GPa wide interval. This suggests that laboratory data obtained at low temperature overestimate the intrinsic rheological properties of olivine and are not suitable for extrapolation to natural conditions.

Here we propose a novel approach to directly measure dislocation mobility in olivine at room temperature. With the advent of nanotechnologies, it has been made possible to investigate the mechanical properties of very small samples, which exhibit very specific properties including a very high toughness. Indeed, the fracture toughness of real olivine is much lower than ideal toughness since it is controlled by the presence of internal flaws. The use of very small samples places very strong geometrical constraints on the size of the defects allowing ductility to be enhanced at low temperature.

We present *in situ* TEM uniaxial tensile experiments performed on a submicron sample of olivine using a single-tilt PicoIndenter from Hysitron Inc (PI 95 TEM) and a special Push-to-Pull (PTP) device dedicated for *in situ* quantified TEM nanotensile tests (Fig. 3.6-19a). The compression (push) of the semi-circular end of the PTP device using the flat punch indenter is converted into a uniaxial tensile loading (pull) on the middle gap of the PTP device. Focused Ion Beamed samples ($4\times1\times0.2$ μm^3 size) from an oriented single crystal of San Carlos olivine were deformed at room conditions. At low temperature, plasticity of olivine is dominated by glide of [001] dislocations in (110) and (100). We have oriented the sample in such a way that the resolved shear stress on the [001](110) slip system is close to maximum (Schmid factor 0.47) and allowing a good visibility on the gliding dislocations. Dislocations are imaged

during the experiment in weak-beam dark-field (WBDF) conditions (Fig. 3.6-19b). Load is raised up on the device to a given value and maintained constant for several minutes before unloading. During the plateau, dislocation motion is observed and characterized under a known and constant applied stress. The sequence is then repeated at a different stress. Dislocations are nucleated on the right side of the sample (Fig. 3.6-19b). The loops expand, pulled by the fast non-screw segments, as the slower screw segment propagates across the sample. We focus here on the measurement of the velocity of the screw segments which control plasticity in bulk olivine.

We used this experimental velocity in a dislocation dynamics model to determine the stress experienced by the dislocations to propose a new rheological law for single crystal olivine deformed in easy slips. It reproduces new evidence of olivine strength at low temperature leading to a description of the lower bound of olivine's rheology at low pressure and temperature conditions.

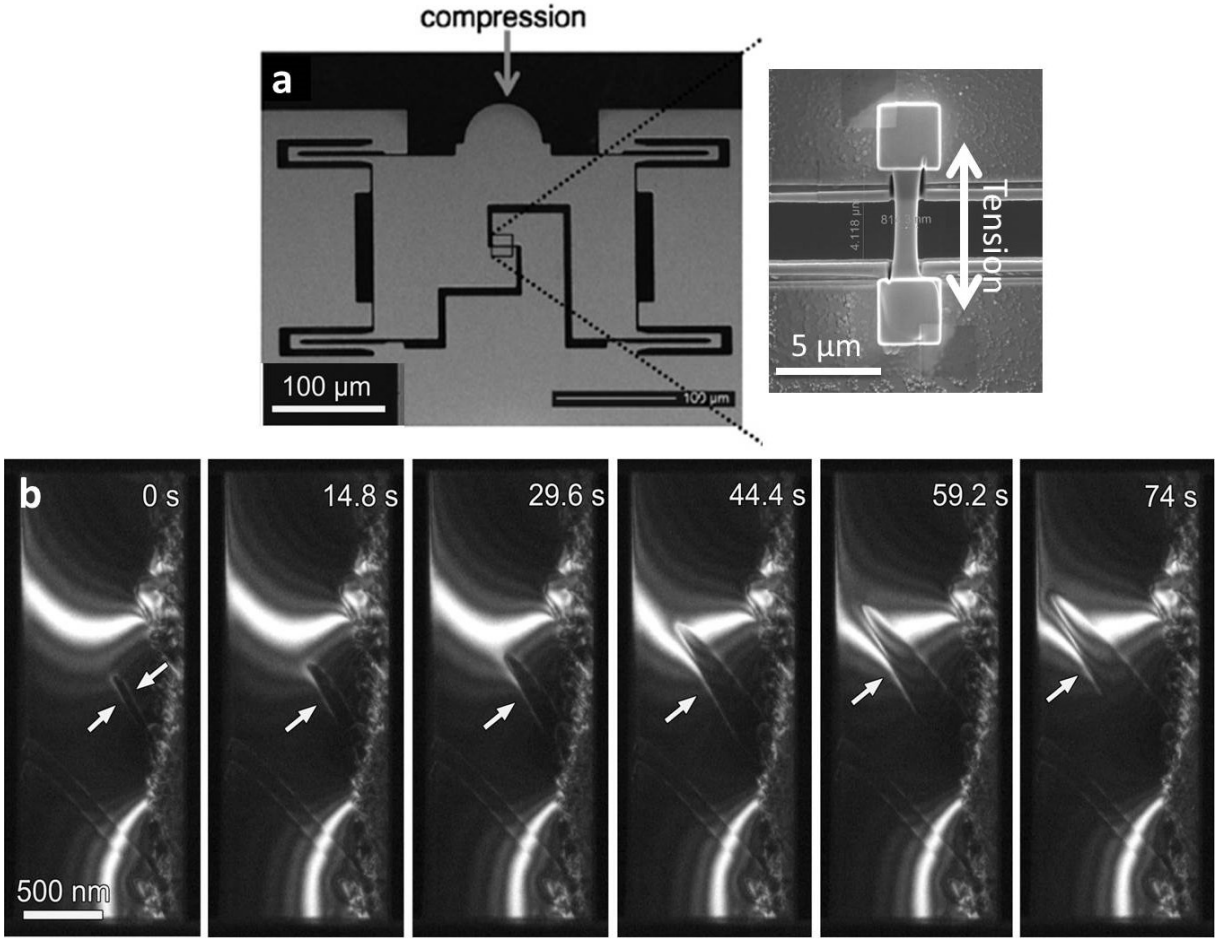

Fig. 3.6-19: (a) Optical image of the PTP device used for *in situ* TEM tensile experiments. (b) Frames captured during the *in situ* deformation of sample under a constant load of 384 µN (resolved shear stress: 0.89 GPa). The loop expands from the scratch and develops allowing propagation the screw segment (arrowed) to be followed across the specimen.

l. *Determining the presence of a Cottrell atmosphere from dislocation recovery experiments (T. Yamamoto and J. Ando/Hiroshima; L. Wang and T. Katsura)*

Dislocations and their associated stress field can interact with the stress field of impurity atoms present in the mineral matrix. This can lead to impurity aggregation at dislocation cores, which is called a "Cottrell atmosphere". The existence of such atmospheres is mainly known for FCC and BCC metals, where they lead to a global hardening and eventually embrittlement during dislocation creep at low strain rate conditions. The Cottrell atmosphere has a strong pinning effect on dislocation glide and prevents dislocation movement so that the plasticity of materials changes. Actually, previous studies and our recent works showed that iron enrichment in the dislocation core of mantle-derived olivine due to the presence of the Cottrell atmosphere is a common phenomenon. Although the presence of a Cottrell atmosphere could in principal affect the rheological properties of olivine, previous studies have been performed at high strain rate condition (10^{-4}~10^{-6} s^{-1}) suggesting that the effect of the Cottrell atmosphere may be difficult to observe. Nevertheless, the study of the effect of low strain rate on olivine plasticity in relation to the Cottrell atmosphere is important to understand the dynamics of the upper mantle and assess the validity of extrapolation from previous deformation experiments under high strain rate condition.

Cubic single crystals of olivine were first deformed in simple shear geometry at a pressure of 3 GPa and a temperature of 1600 K using a multianvil apparatus. Samples were placed in a cell assemblage with the shear direction and plane parallel to the a-axis and on the b-plane in the olivine structure, respectively. This procedure should introduce high-density dislocations in the [100](010) slip system. After the deformation experiment, samples were cut into several pieces and the dislocation density of one of the crystals was measured by means of the etch-pit method and transmission electron microscopy (TEM) observation. Then we tried to enrich dislocations with iron by pipe diffusion. In the first trial, Fe is deposited on the (001) plane, which is normal to the elongation of dislocation, of a forsterite crystal and the crystal was annealed at a temperature of 900 °C and log fO_2, between wustite-magnetite (WM) and iron-wustite (IW) buffers.

Here, we present the preliminary results. Recovered samples from deformation experiments had heterogeneous dislocation microstructures, which are shown in Fig. 3.6-20a. The direction of some long dislocations are subparallel to the [001] axis, while there are a lot of short or point dislocations nearly parallel to the [010] axis. Extinction of long dislocations in the weak-beam dark-field (WBDF) image with $\boldsymbol{g}$ = 002 (Fig. 3.6-20b) suggests that these dislocations probably have a Burgers vector of [100]. On the other hand, short dislocations have strong contrast in this image. This implies that dislocations have a [001] Burgers vector. The averaged dislocation density obtained from etch pit method is about 7.1×10^{-7} cm^{-2}.

SEM and TEM analyses of iron coated forsterite samples showed no iron concentration on dislocations. The cause of the absence of iron concentration by pipe diffusion is considered as follows: (1) short duration of the pipe diffusion experiment, (2) heterogeneity of dislocation

microstructures in deformed samples (the presence of a lot of [010] axis parallel dislocations). We will try to modify the conditions of annealing and deformation experiments.

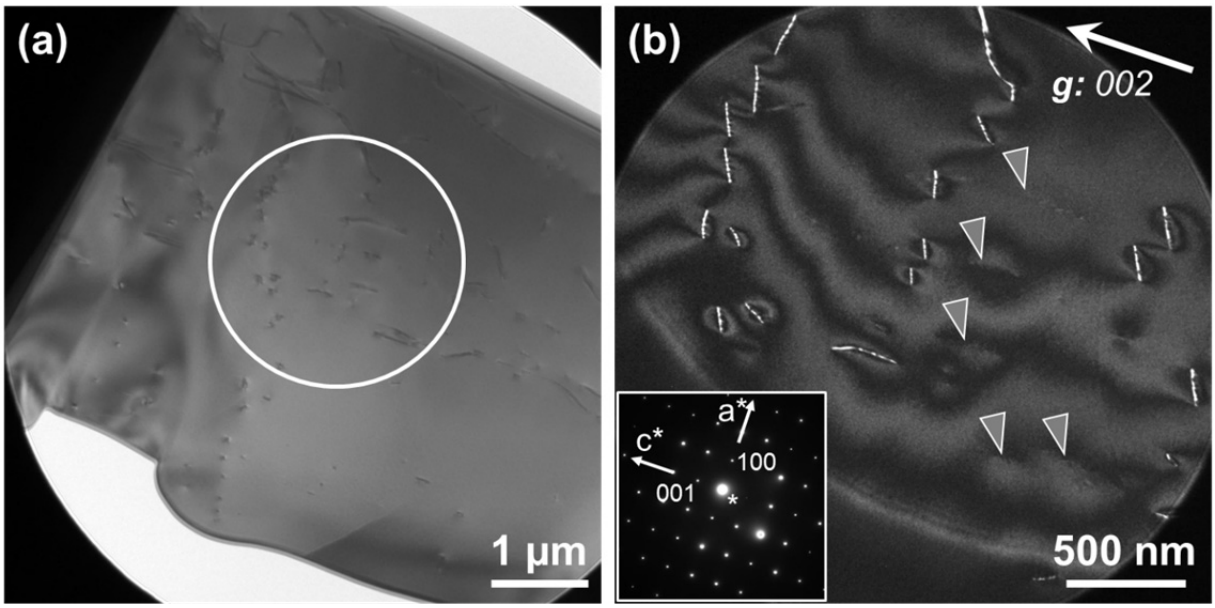

Fig. 3.6-20: (a) Bright field TEM image showing dislocation microstructures of deformed forsterite. The TEM thin foil was made by focused ion beam method. (b) WBDF TEM image corresponding to the white circle portion in (a). Some dislocations (grey allows) become invisible with the diffraction condition of g = 002. Insets are selected electron diffraction showing nearest zone axis in respective imaging condition.

m. *Phase transition processes of olivine in the shocked Martian meteorite Tissint (M. Miyahara/Hiroshima, E. Ohtani/Sendai, A. El Goresy, S. Ozawa/Sendai and Ph. Gillet/ Lausanne)*

The Martian meteorite Tissint is, like the majority of Martian shergottites, heavily shocked and contains numerous round or amoeboid melt-pockets with high-pressure assemblages resulting from the global Martian dynamic event some 190-200 Ma years ago. Tissint contains zoned olivine as phenocrysts; with forsteritic cores and relatively fayalite rich rims. Olivine in and around the melt-pockets transformed into its high-pressure polymorphs ringwoodite and ahrensite (Fe_2SiO_4 end member of ringwoodite). In this study, we clarify the phase transformation mechanisms from forsteritic olivine to ringwoodite and fayalitic end member to ahrensite, respectively. Here we investigated phase transition assemblages in the zoned olivines in the Tissint meteorite using SEM, EPMA, and FIB-TEM in order to unambiguously clarify their nature, spatial distribution in olivine and mechanisms of phase transformations.

FE-SEM investigations revealed distinct spatial localization and texture of the olivine high-pressure polymorphs of ringwoodite and ahrensite. Ahrensite is confined to the original fayalite-rich rims of the olivine phenocrysts. The olivine domains near the melt-pockets are

almost completely replaced by polycrystalline ringwoodite and ahrensite (Fig. 3.6-21a). The lamellar ringwoodite and ahrensite occur in the olivine grains more frequently when located further away from the melt (Fig. 3.6-21b). The lamellae have several sets of crystallographic orientations in the parental olivine. We extracted several TEM slices of the polycrystalline and lamellar textures using a FIB system for TEM observation. TEM images indicate that the polycrystalline domains consist of a fine-grained ringwoodite (or ahrensite) grain (~ 200-300 nm) assemblage (Fig. 3.6-22a). The sets of lamellar ringwoodite domains are also polycrystalline, but individual crystals here have similar crystallographic orientations (Fig. 3.6-22a, 22b). On the other hand, we identified specific crystallographic relations between thin ahrensite lamella (~ 200 nm > width) and olivine; $(001)_{Ol}$ // $\{111\}_{Ahr}$ (Fig. 3.6-22c, 22d).

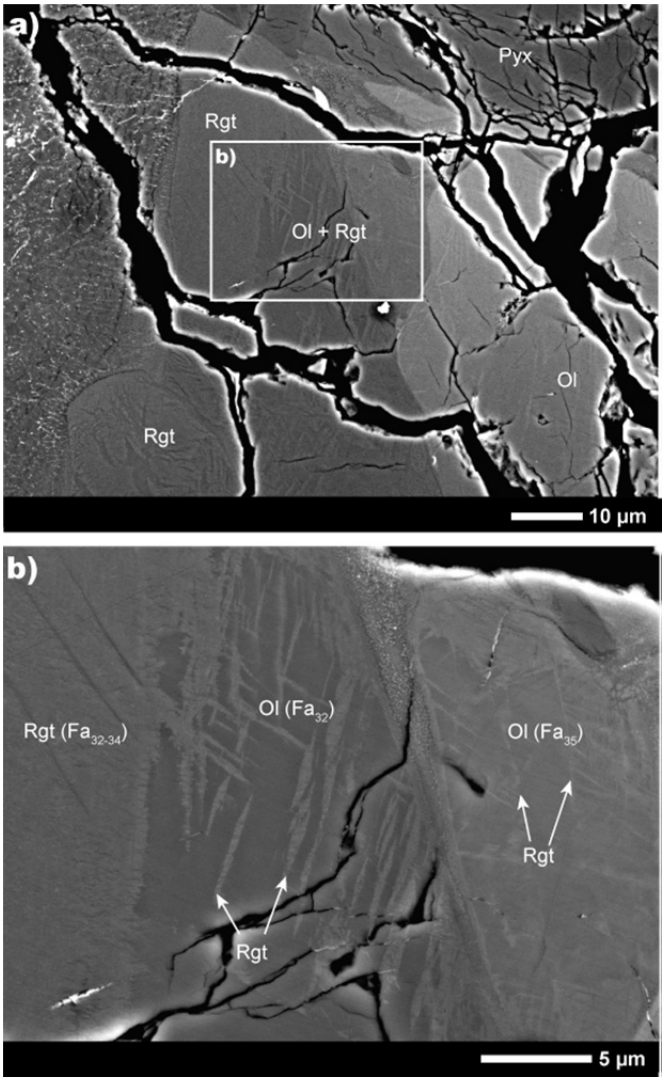

Fig. 3.6-21: Back-scattered electron (BSE) images showing an olivine grain next to a melt-pocket. (a) Olivine completely transforms into ringwoodite around the rim of the melt-pocket. Ringwoodite lamella texture appears in the olivine grain with increasing a distance from the melt-pocket. (b) high-magnification image of the box in (a). Ol: olivine, Rgt: ringwoodite, Pyx: pyroxene, Fa: fayalite component.

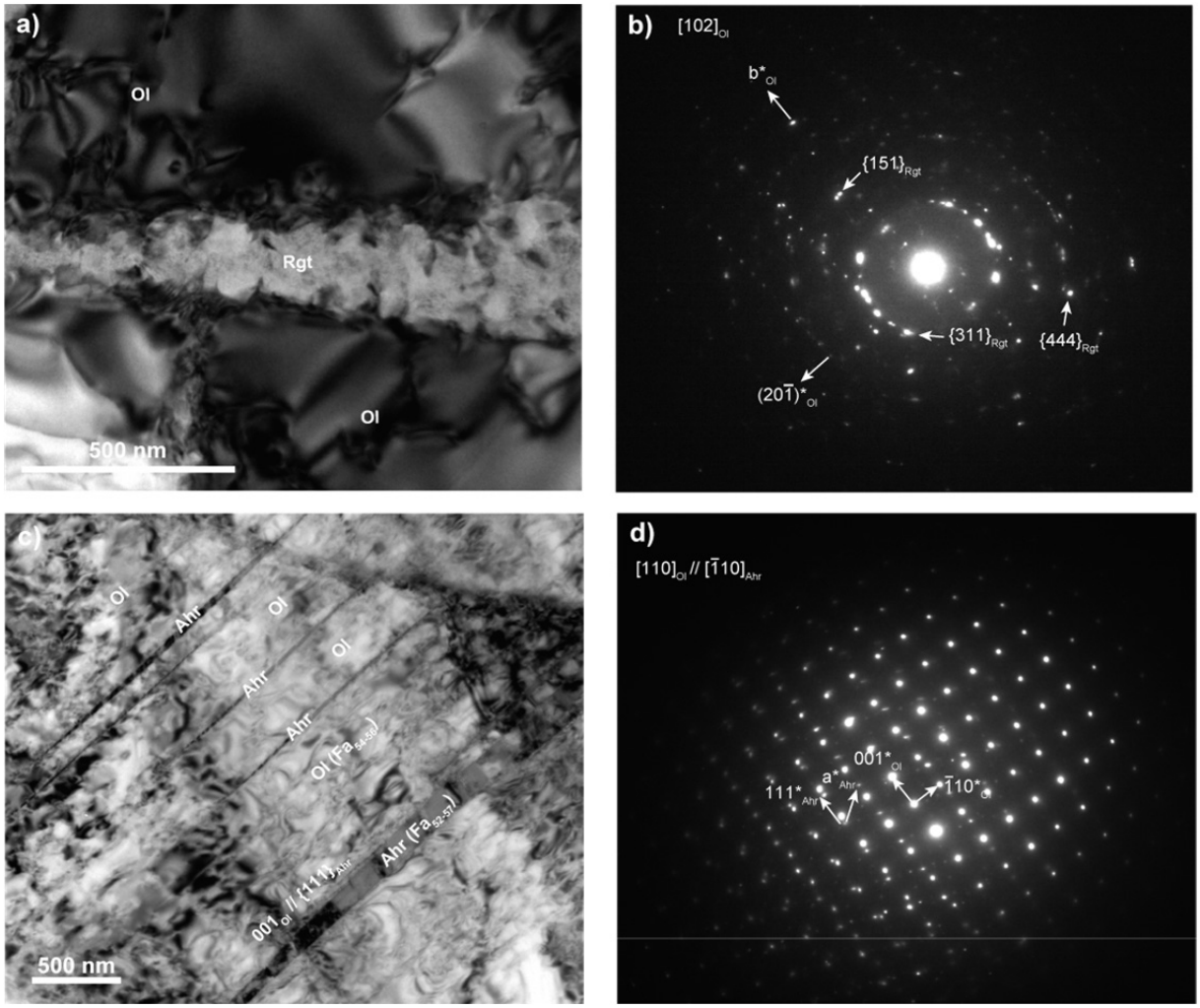

Fig. 3.6-22: TEM images. (a) Ringwoodite lamella evidencing polycrystallinity. (b) Selected area electron diffraction (SAED) patterns corresponding to a). The SAED pattern indicates that the ringwoodite lamella consists of polycrystalline ringwoodite assemblage with similar crystallographic orientations. c) Ahrensite lamellae in an olivine grain. d) SAED patterns corresponding to c). The SAED pattern indicates that a specific crystallographic orientation; 001_{Ol} // $\{111\}_{Ahr}$ occur. Ol: olivine, Rgt: ringwoodite. Fa: fayalite component.

The phase transition mechanism of olivine to ringwoodite and its kinetics have been experimentally investigated through high-pressure and -temperature static experiments. Phase transformation mechanisms obtained in these experiments and the interpretation of TEM observations are as follows. Firstly, stacking faults develop along $(100)_{Ol}$. This is subsequently followed by coherent nucleation and growth of thin ringwoodite platelets of a few atom layers thick at the stacking fault, in which the (111) plane of the ringwoodite platelets are parallel to the (100) plane of parental olivine. This is called a coherent mechanism. Original olivine grains in and around the shock-melt veins in heavily shocked ordinary chondrites transform into wadsleyite, ringwoodite or wadsleyite + ringwoodite assemblage. Two different phase transformation textures from olivine to ringwoodite (or

ahrensite) occur in the olivine grains entrained in or adjacent to the shock-melt veins of heavily shocked ordinary chondrites *i.e.*, a) lamellar ringwoodite texture (more abundant in the originally forsteritic olivine cores) and b) polycrystalline ringwoodite (or ahrensite) assemblage, respectively. Both textural types are observed in the olivine grains adjacent to the melt pocket of Tissint studied here (Fig. 3.6-21, 3.6-22). Ahrensite is more abundant in the fayalitic rims adjacent to the melt pockets or melt veins. Polycrystalline ringwoodite texture is dominant in olivine grains near the melt-pocket, whereas with increasing distance from the melt-pocket, the lamellar texture becomes spatially dominant in the cores of olivine crystals. The phase transformation sequence encountered in Tissint shergottite resembles what was previously reported in heavily shocked L6 ordinary chondrites. Our previous TEM observations of ringwoodite lamellae in the shocked Yamato 791384 L6 ordinary chondrite revealed two subsequent steps, namely coherent phase transformation followed by the incoherent formation process more dominant in the forsteritic olivine cores. However, in most natural findings, ringwoodite formation appears to occur without the initial coherent ringwoodite formation process and could evolve planar fractures induced by shear stress.

3.7 Materials Science

For decades, the driving force behind methodological developments in the field of high-pressure studies (both theoretical and experimental) has been the interest in exploring material properties for applications in Earth and planetary sciences. Novel techniques developed in such a context, however, attract increasing interest in material sciences in two directions: enhanced atomic interaction are of interest in exploring fundamental property changes, and high-pressure routes for synthesis are examined and increasingly used. In order to advance science in both directions, analytical techniques need to be sufficiently sophisticated. One recent revolutionary breakthrough has been in single crystal X-ray diffraction at high pressure, with an increase of accessible range from ~15 GPa to over 150 GPa, with important contributions by scientists at the Bayerisches Geoinstitut. Now the novel technology is applied to address important materials science problems: all experimental reports in this section present results of high-pressure single crystal diffraction studies of various classes of solids – elements, oxides, metal-organic frameworks.

Despite a long history of intensive investigations boron compounds – including elemental boron and transition metal borides – they remain at the focus of scientific activity due to their diverse and unique physical properties and potential technological applicability (extreme hardness, high stability, chemical inertness). Experiments on elemental boron and cobalt boride presented here reveal their low compressibility and shed light on mechanisms controlling the hardness of these materials.

Scandia, Sc_2O_3, has the widest band gap among the transition metal oxides. It is commonly used in industry, particularly for manufacturing high-intensity light sources, in composite ceramics and for different optical coatings. So far, information about its high pressure behaviour - based on powder diffraction data – was highly controversial. Single crystal X-ray diffraction and Raman spectroscopy experiments clarify the sequence of phase transformations in Sc_2O_3, as described in the third contribution to the section.

The crystal-chemistry of phosphates at high pressure is interesting in both materials and mineral physics, where there is a tradition of using them as silicate analogues. Experiments on $TiPO_4$ at relatively moderate pressures (up to 55 GPa) are presented in the fourth contribution to the section. Sinlge crystal X-ray diffraction data are used to resolve four new high-pressure polymorphs of $TiPO_4$ and reveal unusual five-fold coordinated phosphorus in one polymorph.

Dense metal-organic frameworks (MOFs) show promise for a new generation of multi-ferroic materials, which have technological importance in sophisticated multi-state devices. The effect of stress/pressure on MOFs is yet to be explored, but first reports of combined single crystal diffraction and Raman spectroscopy already show that different metal centers yield different phase transition pressures.

The final contribution in this section, by contrast, presents computational methods to look at the localization of charge in excited states of quasi-one-dimensional organic molecules. In addition to well-known mechanisms like polarons or solitons it is described here that charge added to a neutral molecule can localize spontaneously if the length of the polymer exceeds a critical value.

a. *High-pressure investigation of α-boron single crystals (I. Chuvashova, N.A. Dubrovinskaia, E. Bykova, M. Bykov and L.S. Dubrovinsky)*

Despite the centuries of application and decades of intensive studies of boron compounds, including elemental boron, they still remain at the focus of wide scientific interest due to their diverse and unique physical properties (pressure induced metallization and superconductivity, formation of unusual chemical bonds) and potential technological applications due to extreme hardness, as well as chemical stability and inertness. These properties are important for technological applications in nuclear engineering, armor ceramics, abrasives, semiconductor and thermoelectric industries.

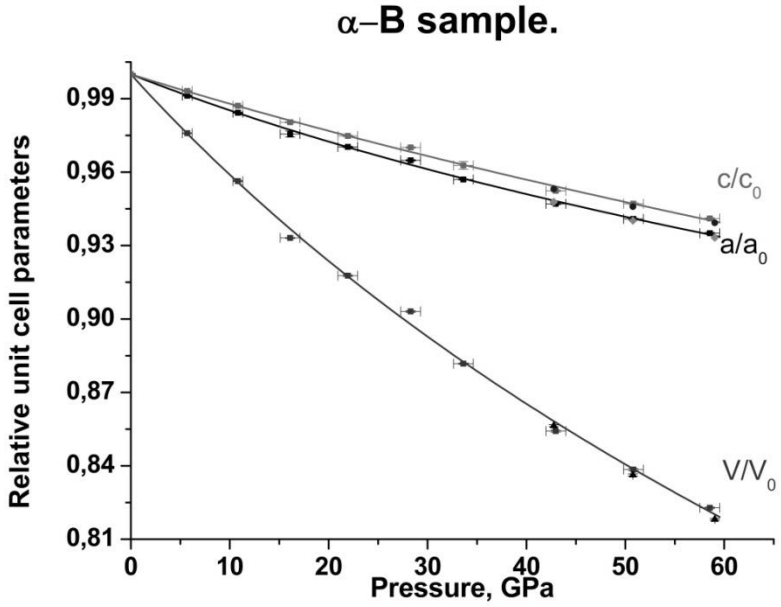

Fig. 3.7-1: Axial compressibility of α-B based on high-pressure single-crystal XRD data. The compressibility of the structure is almost the same along the *a*-direction and *c*-direction. Continuous lines show the fit of the pressure-volume data with the third-order Birch-Murnaghan equation of state. Three points at high pressure represent the data for the second crystal.

The principal building block of α-boron is a B_{12} icosahedron, which is held together within the same close-packing layer by electron deficient B-B bonds of three-center nature and between the layers by two-center bonds. Experimentally, the structure and vibrational

properties of α-B at high pressures were studied by X-ray diffraction and Raman spectroscopy up to 100 GPa and 30 GPa, respectively. There was no sign of an approaching phase transition, in good agreement with calculations. Here we report the results of investigations of the high-pressure behaviour of α-B by means of single crystal X-ray diffraction up to 60 GPa, and its vibrational properties by means of Raman spectroscopy up to 160 GPa, and IR spectroscopy up to 53 GPa.

Experiments were performed using α-B crystals synthesized at high-pressure high-temperature conditions. The crystals were placed in BX90-type diamond anvil cells with diamonds with the culet diameters of 120 and 250 μm and neon as a pressure-transmitting medium. Structure refinement of single-crystal X-ray diffraction data collected at ID27, ESRF revealed no sign of an approaching phase transition up to 60 GPa (Fig. 3.7-1) which is in good agreement with calculations. The similarity of compressibility of α-B and β-B, γ-B indicates that the structural differences boron allotropes have a minor effect on it.

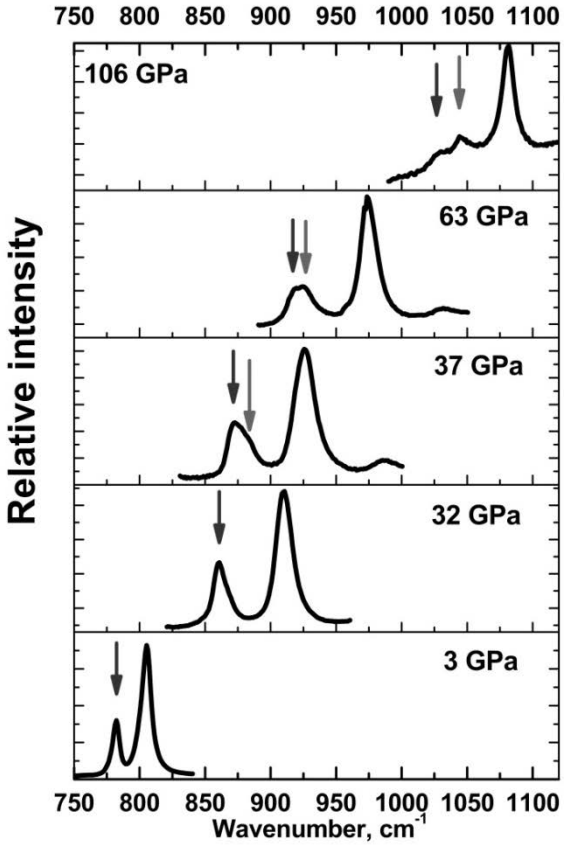

Fig. 3.7-2: Raman spectra of α-B collected at different pressures. The arrow(s) mark the E_g mode which splits at ~ 38 GPa.

The Raman spectra were collected "in-house". Two experiments were performed at room temperature: In the first experiment a monotonous shift of the Raman peak positions of α-B toward higher wavenumbers is observed up to 160 GPa. At ~ 38 GPa the splitting of the E_g mode at 865 cm^{-1} occurs, with a shoulder on the E_g mode (Fig. 3.7-2). In order to check whether splitting of the mode is related to the stress in the sample, an additional experiment

was carried out. On a thinner crystal we observed no splitting. Therefore, the shoulder on the E_g mode at ~ 38 GPa are most likely related to the stress state of the material rather than to phase transition.

b. *Crystal structure and compressibility of novel Co_5B_{16} studied on a single crystal sample (E. Bykova, M. Bykov, H. Gou, N.A. Dubrovinskaia and L.S. Dubrovinsky; M. Hanfland/ Grenoble)*

Transition-metal borides are interesting in both fundamental and applied aspects. Their high hardness related to the rigid boron network can be superimposed on interesting magnetic and electronic properties driven by the transition-metal atom. For example, non-magnetic FeB_4, first synthesized by our group, combines superhardness and superconductivity. However, it is metastable and can be prepared under high pressure only. Cobalt borides share many similarities with the Fe-B compounds but remarkably, no cobalt borides with a Co:B ratio below 1:1 have been reported.

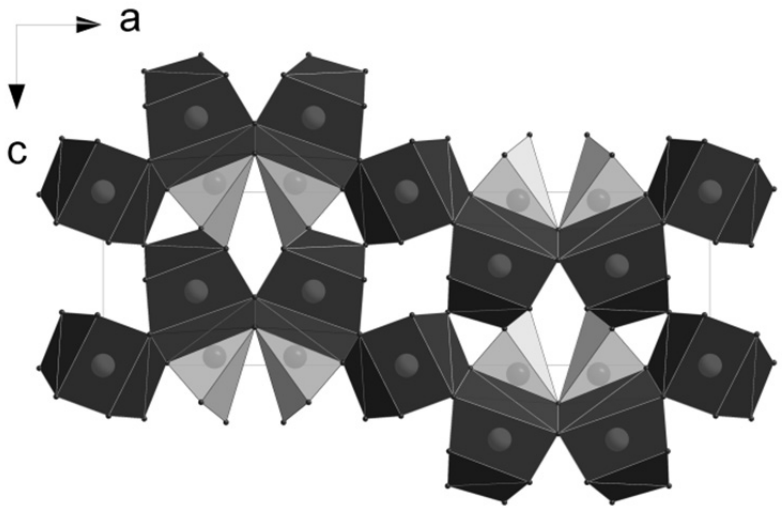

Fig. 3.7-3: A polyhedral model of the crystal structure of Co_5B_{16}. Big spheres represent cobalt atoms and small ones are boron atoms. The crystal structure consists of CoB12 (dark) and CoB9 (light) polyhedra packed in columns along the *b*-axis by sharing common faces.

We conducted a series of experiments aimed at syntheses of new boron-rich cobalt borides using the 1000-ton (Hymag) hydraulic press installed at Bayerisches Geoinstitut. At the pressure of 15 GPa and the temperature of 1873-1573 K a novel phase was observed. Single-crystal X-ray diffraction revealed unusual chemical composition of the novel boride, namely Co_5B_{16} and unique orthorhombic structure (space group *Pmma*, a = 19.1736(12), b = 2.9329(1), and c = 5.4886(2) Å, Fig. 3.7-3). Similar to other boron-rich metal borides like MB_4 (M = Cr, Fe, Mn) and Fe_2B_7, crystal structure of Co_5B_{16} is based on a rigid network of

boron atoms with straight, channel-like voids along the *b*-axis. Cobalt atoms occupy these voids creating infinite rows. Metal-metal distances in the rows are all equal, but they are larger than the sum of metallic radii of Co atoms. The B–B distances in the structure of Co_5B_{16} vary from 1.654(7) to 1.908(7) Å. The shortest bond located at the *ac* plane has the smallest value of the B–B bond length among transition metal borides with related structures. Dense atomic packing and short B–B contacts make Co_5B_{16} rather hard with the measured Vickers hardness H_v = 30±2 GPa, the value slightly higher than reported for CrB_4, but lower than that of superhard FeB_4.

A single crystal of Co_5B_{16} was used to study the compressibility up to 50 GPa. Figure 3.7-4a shows the pressure dependence of the unit cell volume of Co_5B_{16} and corresponding fit with the 3rd order Birch-Murnaghan equation of state. Co_5B_{16} has rather high bulk modulus of 250(2) GPa being comparable with Fe_2B_7 and superhard FeB_4. But unlike Fe_2B_7 and FeB_4 in which one crystallographic direction has been shown to be extremely incompressible (like diamond), Co_5B_{16} demonstrates almost no anisotropy in the axial compressibility (Fig. 3.7-4b). The latter is most probably due to the differences between the crystal structures which have a strong influence on the mechanism of the compression.

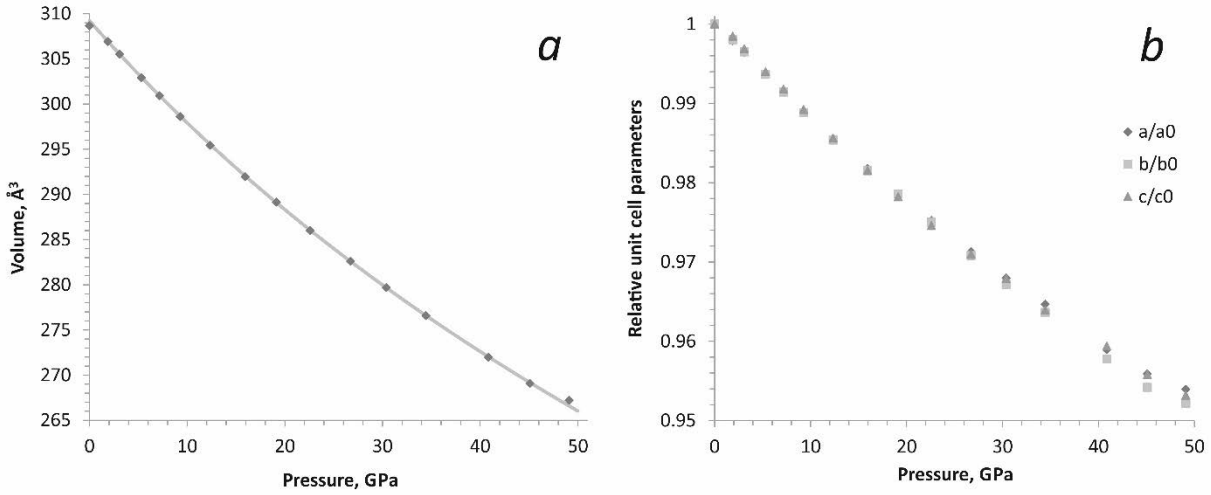

Fig. 3.7-4: Bulk (*a*) and axial (*b*) compressibility of Co_5B_{16} based on high-pressure synchrotron single-crystal X-ray diffraction data. Solid line on the left figure shows fit of the experimental data with the 3rd order Birch-Murnaghan equation of state. The unit cell parameters of Co_5B_{16} change almost uniformly unlike to Fe_2B_7 and FeB_4.

c. *Vibrational and structural properties of Scandia, Sc_2O_3 under high pressure (S.V. Ovsyannikov, E. Bykova, M. Bykov, M.D. Wenz, A.S. Pakhomova and L.S. Dubrovinsky; K. Glazyrin and H.-P. Liermann/Hamburg)*

Scandia, Sc_2O_3, is a transition metal oxide with the simplest electronic configuration of the cation ([Ar]$4s^2 3d^1$) and the widest band gap among the transition metal oxides E_g ~6 eV. It is

commonly used in industry, *e.g.*, in high-intensity light sources, different composite ceramics and for different optical coatings. Contrary to sesquioxides of its nearest neighbors in the Periodic Table (Ti, V, and Cr) that adopt a corundum-type structure at ambient conditions, scandia crystallizes in a cubic bixbyite-type structure. This structure is typical for sesquioxides of rare-earth metals, including yttrium and a whole series of the lanthanides. This circumstance would suggest that the high-pressure behaviour of scandia may be rather similar to those of lanthanide sesquioxides. Previous high-pressure powder X-ray diffraction studies of Sc_2O_3 found that its cubic bixbyite-structured phase (a so-called 'C-Res' phase) transforms to a 'B-Res' phase (monoclinic, space group *C2/m*) above 36 GPa at ambient temperature. At elevated temperature (1600 K) the C-Res → B-Res transition occurred at ~ 10 GPa, and upon further heating to 2000 K resulted in a transition to a very dense α–Ga_2S_3-type phase at 19 GPa (space group *Pnma*).

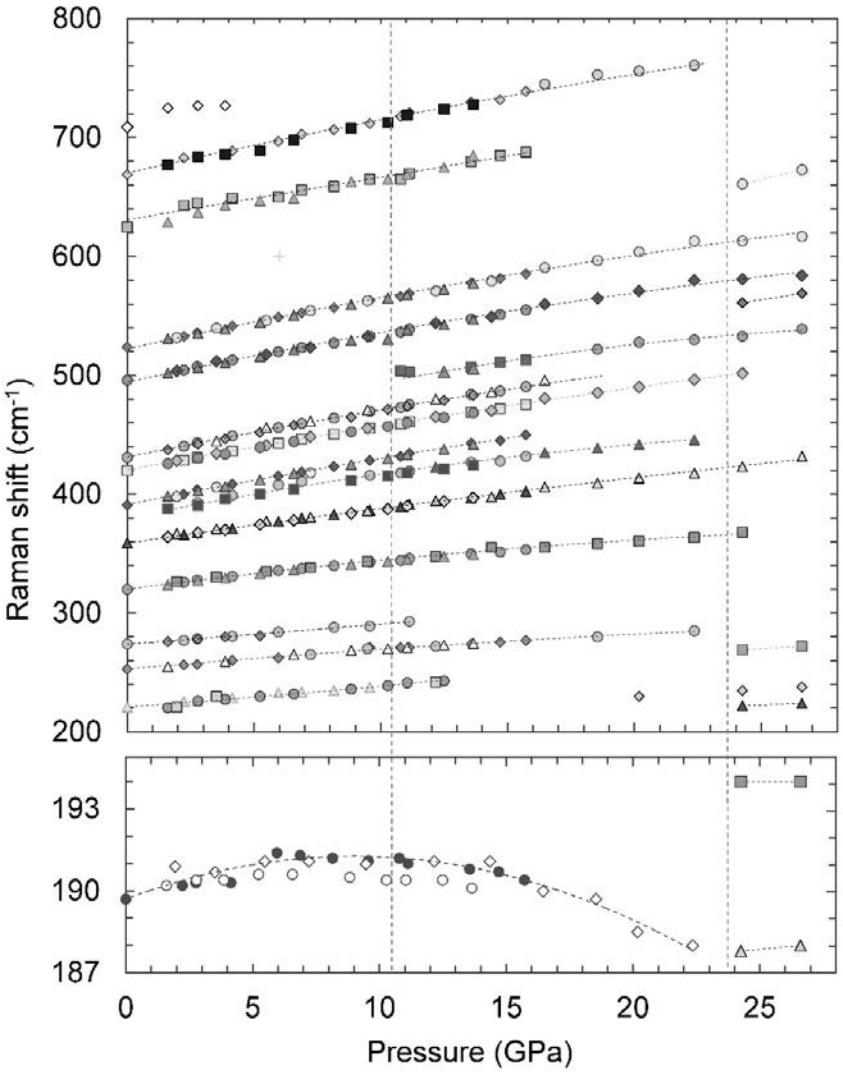

Fig. 3.7-5: Pressure evolution of the phonon frequencies of Sc_2O_3 at 295 K. Different symbols correspond to different experimental runs. The vertical dashed lines indicate the occurrence of a new Raman peak (~ 500 cm^{-1}) above 10 GPa and the onset of the phase transition from the C-Res to the B-Res phase at ~ 24 GPa.

In the present work we have synthesized single-crystalline samples of Sc_2O_3 from commercial Sc_2O_3 powder (ChemPur, 99.99 % of purity) at high-pressure high-temperature conditions (HP-HT) using a 1200-tonne multianvil press at Bayerisches Geoinstitut, and investigated its vibrational and structural properties to 55 GPa. For the structural and spectroscopic investigations we employed BX90 diamond anvil cells equipped with Boehler-Almax-designed and normal-cut diamonds (250 μm culet size) and a rhenium gaskets. In all experiments we used neon pressure-transmitting medium. The Raman spectra were excited with the red 632.8 nm line of a He-Ne laser and were recorded using a LabRam spectrometer in back-scattering geometry. The high-pressure single-crystal X-ray diffraction studies were carried out at the Extreme Conditions Beamline P02.2 of PETRA III (DESY, Hamburg) using a wavelength of 0.28995 Å.

According to an irreducible representations of phonon modes at the Γ-point ($\Gamma = 4A_g + 5A_u + 4E_g + 5E_u + 14F_g + 17F_u$), Sc_2O_3 with the cubic bixbyite structure should have 22 Raman-active modes ($4A_g + 4E_g + 14F_g$). Experimentally, in unpolarized Raman spectra we could detect only 14 modes. With pressure increase the positions of the Raman peaks shifted to higher frequencies (Figs. 3.7-5), which is related to a volume contraction and shortening of the bond lengths. We noticed that hydrostatic pressure made one more mode observable between those at 359 and 391 cm^{-1} at ~ 2 GPa. A single crystal X-ray diffraction study revealed that a transition to the B-Res phase happened around 28 GPa (Fig. 3.7-6) and was accompanied by dramatic changes in the Raman spectra around 26 GPa (Fig. 3.7-5). At 24.3 GPa we detected the beginning of strong alteration of the Raman spectra that was completed to 26.6 GPa (Fig. 3.7-5). The monoclinic B-Res phase was expected to have 21 Raman-active phonon modes ($14A_g + 7B_g$), but in our spectra we could detect only 14 peaks (Fig. 3.7-5).

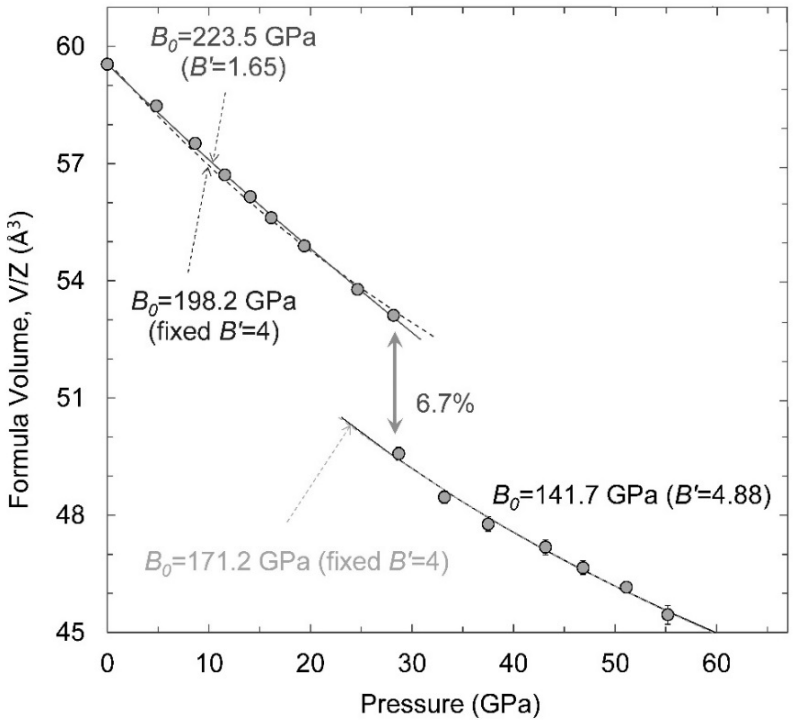

Fig. 3.7-6: Pressure-induced changes in volume of the original cubic-bixbyite and monoclinic high-pressure phases of Sc_2O_3. A volume collapse of 6.7 % on the phase transition near 28 GPa is indicated.

Hydrostatic compression of a single crystal of cubic-bixbyite phase of Sc_2O_3 led to very uniform and monotonous shrinkage in the lattice parameter, average Sc1-O and Sc2-O distances, and ScO_6 octahedra. Fitting a third-order Birch-Murnaghan equation of state to the *V-P* data for the bixbyite Sc_2O_3 resulted in the following fit parameters: V_0/Z = 59.62(6) Å^3/formula unit (p.f.u.), a bulk modulus of B_0 = 198.2(3) GPa for fixed B' = 4, and B_0 = 223.5(0) GPa at B' = 1.6(5) for a three parameter description(Fig. 3.7-6). A single crystal diffraction pattern collected at about 28 GPa corresponded to the B-res. The phase transition was accompanied by a volume reduction of ~ 6.7 % (Fig. 3.7-6). In our single-crystal study we unambiguously confirmed the monoclinic *C2/m* symmetry of this phase for the whole pressure range investigated (28-55 GPa). For instance, at 28.7 GPa the unit cell parameters were found to be as follows: a = 12.5595(3) Å, b = 3.0915(1) Å, c = 7.7720(3) Å, β = 99.68(8)°, V/Z = 49.58(1) Å^3 p.f.u. (Z = 6). Using the Birch-Murnaghan equation of state we found the following fit parameters for the B-Res phase: V_0 /Z = 56.23 Å^3 p.f.u., B_0 = 171.2(1) GPa at fixed B' = 4, V_0 /Z = 57.00 Å^3 p.f.u., B_0 = 141.6(6) GPa for variable B' = 4.8(8) (Fig. 3.7-6). Thus, we found that the monoclinic phase of Sc_2O_3 is apparently more compressible than the cubic bixbyite, with a decrease of 13.6 % in the bulk modulus (using the fixed B' = 4 values) (Fig. 3.7-6).

A decrease of bulk modulus value in a pressure-induced phase transition is not a commonly observed phenomenon. Usually, this is due to profound changes in chemical bonding in a substance that drastically affect its elastic properties: for instance, metallization without structural phase transition, a structural transition that can drastically change the balance between different types of chemical bonding (*e.g.*, partly ionic and partly covalent), or a magnetic phase transition. In the case of Sc_2O_3 insulator, the decrease in the bulk modulus value upon the C-Res to the B-Res transition can not be explained by any of the above-mentioned reasons: the sample remained transparent and colorless suggesting the persistence of a wide band gap. Previous works on powders of lanthanide sesquioxides reported very similar changes in the bulk modulus values of the C-Res and B-Res phases, *e.g.*, in Sm_2O_3, Dy_2O_3, Ho_2O_3, and Lu_2O_3. For the original cubic bixbyite phase we found an abnormally low value of B' = 1.6(5). Some previous works also reported rather unusual B' values for the C-Res, B-Res, and A-Res phases of these lanthanide oxides. Thus, such behaviour may be rather general for many oxides of this group, suggesting a new structural paradox.

d. *High-pressure phase transformations in $TiPO_4$: A route to a pentacoordinate phosphorus (M. Bykov, E. Bykova, L.S. Dubrovinsky, S. van Smaalen/Bayreuth, M. Hanfland/Grenoble, H.-P. Liermann/Hamburg and K. Yusenko/Swansea)*

It is well-known that with increasing pressure the coordination number of cations increases. One of the most notable examples is SiO_2 in which the Si coordination changes from four in the quartz structure to six in the stishovite structure. A link between fourfold and sixfold coordinated silicon, *e.g.*, through fivefold coordinated Si, was found in silica glass under compression and in some silicate minerals. For phosphorus only recently the first example of six-coordinated phosphorus has been found in $AlPO_4$ above 46 GPa, while there are no

examples of phosphorus atoms coordinated by five oxygen atoms in inorganic network structures. Here we report four new high-pressure polymorphs of $TiPO_4$, determined by single-crystal X-ray diffraction in a diamond anvil cell using synchrotron radiation. One of these high-pressure polymorphs contains pentacoordinated phosphorus atoms.

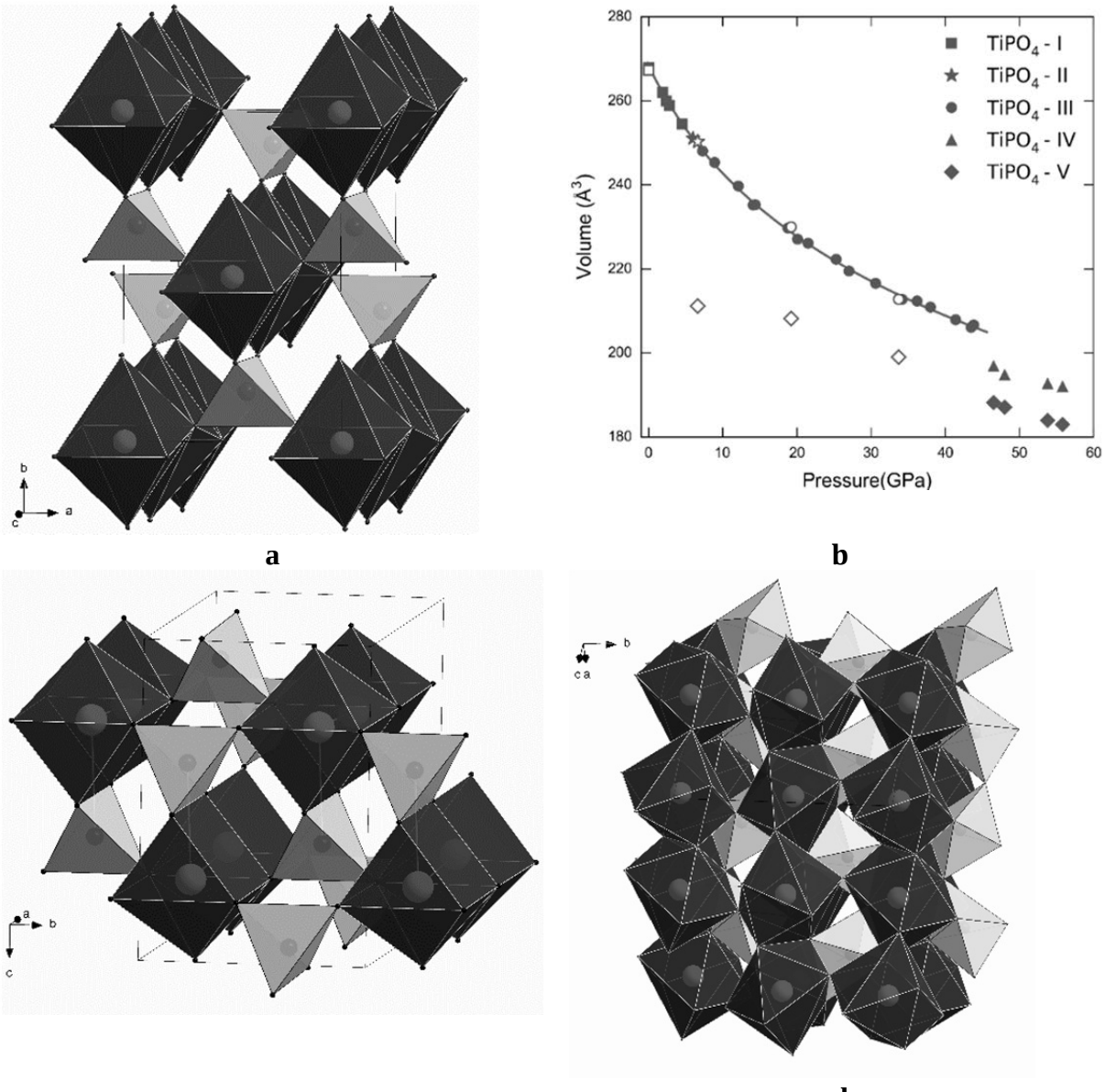

Fig. 3.7-7: (a) Crystal structure of $TiPO_4$-I at ambient conditions (b) Dependence of the unit cell volume of $TiPO_4$ phases on pressure (c) Crystal structure of $TiPO_4$-IV at 48 GPa (d) Crystal structure of $TiPO_4$-V at 48 GPa.

At ambient conditions $TiPO_4$ crystallizes in the $CrVO_4$ structure type (space group *Cmcm*, No. 63, Z = 4). Its structure consists of infinite chains of edge-sharing TiO_6 octahedra, which propagate along the ***c***-axis. These chains are interconnected by sharing corners with PO_4 tetrahedra (Fig. 3.7-7). At a pressure of 4.5-6.0 GPa, $TiPO_4$ undergoes the first phase

transition, evident by the appearance of weak satellite reflections. These were indexed to the Cmcm structure with a modulation vector $\boldsymbol{q}$ = (0.56, 0, 0). We denote this phase as $TiPO_4$-II. Analysis of the diffraction symmetry and systematic absences revealed the superspace group $Cmcm(\sigma_1 00)0s0$. The primary distortion involves formation of Ti–Ti dimers within Ti chains along the ***c***-axis.

The next incommensurate-commensurate phase transition occurs between 6.0 and 7.3 GPa. Similarly to $TiPO_4$-II, the structure of $TiPO_4$-III can be described within the superspace group $Cmcm(\sigma_1 00)0s0$, but with $\sigma_1 = 1/2$. The evolution of $TiPO_4$-III with pressure up to 43 GPa does not reveal any further anomalies. It is characterized by a smooth decrease of the average Ti–Ti distances and the saturation of the modulation amplitude above 20 GPa. It should be noted that the compression of $TiPO_4$ is strongly anisotropic. The most compressible direction in the crystal is parallel to the TiO_4 ribbon chains (along the *c*-axis). The *a*-direction is the most incompressible, and even possess negative linear compressibility up to 18 GPa.

The $TiPO_4$-II and $TiPO_4$-III phases appear also at low temperatures (below 111 and 74 K, respectively) and ambient pressures due to the spin-Peierls distortions. It is known that the temperature of the spin-Peierls transition (T_{sp}) is proportional to the ratio between intrachain and interchain spin exchange interacitons. So, the pressure induced increase of T_{sp} is related to crystal chemistry of $TiPO_4$ material. The relative rigidity of *a* and *b* axes compared to the softness of the *c* axis implies that the intrachain exchange interaction is more strongly affected by the applied pressure, and therefore leads to the substantial increase of T_{sp} up to 293 K.

The diffraction pattern of $TiPO_4$ changes drastically at 46 GPa. A thorough analysis of the diffraction pattern revealed two lattices which are not related to each other neither by any symmetry operation nor by any setting transformation, suggesting that at these conditions two polymorphs coexist. The formation of these polymorphs is accompanied by pronounced volume drops of 4.5 and 7.6 % relative to $TiPO_4$-II, respectively. The structure of $TiPO_4$-IV (Fig. 3.7-7) consists of square-face-capped trigonal prisms TiO_7, sharing common trigonal faces and thus forming infinite chains along the *c*-axis. The coordination number of phosphorus atom does not change: TiO_7 prisms are interconnected by PO_4 groups. The volume collapse in the lattice is related to an increase of the polyhedral coordination around the titanium atoms. The formation of $TiPO_4$-V, by contrast, requires drastic atomic rearrangement: Ti atoms have a highly distorted snub disphenoid coordination, while phosphorus is coordinated by five oxygen atoms forming a trigonal bipyramide (Fig. 3.7-7). To the best of our knowledge, this is the first example of such phosphorus coordination in inorganic phosphate materials.

e. *Structure-property relationships in multiferroic metal-organic frameworks at high pressure (I.E. Collings, N.A. Dubrovinskaia/Bayreuth, L.S. Dubrovinsky, E. Bykova and M. Bykov)*

Dense metal-organic frameworks (MOFs) show promise for a new generation of multiferroic materials, which have technological importance in sophisticated multistate devices. MOFs

present several advantages over already known multiferroic ceramic materials, such as increased framework flexibility, a vast chemical diversity, and numerous host–guest interactions. These characteristics could lead to increased ferroelectric responses and guest-tuned multiferroic properties. However, so far the study of multiferroic MOFs is in its infancy, and a much greater understanding of the structure–property relationships is needed in order to direct the design of functional multiferroic MOFs.

The dense MOF families of ammonium metal formates, $[NH_4][M(HCOO)_3]$, and dimethylammonium metal formates, $[(CH_3)_2NH_2][M(HCOO)_3]$, have shown great potential for multiferroic behaviour. The metal cations in the MOF – connected via organic ligands – provide the magnetic property, while the guest cation in the framework pore yields the ferroelectric response; host-guest interactions may then lead to coupling between the two ferroic parameters. Both these families of MOFs contain disordered A-site cations, which order in a preferential direction at low temperature (below 250 K) to create a switchable uniaxial electric dipole (Fig. 3.7-8). Hydrogen bonding between the A-site cation and the formate linker, which connects the metal cations, provides a way to couple the electric and magnetic ordering.

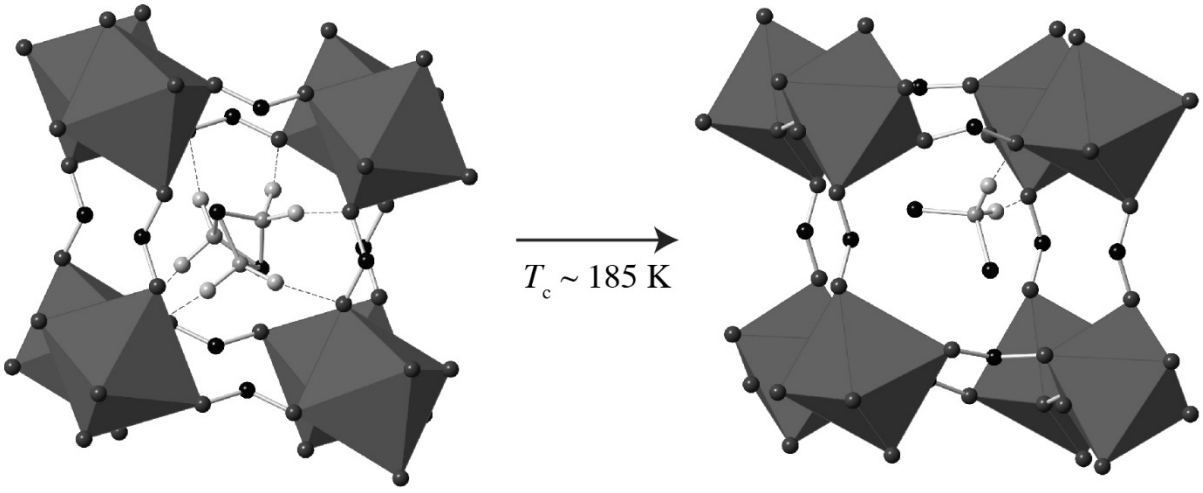

Fig. 3.7-8: Ferroelectric phase transition of $[(CH_3)_2NH_2][Mn(HCOO)_3]$ induced upon cooling from ambient temperature to below 185 K, creating a uniaxial electric dipole. Hydrogen bonds are shown in dotted lines, and octahedral coordination about Mn^{2+} is represented by polyhedra.

In this project, we use high-pressure conditions in order to evoke electric and magnetic ordering in dense MOFs, which have already shown multiferroic behaviour at low temperature and ambient pressure. Investigating the structural evolution under pressure is important for determining the way chemical pressure (*i.e.*, how different sizes of chemical components can mimic the effect of hydrostatic pressure) should be used in order to obtain desirable ferroelectric and ferromagnetic properties at ambient conditions.

Our initial results from high-pressure single-crystal X-ray diffraction and Raman spectroscopy indicate that structural distortion of the metal-formate framework can induce cation polar displacement at high pressure in the ammonium metal formate compounds. The pressures needed to induce this phase transition are dependent on the metal center: for $[NH_4][Fe(HCOO)_3]$ we find a lower transition pressure lower than for $[NH_4][Ni(HCOO)_3]$, due to the weaker bonding in Fe-formate compared to Ni-formate. This mechanism of pressure-induced charge polarity may have interesting consequences on the magnetic behaviour of these compounds at high pressure. In addition to this work, we observed that the transition can be suppressed by using a pressure-transmitting medium that can enter into the metal-formate framework pores, and show the formation of a high-pressure phase of neon-containing ammonium metal formates: $Ne_x[NH_4][M(HCOO)_3]$.

f. *Spontaneous charge carrier localization in extended one-dimensional systems (V. Vlček and G. Steinle-Neumann, in collaboration with H.R. Eisenberg and R. Baer/Jerusalem)*

From a theoretical and practical perspective, it is of crucial importance to understand, predict and successfully model possible localization of charge density and quasiparticles. Most notably, such phenomena were predicted and observed for conjugated organic polymers. Here we explore the possibility of charge carrier localization in large quasi-one-dimensional polymer strands of trans-polyacetylene (tPA) and polythiophene (PT) with ideal periodic (undistorted) repeat geometries (Fig. 3.7-9). These systems have high relevance in electronic and photovoltaic technology, and their charge density is known to be significantly affected by the presence of polarons, bipolarons and solitons.

One way to identify localization of excitations is through the dependence of their energy on the system size L; the excitation energy typically increases with L due to quantum confinement effects. However, once the length of the polymer strand is larger than some critical value, the excitation energy reaches an asymptotic constant value, independent of the system size and one can regard this to be due to the quasiparticle localization.

We use various computational approaches to describe quantum effects of electron interaction in order to explore this type of behaviour for tPA and PT: Hartree-Fock and density functional theory using standard local density approximation, the B3LYP hybrid functional and the range-separated BNL functional. The latter one contains a system-dependent range separation parameter which is chosen such that the energy of the highest occupied eigenstate coincides with the electron removal energy, *i.e.*, it enforces the ionization potential theorem and we can regard the eigenvalue of the highest occupied state to truly represent the quasiparticle energy (Fig. 3.7-9).

Using these calculations, we are indeed able to observe localization of the quasiparticles (holes) for very large polymer chains if Hartree-Fock or BNL functionals are used and we

find that the localization is governed by the exchange interaction. Two points should be noted: (i) since we consider the underlying ionic geometry to be fully periodic, we conclude that it represents a case of *spontaneous symmetry breaking of the continuous translational symmetry in charge density*. (ii) A symmetric solution would be restored if static correlation is fully taken into account, *i.e.*, if the electronic many-body states are described by the multi-determinant wave function that can capture all the symmetry related (degenerate) states. We also show that the energy gain in the spatially unrestricted (symmetry broken) solution thus represents the contribution of the static correlation and leads to the correct description of the quasiparticle energies.

The observed spontaneous quasiparticle localization can moreover explain the fast formation of polarons in the polymers in which the hole can serve as a precursor for the geometric distortion of the ionic lattice.

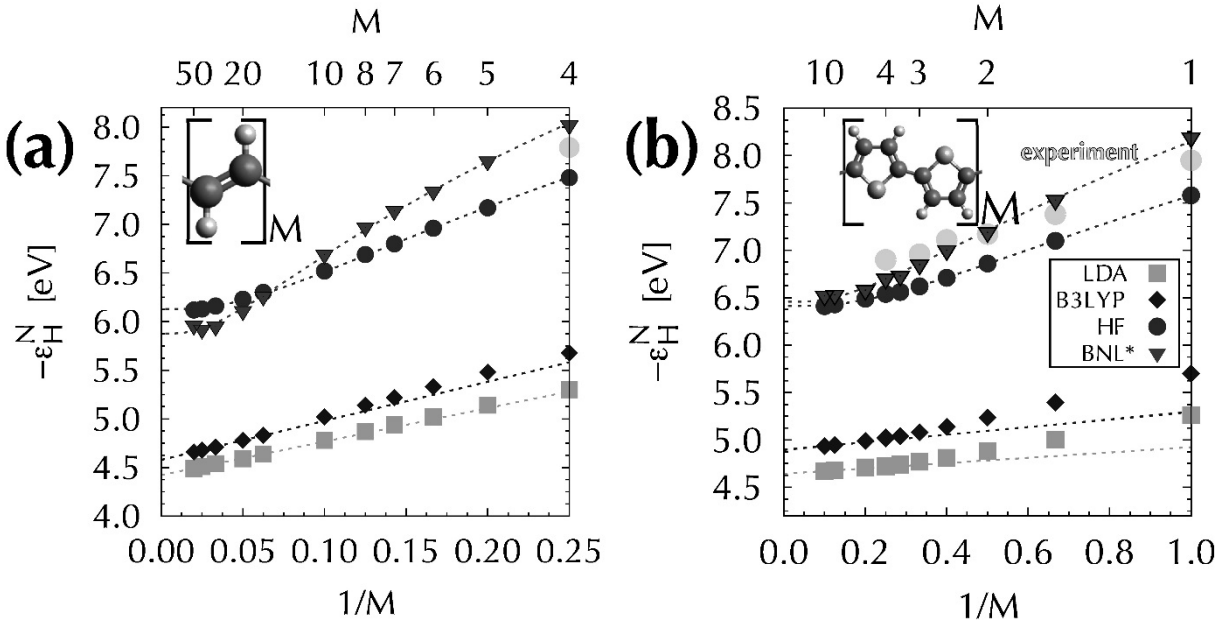

Fig. 3.7-9: Ionization potentials computed as the highest occupied eigenvalue $-\varepsilon^N_H$ for (a) trans-polyacetylene (tPA) and (b) polythiophene (PT) are shown against the inverse number of repeat units M in the respective polymer. The repeat unit for each polymer is illustrated in the insets (C, H and S are shown by black, small and large grey spheres, respectively). Results obtained from different computational approaches are indicated by symbols and labeled in the legend. Experimental data for the ionization potentials are shown by grey circles. The dashed lines represent the numerical models used for describing the behaviour of the ionization potential.

3.8 Methodological Developments

An essential on-going goal in experimental studies in the Earth and material sciences is to improve existing techniques and to devise new ones. For example, such developments are applicable to (1) the expansion of high pressure-temperature conditions and their improved characterization, as required to obtain a better understanding of the Earth's deep interior, (2) making new measurements of physical and chemical properties of materials, and (3) characterizing the chemical composition and crystal defects of natural and experimental samples. The contributions in this section cover many of these aspects of methodological developments.

A new multianvil press 'IRIS-15' was installed at BGI in 2014. The target region of studies with this press is the upper and middle regions of the lower mantle, where pressure conditions exceed 23 GPa. The first contribution reports technical developments using tapered tungsten carbide anvils, which have enabled experiments to be performed up to 44 GPa and 2000 K with a relatively large sample volume and stable heating.

Neutron diffraction experiments provide important information about the behavior of light elements (e.g. H and C) and neighboring elements (e.g. Mg, Al and Si) in crystal structures because the scattering cross section is different from that of X-rays. A six hydraulic-ram multianvil press was installed at the neutron facility FRM II in Garching in 2011. The second contribution describes development of the detectors for neutron diffraction and reports their performance.

Four contributions present the results of methodological developments in generating and measuring high pressures and temperatures in diamond anvil cells (DAC) a goal which is essential for high-pressure studies. The third contribution describes expanding the pressure range of DAC experiments to 800-1000 GPa by introducing gaskets for the double-stage DAC technique. Three contributions describe improvements to the generation and measurement of high temperatures in the DAC. Stable heating of a sample is essential for measurements of high-temperature properties of materials by single-crystal X-ray diffraction and Brillouin and Raman spectroscopies. The fourth contribution describes stable heating up to 1500 K by using an internal high-temperature setup with a graphite heating element. Moreover, pulsed laser heating, instead of continuous heating, enables thermal conductivity and the kinetics of chemical reactions and phase transformations in the DAC to be studied. The fifth contribution describes the setup for double-sided pulsed laser heating with temperature measurement with a fine spatial resolution and reports its performance. Furthermore, characterization of temperature gradients over a laser-heated sample is important for studying the effects of temperature on material properties. The sixth contribution introduces the use of center shifts of synchrotron Mössbauer spectra for evaluating the temperature gradient in the laser-heated samples.

Two contributions describe new developments to the DAC and a moissanite anvil cell in order to study the properties of aqueous fluid and magma. Properties of aqueous fluids are

important for understanding the growth of the continental crust because they control the formation of magmas in subduction zones. The seventh contribution describes developing a new assembly for the measurement of electrical conductivity of aqueous fluids in order to understand the degree of dissociation in the aqueous fluid (i.e. pH). Bubble nucleation and growth in magmas in the magma chamber of a volcano are fundamental processes for understanding the characteristics of volcanic eruptions. In the eighth contribution, pressure-temperature conditions in a moissanite anvil cell have been expanded to magma chamber conditions and have enabled a detailed study to be made on the behavior of the bubbles in magma during volcanic eruptions.

The last two contributions in this section describe advances in sample analysis. Observation and characterization of dislocations in crystals are essential in studies of rheological properties that are controlled by dislocation motion. The ninth contribution describes introducing electron channeling contrast imaging (ECCI) to the Earth sciences as a new method for observing dislocations in oxides using a field-emission scanning electron microscope. A scanning transmission electron microscope Titan G^2 80-200 (FEI) was installed at BGI in 2013. The final contribution reports the origin of negative crystals in diamonds from the lower mantle, on the basis of detailed analyses, utilizing this system.

a. *Generation of pressures over 40 GPa using a Kawai-type multianvil apparatus with tungsten carbide anvils (T. Ishii, L. Shi, R. Huang, N. Tsujino/Misasa, D. Druzhbin, R. Myhill, Y. Li, L. Wang, T. Yamamoto/Hiroshima, N. Miyajima, T. Kawazoe, N. Nishiyama/Hamburg, Y. Higo/Kouto, Y. Tange/Kouto and T. Katsura)*

A Kawai-type multianvil apparatus (KMA) has been widely used to study material properties under high-pressure and high-temperature conditions. Pressure ranges are limited to 25 GPa when using tungsten carbide (WC) anvils, which corresponds to conditions of the uppermost part of the lower mantle. Sintered diamond (SD) anvils allow us to generate pressures up to 60 GPa. However, it is difficult to routinely use SD anvils because of their high cost. Therefore, it is desired to generate pressures higher than 25 GPa using WC anvils. In this study, we have developed techniques to simultaneously generate high temperatures up to 2000 K and pressures exceeding 40 GPa using a KMA with WC anvils.

We mainly used a KMA with DIA-type guide blocks, IRIS-15, installed at BGI in September 2014. After the optimization of the cubic compression space formed by the inner surfaces of the first-stage anvils, we generated pressures using WC anvils (TF05, Fujilloy Co., Ltd) with a truncation of 1.5 mm and a taper of 1.0° and semi-sintered MgO + 5 wt. % Cr_2O_3 octahedra as the pressure media. Generated pressure was estimated based on resistance changes in ZnS, GaP and Zr at room temperature and the Al_2O_3 content in bridgmanite coexisting with corundum at 2000 K. High temperature of 2000 K was generated using a Re furnace in a $LaCrO_3$ thermal insulator, and measured with a W3%Re-W25%Re thermocouple. Al_2O_3 lids were placed on the both sides of the pressure calibrant in the furnace for high efficiency in

pressure generation. The starting material was sintered ilmenite-type $Mg_3Al_2Si_3O_{12}$ synthesized at 1173 K and 26 GPa. Another KMA, SPEED-*Mk*.II at the synchrotron radiation facility, SPring-8, was used for testing pressure generation at room temperature based on the equation of states of MgO (Tange *et al.*, 2009) and Au (Yokoo *et al.*, 2009).

Figure 3.8-1 shows a comparison of pressure generation using flat and tapered anvils respectively with IRIS-15. We observed phase transitions of Zr ω-β (34 GPa) at room temperature and 10.8 MN and 7.5 MN using the flat and tapered anvils, respectively, demonstrating that the tapered anvils has 30 % higher efficiency in pressure generation than the flat anvils. The pressure generated with SPEED-*Mk*.II reached 43 GPa at the maximum press load of 15 MN (Fig. 3.8-2). The sample synthesized at 2000 K and 15 MN has a pyrope composition with the $LiNbO_3$-type structure, suggesting that the structure of the sample was bridgmanite-type under high pressure and high temperature. The phase relations in the $MgSiO_3$-Al_2O_3 system at 2000 K suggest generation of 44 GPa at high temperature (Fig. 3.8-2).

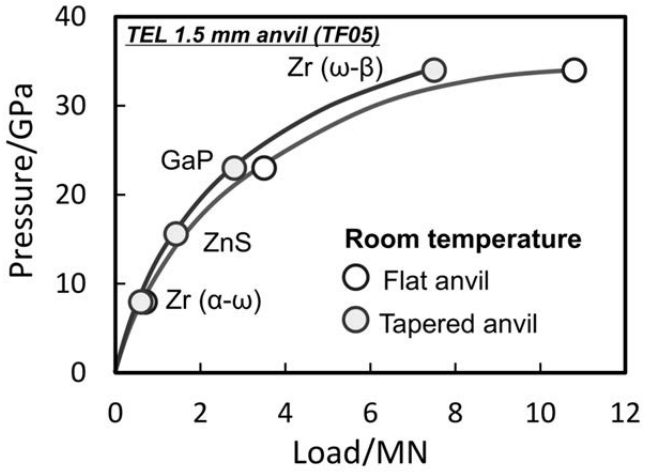

Fig. 3.8-1: Pressure calibration curves at room temperature with flat and tapered anvils. ZnS, GaP and Zr were pressure calibrants. Solid and open circles show the results using flat and tapered anvils, respectively. TEL: truncated edge length.

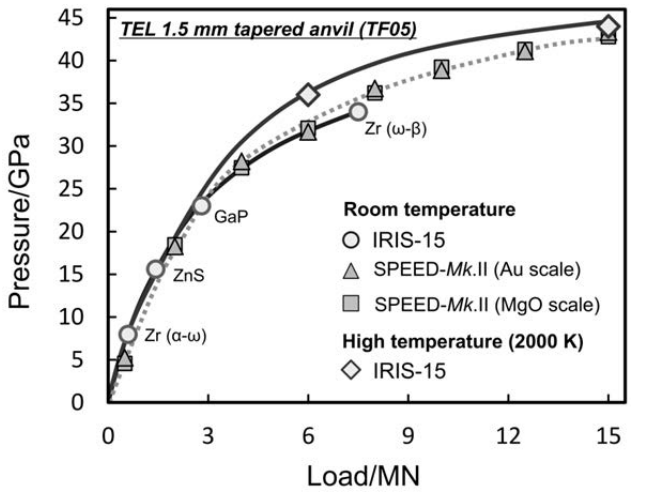

Fig. 3.8-2: Pressure generation using the TF05 anvils with a 1.5 mm truncation and 1° tapered faces at room temperature and high temperature (2000 K). Circles and diamonds show pressures generated with IRIS-15 at room temperature and 2000 K, respectively. Triangles and squares are pressures generated with SPEED-*Mk*.II at room temperature using equation of states of Au (Yokoo *et al.*, 2009) and MgO (Tange *et al.*, 2009), respectively. ZnS, GaP and Zr were pressure calibrants at room temperature. TEL: truncated edge length.

b. *The SAPHiR neutron detectors (N. Walte, K. Zeitelhack/Munich, A. Wiens/Munich and H. Keppler)*

SAPHiR is an instrument under construction for neutron diffraction and radiography under extreme pressure and temperature conditions at the MLZ neutron source in Garching. In 2015 the major task was the construction and assembly of the detectors for neutron diffraction, which was done in collaboration with the FRM II detector group (lead by K. Zeitelhack). The main requirements for the detector system were to (i) provide a large detector area despite the geometric constraints of a multianvil press, (ii) cover *d*-values of typical minerals including glasses and sheet silicates, and (iii) achieve a $\Delta d/d$ resolution in the 10^{-3} range.

Since the neutrons can only enter and exit the sample through the four vertical anvil gaps, the time-of-flight (TOF) methodology is used for neutron diffraction, for which the beam is separated into short pulses with a wavelength range of 1-2.4 Å by a cascade of disc choppers, whose wavelength can then be discriminated by measuring the flight time from the pulse chopper to the detector. Over the duration of one pulse a range of *d*-values can thus be measured at a given 2Θ angle (Fig. 3.8-3). For example, the main 90° detector banks measure a *d*-range of ~ 0.7-1.8 Å ($Q \approx$ 3.3-9 Å^{-1}). The main detector banks are complemented by a backscatter detector system and a forward scatter detector bank in order to increase the *Q*-range and the overall detector area. The whole detector system covers 2Θ angles from ~ 5-160° and *d*-values of ~ 0.6-15 Å (Fig. 3.8-3). The TOF resolution is given by

$$\frac{\Delta d}{d} = \sqrt{\left(\frac{\Delta t}{t}\right)^2 + \left(\frac{\Delta L}{L}\right)^2 + \left(\frac{\Delta\Theta}{\tan\Theta}\right)^2} \qquad (1)$$

with the total flight length *L*, the TOF *t*, the scattering angle Θ and the uncertainty Δ of each parameter. The third term is especially dominant at small diffraction angles; hence, the potential resolution strongly increases with the scattering angle.

For the detector banks perpendicular to the primary beam and in the forward scattering regime, 8 mm wide position sensitive detector tubes (PSD) from GE Reuter-Stokes are used that had been purchased and tested at the end of 2013 (see annual report 2013). The aim for the PSD arrangement was to form and maintain an arc with an equidistance of 1500 mm from the sample centre and with an opening angle of 70° regardless of the positioning of the press. For easier construction and maintenance, each detector bank is separated into five segments, each containing 48 PSD that are attached to a large aluminium rack (Fig. 3.8-4). The signals of the PSDs are amplified and processed by MPSD electronic modules that are situated directly behind the detectors. The racks are positioned and aligned on rails in the detector frame that is attached to the SAPHiR press (Fig. 3.8-4). Prior to the assembly, the individual segments were measured at a californium neutron source in the detector laboratory to confirm their proper operation and the required position resolution of 3 mm by using a slit-screen (Fig. 3.8-4d-e). Depending on the beam divergence a $\Delta d/d$ resolution between 5×10^{-3} and 1×10^{-2} is thus achieved according to Eq. (1).

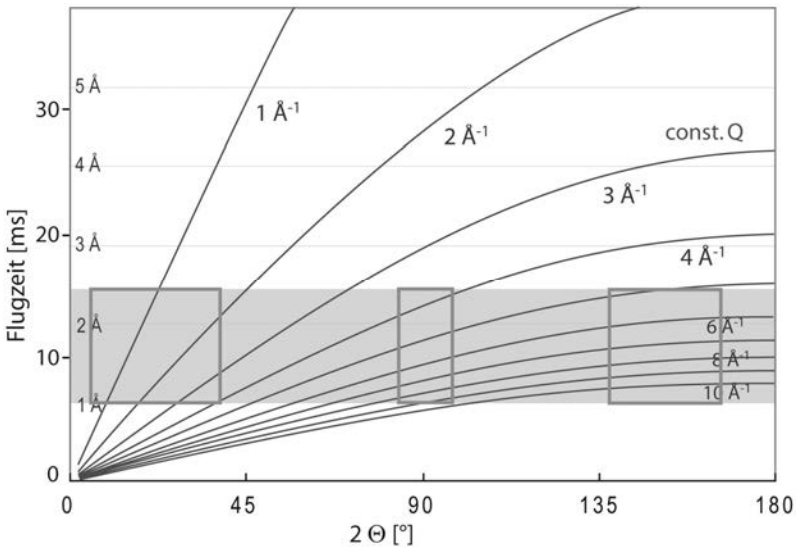

Fig. 3.8-3: *Q*-range of the SAPHiR detectors. The shaded area represents the TOF wavelength range. The boxes indicate the *Θ*-range of the detector banks.

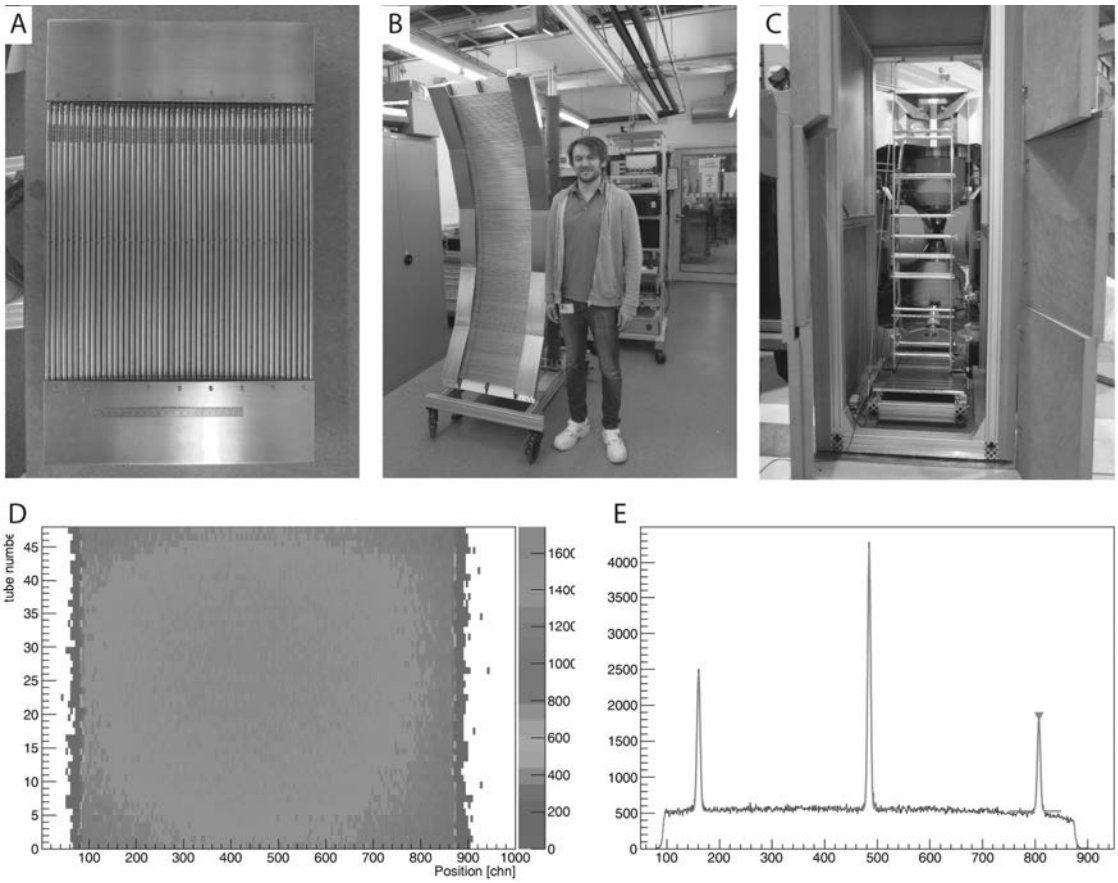

Fig. 3.8-4: Setup of the helium-3 detector banks. (A) Detector segment with 48 PSD. Note that the mount is already curved. (B) 90° detector rack with five segments. The electronic modules are situated behind the PSDs. (C) SAPHiR detector frame with a detector rack before attachment of the segments. (D) Test of segment at Cf neutron source. (E) Position resolution with three 2 mm wide slits.

The potential resolution of the *d*-values ($\Delta d/d$) increases according to Eq (1) with the scattering angle Θ. Accordingly, the backscatter range is particularly suitable for high-resolution detectors. Here, the smallest *d*-values can be detected with a range between 0.55-1.2 Å. In order to combine a superior position resolution with good detection efficiency for thermal neutrons, a new wavelength-shifting-fibre (WLSF) detector system has been chosen, that was developed and built by the ZEA group of the Forschungszentrum Jülich. These detectors consist of two 0.5 mm thick 6LiF/ZnS:Ag scintillator plates, in which the neutrons are captured and produce blue photons. The photons are trapped in a layer of cross-cutting WLS-fibers that is sandwiched between the scintillator plates. The fibres shift the wavelength to green and transport the photons to five photomultipliers. The position reconstruction is achieved by combining the position of the fibres that deliver the largest signal (Fig. 3.8-5). Measurements of the detectors by R. Engels (ZEA II FZ Jülich) at the FRM II instrument TREFF confirmed the required position resolution of 2 × 2 mm and a detection efficiency of > 50 % in the SAPHiR wavelength range of 1-2.4 Å. A $\Delta d/d$ resolution < 2×10^{-3} is thus achieved according to Eq. (1). The four detector segments were delivered and attached in September 2015 (Fig. 3.8-5).

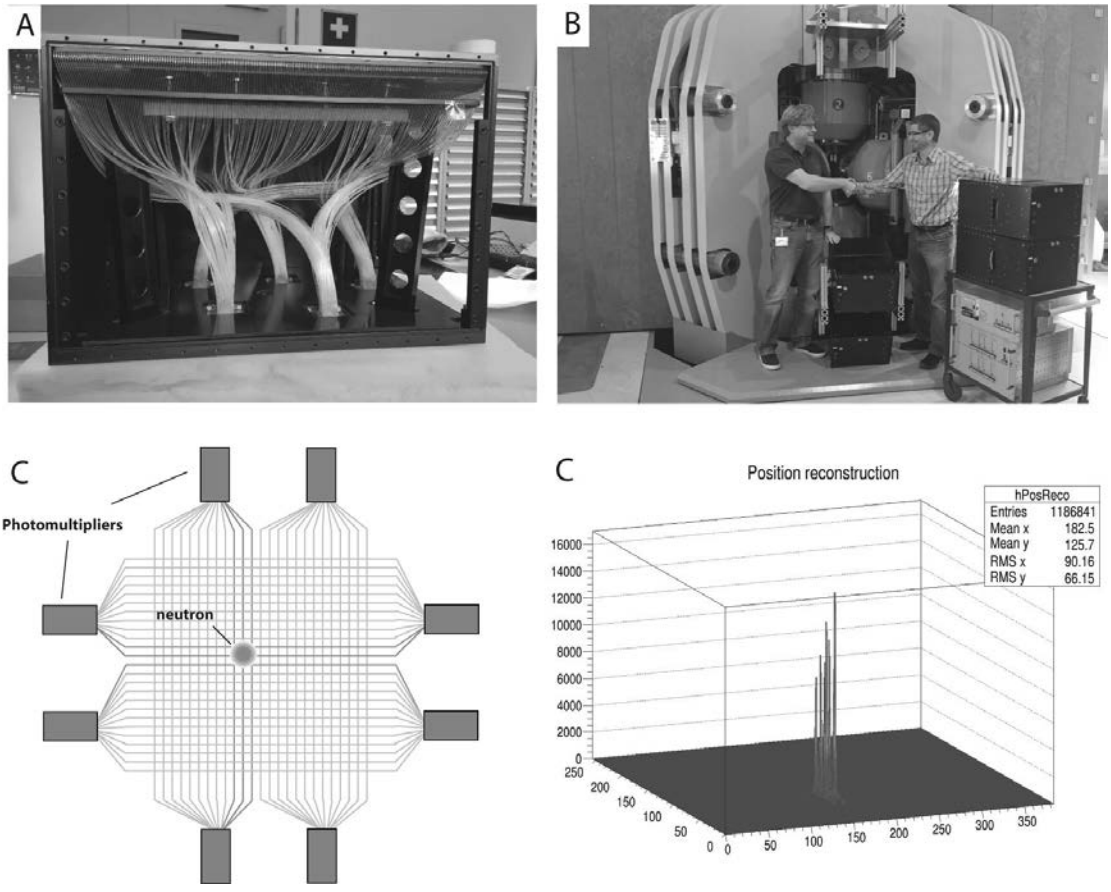

Fig. 3.8-5: (A) WLSF detectors (photo from R.Engels, ZEA II – FZ Jülich). The fibres from the scintillator plates (top) are bundled and connected to the photomultipliers (bottom). (B) Attachment of detector boxes to SAPHiR. (C) Position reconstruction of the WLSF detector. (D) Test of the detectors with pinholes (plot from R.Engels, ZEA II – FZ Jülich).

The SAPHiR detectors and the detector electronics are currently being completed. The detector commissioning will start in 2016 with a mobile Cf neutron source so that SAPHiR will be ready for neutron diffraction when the neutron infrastructure is completed.

c. *Gasketed double-stage diamond anvil cell (L.S. Dubrovinsky, N.A. Dubrovinskaia, M. Bykov, E. Bykova, S. Petitgirard, I. Collings, K. Glazyrin/Hamburg, H.-P. Liermann/ Hamburg, M. Hanfland/Grenoble and V. Prakapenka/Chicago)*

The double-stage diamond anvil cell (ds-DAC) technique enables ultra-high static pressures in excess of 500 GPa to be generated. However, so far ds-DACs were used without gaskets, *i.e.*, samples were compressed directly between secondary anvils made of nanocrystalline diamond (NCD). This limited the application of the technique to solid materials at ambient conditions which additionally should be easily stuck on the surface of secondary anvils. Using a novel NCD material which could sustain much higher stresses than before and further developing the technique of gasket preparation (Fig. 3.8-6) we performed experiments in gasketed ds-DACs. In one of the experiments, a mixture of Au and paraffin wax was loaded in a ~ 3 μm diameter pressure chamber and compressed to 688(10) GPa. Upon compression, the diameter of the pressure chamber increased to ~ 5 μm and Au occupied only a portion of it.

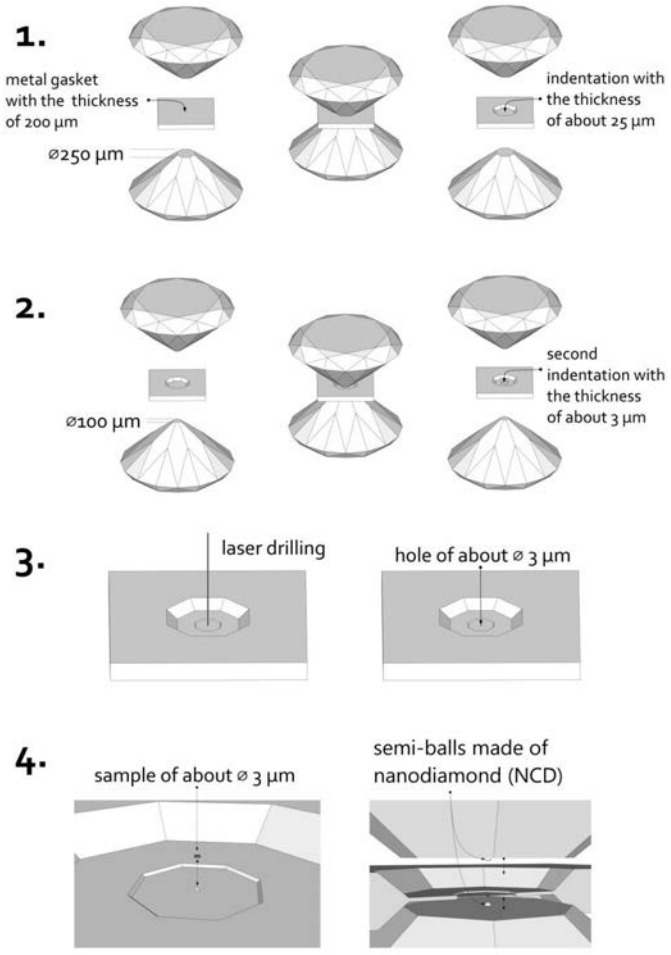

Fig. 3.8-6: Scheme of the gasket preparation for ds-DACs. (1) Re foil with an initial thickness ~ 200 μm is indented to ~ 25 μm using a conventional DAC with diamonds having culets of 250 μm. (2) In the middle part of initial indentation an additional indentation to ~ 3 μm final thicknesses was made using 100 μm culet diamonds. (3) Using a pulsed laser, a hole with diameter ~ 3-4 μm was drilled in the center of the secondary indentation. (4) A sample (Au or Pt in our experiments) was loaded using a micromanipulator in the center of the secondary pressure chamber. NCD hemispherical secondary anvils were attached to the gasket using traces of the wax, and the whole assembly was mounted on the primary anvils (flat 250 μm or beveled 120 μm in diameter in our experiments). Empty space in the secondary chamber in our experiments was filled by wax or by Ar (loaded at 1.3 kbar).

As a result one could observed light (Fig. 3.8-7) passing through material (paraffin wax) that was compressed to almost 700 GPa and we confirmed that NCD remains optically transparent even at such high pressures. Gasketed ds-DACs allow loading and compressing not only materials which are solid at ambient conditions but even gases. For example, Pt was loaded with Ar at 1.3 kbar and compressed using beveled first-stage anvils directly to 120 GPa and then to 135 GPa. Diffraction peaks of both Pt and Ar were clearly identifiable but pressure reached between secondary anvils is not easy to characterize precisely due to the absence of experimental EOSs of Pt above ~ 500 GPa and Ar above ~ 100 GPa. Still, available data suggest that materials have been compressed to the range 800 to 970 GPa.

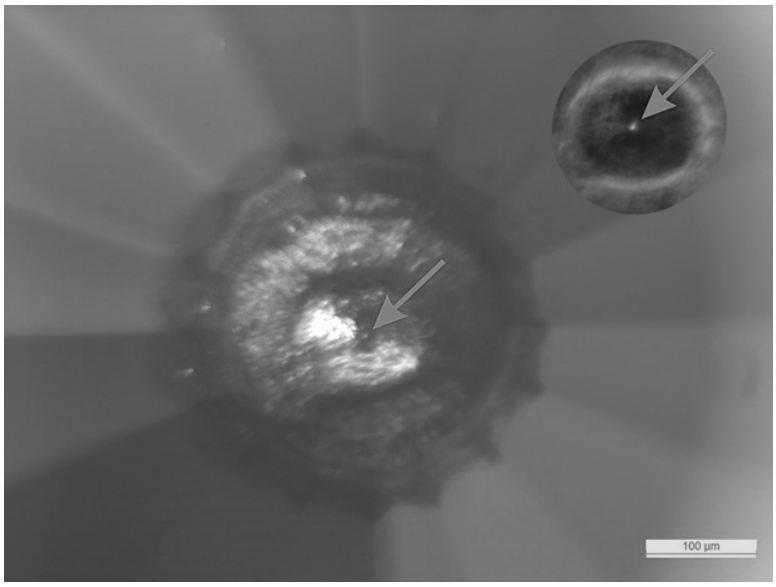

Fig. 3.8-7. Photo of the sample (Au and paraffin wax) compressed in gasketed ds-DAC at 688(10) GPa. The size of the pressure chamber is about 5 µm and Au occupy only a portion of it. As a result one could clearly see transmitted light (light arrow) passing through material (paraffin wax) and confirm that NCD remains optically transparent even at such high pressures. The insert in the upper right corner shows the central part of the gasket and pressure chamber just slightly illuminated by reflected light.

d. *Development of a high-temperature setup for BX-90 diamond anvil cell based on a graphite heating element (A. Kurnosov, H. Marquardt and T. Boffa Ballaran)*

An internal-DAC resistive heating assembly for single crystal X-ray diffraction, Brillouin spectroscopy and Raman measurements has been constructed and tested up to temperatures of 1500 K. The construction features of the heater result in significant temperature gradients which make it possible to create a very high temperature around the pressure chamber of the DAC while the temperature of the cell body remains reasonably low. Such an assembly enables relatively high temperatures to be reached by resistive heating and at the same time preventing oxidation or thermal expansion of the cell parts. Another advantage is that the heating element is made of flexible graphite which is cheap and easy to prepare. Moreover,

this component is the only part of the assembly which has to be replaced after a high-temperature experiment. The other parts of the heating element include molybdenum electrodes and insulation insets made of Macor machinable ceramics (see Fig. 3.8-8, 2-3). The molybdenum part is not centered into the ceramic insulation in order to enable it to fit all different BX-90 DACs used at BGI. The off-centre can be used during the preparation of the DAC to adjust the electrodes to the level of the gasket. In this way it is not necessary to manufacture different electrodes for every size of the diamonds/backing plates used in the different cells. The electrodes and ceramic insets fit perfectly in the cell with no changes of the outer dimensions so that the DAC can be used for gas loading, gas-membrane assembly and for any other additional equipment required for different experiments with the BX-90 DACs.

Due to the large temperature gradients, however, it is very challenging to determine the temperature of the sample using a thermocouple. For this reason we aim to calibrate fluorescence standards such as ruby, Sm:YAG and Sm:SrB_4O_7 at very high temperatures using the melting points of aluminium and gold at low pressure. We are at the moment performing a series of experiments using no pressure medium, as well as sodium chloride and argon as pressure-transmitting media.

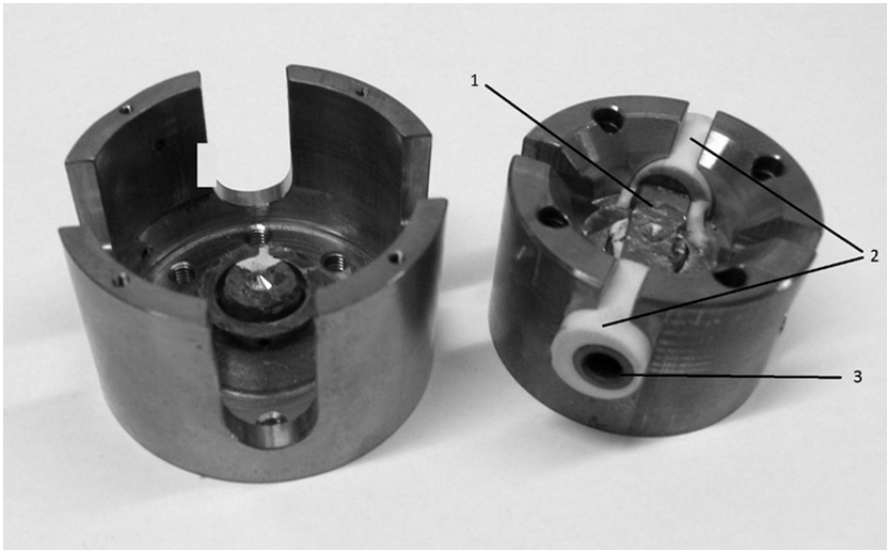

Fig. 3.8-8: BX-90 DAC with graphite heater assembly. 1 – Heating element with a Re gasket inside indented by diamond anvils. 2 – Ceramic insets for electric insulation and adjustment of rod's level. 3 – Molybdenum rods for electric connections.

e. *Pulsed laser heating setup for time resolved geoscience and materials science applications (G. Aprilis/Bayreuth, L.S. Dubrovinsky, D. Vasiukov/Bayreuth, I. Kupenko/Grenoble, S. Linhardt, C. Strohm/Hamburg, C.A. McCammon and N.A. Dubrovinskaia/Bayreuth)*

Laser heating is a widely used technique to achieve high temperatures in a DAC and is necessary, for example, for simulating conditions of Earth's deep interior. Continuous laser

heating in DACs has already been used for many years and has found numerous applications in mineral physics and high-pressure material science research. Use of a pulsed laser instead of a continuous one improves this experimental technique significantly. A short laser pulse followed by a short “dark” period creates a repetition of cycles of sample heating and cooling. This repetitive procedure makes time an extra variable, in addition to pressure and temperature, something that is not possible with constant wave laser heating. A whole new field of research opens up and enables information about time-dependent material properties, including heat flow and kinetics of chemical reactions at extreme conditions, to be obtained. The method of pulsed heating also allows higher temperatures to be reached due to a concentration of a high laser power in a short impulse.

A pulsed laser double-sided heating setup has been developed aiming to acquire precise temperature measurements at very narrow intervals of time (Fig. 3.8-9). Two SPI® RedPower R4 fiber lasers at 1070 nm are synchronized using custom-made electronic components in order to heat a sample under pressure inside a DAC.

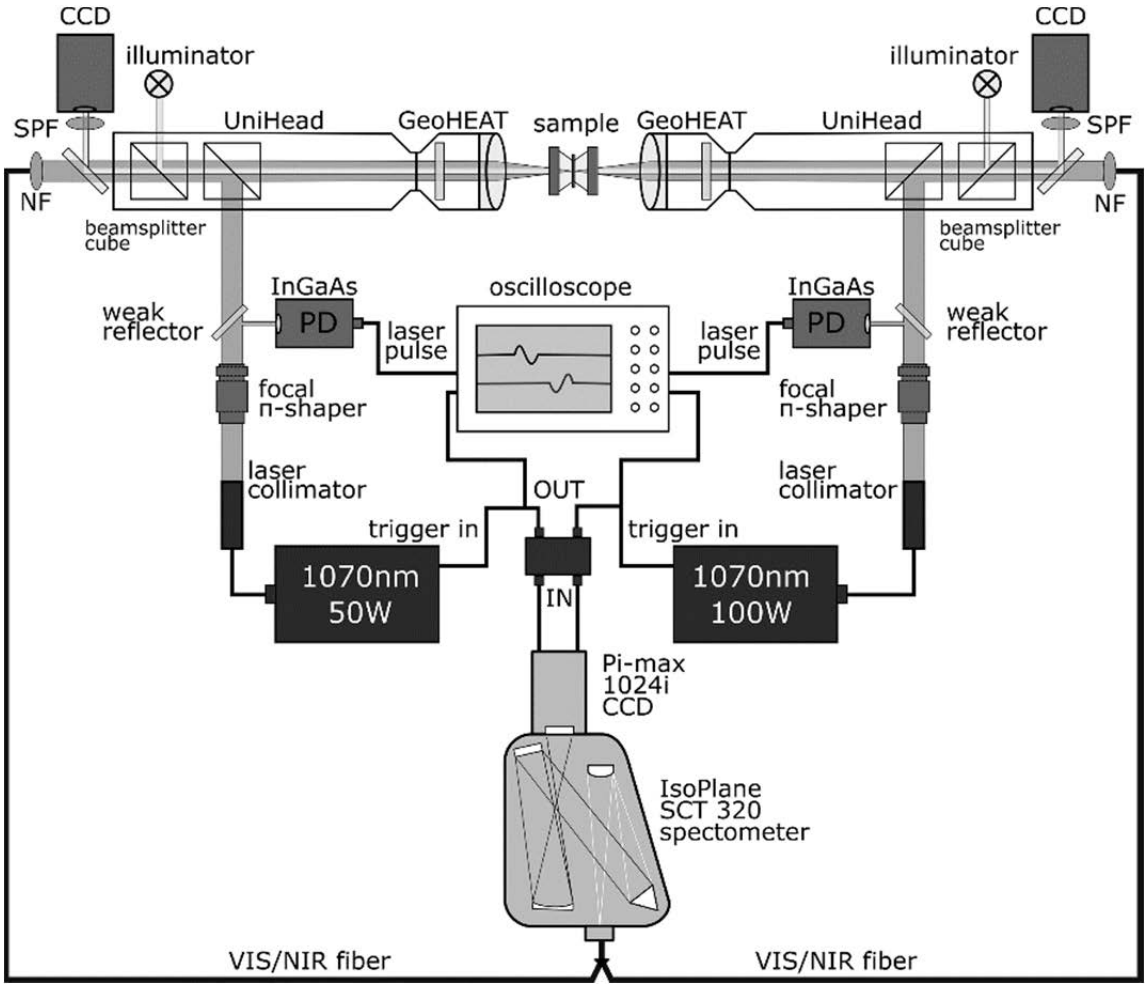

Fig. 3.8-9: Double-sided pulsed laser heating system for DACs. SPF is the short-pass filter with a cut-off at 850 nm; CCD is the camera for sample visual observation; NF is the notch filter at 1064 nm to isolate the laser beam from the detector; PD is the fast InGaAs photodetector to capture laser pulses.

The laser beams are focused using two geoHEAT 40_NIR achromatic lenses, designed to minimize chromatic aberrations, thus allowing optimal laser heating and thermal radiation collection for the sample temperature determination. The lasers are modulated using the internal pulse generator of a Pi-Max 4 1024i high speed CCD camera, which is used also to collect the thermal radiation spectra. Temperature is determined using Planck's law of black body spectral radiance. Laser response is captured using two fast photodiode detectors (InGaAs) and recorded with an oscilloscope. The triggers of the Pi-Max camera can be adjusted to produce the desired response, in terms of the pulse duration, shape and synchronization between the two laser pulses, from both sides of the sample. The sample's heat radiation is collected via optical fibers into a SCT 320 spectrometer. A time series of the sample temperature response can be created by gating the exposure of the CCD detector with respect to the laser triggers (Fig. 3.8-10).

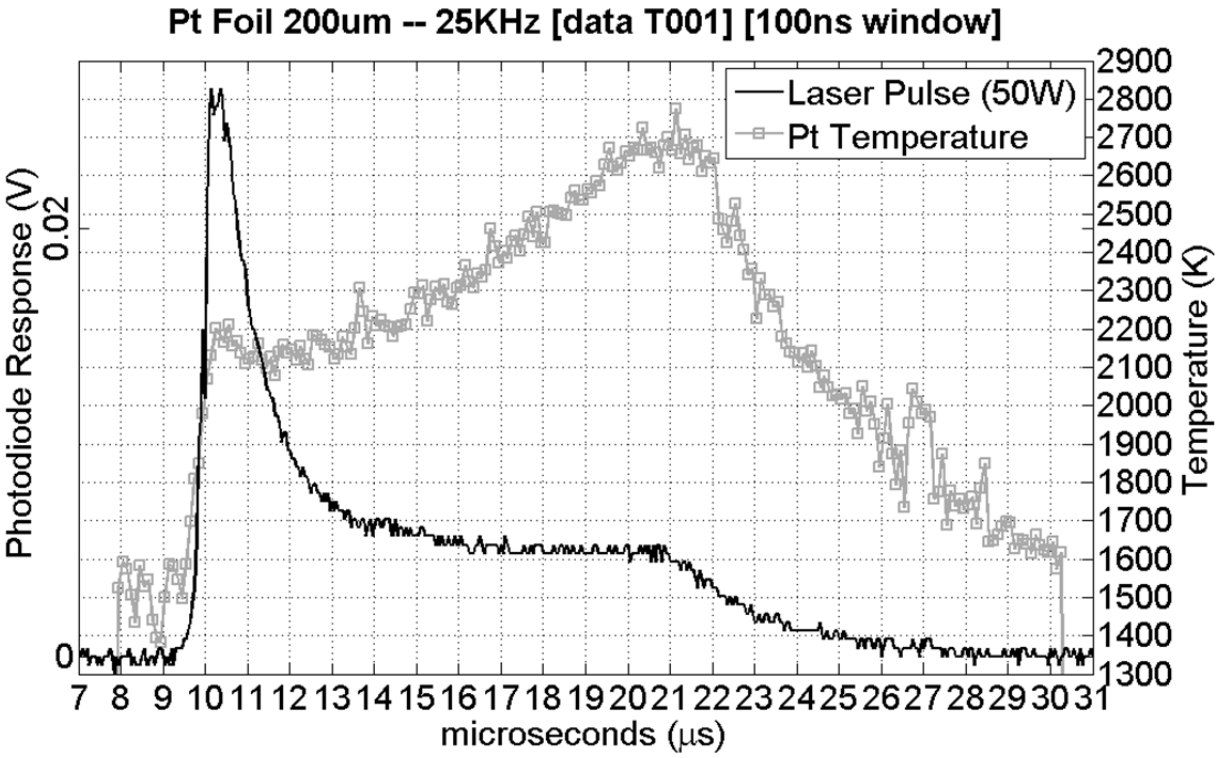

Fig. 3.8-10: Time resolved temperature determination during one-side pulsed laser heating of a Pt foil at ambient pressure. Time resolution of temperature is 100 ns; the gating window of the detector. Total exposure time for every temperature point includes some thousands of repetitions.

Use of a round to linear multi-fiber optic bundle enables us to obtain spatial mapping of the sample temperature *in situ*, upon heating. The fiber bundle contains 15 fibers from each side in the configuration seen in Fig. 3.8-11, providing a linear setup that guides the light onto the spectrometer and the CCD detector, making it possible to separate the regions on the detector array that correspond to each particular temperature. With this method, a spatial temperature

distribution of the heated sample can be determined with the precision of a few micrometers. Double-sided pulsed laser heating in DACs can expand the knowledge of the behaviour of various materials giving a deeper insight in their properties as a function of pressure, temperature, and time. The time resolved heating technique, combined with the space resolved temperature determination, is a powerful method that can be employed in different studies, such as investigations of the thermal conductivity, melting, and phase transformations.

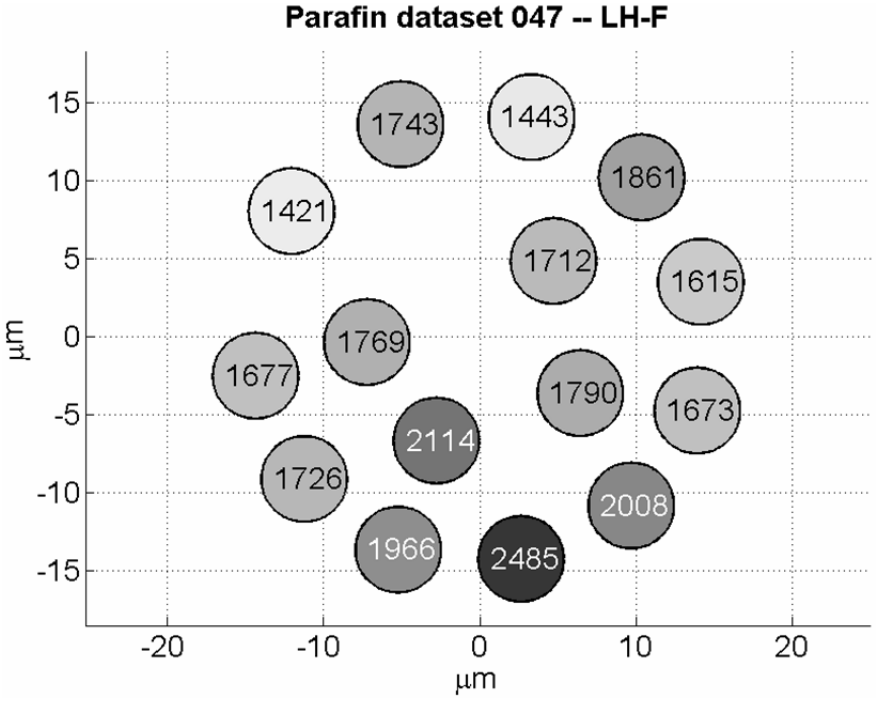

Fig. 3.8-11: Spatial temperature mapping of Fe-bearing silicate glass loaded in paraffin at 4.2(3) GPa and heated continuously from one side.

f. *Comparison of surface and bulk temperatures in laser heated diamond anvil cells (I. Kupenko/Grenoble, C.A. McCammon, V. Cerantola, S. Petitgirard, D. Vasiukov/Bayreuth, G. Aprilis/Bayreuth, L.S. Dubrovinsky, K. Glazyrin and C. Strohm/Hamburg; A.I. Chumakov and R. Rüffer/Grenoble)*

Over the last decades *in situ* experiments at extreme conditions of pressure and temperature have provided many exciting results in the fields of experimental geosciences, solid state physics, chemistry, and material sciences. Laser heating in DACs is a commonly used technique to achieve temperatures of several thousands of degrees at pressures above 1 Mbar (100 GPa). The recently developed Synchrotron Mössbauer Source (SMS) provides a powerful tool for the study of laser-heated materials for geophysical applications. Moreover, it provides the novel possibility of an internal thermometer: the temperature dependence of the centre shift (CS) enables determination of temperature of the same atoms that are responsible

for the absorption. Mössbauer spectroscopy is demanding with regard to the amount of sample; hence sample thickness is an important parameter. On the other hand, relatively thick samples may introduce temperature gradients in experiments utilizing laser-heated DACs. In order to investigate these trade-offs, we coupled SMS measurements with time-resolved incandescent light spectroradiometry to enable comparison of surface temperatures from spectroradiometry with temperatures determined from changes of the CS.

The collected SMS spectra from hot and cold samples are presented in Fig. 3.8-12. The SMS spectrum of the cold sample can be fitted with a superposition of absorption arising from the three phases: FeO, Fe_3C and ε-Fe. High temperature causes a decrease of the recoil free fraction of resonant absorption of X-rays by nuclei, collapse of the magnetic hyperfine field and quadrupole splitting, and a decrease of CS. The temperature of the hot material determined from the CS difference for all three phases is the same within the experimental error and is 1700(100) K.

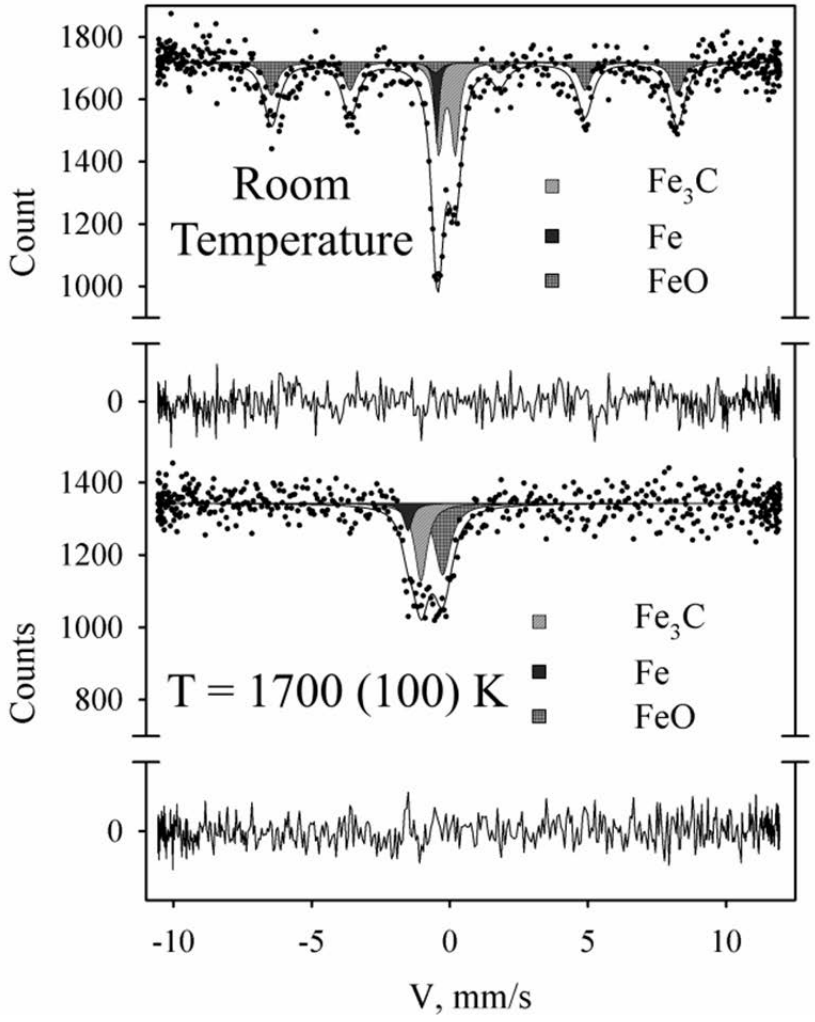

Fig. 3.8-12: SMS spectra of FeO, Fe_3C and ε-Fe at 59(1) GPa at the indicated temperatures as determined from the CS difference between cold and hot sample. The solid lines show the theoretical fit and the residuals are indicated below each spectrum.

The surface temperature of the sample measured using spectroradiometry is shown in Fig. 3.8-13. We find the average temperature of the sample during SMS data collection calculated from the CS difference between cold and hot material to be lower than the surface temperature measured by spectroradiometry. There are several reasons for this difference. Firstly, the spectroradiometry method is more sensitive to the highest temperature due to the significant temperature dependence of the intensity of emitted thermal radiation. Secondly, the samples used for the current experiment are opaque; therefore the incident laser radiation is absorbed in a thin surface layer, resulting in temperature gradients along the heating axis, with a minimum temperature along the axis 5-10 % lower than measured. Finally, the recoil free fraction becomes smaller with temperature, which suppresses absorption from the hottest parts of the sample and therefore slightly shifts the determination towards lower temperatures in calculating the average temperature from the difference in CS values.

Our results clearly demonstrate that temperatures measured using the commonly used spectroradiometry method should be applied with caution in experiments where laser heated DACs are probed with techniques utilizing a relatively large X-ray beam.

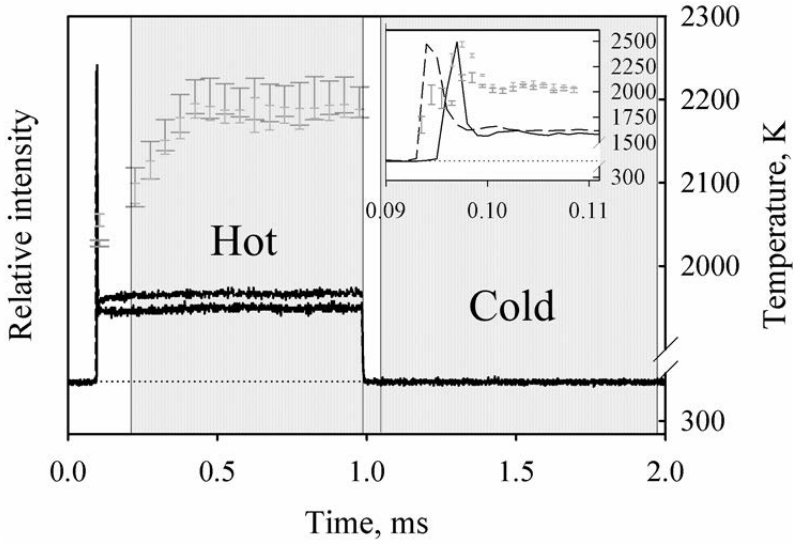

Fig. 3.8-13: Sample surface temperature measured using spectroradiometry (dark and light grey symbols) from two sides of the DAC. Solid and dashed black curves show the time dependence of the laser pulse from two sides. The inset shows an expanded view of time resolved measurements close to the start of laser pulses. Error bars indicate the standard deviations of measurements taken at ~ 5 min intervals during a 30 min heating period. Shadings show the time gates for collection of data from hot and cold sample.

g. *Development of the diamond anvil cell for electrical conductivity measurements of fluids in the crust and mantle (R. Sinmyo and H. Keppler)*

Aqueous fluids are important agents of chemical transport in the crust and mantle. They control the formation of magmas in subduction zones and therefore the growth of the

continental crust. Yet, even some very fundamental properties of fluids at the elevated pressures and temperatures in the crust and mantle are poorly known. This includes, for example, the degree of dissociation and ion association in these fluids or the pH of the fluid. Understanding these fluid properties is not only important for basic research in Earth sciences, but also for the use of geothermal energy, for solvent extraction in the chemical industry and for understanding processes occurring inside pressurized nuclear reactors. Measurements of electrical conductivity are the most powerful tool for understanding the properties of aqueous fluids at high pressure and temperature, as they provide direct insights into dissociation. We have developed an instrument that is capable of expanding the accessible range of electrical conductivity measurement of fluids in a DAC to the typical pressure and temperature conditions of the upper mantle (Fig. 3.8-14). A 0.5 mm thick platelet of diamond with a laser-ablated pinhole in the center is sandwiched between two gaskets and the diamond anvils. Our preliminary results showed that the platelet of single-crystal diamond was often broken due to cracks along the cleavage, and thus, we have employed nano-polycrystalline diamond for the platelet. The gold-rhenium composite gasket was used to trap fluid inside the sample chamber under high-pressure and -temperature conditions. Temperature was monitored by type-K thermocouple and the pressure was determined by using the Raman band of zircon inside the sample. The obtained pressure was consistent with the conventional method that utilizes homogenization temperature. We successfully measured the electrical conductivity of H_2O-NaCl fluid up to 1020 MPa using the developed DAC, which has the potential of expanding the maximum pressure to beyond 1 GPa.

Acknowledgement: Nano-crystalline diamonds were kindly provided by Prof. Tetsuo Irifune via the PRIUS program of Ehime University.

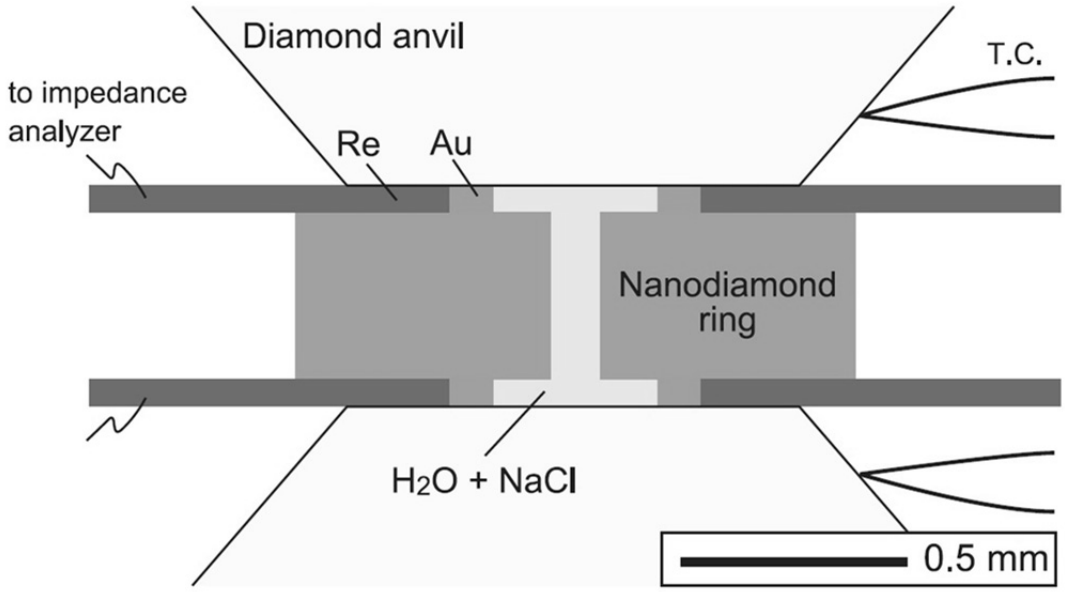

Fig. 3.8-14: Schematic illustration of the DAC that has been developed for electrical conductivity measurements of fluids.

h. *A new hydrothermal moissanite cell (M. Masotta and H. Keppler)*

The moissanite cell allows *in situ* crystal and bubble growth to be investigated at temperatures up to 1240 °C and a pressure of 1 bar. The effect of pressure on crystal growth is likely minimal at shallow crustal conditions, but it becomes extremely important when studying bubble growth. For this reason, we have modified the original design of the moissanite cell by introducing new components that will allow the cell to be used under precisely controlled pressures of several 1000 bar. The key part is a cylindrical sample chamber attached to a pressure capillary that extends outside the cell toward an external pressure line. This part was machined out of a single piece of Nimonic® super alloy. The sample chamber is sandwiched between the two anvils and is sealed by Au-gaskets. Pyrophyllite parts support the three-layered Pt-Rh heaters, while Inconel plates and rings support the moissanite anvils. Preliminary tests showed that the new HP-moissanite cell holds pressure up to 1000 bar at a temperature of 950 °C (Fig. 3.8-15).

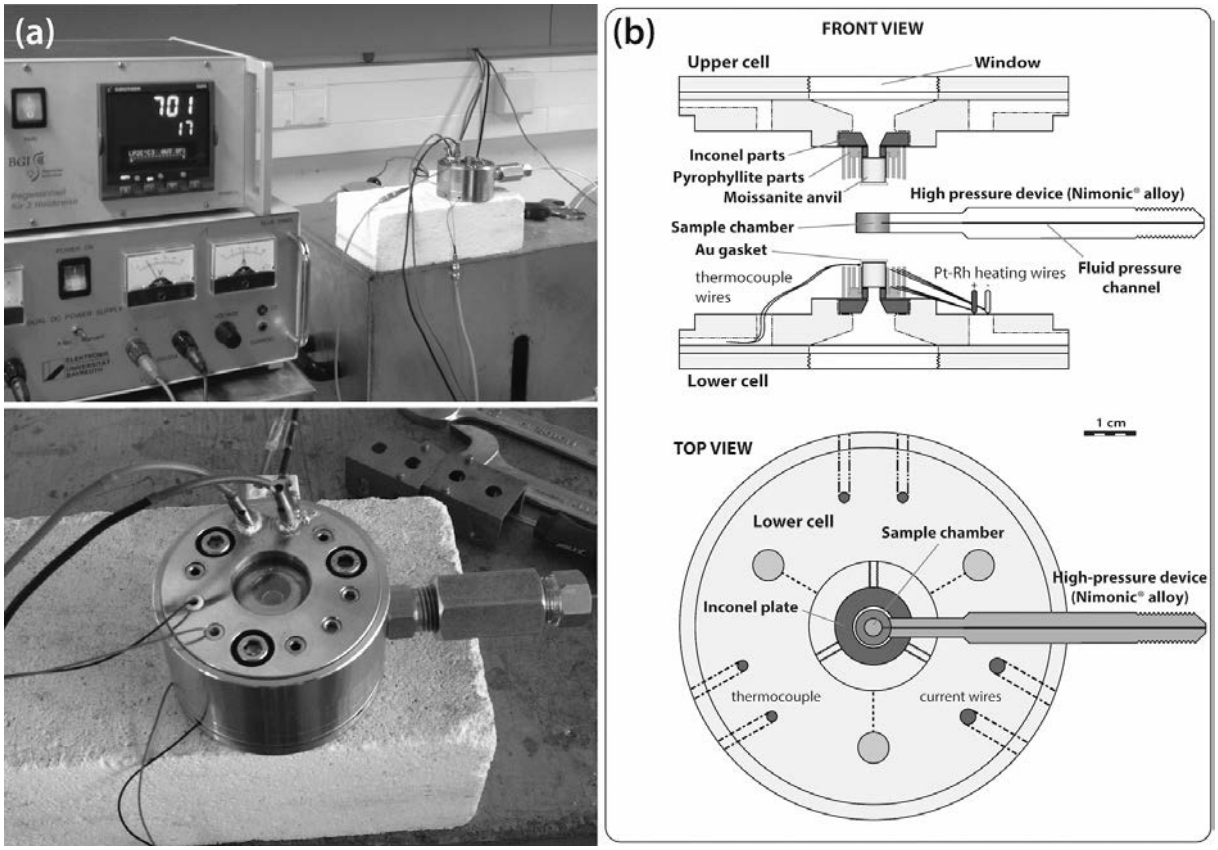

Fig. 3.8-15: (a) Test of the hydrothermal moissanite cell at 700 °C and 1000 bar. (b) Construction drawing of the moissanite cell.

The HP-moissanite cell will enable bubble nucleation and bubble growth to be observed in magmas *in situ* under realistic P-T conditions. Future studies will focus on observing the

behaviour of bubbles during various processes in volcanic systems, including: (i) flank collapse (pressure drop due to the sudden reduction of the lithostatic overload), (ii) continuous eruptions (continuous drop in pressure with either constant or exponentially decaying rate), and (iii) eruption triggering by distant earthquakes (small, sinusoidal pressure perturbations will simulate the effect of seismic waves on a magma chamber before eruption, giving insights into bubble nucleation at small supersaturations).

i. *Potential new technique for imaging dislocations in a natural olivine by electron channeling contrast in a conventional field emission SEM (Y. Li, N. Miyajima and F. Heidelbach)*

Transmission electron microscopy (TEM) is one of the most established methods for characterizing individual dislocations in olivine. While SEM can be an alternative to detect dislocations in olivine, the conventional dislocation decoration method requires oxidizing the sample to precipitate magnetite on the dislocations and this process irreversible damages the sample. Here we report electron channeling contrast imaging (ECCI) to visualize individual dislocations in natural olivine by scanning electron microscopy (SEM). The imaging technique, based on orientation contrast in back-scattered electron (BSE) images, provides an alternative to TEM for characterizing dislocations in olivine.

A natural olivine from the Finero lherzolite was examined in a field emission SEM. The bulk rock specimen was polished mechanically and chemically using a colloidal silica suspension. The polished surface was coated with amorphous carbon. The FE-SEM was operated at 30 kV-acceleration voltage and 120 μm aperture with high current mode. The BSE images were obtained with slow scanning speed (5.5 min/frame) at 6.8 mm working distance. To detect a weak orientation contrast in the vicinity of dislocations at high magnifications of ×8,000 to ×10,000, accurate beam alignments such as aperture alignment and astigmatism correction are necessary. The crystal orientations of the target grains were determined by electron back-scattered diffraction (EBSD). The Kikuchi bands in the EBSD patterns are also indexed by using the SFC software (Courtesy of Prof. T. Kogure/Tokyo).

The ECC images of the olivine (Fig. 3.8-16) display visibility to invisibility of the [100] dislocations along a sub-grain boundary with changing sample-tilt conditions, *i.e.*, with different diffraction conditions. The experimental and simulated EBSD patterns are shown in Fig. 3.8-17. The indexing result indicates a two-beam condition of the (240) Kikuchi band, which is consistent with the visibility criterion of the [100] dislocations. To further improve the ECCI of individual dislocations, more precise orientation determination and its control system are necessary by using selected area electron channeling pattern and a eucentric double tilt stage. On the practical side, high-pressure minerals which cannot be oxidized for dislocation decorations should be ideal targets for the ECCI technique. Also, the observation on the bulk samples in SEM has many advantages over a standard observation on thin foils in TEM.

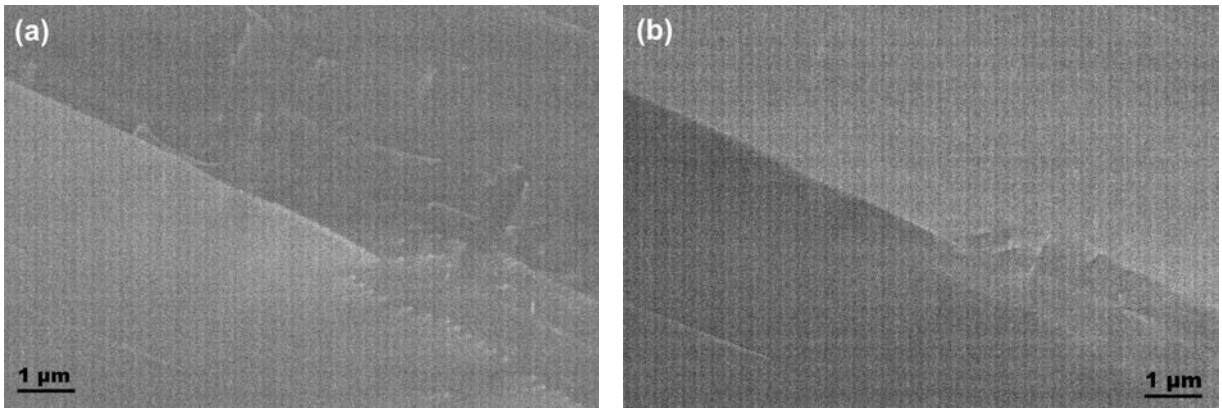

Fig. 3.8-16: ECC images of dislocations along a sub-grain boundary under different sample-tilt conditions of (a) 2° and (b) 1.5°.

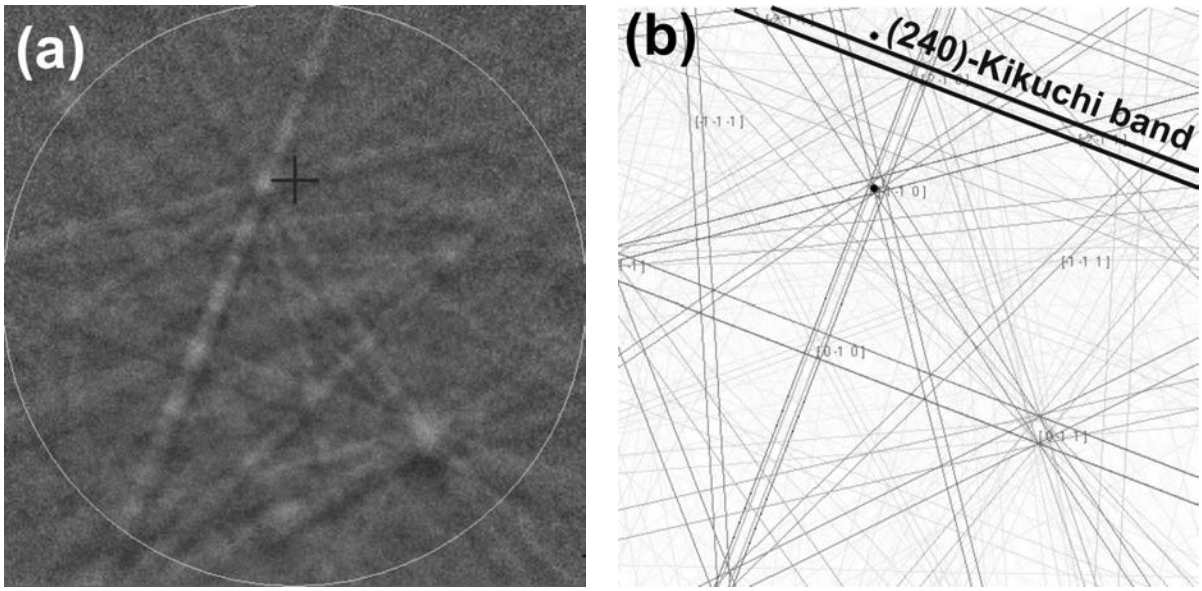

Fig. 3.8-17: (a) The experimental Kikuchi pattern of the ECCI domain in the olivine. (b) The simulation with indexing of the (240) Kikuchi band close to the sample normal direction.

j. *Nitrogen mapping of nano-inclusions in milky diamonds from Juina, Brazil, using BGI's Chemi-STEM (J. Rudloff-Grund and F.E. Brenker/Frankfurt/M.; K. Marquardt and F.V. Kaminsky/Vancouver)*

Diamond is regarded as a chemically inert container that protects inclusions originating from deep parts of the Earth's interior from further chemical reactions with their surroundings. However, the structure of diamond can accommodate nitrogen by different defect mechanisms, ranging from N–vacancy–pairs of different dimensions over N-platelets to N-bearing negative crystals. Based on the first interpretation as being 'empty' these features

were named ‘voidites’. The nature of N in the latter is debated since the 1970s when these negative crystals were mainly studied by electron energy-loss spectroscopy.

We have investigated the spatial nitrogen distribution in milky diamonds from Rio Soriso, Juina area, Brazil, that are considered to originate from a depth greater than 660 km. We used energy dispersive X-ray (EDX) spectroscopy in a scanning transmission electron microscope, Titan^{TM} G^2 80-200 with ChemiSTEM^{TM} technology, to map the nitrogen content with respect to the observed negative crystals (Fig. 3.8-18a). The combination of the FE generated electron beam with a windowless silicon drift detector (SDD) covering a solid-angle of 0.7 srad and an active area of 120 mm^2 results in an energy resolution at 100 000 cps of ≤ 127 eV (Mn Kα) and detection of light elements down to boron (Z = 5) at low concentrations. We found that more than 60 % of the inclusions show a marked N-signal, whereas the remaining negative crystals show no clear increase of the N-signal. We interpret the missing N-signal at locations where negative crystals are clearly present as a result of the FIB preparation process that opened the nanoinclusions near the surface by the impacting Ga-ions. The boxed region in Fig. 3.8-18a was mapped (Fig. 3.8-18b), and the presence and distribution of nitrogen is displayed in Fig. 3.8-18c. To highlight the N-peak significance, an EDX spectrum is displayed in Fig. 3.8-18d.

We conclude that these negative crystals called ‘voidites’ are in all probability generally filled with nitrogen. However, sample preparation may lead to nitrogen loss – supporting former indications of a gaseous N-phase, which caused the long standing debate of ‘empty’ versus ‘N-filled’ negative crystals.

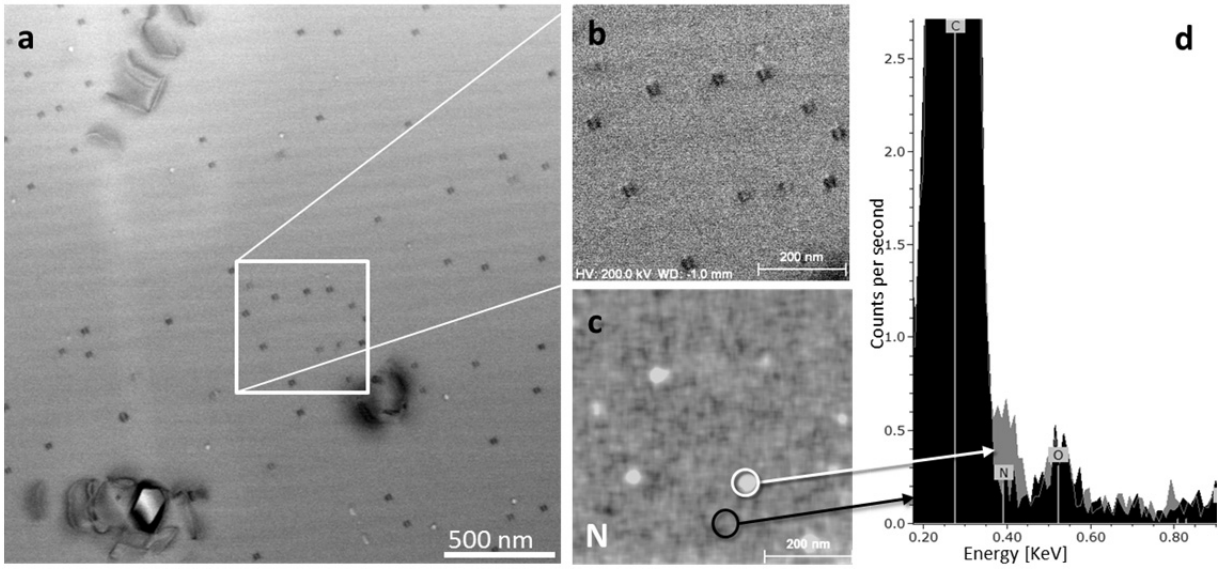

Fig. 3.8-18: (a) Bright-field overview image of the focused ion beam cut electron transparent diamond lamella. (b) Enlarged region mapped using the windowless EDS - SDD detector using its full 120 mm² active area. (c) Nitrogen map. (d) Comparison of two overlaying integrated EDX spectra where the signal was integrated over the areas indicated by the circles in (c). The gray spectrum is from a nitrogen-rich inclusion, whereas the black spectrum is from defect-free nitrogen-poor diamond.

4. Publications, Conference Presentations, Seminars

4.1 Publications (published)

Supplement to **2014** (papers published at the end of 2014):

FEI, H.; WIEDENBECK, M.; YAMAZAKI, D.; KATSURA, T. (2014): No effect of water on oxygen self-diffusion rate in forsterite. Journal of Geophysical Research 119, 7598-7606

KLÉBÉSZ, R.; GRÁCZER, Z.; SZANYI, Gy.; LIPTAI, N.; KOVÁCS, I.; PATKÓ, L.; PINTÉR, Zs.; FALUS, Gy.; WESZTERGOM, V.; SZABÓ, Cs. (2014): Constraints on the thickness and seismic properties of the lithosphere in an extensional setting (Nógrád-Gömör Volcanic Field, Northern Pannonian Basin). Acta Geodaetica et Geophysica 50(2), 133-149

ORIOLO, S.; OYHANTÇABAL, P.; HEIDELBACH, F.; WEMMER, K.; SIEGESMUND, S. (2014): Structural evolution of the Sarandí del Yí shear zone, Uruguay: Kinematics, deformation conditions and tectonic significance. International Journal of Earth Sciences 104, 1759-1777

OVSYANNIKOV, S.V.; KARKIN, A.E.; MOROZOVA, N.V.; SHCHENNIKOV, V.V.; BYKOVA, E.; ABAKUMOV, A.M.; TSIRLIN, A.A.; GLAZYRIN, K.; DUBROVINSKY, L. (2014): A hard oxide semiconductor with a direct and narrow bandgap and switchable *p-n* electrical conduction. Advanced Materials 26, 8185-8191

2015

a) Refereed international journals

AUDÉTAT, A. (2015): Compositional evolution and formation conditions of magmas and fluids related to porphyry Mo mineralization at Climax, Colorado. Journal of Petrology 56, 1519-1546

AUDÉTAT, A.; GARBE-SCHÖNBERG, D.; KRONZ, A.; PETTKE, T.; RUSK, B.; DONOVAN, J.J.; LOWERS, H.A. (2015): Characterisation of a natural quartz crystal as a reference material for microanalytical determination of Ti, Al, Li, Fe, Mn, Ga and Ge. Journal of Geostandards and Geoanalytical Research 39, 171-184

AUZENDE, A.L.; ESCARTIN, J.; WALTE, N.P.; GUILLOT, S.; HIRTH, G.; FROST, D.J. (2015): Deformation mechanisms of antigorite serpentinite at subduction zone conditions determined from experimentally and naturally deformed rocks. Earth and Planetary Science Letters 411, 229-240

BEKHEET, M.F.; DUBROVINSKY, L.; GURLO, A. (2015): Compressibility and structural stability of spinel-type $MnIn_2O_4$. Journal of Solid State Chemistry 230, 301-308

BEYER, C.; FROST, D.J.; MIYAJIMA, N. (2015): Experimental calibration of a garnet-clinopyroxene geobarometer for mantle eclogites. Contributions to Mineralogy and Petrology 169:18, doi: 10.1007/s00410-015-1113-z

BLYTHE, L.S.; DEEGAN, F.M.; FREDA, C.; JOLIS, E.M.; MASOTTA, M.; MISITI, V.; TADDEUCCI, J.; TROLL, V.R. (2015): Rapid CO_2 bubble generation and migration during magma-carbonate interaction. Contributions to Mineralogy and Petrology 169, 42

BOFFA BALLARAN, T.; UENVER-THIELE, L.; WOODLAND, A.B. (2015): Complete substitution of Fe^{2+} by Mg in Fe_4O_5: The crystal structure of the $Mg_2Fe_2O_5$ end-member. American Mineralogist 100, 628-632

BOLLINGER, C.; RATERRON, P.; CORDIER, P.; MERKEL, S. (2015): Deformation of forsterite polycrystals at mantle pressure: comparison with Fe-bearing olivine and the effect of iron on its plasticity. Physics of the Earth and Planetary Interiors 240, 95-104

BONS, P.; BAUR, A.; ELBURG, M.; LINDHUBER, M.J.; MARKS, M.A.W.; SOESOO, A.; VAN MILLIGEN, B.P.; WALTE, N.P. (2015): Layered intrusions and traffic jams. Geology 43, 71-74

BYKOV, M.; BYKOVA, E.; DYADKIN, V.; BAUMANN, D.; SCHNICK, W.; DUBROVINSKY, L.; DUBROVINSKAIA, N. (2015): Crystal structures of cristobalite-type and coesite-type PON refined by single-crystal X-ray diffraction. Acta Crystallographica E71, 1325-1327

BYKOV, M.; BYKOVA, E.; DUBROVINSKY, L.; HANFLAND, M.; LIERMANN, H.-P.; VAN SMAALEN, S. (2015): Pressure-induced normal-incommensurate and incommensurate-commensurate phase transitions in CrOCl. Scientific Reports 5, 9647

BYKOVA, E.; GOU, H.; BYKOV, M.; HANFLAND, M.; DUBROVINSKAIA, N.; DUBROVINSKY, L. (2015): Crystal structures and compressibility of novel iron borides Fe_2B_7 and Fe_xB_{50} synthesized at high pressure and high temperature. Journal of Solid State Chemistry 230, 102-109

CERANTOLA, V.; MCCAMMON, C.; KUPENKO, I.; KANTOR, I.Y.; MARINI, C.; ISMAILOVA, L.; WILKE, M.; SOLOPOVA, N.; CHUMAKOV, A.; PASCARELLI, S.; DUBROVINSKY, L.S. (2015): Spectroscopic study of siderite ($FeCO_3$) to Earth's lower mantle pressures. American Mineralogist 100, 2670-2681

CERANTOLA, V.; WALTE, N.; RUBIE, D.C. (2015): Deformation of a crystalline system with two immiscible liquids: Implications for early core-mantle differentiation. Earth and Planetary Science Letters 417, 67-77

CHEMIA, Z.; DOLEJS, D.; STEINLE-NEUMANN, G. (2015): Thermal effects of variable material properties and metamorphic reactions in a three-component subducting slab, Journal of Geophysical Research 120, 6823-6845

CHEREPANOV, P.V.; MELNYK, I.; SKORB, E.V.; FRATZL, P.; ZOLOTOYABKO, E.; DUBROVINSKAIA, N.; DUBROVINSKY, L. (2015): The use of ultrasonic cavitation for near-surface structuring of robust and low-cost AlNi catalysts for hydrogen production. Green Chemistry 17, 2745-2749

CONSOLMAGNO, G.J.; GOLABEK, G.J.; TURRINI, D.; JUTZI, M.; SIRONO, S.; SVETSOV, V.; TSIGANIS, K. (2015): Is Vesta an intact and pristine protoplanet? Icarus 254, 190-201

DUBROVINSKY, L.; DUBROVINSKAIA, N.; BYKOVA, E.; BYKOV, M.; PRAKAPENKA, V.; PRESCHER, C.; GLAZYRIN, K.; LIERMANN, H.P.; HANFLAND, M. (2015): The most incompressible metal osmium at static pressures above 750 gigapascals. Nature 525, 226-230

DUC-TIN, Q.; KEPPLER, H. (2015): Monazite and xenotime solubility in granitic melts and the origin of the lanthanide tetrad effect. Contributions to Mineralogy and Petrology 169, 8

FARLA, R.J.M.; AMULELE, G.; GIRARD, J.; MIYAJIMA, N.; KARATO, S. (2015): High-pressure and high-temperature deformation experiments on polycrystalline wadsleyite using the rotational Drickamer apparatus. Physics and Chemistry of Minerals 42, 541-558

FEI, H.; KATSURA, T. (2015): Si and O self-diffusion in forsterite and iron-bearing olivine from the perspective of defect chemistry. Physics and Chemistry of Minerals 43(2), 119-126

FISCHER, R.A.; NAKAJIMA, Y.; CAMPBELL, A.J.; FROST, D.J.; HARRIES, D.; LANGENHORST, F.; MIYAJIMA, N.; POLLOK, K.; RUBIE, D.C. (2015): High pressure metal-silicate partitioning of Ni, Co, V, Cr, Si, and O. Geochimica et Cosmochimica Acta 167, 177-194

GARCIA-DOMENE, B.; SANS, J.A.; MANJON, F.J.; OVSYANNIKOV, S.V.; DUBROVINSKY, L.S.; MARTINEZ-GARCIA, D.; GOMIS, O.; ERRANDONEA, D.; MOUTAABBID, H.; LE GODEC, Y.; ORTIZ, H.M.; MUNOZ, A.; RODRIGUEZ-HERNANDEZ, P.; POPESCU, C. (2015): Synthesis and high-pressure study of corundum-type In_2O_3. Journal of Physical Chemistry C 119, 29076-29087

GIRARD, J.; AMULELE, G.; FARLA, R.J.M.; MOHIUDDIN, A.; KARATO, S. (2015): Shear deformation of bridgmanite and magnesiowüstite aggregates at lower mantle conditions. Science 351 (6269), 144-147

HUANG, R.; KEPPLER, H. (2015): Anhydrite stability and the effect of Ca on the behavior of sulfur in felsic magmas. American Mineralogist 100, 257-266

HUMPHREYS, M.; BROOKER, R.; FRASER, D.; BURGISSER, A.; MANGAN, M.; MCCAMMON, C. (2015): Coupled interactions between volatile activity and Fe oxidation state during arc crustal processes. Journal of Petrology 56, 795-814

ISMAILOVA, L.; BOBROV, A.; BYKOV, M.; BYKOVA, E.; CERANTOLA, V.; KANTOR, I.; KUPENKO, I.; MCCAMMON, C.; DYADKIN, V.; CHERNYSHOV, D.; PASCARELLI, S.; CHUMAKOV, A.; DUBROVINSKAIA, N.; DUBROVINSKY, L. (2015): High-pressure synthesis of skiagite-majorite garnet and investigation of its crystal structure. American Mineralogist 100, 2650-2654

JACOBSON, S.A.; WALSH, K.J. (2015): Earth and terrestrial planet formation. – In: BADRO, J.; WALTER, M.J. (Eds.): The early Earth: accretion and differentiation. AGU Geophysical Monograph Series, AGU/John Wiley & Sons, Inc., Washington, DC, USA

JOACHIM, B.; PAWLEY, A.; LYON, I.; MARQUARDT, K.; HENKEL, T.; CLAY, P.; RUZIÉ, L.; BURGESS, R.; BALLENTINE, C. (2015): Experimental partitioning of F and Cl between olivine, orthopyroxene and silicate melt at Earth's mantle conditions. Chemical Geology 416, 65-78, doi: 10.1016/j.chemgeo.2015.08.012

KAMINSKY, F.; RYABCHIKOV, I.D.; MCCAMMON, C.A.; LONGO, M.; ABAKUMOV, A.A.; TURNER, S.; HEIDARI, H. (2015): Oxidation potential in the Earth's lower mantle as recorded by ferropericlase inclusions in diamond. Earth and Planetary Science Letters 417, 49-56

KALLISTOVA, A.; SKALA, R.; HORACEK, I.; MIYAJIMA, N.; MALIKOVA, R. (2015): Influence of sample preparation on the microstructure of tooth enamel apatite. Journal of Applied Crystallography 48, 763-768, doi: 10.1107/S1600576715005208

KATSURA, T.; YOSHINO, T. (2015): Conductivity heterogeneity in the oceanic mantle. – In: KHAN, A.; DESCHAMPS, F.; KAWAI, K. (Eds.): The Earth's Heterogeneous Mantle. Springer -Verlag Berlin, 173-204

KAWAZOE, T.; BUCHEN, J.; MARQUART, H. (2015): Synthesis of large wadsleyite single crystals by solid-state recrystallization. American Mineralogist 100, 2336-2339

KICHANOV, S.E.; KOZLENKO, D.P.; WASICKI, J.; NAWROCIK, W.; DUBROVINSKY, L.S.; LIERMANN, H.P.; MORGENROTH, W.; SAVENKO, B.N. (2015): The polymorphic phase transformations in the chlorpropamide under pressure. Journal of Pharmaceutical Sciences 104, 81-86

KING, S.D.; FROST, D.J.; RUBIE, D.C. (2015): Why cold slabs stagnate in the transition zone. Geology 43, 231-234

KOZLENKO, D.P.; DANG, N.T.; KICHANOV, S.E.; LUKIN, E.V.; PASHAYEV, A.M.; MAMMADOV, A.I.; JABAROV, S.H.; DUBROVINSKY, L.S.; LIERMANN, H.P.; MORGENROTH, W. (2015): Competing magnetic and structural states in multiferroic YMn_2O_5 at high pressure. Physical Review B 92, 134409

KULIK, E.; NISHIYAMA, N.; MASUNO, A.; ZUBAVICHUS, Y.; MURZIN, V.; KHRAMOV, E.; YAMADA, A.; OHFUJI, H.; WILLE, H.-C.; IRIFUNE, T.; KATSURA, T. (2015): A complete solid solution with rutile-type structure in SiO_2–GeO_2 system at 12 GPa and 1600 °C. Journal of the American Ceramic Society, 98 (12), 4111-4116

KUPENKO, I.; MCCAMMON, C.; SINMYO, R.; CERANTOLA, V.; POTAPKIN, V.; CHUMAKOV, A.I.; KANTOR, A.; RÜFFER, R.; DUBROVINSKY, L. (2015): Oxidation state of the lower mantle: *in situ* observations of the iron electronic configuration in bridgmanite at extreme conditions. Earth and Planetary Science Letters 423, 78-86

KUPENKO, I.; STROHM, C.; MCCAMMON, C.; CERANTOLA, V.; GLAZYRIN, K.; PETITGIRARD, S.; VASIUKOV, D.; APRILIS, G.; CHUMAKOV, A.; RÜFFER, R.; DUBROVINSKY, L. (2015): Time differentiated nuclear resonance spectroscopy coupled with pulsed laser heating in diamond anvil cells. Reviews of Scientific Instruments 86, 114501, 1-8

KUSIAK, M.A.; DUNKLEY, D.J.; WIRTH, R.; WHITEHOUSE, M.J.; WILDE, S.A.; MARQUARDT, K. (2015): Metallic lead nanoparticles discovered in ancient zircon. PNAS 112 (16), doi: 10.1073/pnas.1415264112

LI, W.; AUDÉTAT, A.; ZHANG, J. (2015): The role of evaporites in the formation of magnetite-apatite deposits along the Middle and Lower Yangtze River, China: evidence from LA-ICP-MS analysis of fluid inclusions. Ore Geology Reviews 67, 264-278

LI, Y.; AUDÉTAT, A. (2015): Effects of temperature, silicate melt composition, and oxygen fugacity on the partitioning of V, Mn, Co, Ni, Cu, Zn, As, Mo, Ag, Sn, Sb, W, Au, Pb, and Bi between sulfide phases and silicate melt. Geochimica et Cosmochimica Acta 162, 25-45

LI, Y.; WIEDENBECK, M.; HUANG, R.; KEPPLER, H. (2015): Nitrogen distribution between aqueous fluids and silicate melts. Earth and Planetary Science Letters 411, 218-228

LIERMANN, H.-P.; KONOPKOVA, Z.; MORGENROTH, W.; GLAZYRIN, K.; BEDNARCIK, J.; MCBRIDE, E.E.; FRANZ, H. (2015): The Extreme Conditions Beamline P02.2 and the Extreme Conditions Science Infrastructure at PETRA III. Journal of Synchrotron Radiation 22(4), 908-924

LIU, X.; XIONG, X.; AUDÉTAT, A.; LI, Y. (2015): Partitioning of Cu between mafic minerals, Fe-Ti oxides and intermediate to felsic melts. Geochimica et Cosmochimica Acta 151, 86-102

MARGOT, J.-L.; PRAVEC, P.; TAYLOR, P.A.; CARRY, B.; JACOBSON, S.A. (2015): Properties of asteroid systems: binaries, triples, and pairs. – In: MICHEL, P.; DEMEO, F.E.; BOTTKE W.F. (Eds.): Asteroids IV. U. Arizona-Press, Tucson, AZ, USA

MARQUARDT, H.; SPEZIALE, S.; KOCH-MÜLLER, M.; MARQUARDT, K.; CAPITANI, G. (2015): Structural insights and elasticity of single-crystal antigorite from high-pressure Raman and Brillouin spectroscopy measured in the (010) plane. American Mineralogist 100, 1932-1929

MARQUARDT, H.; MIYAGI, L. (2015): Slab stagnation in the shallow lower mantle linked to an increase in mantle viscosity. Nature Geoscience 8, 311-314, doi: 10.1038/ngeo2393

MARQUARDT, K.; ROHRER, G.S.; MORALES, L.; RYBACKI, E.; MARQUARDT, H.; LIN, B. (2015): The most frequent interfaces in olivine aggregates: The GBCD and its importance for grain boundary related processes. Contributions to Mineralogy and Petrology, 170, 40, doi: 10.1007/s00410-015-1193-9

MARTIN, A.P.; PRICE, R.C.; COOPER, A.F.; MCCAMMON, C.A. (2015): Petrogenesis of the rifting Southern Victoria Land lithospheric mantle, Antarctica, inferred from petrography, geochemistry, thermobarometry and oxybarometry of peridotite and pyroxenite xenoliths from Mount Morning. Journal of Petrology 56, 193-226

MASOTTA M.; KEPPLER H. (2015): Anhydrite solubility in differentiated arc magmas. Geochimica et Cosmochimica Acta 185, 79-102

MCGOWAN, N.M.; GRIFFIN, W.L.; GONZÁLEZ-JIMÉNEZ, J.M.; BELOUSOVA, E.; AFONSO, J.C.; SHI, R.; MCCAMMON, C.A.; PEARSON, N.J.; O'REILLY, S.Y. (2015): Tibetan chromitites: excavating the slab graveyard. Geology 43, 179-182

MERLINI, M.; HANFLAND, M.; SALAMAT, A.; PETITGIRARD, S.; MUELLER, H. (2015): The crystal structures of $Mg_2Fe_2C_4O_{13}$, with tetrahedrally coordinated carbon, and $Fe_{13}O_{19}$, synthesized at deep mantle conditions. American Mineralogist 100(8-9), 2001-2004

MILLOT, M.; DUBROVINSKAIA, N.; ČERNOK, A.; BLAHA, S.; DUBROVINSKY, L.; BRAUN, D.G.; CELLIERS, P.M.; COLLINS, G.W.; EGGERT, J.H.; JEANLOZ, R. (2015): Melting of silica at planetary interior conditions using shock compression of stishovite. Science 347, 418-420

MIYAHARA, M.; OHTANI, E.; EL GORESY, A.; LIN, Y.; FENG, L.; ZHANG, J.-C.; GILLET, Ph.; NAGASE, T.; MUTO, J.; NISHIJIMA, M. (2015): Unique diamonds in an ureilite from Almahata 2008 TC_3 asteroid. Geochimica et Cosmochimica Acta 163, 14-26

MIYAJIMA, N.; KAWAZOE, T. (2015): Dislocation microstructures in simple-shear-deformed wadsleyite at transition-zone conditions: Weak-beam dark-field TEM characterization of dislocations on the (010) plane. American Mineralogist 100, 2749-2752

MOLLO, S.; MASOTTA, M.; FORNI, F.; BACHMANN, O.; DE ASTIS, G.; MOORE, G.; SCARLATO, P. (2015): A K-feldspar–liquid hygrometer specific to alkaline differentiated magmas. Chemical Geology 392, 1-8

MOOKHERJEE, M.; SPEZIALE, S.; MARQUARDT, H.; JAHN, S.; WUNDER, B.; KOCH-MÜLLER, M.; LIERMANN, H.-P. (2015): Equation of state and elasticity of the 3.65 Å phase – a candidate cause of the seismic X-discontinuity. American Mineralogist 100, 2199-2208

MORBIDELLI, A.; LAMBRECHTS, M.; JACOBSON, S.A.; BITSCH, B. (2015): The great dichotomy of the solar system: small terrestrial embryos and massive giant planet cores. Icarus 258, 418-429

MOROZOVA, N.V.; KARKIN, A.E.; OVSYANNIKOV, S.V.; UMEROVA, Y.A.; SHCHENNIKOV, V.V.; MITTAL, R.; THAMIZHAVEL, A. (2015): Electronic transport properties of MFe$_2$As$_2$ (M = Ca, Eu, Sr) at ambient and high pressures up to 20 GPa. Superconductor Science and Technology 28, 125010

MOROZOVA, N.V.; SHCHENNIKOV, V.V.; OVSYANNIKOV, S.V. (2015): Features and regularities in behavior of thermoelectric properties of rare-earth, transition and other metals under high pressure up to 20 GPa. Journal of Applied Physics 118, 225901

MROSKO, M.; KOCH-MÜLLER, M.; MCCAMMON, C.; RHEDE, D.; SMYTH, J.; WIRTH, R. (2015): Water, iron, redox environment: Effects on the wadsleyite-ringwoodite phase transition. Contributions to Mineralogy and Petrology 170:9, 1-12

NI, H.; CHEN, Q.; KEPPLER, H. (2015): Electrical conductivity measurements of aqueous fluids under pressure with a hydrothermal diamond anvil cell. Reviews of Scientific Instruments 85, 115107

NI, H.W.; HUI, H.; STEINLE-NEUMANN, G. (2015): Transport properties of silicate melts. Reviews of Geophysics 53, 715-744

NIMIS, P.; GONCHAROV, A.; IONOV, D.A.; MCCAMMON, C. (2015): Fe^{3+} partitioning systematics between orthopyroxene and garnet in mantle peridotite xenoliths and implications for thermobarometry of oxidized and reduced mantle rocks. Contributions to Mineralogy and Petrology 169:6, 1-18

OHUCHI, T.; KAWAZOE, T.; HIGO, Y.; FUNAKOSHI, K.; SUZUKI, A.; KIKEGAWA, T.; IRIFUNE, T. (2015): Dislocation-accommodated grain boundary sliding as the major deformation mechanism of olivine in the Earth's upper mantle. Science Advances 1, e1500360

OHUCHI, T.; NISHIHARA, Y.; SETO, Y.; KAWAZOE, T.; NISHI, M.; MARUYAMA, G.; HASHIMOTO, M.; HIGO, Y.; FUNAKOSHI, K.; SUZUKI, A.; KIKEGAWA, T.; IRIFUNE, T. (2015): *In situ* observation of crystallographic preferred orientation of deforming olivine at high pressure and high temperature. Physics of the Earth and Planetary Interiors 243, 1-21

OVSYANNIKOV, S.V.; MOROZOVA, N.V.; KOROBEINIKOV, I.V.; LUKYANOVA, L.N.; MANAKOV, A.Y.; LIKHACHEVA, A.Y.; ANCHAROVA, A.I.; VOKHMYANIN, A.P.; BERGER, I.F.; USOV, O.A.; KUTASOV, V.A.; KULBACHINSKII, V.A.; OKADA, T.; SHCHENNIKOV, V.V. (2015): Enhanced power factor and high-pressure effects in $(Bi,Sb)_2(Te,Se)_3$ thermoelectrics. Applied Physics Letters 106, 143901

OVSYANNIKOV, S.V.; BYKOVA, E.; BYKOV, M.; WENZ, M.D.; PAKHOMOVA, A.S.; GLAZYRIN, K.; LIERMANN, H.-P.; DUBROVINSKY, L. (2015): Structural and vibrational properties of single crystals of Scandia, Sc_2O_3 under high pressure. Journal of Applied Physics 118, 165901

PAMATO, M.G.; MYHILL, R.; BOFFA BALLARAN, T.; FROST, D.J.; HEIDELBACH, F.; MIYAJIMA, N. (2015): Lower-mantle water reservoir implied by the extreme stability of a hydrous aluminosilicate. Nature Geoscience 8, 75-79

PAMATO, M.G.; KURNOSOV, A.; BOFFA BALLARAN, T.; TROTS, D.M.; CARACAS, R.; FROST, D.J. (2015): Hexagonal $Na_{0.41}[Na_{0.125}Mg_{0.79}Al_{0.085}]_2[Al_{0.79}Si_{0.21}]_6O_{12}$ (NAL phase): Crystal structure refinement and elasticity. American Mineralogist 99(8-9), 1562-1569

PETITGIRARD, S.; MALFAIT, W.; SINMYO, R.; KUPENKO, I.; HENNET, L.; HARRIES, D.; DANE, T.; BURGHAMMER, M.; RUBIE, D.C. (2015): Fate of $MgSiO_3$ melts at core-mantle boundary conditions. PNAS 112(46), 14186-14190

PINTÉR, Zs.; PATKÓ, L.; DOUKAM, T.J.; KOVÁCS, I.; TCHAOUNKE, J.P.; FALUS, Gy.; KONC, Z.; TOMMASI, A.; BAROU, F.; MIHÁLY, J.; NÉMETH, Cs. (2015): Characterization of the sub-continental lithospheric mantle beneath the Cameroon Volcanic Line inferred alkaline basalt hosted peridotite xenoliths from Barombi Mbo and Nyos Lakes. Journal of African Earth Sciences 111, 170-193

PRESCHER, C.; DUBROVINSKY, L.; BYKOVA, E.; KUPENKO, I.; GLAZYRIN, K.; KANTOR, A.; MCCAMMON, C.; MOOKHERJEE, M.; NAKAJIMA, Y.; MIYAJIMA, N.; SINMYO, R.; CERANTOLA, V.; DUBROVINSKAIA, N.; PRAKAPENKA, V.; RÜFFER, R.; CHUMAKOV, A.; HANFLAND, M. (2015): High Poisson's ratio of Earth's inner core explained by carbon alloying. Nature Geoscience 8, 220-223

RASHCHENKO, S.V.; KURNOSOV, A.; DUBROVINSKY, L.; LITASOV, K.D. (2015): Revised calibration of the $Sm:SrB_4O_7$ pressure sensor using the Sm-doped yttrium-aluminum garnet primary pressure scale. Journal of Applied Physics 117(14), 145902

RAZA, Z.; SHULUMBA, N.; CAFFREY, N.M.; DUBROVINSKY, L.; ABRIKOSOV, I.A. (2015): First-principles calculations of properties of orthorhombic iron carbide Fe_7C_3 at the Earth's core conditions. Physical Review B, 91, 214112

ROBERGE, M.; BUREAU, H.; BOLFAN-CASANOVA, N.; FROST, D.J.; RAEPSAET, C.; SURBLE, S.; KHODJA, H.; AUZENDE, A.-L.; FIQUET, G. (2015): Is the transition zone a deep reservoir for fluorine? Earth and Planetary Science Letters 429, 25-32

ROSENTHAL, A.; HAURI, E.H.; HIRSCHMANN, M.M. (2015): Experimental determination of C, F, and H partitioning between upper minerals and carbonated basalt, CO_2/Ba and CO_2/Nb systematics of partial melting, and the CO_2 contents of basaltic source regions. Earth and Planetary Science Letters 412, 77-87

ROZEL, A.; GOLABEK, G.J.; NÄF, R.; TACKLEY, P.J. (2015): Formation of ridges in a stable lithosphere in mantle convection models with a visco-plastic rheology. Geophysical Research Letters 42, 4770-4777

RUBIE, D.C.; JACOBSON, S.A. (2015): Mechanisms and geochemical models of core formation. – In: TERASAKI, H.; FISCHER, R. (Eds.): Deep Earth: Physics and Chemistry of the Lower Mantle and Core. AGU Geophysical Monograph Series, AGU/John Wiley & Sons, Inc., Washington, DC, USA

RUBIE, D.C.; NIMMO, F.; MELOSH, H.J. (2015): Formation of the Earth's core. – In: STEVENSON, D.J. (Ed.): Treatise on Geophysics 2nd Edition, Vol. 9: Evolution of the Earth. Elsevier, Amsterdam, 43-79

RUBIE, D.C.; JACOBSON, S.A.; MORBIDELLI, A.; O'BRIEN D.P.; YOUNG, E.D.; DE VRIES, J.; NIMMO, F.; PALME, H.; FROST, D.J. (2015): Accretion and differentiation of the terrestrial planets with implications for the compositions of early-formed solar system bodies and accretion of water. Icarus 248, 89-108

SCHEIRICH, P.; PRAVEC P.; JACOBSON, S.A.; DURECH, J.; KUSNIRA P.; HORNOCH, K.; MOTTOLA, S.; MOMMERT, M.; HELLMICH, S.; PRAY, D.; POLISHOOK, D.; KRUGLY, YU.N.; INASARIDZE, R.YA.; KVARATSKHELIA, O.I.; AYVAZIAN, V.; SLYUSAREV, I.; PITTICHOVA, J.; JEHIN, E.; MANFROID, J.; GILLON, M.; GALAD, A.; POLLOCK, J.; LICANDRO, J.; ALI-LAGOA, V.; BRINSFELD, J.; MOLOTOV, I.E. (2015): The binary near-Earth asteroid 175706 (1996 FG3) – An observational constraint on its orbital evolution. Icarus 245, 56-63

SERGHIOU, G.; JI, G.; ODLING, N.; REICHMANN, H.J.; FROST, D.J.; WRIGHT, J.P. (2015): Synthesis and high-resolution study distinguishing between very similar interstitial iron nitride structures. High Pressure Research 35, 28-36

SOLFERINO, G.F.D.; GOLABEK, G.J.; NIMMO, F.; SCHMIDT, M.W. (2015): Fast grain growth of olivine in liquid Fe-S and the formation of pallasites with rounded olivine grains. Geochimica et Cosmochimica Acta 162, 259-275

SOLOPOVA, N.A.; DUBROVINSKY, L.; SPIVAK, A.V.; LITVIN, Y.A.; DUBROVINSKAIA, N. (2015): Melting and decomposition of $MgCO_3$ at pressures up to 84 GPa. Physics and Chemistry of Minerals 42, 73-81

SOLOPOVA, N.A.; DUBROVINSKAIA, N.; DUBROVINSKY, L. (2015): Synthesis of nanocrystalline diamond from glassy carbon balls. Journal of Crystal Growth 412, 54-59

SPIVAK, A.V.; SOLOPOVA, N.A.; DUBROVINSKY, L.S.; LITVIN, Yu.A. (2015): The system $MgCO_3$-$FeCO_3$-$CaCO_3$-Na_2CO_3 at 12-23 GPa: Phase relations and significance for the genesis of ultradeep diamonds. Doklady Earth Sciences 464, 946-950

SPIVAK, A.; SOLOPOVA, N.; DUBROVINSKY, L.; LITVIN, Yu. (2015): Melting relations of multicomponent carbonate $MgCO_3$-$FeCO_3$-$CaCO_3$-Na_2CO_3 system at 12-26 GPa: application to deeper mantle diamond formation. Physics and Chemistry of Minerals 42, 817-824

STAGNO, V.; FROST, D.J.; MCCAMMON, C.A.; MOHSENI, H.; FEI, Y. (2015): The oxygen fugacity at which graphite or diamond forms from carbonate-bearing melts in eclogitic rocks. Contributions to Mineralogy and Petrology 169:16, doi 10.1007/s00410-015-1111-1

SWAMY, V.; OOI, J.B.; KURNOSOV, A.; DUBROVINSKY, L.S.; KUZNETSOV, A.Y.; NOOR, A.F.M. (2015): Hydrostatic compression of graphite oxide to 49 GPa: A Raman spectroscopic study. MRS Proceedings 1727, mrsf14-1727-k10-10, doi: 10.1557/opl.2015.261

THOMAS, S.-M.; WILSON, K.; KOCH-MÜLLER, M.; HAURI, E.; MCCAMMON, C.; JACOBSEN, S.D.; LAZARZ, J.; RHEDE, D.; REN, M.; BLAIR, N.; LENZ, S. (2015): Quantification of water in majoritic garnet. American Mineralogist 100, 1084-1092

VLČEK, V.; EISENBERG, H.R.; STEINLE-NEUMANN, G.; KRONIK, L.; BAER, R. (2015): Deviations from piecewise linearity in the solid-state limit with approximate density functionals. Journal of Chemical Physics 142, 034107

VLČEK, V.; STEINLE-NEUMANN, G.; LEPPERT, L.; ARMIENTO, R.; KÜMMEL, S. (2015): Improved ground-state electronic structure and optical dielectric constants with a semilocal exchange functional. Physical Review B 91, 035107

WALSH, K.J.; JACOBSON, S.A. (2015): Formation and dynamics of asteroid binaries. – In: MICHEL, P.; DEMEO, F.E.; BOTTKE, W.F. (Eds.): Asteroids IV. U. Arizona-Press, Tucson, AZ, USA

WANG Z.; LAURENZ, V.; PETITGIRARD S.; BECKER, H. (2016): Earth's moderately volatile element composition may not be chondritic: Evidence from In, Cd and Zn. Earth and Planetary Science Letters 435, 136-146

WESSEL, P.; MATTHEWS, K.J.; MÜLLER, R.D.; MAZZONI, A.; WHITTAKER, J.M.; MYHILL, R.; CHANDLER, M.T. (2015): Semiautomatic fracture zone tracking. Geochemistry, Geophysics, Geosystems 16, 2462-2472. doi: 10.1002/2015GC005853

YOSHIOKA, T.; MCCAMMON, C.; SHCHEKA, S.; KEPPLER, H. (2015): The speciation of carbon monoxide in silicate melts and glasses. American Mineralogist 100, 1641-1644

YUSENKO, K.V.; BYKOVA, E.; BYKOV, M.; GROMILOV, S.A.; KURNOSOV, A.V.; PRESCHER, C.; PRAKAPENKA, V.B.; HANFLAND, M.; VAN SMAALEN, S.; MARGADONNA, S.; DUBROVINSKY, L.: (2015): Compressibility of Ir-Os alloys under high pressure. Journal of Alloys and Compounds 622, 155-161

4.2 Publications (submitted, in press)

BEYER, C.; FROST, D.: The depth of sub-lithopsheric diamond formation and the redistribution of carbon in the deep mantle. Science (submitted)

BEYER, C.; KLEMME, S.; GRÜTZNER, T.; IRELAND, T.R.; MAGEE, C.W.; FROST, D.: Fluorine partitioning between eclogitic garnet, clinopyroxene, and melt at upper mantle conditions. Chemical Geology (submitted)

BOLLINGER, C.; RATERRON, P.; CASTELNAU, O.; DETREZ, F.; MERKEL, S.: Textures in deforming forsterite aggregates up to 8 GPa and 1673 K. Physics and Chemistry of Minerals (in press)

BYKOVA, E.; DUBROVINSKY, L.; DUBROVINSKAIA, N.; BYKOV, M.; MCCAMMON, C.; OVSYANNIKOV, S.V.; LIERMANN, H.-P.; KUPENKO, I.; CHUMAKOV, A.I.; RÜFFER, R.; HANFLAND, M.; PRAKAPENKA, V.: Structural complexity of simple Fe_2O_3 oxide at high pressures and temperatures. Nature Communications (submitted)

ČERNOK, A.; MARQUARDT, K.; CARACAS, R.; BYKOVA, E.; HABLER, G.; LIERMANN, H.-P.; HANFLAND, M.; DUBROVINSKY, L.: High-pressure behaviour of cristobalite: bridging the gap towards the "seifertite enigma". American Mineralogist (submitted)

CHANG, Y.-Y.; JACOBSEN, S.D.; BINA, C.R.; THOMAS, S.-M.; SMYTH, J.R.; FROST, D.J.; BOFFA BALLARAN, T.; MCCAMMON, C.A.; HAURI, E.H.; INOUE, T.; MENG, Y.; DERA, P.: Comparative compressibility of hydrous wadsleyite and ringwoodite: Effect of H_2O and implications for detecting water in the transition zone. Journal of Geophysical Research – Solid Earth (in press)

CHANTEL, J.; MANTHILAKE, G.M.; FROST, D.J.; BEYER, C.; BOFFA BALLARAN, T.; JING, Z.; WANG, Y.: Elastic wave velocities in polycrystalline $Mg_3Al_2Si_3O_{12}$-pyrope garnet to 24 GPa and 1300 K. American Mineralogist (submitted)

DE VRIES, J.; NIMMO, F.; MELOSH, H.J.; JACOBSON, S.A.; MORBIDELLI, A.; RUBIE, D.C.: Impact-induced melting during the accretion of the Earth. Progress in Earth and Planetary Sciences (submitted)

DORFMAN, S.M.; DUTTON, S.E.; POTAPKIN, V.; CHUMAKOV, A.I.; RUEFF, J.-P.; CHOW, P.; XIAO, Y.; CAVA, R.J.; DUFFY, T.S.; MCCAMMON, C.A.; GILLET, P.: Electronic transitions of iron in almandine-composition glass to 91 GPa. American Mineralogist (submitted)

FEI, H.; KOIZUMI, S.; SAKAMOTO, N.; HASHIGUCHI, M.; YURIMOTO, H.; MARQUARDT, K.; MIYAJIMA, N.; YAMAZAKI, D.; KATSURA, T.: New constraints on the transition from diffusion to dislocation creep in the upper-mantle. Earth and Planetary Science Letters (in press), doi: 10.1016/j.epsl.2015.11.014

FROST, D.J.; MYHILL, R.: Chemistry of the lower mantle. - In: TERASAKI, H.; FISCHER, R. (Eds): Deep Earth: Physics and Chemistry of the Lower Mantle and Core, AGU Geophysical Monograph Series, AGU/John Wiley & Sons, Inc., Washington, DC, USA (in press)

GARCIA-DOMENE, B.; SANS, J.A.; MANJON, F.J.; OVSYANNIKOV, S.V.; DUBROVINSKY, L.S.; MARTINEZ-GARCIA, D.; GOMIS, O.; ERRANDONEA, D.; MOUTAABBID, H.; LE GODEC, Y.; ORTIZ, H.M.; MUNOZ, A.; RODRIGUEZ-HERNANDEZ, P.; POPESCU, C.: Synthesis and high-pressure study of corundum-type In_2O_3. Journal of Physical Chemistry C (submitted)

GENTILI, S.; BIAGIONI, C.; COMODI, P.; PASERO, M.; MCCAMMON, C.; BONADIMAN, C.: Ferri-kaersutite, $NaCa_2(Mg_3TiFe^{3+})(Si_6Al_2)O_{22}O_2$, a new anhydrous amphibole from Harrow Peaks, Northern Victoria Land, Antarctica. American Mineralogist (submitted)

GILLMANN, C.; GOLABEK, G.J.; TACKLEY, P.J.: Effect of a single large impact on the coupled atmosphere-interior evolution of Venus. Icarus (submitted)

GUO, X.; ZHANG, L.; BEHRENS, H.; NI, H.W.: Probing the status of felsic magma reservoirs: constraints from the P-T-H_2O dependences of electrical conductivity of rhyolitic melt. Earth and Planetary Science Letters (in press)

GUTIERREZ, X.; SCHIAVI, F.; KEPPLER, H.: The adsorption of HCl on volcanic ash. Earth and Planetary Science Letters (submitted)

IDRISSI, H.; BOLLINGER, C.; BOIOLI, F.; SCHRYVVERS, N.; CORDIER, P.: Low temperature plasticity of olivine revisited with *in situ* TEM nanomechanical testing. Science Advances (in press)

ISHII, T.; SHI, L.; HUANG, R.; TSUJINO, N.; DRUZHBIN, D.; MYHILL, R.; LI, Y.; WANG, L.; YAMAMOTO, T.; MIYAJIMA, N.; KAWAZOE, T.; NISHIYAMA, N.; LIU, Z.; IRIFUNE, T.; HIGO, Y.; TANGE, Y.; KATSURA, T.: Generation of pressures over 40 GPa using Kawai-type multi-anvil apparatus with tungsten carbide anvils. Review of Scientific Instruments (submitted)

ISHII, T.; SHI, L.; HUANG, R.; TSUJINO, N.; DRUZHBIN, D.; MYHILL, R.; LI, Y.; WANG, L.; YAMAMOTO, T.; MIYAJIMA, N.; KAWAZOE, T.; NISHIYAMA, N.; HIGO, Y.; TANGE, Y.; KATSURA, T.: Generation of pressures over 40 GPa using Kawai-type multi-anvil apparatus with tungsten carbide anvils. Review of Scientific Instruments (submitted)

JACOBSON, S.A.; MARZARI, F.; ROSSI, A.; SCHEERES, D.J.: Testing the YORP-induced rotational fission hypothesis. Icarus (submitted)

JACOBSON, S.A.; HERNLUND, J.; RUBIE, D.C.; MORBIDELLI, A.: Formation, stratification, and mixing of Earth's core. Nature (submitted)

KAWAZOE, T.; CHAUDHARI, A.; SMYTH, J.R.; MCCAMMON, C.: Coupled substitution of Fe^{3+} and H^{+} for Si in wadsleyite: a study by polarized infrared and Mössbauer spectroscopies and single-crystal X-ray diffraction. American Mineralogist (submitted)

KEPPLER, R.; STIPP, M.; BEHRMANN, J.H.; ULLEMEYER, K.; HEIDELBACH, F.: Deformation inside a subduction channel – Insights from microstructures and crystallographic preferred orientations of eclogites from the Tauern Window, Austria. Journal of Structural Geology (in press)

KEPPLER, H.: Fluids and trace element transport in subduction zones. American Mineralogist (submitted)

LAURENZ, V.; RUBIE, D.C.; FROST, D.J.; VOGEL, A.K.: The importance of sulfur for the behaviour of highly-siderophile elements during Earth's differentiation. Geochimica et Cosmochimica Acta (submitted)

LICHTENBERG, T.; GOLABEK, G.J.; GERYA, T.V.; MEYER, M.R.: The impact of short-lived radionuclides and porosity on the early thermomechanical evolution of planetesimals. Icarus (submitted)

MARQUARDT, K.; ROHRER, G.S.; MORALES, L.F.G.; RYBACKI, E.; MARQUARDT, H.; LIN, B.: The most frequent interfaces in olivine aggregates: The GBCD and its importance for grain boundary related processes. Contributions to Mineralogy and Petrology (accepted)

MARTIN, R.F.; ALARIE, É.; MINARIK, W.; WÁCZEK, Z.; MCCAMMON, C.A.: Titanian magnesio-hastingsite macrocrysts, Lafarge quarry, east-end Montreal: Disequilibrium crystallization in a pseudo-unary system. Canadian Mineralogist (in press)

MASOTTA, M.; KEPPLER, H.; CHAUDHARI, A.: Fluid-melt partitioning of sulfur in differentiated arc magmas and the sulfur yield of explosive volcanic eruptions. Geochimica et Cosmochimica Acta (submitted)

MASOTTA, M.; MOLLO, S.; GAETA, M.; FREDA, C.: Melt extraction in mush zones: the case of crystal-rich enclaves at the Sabatini Volcanic District (central Italy). Lithos (submitted)

MCCAMMON, C.; CARACAS, R.; GLAZYRIN, K.; POTAPKIN, V.; KANTOR, A.; SINMYO, R.; PRESCHER, C.; KUPENKO, I.; CHUMAKOV, A.; DUBROVINSKY, L.: Sound velocities of bridgmanite from density of states determined by nuclear inelastic scattering and first principles calculations. Progress in Earth and Planetary Science (submitted)

MIYAHARA, M.; OHTANI, E.; EL GORESY, A.; GILLET, Ph.: Phase transition processes of olivine and pyroxene in the Martian meteorite Tissint: Clues to origin of ringwoodite-, bridgmanite- and magnesiowüstite-bearing assemblages in shocked Martian meteorites. Geochimica et Cosmochimica Acta (submitted)

MORBIDELLI, A.; BITSCH, B.; CRIDA, A.; GOUNELLE, M.; GUILLOT, T.; JACOBSON, S.A.; JOHANSEN, A.; LAMBRECHTS, M.; LEGA, E.: Fossilized condensation lines in the solar system protoplanetary disk. Icarus (in press)

MYHILL, R.: Excess thermodynamic and elastic properties of mineral and melt solutions: modelling and implications for phase relations and seismic velocities. Contributions to Mineralogy and Petrology (submitted)

MYHILL, R.; OJWANG, D.O.; ZIBERNA, L.; FROST, D.J.; BOFFA BALLARAN, T.; MIYAJIMA, N.: On the P-T-fO_2 stability of Fe_4O_5 and Fe_5O_6 and Fe_4O_5-rich solid solutions. Contributions to Mineralogy and Petrology (submitted)

MYHILL, R.; NOVELLA, D.; FROST, D.J.: Hydrous melting and partitioning in and above the mantle transition zone: insights from water-rich MgO-SiO_2-H_2O experiments. Geochimica et Cosmochimica Acta (submitted)

NAMUR, O.; COLLINET, M.; CHARLIER, B.; GROVE, T.L.; HOLTZ, F.; MCCAMMON, C.: Melting processes and mantle sources of Mercury surface lavas Earth and Planetary Science Letters (submitted)

NOVELLA, D.; DOLEJŠ, D.; MYHILL, R.; PAMATO, M.; MANTHILAKE, G.; FROST, D.J.: Melting phase relations in the systems Mg_2SiO_4-H_2O and $MgSiO_3$-H_2O at upper mantle conditions. Geochimica et Cosmochimica Acta (submitted)

OVSYANNIKOV, S.V.; BYKOV, M.; BYKOVA, E.; KOZLENKO, D.P.; TSIRLIN, A.A.; KARKIN, A.E.; SHCHENNIKOV, V.V.; KICHANOV, S.E.; GOU, H.; ABAKUMOV, A.M.; EGOAVIL, R.; VERBEECK, J.; MCCAMMON, C.; DYADKIN, V.; CHERNYSHOV, D.; SMAALEN, S.V.; DUBROVINSKY, L.S.: Incommensurate crystallographic transition with competing dimeric and trimeric orders in iron oxide Fe_4O_5. Nature Chemistry (submitted)

PAKHOMOVA, A.S.; KRIVOVICHEV S.V.; YUDINTSEV, S.V.; STEFANOVSKY, S.V.: Polysomatism and structural complexity: structure model for murataite-8C, a complex crystalline matrix for the immobilization of high-level radioactive waste. European Journal of Mineralogy (accepted)

PALOT, M.; JACOBSEN, S.D.; TOWNSEND, J.P.; NESTOLA, F.; MARQUARDT, K.; HARRIS, J.W.; STACHEL, T.; MCCAMMON, C.A.; PEARSON, D.G.: Evidence for water in the lower mantle from ferropericlase included in diamond. Nature (submitted)

PAMATO, M.G.; KURNOSOV, A.; BOFFA BALLARAN, T.; FROST, D.J.; ZIBERNA, L.; GIANNINI, M.; SPEZIALE, S., TKACHEV, S.N., ZHURAVLE, K.K., PRAKAPENKA; V.B.: Single crystal elasticity of majoritic garnets: stagnant slabs and thermal anomalies at the base of the transition zone. Earth and Planetary Science Letters (submitted)

POSNER, E.S.; GANGULY, J.; HERVIG, R.: Diffusion kinetics of Cr in spinel: Experimental studies and implications for ^{53}Mn-^{53}Cr cosmochronology. Geochimica et Cosmochimica Acta (in press)

RASSIOS, A.; GRIECO, G.; BATSI, A.; MYHILL, R.; GHIKAS, C.: Preserving the non-preservable geoheritage of the Aliakmon River: A case study in geo-education leading to cutting-edge science. Bulletin of the Geological Society of Greece (submitted)

RAYMOND, S.N.; IZIDORO, A.; BITSCH, B.; JACOBSON, S.A.: Did Jupiter's core form in the innermost parts of the Sun's protoplanetary disk? Monthly Notices of the Royal Astronomical Society (submitted)

ROBINSON, P.; MCENROE, S.A.; MIYAJIMA, N.; KARL, F.; NATHAN, C.: Remanent magnetization, magnetic coupling and indterface ionic configurations of intergrown rhombohedral and cubic Fe-Ti oxides: a short survey. American Mineralogist (in press)

RUBIE, D.C.; JACOBSON, S.A.: Mechanisms and geochemical models of core formation. – In: TERASAKI, H.; FISCHER, R. (Eds): Deep Earth: Physics and Chemistry of the Lower Mantle and Core, AGU Geophysical Monograph Series, AGU/John Wiley & Sons, Inc., Washington, DC, USA (in press)

SINMYO, R.; BYKOVA, E.; OVSYANNIKOV, S.V.; MCCAMMON, C.; KUPENKO, I.; ISMAILOVA, L.; DUBROVINSKY, L.: Discovery of Fe_7O_9: a new iron oxide with a complex monoclinic structure. Nature Communications (submitted)

STECKLOFF, J.K.; JACOBSON, S.A.: The formation striae within cometary dust tails by a sublimation-driven YORP-like effect. Icarus (in press)

VLČEK, V.; EISENBERG, H.; STEINLE-NEUMANN, G.; BAER, R.: Spontaneous charge-carrier localization in extended one-dimensional systems. Physical Review Letters (submitted)

WANG, L.; BLAHA, S.; PINTÉR, S.; FARLA, R.J.M.; KAWAZOE, T.; MIYAJIMA, N.; MICHIBAYASHI, K.; KATSURA, T.: Pressure and temperature dependence of dislocation mobility in the [100](010) and [001](010) slip systems in olivine. Earth and Planetary Science Letters (submitted)

WANG, Z.; LAURENZ, V.; PETITGIRARD, S.; BECKER, H.: Earth's moderately volatile element composition may not be chondritic: Evidence from In, Cd and Zn. Earth and Planetary Science Letters (in press)

WU, Y.; WU, X.; LIN, J.-F.; MCCAMMON, C.A.; XIAO, Y.; CHOW, P.; PRAKAPENKA, V.B.; YOSHINO, T.; ZHAI, S.; QIN, S.: Spin transition of Fe^{3+} in the NAL phase: Implications for the seismic heterogeneities of subducted slabs in the uppermost lower mantle. Earth and Planetary Science Letters (in press)

YOUNG, E.D.; KOHL, I.E.; WARREN, P.H.; RUBIE, D.C.; JACOBSON, S.A.; MORBIDELLI, A.: Oxygen isotopic evidence for vigorous mixing during the Moon-forming giant impact. Science (in press)

4.3 Presentations at scientific institutions and at congresses

AUDÉTAT, A.: 30.04.2015, Eötvös Lorand University, Budapest, Hungary: "Vapor or brine – which fluid does the job?", SEG International Exchange Lecturer talk

AUDÉTAT, A.: 18.-21.05.2015, Geological Society of Nevada Symposium 2015, Reno, USA: "The genesis of Climax-type porphyry Mo deposits: insights from fluid and melt inclusions", SEG International Exchange Lecturer talk

AUDÉTAT, A.: 29.06.2015, University of São Paulo, Brazil: "Magmatic controls on porphyry Cu (±Au, Mo) formation", SEG International Exchange Lecturer talk

AUDÉTAT, A.: 01.-04.07.2015, XXXIII UNESCO-SEG-SGA Latin American Metallogeny Course 2015, 'Hydrothermal systems: a voyage from the source to the ore', Campinas, Brazil: "Introduction to fluid and melt inclusion studies"; "The metal content of magmatic-hydrothermal fluids and its relation to mineralization potential", SEG International Exchange Lecturer talks

AUDÉTAT, A.: 16.-21.08.2015, Goldschmidt 2015, Prague, Czech Republic (*invited*): "The genesis of climax-type porphyry Mo deposits: Insights from fluid and melt inclusions", Goldschmidt Abstracts, 2015, 140

AUDÉTAT, A.: 22.09.2015, James Cook University, Townsville, Australia: "The metal content of magmatic-hydrothermal fluids and its relation to mineralization potential"; "Magmatic controls on porphyry Cu (±Au, Mo) formation", SEG International Exchange Lecturer talks

AUDÉTAT, A.: 24.09.2015, Australian National University, Canberra, Australia: "Magmatic controls on porphyry Cu (±Au, Mo) formation", SEG International Exchange Lecturer talk

AUDÉTAT, A.: 25.09.2015, Australian National University, Canberra, Australia: "The metal content of magmatic-hydrothermal fluids and its relation to mineralization potential", SEG International Exchange Lecturer talk

AUDÉTAT, A.: 16.10.2015, Aristotle University of Thessaloniki, Greece: "The metal content of magmatic-hydrothermal fluids and its relation to mineralization potential"; "Magmatic controls on porphyry Cu (±Au, Mo) formation", SEG International Exchange Lecturer talks

AUDÉTAT, A.: 13.11.2015, University of Bucharest, Romania: "The metal content of magmatic-hydrothermal fluids and its relation to mineralization potential"; "Magmatic controls on porphyry Cu (±Au, Mo) formation", SEG International Exchange Lecturer talks

AUDÉTAT, A.: 02.12.2015, University of Freiberg, Germany: "Magmatic controls on porphyry Cu (±Au, Mo) formation", SEG International Exchange Lecturer talk

BEYER, C.; BOFFA BALLARAN, T.; KURNOSOV, A.; FROST, D.: 16.-21.08.2015, Goldschmidt 2015, Prague, Czech Republic: "P-V-T of complex garnet solid solutions up to 16 GPa and 800 K", Goldschmidt Abstracts, 2015, 285

BOFFA BALLARAN, T.; UENVER-THIELE, L.; SIERSCH, N.; WOODLAND, A.B.: 23.-28.08.2015, The 29th European Crystallographic Meeting ECM29, Rovinj, Croatia: "$Mg_2Fe_2O_5$ a novel breakdown product of $MgFe_2O_4$ at high pressure"

BOFFA BALLARAN, T.; KURNOSOV, A.; FROST, D.J.; MARQUARDT, H.: 02.-04.09.2015, Congresso SIMP, SGI, So.Ge.I, AIV, 'Il Pianeta dinamico: sviluppi e prospettive a 100 anni da Wegener', Firenze, Italy (*keynote lecture*): "The influence of cation substitution on the elastic behaviour of $MgSiO_3$ bridgmanite in the lower mantle"

BOLLINGER, C.; IDRISSI, H.; BOIOLI, F.; CORDIER, P.: 04.-07.10.2015, GeoBerlin 2015, Berlin, Germany[*A]: "*In situ* deformation of olivine in the Transmission Electron Microscope: from dislocation velocity measurements to stress-strain curves"

BOLLINGER, C.; IDRISSI, H.; BOIOLI, F.; CORDIER, P.: 14.-18.12.2015**,** AGU Fall Meeting, San Francisco, USA[*B]: "*In situ* deformation of olivine in the Transmission Electron Microscope: from dislocation velocity measurements to stress-strain curves", Abstract MR23A-2637, 2015

BUCHEN, J.; MARQUARDT, H.; KAWAZOE, T.; BOFFA BALLARAN, T.; KURNOSOV, A.: 26.-27.06.2015, Joint Meeting of the Petrology/Petrophysics and Geochemistry Sections of the Deutsche Mineralogische Gesellschaft, Potsdam, Germany: "High-pressure single-crystal elasticity of wadsleyite: from synthesis to sound wave velocities"

BUCHEN, J.; MARQUARDT, H.; KAWAZOE, T.; KURNOSOV, A.; BOFFA BALLARAN, T.: 16.-21.08.2015, Goldschmidt 2015, Prague, Czech Republic: "Internally consistent high-pressure elasticity of single-crystal $(Mg,Fe)_2SiO_4$ wadsleyite", Goldschmidt Abstracts, 2015, 412

BUCHEN, J.; MARQUARDT, H.; KAWAZOE, T.; BOFFA BALLARAN, T.; SPEZIALE, S.; KURNOSOV, A.: 04.-07.10.2015, GeoBerlin 2015, Berlin, Germany[*A]: "High-pressure single-crystal elasticity of wadsleyite: constraints on seismic anisotropy in the transition zone", p. 105

BYKOV, M.; BYKOVA, E.; DUBROVINSKY, L.; VAN SMAALEN, S.: 30.08.-04.09.2015, Joint AIRAPT-25 & EHPRG-53 Meeting, Madrid, Spain: "Pressure-induced phase transitions in TiOCl: an interplay between low-dimensional magnetism and crystal structure"

BYKOVA, E.; BYKOV, M.; MCCAMMON, C.; OVSYANNIKOV, S.V.; LIERMANN, H.-P.; KUPENKO, I.; CHUMAKOV, A.I.; RÜFFER, R.; HANFLAND, M.; PRAKAPENKA, V.; DUBROVINSKAIA, N.; DUBROVINSKY, L.: 30.08.-04.09.2015, Joint AIRAPT-25 & EHPRG-53 Meeting, Madrid, Spain: "Crystal chemistry of the Fe-O system at high pressure and high temperature

CERANTOLA, V.; BYKOVA, E.; MCCAMMON, C.; MERLINI, M.; DUBROVINSKY, L.: 12.-17.04.2015, European Geosciences Union General Assembly 2015, Vienna, Austria: "Investigation on the stability of $FeCO_3$ down to the core mantle boundary", Geophysical Research Abstracts 17, EGU2015-13699, 2015

CERANTOLA, V.; MCCAMMON, C.; MERLINI, M.; BYKOVA, E.; KUPENKO, I.; ISMAILOVA, L.; CHUMAKOV, A.; KANTOR, I.; DUBROVINSKY, L.; PRESCHER, C.: 14.-18.12.2015, AGU Fall Meeting, San Francisco, USA[*B] (*invited*): "Iron carbonates in the Earth's lower mantle: reality or imagination?", Abstract V14C-04, 2015

ČERNOK, A.; MARQUARDT, K.; BYKOVA, E.; LIERMANN, H.-P.; DUBROVINSKY, L.: 12.-17.04.2015, European Geosciences Union General Assembly 2015, Vienna, Austria: "Compression of α-cristobalite under different hydrostatic conditions", Geophysical Research Abstracts 17, EGU2015-4236, 2015

ČERNOK, A.; MARQUARDT, K.; BYKOVA, E.; LIERMANN, H.-P.; DUBROVINSKY, L.: 16.-20.03.2015, 46th Lunar and Planetary Science Conference, The Woodlands, Houston, USA: "Response of α-cristobalite to high pressures under different hydrostatic conditions", Abstract 1777

CHUST, T.; STEINLE-NEUMANN, G.: 23.-25.09.2015, 4th Joint Workshop on High Pressure, Planetary and Plasma Physics, Bayreuth, Germany: "Crystallizing the Martian magma ocean"

COLLINGS, I.E.; DUBROVINSKAIA, N.; DUBROVINSKY, L.: 23.-28.08.2015, The 29th European Crystallographic Meeting ECM29, Rovinj, Croatia: "Structure-property relationships in multiferroic metal-organic frameworks at high pressure"

COLLINGS, I.E.; DUBROVINSKAIA, N.; DUBROVINSKY, L.: 30.08.-04.09.2015, Joint AIRAPT-25 & EHPRG-53 Meeting, Madrid, Spain: "Structure-property relationships in multiferroic metal-organic frameworks at high pressure"

DORFMAN, S.; POTAPKIN, V.; CHUMAKOV, A.; RUEFF, J.-P.; DUFFY, T.; MCCAMMON, C.; GILLET, P.: 16.-21.08.2015, Goldschmidt 2015, Prague, Czech Republic: "Electronic properties of iron in silicate glasses in the lower mantle", Goldschmidt Abstracts, 2015, 765

DUBROVINSKY, L.: 05.05.2015, Erskine Williamson Day 2015, University of Edinburgh, Center for Science at Extreme Conditions, Edinburgh, U.K.: "Ultra high pressure crystallography"

DUBROVINSKY, L.; ISMAILOVA, L.; BYKOVA, E.; BYKOV, M.; SINMYO, R.; DUBROVINSKAIA, N.: 30.08.-04.09.2015, Joint AIRAPT-25 & EHPRG-53 Meeting, Madrid, Spain: "Stability of Fe,Al bearing bridgmanite in the Earth's lower mantle"

DUCHOSLAV, M.; MARKS, M.; MCCAMMON, C.; MARSCHALL, H.; WENZEL, T.; MARKL, G.: 16.-21.08.2015, Goldschmidt 2015, Prague, Czech Republic: "Changes in tourmaline trace element geochemistry during magmatic differentiation and hydrothermal ore deposition", Goldschmidt Abstracts, 2015, 781

DUCHOSLAV, M.; MARKS, M.A.W.; MCCAMMON, C.; MARSCHALL, H.; WENZEL, T.; MARKL, G.: 04.-07.10.2015, GeoBerlin 2015, Berlin, Germany[*A]: "Major-, minor and trace element variations in tourmaline as monitors for magmatic differentiation, fluid un-mixing and associated ore precipitation"

EL GORESY, A.; LIN, Y.; MIYAHARA, M.; GANNOUN, A.-M.; BOYET, M.; OHTANI, E.; TRIELOFF, M.: 16.-21.08.2015, Goldschmidt 2015, Prague, Czech Republic: "Evidence for change in C/O ratio during evolution of enstatite chondrites", Goldschmidt Abstracts, 2015, 821

FACQ, S.; DANIEL, I.; PETITGIRARD, S.; CARDON, H.; SVERJENSKY, D.: 16.-21.08.2015, Goldschmidt 2015, Prague, Czech Republic: "Solubility of aragonite in aqueous fluids under HP-HT conditions", Goldschmidt Abstracts, 2015, 859

FARLA, R.J.M.; ROSENTHAL, A.; BOLLINGER, C.; PETITGIRARD, S.; KAWAZOE, T.; GUIGNARD, J.; FROST, D.: 24.-28.05.2015, Japan Geoscience Union Meeting (JpGU), Makuhari Messe, Chiba, Japan: "*In situ* deformation of eclogite at high pressure and temperature"

FARLA, R.J.M.; ROSENTHAL, A.; BOLLINGER, C.; PETITGIRARD, S.; KAWAZOE, T.; GUIGNARD, J.; FROST, D.: 04.-07.10.2015, GeoBerlin 2015, Berlin, Germany[*A]: "High pressure deformation of eclogite combined with *in situ* X-ray diffraction"

FEI, H.; KATSURA, T.: 24.-28.05.2015, Japan Geoscience Union Meeting (JpGU), Makuhari Messe, Chiba, Japan: "Defect chemistry and diffusion in hydrous forsterite"

FEI, H.; YAMAZAKI, D.; OHFUJI, H.; YAMAMOTO, T.: 24.-28.05.2015, Japan Geoscience Union Meeting (JpGU), Makuhari Messe, Chiba, Japan: "Dislocation mobility in ringwoodite as a function of temperature and water content"

FEI, H.: 29.12.2015, Nanjing University, Nanjing, P.R. China (*invited*): "Dislocation mobility in ringwoodite and bridgmanite and implications to mantle rheology"

FISCHER, R.; CAMPBELL, A.J.; MIYAJIMA, N.; RUBIE, D.C.; HARRIES, D.; POLLOK, K.; NAKAJIMA, Y.; LANGENHORST, F.; FROST, D.J.: 26.-30.10.2015, CECAM Workshop: Carbon at Extreme Conditions, Lugano, Switzerland: "Metal-silicate partitioning of Ni, Co, V, Cr, Si, and O in the presence of carbon to 100 GPa and 5500 K with application to Earth's core formation"

FROST, D.J.: 27.01.2015, University of Cambridge, Department of Earth Sciences, Cambridge, U.K.: "The composition of the lower mantle and its influence on the redox state of the Earth"

FROST, D.J.: 27.-31.01.2015, International Diamond School, Brixen, Italy: "Experimental petrology of the mantle"

FROST, D.J.; BEYER, C.: 08.-11.06.2015, Gordon Research Conference, Interior of the Earth, South Hadley, USA: "The redox state and carbon cycle in the Earth's deep mantle"

FROST, D.J.; BEYER, C.: 06.-09.07.2015, Diamond Conference 2015, Warwick University, Coventry, U.K.: "Diamond formation and the deep carbon cycle"

FROST, D.J.: 07.07.2015, University of Cambridge, Department of Earth Sciences, Cambridge, U.K.: "Diamond formation and its role in the deep carbon cycle"

FROST, D.; BEYER, C.; STAGNO, V.: 16.-21.08.2015, Goldschmidt 2015, Prague, Czech Republic (*keynote lecture*): "The speciation of carbon with respect to the redox state of the mantle", Goldschmidt Abstracts, 2015, 958

FROST, D.; KURNOSOV, A.; BOFFA BALLARAN, T.; MARQUARDT, H.; ZIBERNA, L.; CHANTEL, J.: 16.-21.08.2015, Goldschmidt 2015, Prague, Czech Republic (*invited*): "The influence of iron partitioning on seismic wave velocities in the lower mantle", Goldschmidt Abstracts, 2015, 959

FROST, D.J.: 24.-28.08.2015, CSH Summer School 2015, From dust to planets & geology, University of Bern, Leukerbad, Switzerland: "Experimental simulation of planetary differentiation processes"

GOLABEK, G.: 24.03.2015, Vesta workshop, Nürnberg, Germany: "Geophysical constraints on Vesta's internal structure"

GOLABEK, G.: 13.-14.05.2015, ACCRETE Group Meeting, Bayreuth, Germany: "Formation of pallasites with rounded olivine grains"

GOLABEK, G.: 30.06.2015, Gordon Conference, Mount Holyoke, USA: "Towards coupled giant impact and longer-term interior evolution models"

GOLABEK, G.: 01.09.2015, International Workshop on Modelling Mantle and Lithosphere Deformation, Ile d'Oleron, France: "Towards coupled giant impact and longer-term interior evolution models"

GOLABEK, G.: 16.10.2015, Forschungskollegium Physik des Erdkörpers, Freiberg, Germany: "Early thermochemical evolution of planetesimal"

GOLABEK, G.: 21.10.2015, Charles University, Prague, Czech Republik: "Early thermochemical evolution of planetesimal"

GOLABEK, G.; JUTZI, M.; EMSENHUBER, A.; GERYA, T., ASPHAUG; E.: 14.-18.12.2015, AGU Fall Meeting, San Francisco, USA[*B]: "Coupling giant impacts and long-term evolution models", Abstract P11A-2059, 2015

GUTIERREZ, X.; KEPPLER, H.: 16.-21.08.2015, Goldschmidt 2015, Prague, Czech Republic: "Adsorption of hydrogen chloride on volcanic ashes", Goldschmidt Abstracts, 2015, 1132

HEIDELBACH, F.: 04.-07.10.2015, GeoBerlin 2015, Berlin, Germany[*A]: "Garnet formation in the CMAS system under deviatoric stress"

HEIDELBACH, F.: 14.-18.12.2015, AGU Fall Meeting, San Francisco, USA[*B]: "Experimental investigation of the garnet formation in the CMNAS system at high pressure under deviatoric stress", Abstract T41C-2915, 2015

IIZUKA, R.; VINCENT, S.; MIYAJIMA, N.; FROST, D.J.; YAGI, T.: 24.-28.05.2015, Japan Geoscience Union Meeting (JpGU), Makuhari Messe, Chiba, Japan: "Crystallographic preferred orientation of deformed lawsonite: Implication for low velocity layers in subduction zones"

ISMAILOVA L.; BOBROV, A.; BYKOV, M.; BYKOVA, E.; CERANTOLA. V.; KUPENKO, I.; MCCAMMON, C.; HANFLAND, M.; DUBROVINSKAIA, N.; DUBROVINSKY, L.: 16.-21.08.2015, Goldschmidt 2015, Prague, Czech Republic: "Equation of state of skiagite-majorite garnet up to 100 GPa", Goldschmidt Abstracts, 2015, 1389

ISMAILOVA, L.; BYKOV, M.; CERANTOLA, V.; BYKOVA, E.; VASYUKOV, D.; BOBROV, A.; MCCAMMON, C.; DUBROVINSKAIA, N.; DUBROVINSKY, L.: 14.-18.12.2015, AGU Fall Meeting, San Francisco, USA[*B]: "High-pressure behavior of Fe-bearing silicate garnets up to 100 GPa", Abstract MR13C-2706, 2015

JACOBSON, S.A.: 02.01.2015, Planetary Science Group, Purdue University, West Lafayette, USA: "Moon formation in the context of the protoplanetary disk"

JACOBSON, S.A.; YOUNG, E.D.; RUBIE, D.C.; MORBIDELLI, A.: 04.-06.02.2016, Workshop on Early Solar System Bombardment III, Houston, USA: "Composition of the terrestrial planets in the Grand Tack model", Abstract 3034

JACOBSON, S.A.; RUBIE, D.C.; HERNLUND, J.; MORBIDELLI, A.: 16.-20.03.2015, 46th Lunar and Planetary Science Conference, The Woodlands, Houston, USA: "A late giant impact is necessary to create Earth's magnetic field", Abstract 1882

JACOBSON, S.A.: 07.-11.07.2015, IAU Symposium 318: Asteroids: New Observations, New Models, Honolulu, USA: "Evolutionary pathways for asteroid satellites"

JACOBSON, S.A.: 24.-28.08.2015, CSH Summer School 2015, From dust to planets & geology, University of Bern, Leukerbad, Switzerland: "Topics in planet formation"

KAMINSKY, F.; RYABCHIKOV, I.; MCCAMMON, C.; LONGO, M.; ABAKUMOV, A.; TURNER, S.; HEIDARI, H.: 16.-21.08.2015, Goldschmidt 2015, Prague, Czech Republic: "Oxidation potential in the Earth's lower mantle", Goldschmidt Abstracts, 2015, 1502

KATSURA, T.: 27.02.2015, Friday Seminar, University of Tokyo, Earthquake Research Institute, Tokyo, Japan: "Measurement of Si self-diffusion coefficient as a function of pressure, temperature and water content, and its application to upper-mantle rheology"

KATSURA, T.: 03.-06.03.2015, A symposium on 'Structure and Dynamics of the Oceanic Lithosphere/Asthenosphere System', Miyagi, Japan: "Estimation of temperature, pressure, and water-content dependence of olivine creep from indirect observations"

KATSURA, T.: 12.03.2015, Ocean Hemisphere Research Center Seminar, University of Tokyo, Earthquake Research Institute, Tokyo, Japan: "Measurement of ionic conduction at high pressures and ultrahigh temperatures"

KATSURA, T.; WANG, L.: 24.-28.05.2015, Japan Geoscience Union Meeting (JpGU), Makuhari Messe, Chiba, Japan: "Estimation of dislocation mobility in different slip systems in olivine as a function of pressure and temperature"

KATSURA, T.: 06.07.2015, US Large Multi-Anvil Workshop, Colorado Springs, USA: "Development of large-volume HP-HT *in situ* observation systems in the neutron and synchrotron radiation facilities in Germany"

KATSURA, T.: 06.-09.07.2015, COMPRES Annual Meeting, Colorado Springs, USA: "Development of large-volume HP-HT *in situ* observation systems in the neutron and synchrotron radiation facilities in Germany"

KATSURA, T.: 13.-15.09.2015, The first 'Deep Volatiles' Meeting, Oxford, U.K.: "Breakdown of phase D by formation of aluminous bridgmanite"

KATSURA, T.: 21.09.2015, GL Seminars, Carnegie Institution, Geophysical Laboratory, Washington DC, USA: "Measurement of Si self-diffusion coefficients of forsterite as a function of pressure, temperature and water content, and its applications to the upper-mantle rheology", Abstract SIT06-15, 2015

KATSURA, T.; ISHII, T.; MIYAJIMA, N.; PETITGIRARD, S.; MCCAMMON, C.: 14.-18.12.2015, AGU Fall Meeting, San Francisco, USA[*B]: "Breakdown of phase D by formation of aluminous bridgmanite", Abstract DI21B-06, 2015

KAWAZOE, T.; NISHIHARA, Y.; OHUCHI, T.; MARUYAMA, G.; HIGO, Y.; FUNAKOSHI, K.; IRIFUNE, T.: 24.-28.05.2015, Japan Geoscience Union Meeting (JpGU), Makuhari Messe, Chiba, Japan: "*In situ* creep strength measurement on ringwoodite up to 1700 K at 17-18 GPa using a deformation-DIA apparatus", Abstract SIT04-13

KAWAZOE, T.; MIYAJIMA, N.: 24.-28.05.2015, Japan Geoscience Union Meeting (JpGU), Makuhari Messe, Chiba, Japan: "Weak-beam dark-field TEM characterization of dislocations in wadsleyite deformed in simple shear at 18 GPa and 1800 K", Abstract SIT04-P05

KEPPLER, H.: 19.11.2015, Humboldt University Berlin, public Helmholtz Lecture, Berlin, Germany: "Vulkane: Gefahren und Vorhersagen"

KEPPLER, H.: 03.12. 2015, University Freiburg, Germany: "Volcanoes and the atmosphere"

KRESSALL, R.; FEDORTCHOUK, Y.; MCCAMMON, C.: 14.-18.12.2015, AGU Fall Meeting, San Francisco, USA[*B]: "Application of Fe-Ti oxide dissolution experiments to the petrogenesis of the Ekati Diamond Mine kimberlites, Northwest Territories, Canada", Abstract V23B-3139, 2015

KULIK, E.; NISHIYAMA, N.; MASUNO, A.; KHRAMOV, E.; MURZIN, V.; ZUBAVICHUS, Ya.; WILLE, H.-C.; KATSURA, T.: 28.-30.01.2015, DESY Photon Science Users' Meeting 2015, Hamburg, Germany: "Synthesis of rutile-type solid solution in SiO_2-GeO_2 system under high pressure and high temperature"

KULIK, E.; NISHIYAMA, N.; ZUBAVICHUS, Y.V.; MASUNO, A.; YAMADA, A.; OHFUJI, H.; WILLE, H.C.; KATSURA, T.: 30.08.-04.09.2015, Joint AIRAPT-25 & EHPRG-53 Meeting, Madrid, Spain: "Synthesis of complete series rutile- type solid solutions in SiO2-GeO2 system under high pressure and temperature"

KUPENKO, I.; STROHM, C.; MCCAMMON, C.; CERANTOLA, V.; GLAZYRIN, K.; PETITGIRARD, S.; VASIUKOV, D.; APRILIS, G.; CHUMAKOV, A.I.; RÜFFER, R.; DUBROVINSKY, L.: 16.-21.08.2015, Goldschmidt 2015, Prague, Czech Republic: "Time differentiated nuclear resonance spectroscopy with pulsed laser heating in diamond anvil cells", Goldschmidt Abstracts, 2015, 1718

KUPENKO, I.; STROHM, C.; MCCAMMON, C.; CERANTOLA, V.; GLAZYRIN, K.; PETITGIRARD, S.; VASIUKOV, D.; APRILIS, G.; CHUMAKOV, A.I.; RÜFFER, R.; DUBROVINSKY, L.: 13.-18.09.2015, International Conference on the Applications of Mössbauer Spectroscopy 2015, Hamburg, Germany: "Time differentiated nuclear resonance spectroscopy with pulsed laser heating in diamond anvil cells"

KURNOSOV, A.; MARQUARDT, H.; BOFFA BALLARAN, T.; FROST, D.: 16.-21.08.2015, Goldschmidt 2015, Prague, Czech Republic: "Single-crystal elastic properties of $Mg_{0.88}Fe_{0.12}Si_{0.09}Al_{0.11}O_3$ – bridgmanite at high pressure", Goldschmidt Abstracts, 2015, 1720

KURNOSOV, A.; MARQUARDT, H.; BOFFA BALLARAN, T.; FROST, D.J.: 16.-21.08.2015, Goldschmidt 2015, Prague, Czech Republic: "Single-crystal elastic properties of $Mg_{0.88}Fe_{0.12}Si_{0.09}Al_{0.11}O_3$ – bridgmanite at high pressure"

KURNOSOV, A.; MARQUARDT, H.; BOFFA BALLARAN, T.; FROST, D.J.: 04.-07.10.2015, GeoBerlin 2015, Berlin, Germany[*A]: "Incorporation on the single-crystal elasticity of bridgmanite at high pressure"

KURNOSOV, A.; MARQUARDT, H.; BOFFA BALLARAN, T.; FROST, D.J.: 14.-18.12.2015, AGU Fall Meeting, San Francisco, USA[*B]: "The effect of iron and aluminium incorporation on the single-crystal elasticity of bridgmanite at high pressure", Abstract MR13B-2701, 2015

KUSIAK, M.A.; WHITEHOUSE, M.J.; WIRTH, R.; WILDE, S.A.; DUNKLEY, D.J.; MARQUARDT, K.: 12.-13.10.2015, NanoSIMS Workshop, Manchester, U.K.: "Ion imaging of Pb isotopes and implications for Hdaean geochronology", Abstract 4963

LAURENZ, V.; RUBIE, D.C.; FROST, D.J.; VOGEL, A.K.: 16.-21.08.2015, Goldschmidt 2015, Prague, Czech Republic: "Sulfide-silicate partitioning of the HSEs and S-solubility in peridotite melt at high P and T", Goldschmidt Abstracts, 2015, 1786

LAURENZ, V.; RUBIE, D.C.; FROST, D.J.; JACOBSON, S.A.; MORBIDELLI, A.; PALME, H.: 11.-13.11.2015, Joint meeting 'Paneth Kolloquium', 'The first 10 million years of the solar system' (DFG SPP 1385), Nördlingen, Germany: "The significance of sulfur for the highly siderophile element budget of the Earth's mantle"

LAURENZ, V.: 09.12.2015, Research Seminar, Scripps Institution of Oceanography, UC San Diego, USA: "Unravelling the origin of HSE abundances in the Earth's mantle – Combining accretion/core formation models with high P-T experiments"

LAURENZ, V.; RUBIE, D.C.; FROST, D.J.; JACOBSON, S.A.; MORBIDELLI, A.; PALME, H.; VOGEL, A.K.: 14.-18.12.2015, AGU Fall Meeting, San Francisco, USA[*B]: "The origin of non-chondritic HSE ratios in the Earth's mantle", Abstract V52A-01, 2015

LEE, K.; GU, T.; LI, M.; MCCAMMON, C.: 14.-18.12.2015, AGU Fall Meeting, San Francisco, USA[*B]: "The mantle-atmosphere connection: Oxidation of the atmosphere through mantle convection", Abstract DI44A-05, 2015

LIERMANN, H.-P.; EHNES, A.; SPEZIALE, S.; MARQUARDT, H.; MIYAGI, L.; SINGH, A.K.: 09.-11.02.2015, ESRF Users Meeting 2015, Grenoble, France: "A new setup for remote-controlled compression/decompression radial X-ray diffraction at extreme pressures and temperatures"

LIN, Y.; EL GORESY, A.; ZHANG, J.; MIYAHARA, M.; HAO, J.; ZHANG, M.; OHTANI, E.; GILLET, P.: 16.-21.08.2015, Goldschmidt 2015, Prague, Czech Republic: "NanoSIMS analysis of C-grains from Martian meteorite NWA 6162", Goldschmidt Abstracts, 2015, 1868

LINSLER, S.A.; NAMUR, O.; ALBRECHT, M.; CHARLIER, B.; HOLTZ, F.; MCCAMMON, C.: 04.-07.10.2015, GeoBerlin 2015, Berlin, Germany[*A]: "Metal-silicate trace element partitioning at reducing conditions: Implications for Mercury's differentiation"

MALFAIT, W.; PETITGIRARD, S.; SEIFERT, R.; SANCHEZ-VALLE, C.: 16.-21.08.2015, Goldschmidt 2015, Prague, Czech Republic (*invited*): "Magma bouyancy: From supervolcano magma chambers to the core-mantle boundary", Goldschmidt Abstracts, 2015, 1984

MARQUARDT, H.; MIYAGI, L.; SPEZIALE, S.; LIERMANN, H.-P.: 16.-21.08.2015, Goldschmidt 2015, Prague, Czech Republic (*invited*): "Strength of (Mg,Fe)O ferropericlase at high-pressures and high-temperatures and slab stagnation in the shallow lower mantle", Goldschmidt Abstracts, 2015, 2016

MARQUARDT, H.; KURNOSOV, A.; BOFFA BALLARAN, T.; MARQUARDT, K.; FROST, D.; BUCHEN, J.; SCHULZE, K.: 12.-15.09.2015, 2015 IUCr High-Pressure Workshop, Campinas, Sao Paulo, Brazil: "Internally consistent elasticity measurements of FIB-prepared single-crystals at high pressure and high temperature by Brillouin spectroscopy and X-ray diffraction"

MARQUARDT, H.; MIYAGI, L.; SPEZIALE, S.; LIERMANN, H.-P.: 23.-25.09.2015, 4th Joint Workshop on High Pressure, Planetary and Plasma Physics, Bayreuth, Germany: "Strength of (Mg,Fe)O ferropericlase at high-pressures and high-temperatures and slab stagnation in the shallow lower mantle"

MARQUARDT, H.; GOLABEK, G.J.; MIYAGI, L.; GERYA, T.V.: 04.-07.10.2015, GeoBerlin 2015, Berlin, Germany[*A]: "The response of subducting slabs to a strength increase in the shallow lower mantle constrained by numerical modelling"

MARQUARDT, H.; KURNOSOV, A.; BOFFA BALLARAN, T.; MARQUARDT, K.; FROST, D.; BUCHEN, J.; SCHULZE, K.: 14.-18.12.2015, AGU Fall Meeting, San Francisco, USA[*B]: "Internally consistent elasticity measurements of mantle minerals at high-pressure and high-temperature by Brillouin spectroscopy and X-ray diffraction", Abstract MR13B-2693, 2015

MARQUARDT, H.: 22.01.2015, University of Münster, Germany: "From diamond-anvil cell experiments to deep Earth processes"

MARQUARDT, K.; ROHRER, G.: 14.-18.12.2015, AGU Fall Meeting, San Francisco, USA[*B]: "The energy of olivine grain boundaries deduced from grain boundary frequency analyses", Abstract MR23A-2640, 2015

MASOTTA, M.; KEPPLER, H.; CHAUDHARI, A.: 16.-21.08.2015, Goldschmidt 2015, Prague, Czech Republic: "Sulfur budget in differentiated arc magmas", Goldschmidt Abstracts, 2015, 2045

MCCAMMON, C.: 04.02.2015, University of Texas, Austin, USA: "Spotlight on hot and squashed iron phases in the deep mantle"

MCCAMMON, C.: 05.02.2015, University of Texas, Austin, USA: "The fate of carbonate in the deep Earth"

MCCAMMON, C.: 06.02.2015, University of Texas, Austin, USA: "Geophysical constraints on the early Earth"

MCCAMMON, C.: 09.-11.02.2015, ESRF Users Meeting 2015, Grenoble, France: "A synchrotron journey to the Earth's core"

MCCAMMON, C.: 07.-13.02.2015, 26. Edgar Lüscher Seminar, Klosters, Switzerland: "Geophysical constraints on the early Earth"

MCCAMMON, C.: 17.-18.02.2015, Kick-off Meeting of the FOR 2125, Hamburg, Germany: "Elastic wave velocities of carbonates at high P, T and their seismic signature"

MCCAMMON, C.: 10.-13.03.2015, 5th PlanetMag Meeting, Nördlingen, Germany: "New constraints on the light element in the core"

MCCAMMON, C.; DUBROVINSKY, L.; CERANTOLA, V.; KUPENKO, I.; SINMYO, R.; KANTOR, A.; CHUMAKOV, A.: 26.-28.03.2015, 2nd Deep Carbon Observatory International Science Meeting, Munich, Germany: "Does deep carbon have a seismic signature?"

MCCAMMON, C.: 03.-07.05.2015, Joint Assembly 2015, Montreal, Canada: "Transition metal chemistry meets the perovskite structure"

MCCAMMON, C.: 09.-11.09.2015, European Conference on Mineralogy and Spectroscopy 2015, Rome, Italy: "Magnetism meets Mössbauer spectroscopy and the stories they tell"

MCCAMMON, C.: 12.-13.11.2015, 2nd Meeting of the FOR 2125, Wehrheim, Germany: "Progress and plans for project 6"

MCCAMMON, C.; CERANTOLA, V.; KUPENKO, I.; SINMYO, R.; POTAPKIN, V.; CHUMAKOV, A.I.; RÜFFER, R.; DUBROVINSKY, L.: 26.-30.10.2015, CECAM Workshop: Carbon at Extreme Conditions, Lugano, Switzerland: "Redox chemistry of carbonates at megabar pressure range"

MCCAMMON, C.; VAN DRIEL, J.; KUPENKO, I.; SINMYO, R.; CERANTOLA, V.; POTAPKIN, V.; CHUMAKOV, A.I.; RÜFFER, R.; DUBROVINSKY, L.: 14.-18.12.2015, AGU Fall Meeting, San Francisco, USA^{*B} (*invited*): "The deep oxygen cycle in the early Earth", Abstract DI44A-04, 2015

MCCAMMON, C.; DUBROVINSKY, L.; CARACAS, R.; GLAZYRIN, K.; POTAPKIN, V.; KANTOR, A.; SINMYO, R.; PRESCHER, C.; KUPENKO, I.; CHUMAKOV, A.: 24.-28.05.2015, Japan Geoscience Union Meeting (JpGU), Makuhari Messe, Chiba, Japan: "Seeking constraints on lower mantle composition through nuclear resonance combined with computations"

MCCAMMON, C.; DUBROVINSKY, L.; KUPENKO, I.; CERANTOLA, V.; GLAZYRIN, K.; POTAPKIN, V.; KANTOR, A.; KANTOR, I.; SINMYO, R.; PRESCHER, C.; NARYGINA, O.; PETITGIRARD, S.; SERGUEEV, I.; STROHM, C.; APRILIS, G.; VASIUKOV, D.; ISMAILOVA, L.; SMIRNOV, G.; RÜFFER, R.; CHUMAKOV, A.: 13.-18.09.2015, International Conference on the Applications of Mössbauer Spectroscopy 2015, Hamburg, Germany: "Descent to the underworld or a synchrotron opera in many acts"

MCCAMMON, C.; PRESCHER, C.; SINMYO, R.; GLAZYRIN, K.; KUPENKO, I.; KANTOR, A.; POTAPKIN, V.; CERANTOLA, V.; CHUMAKOV, A.I.; RÜFFER, R.; DUBROVINSKY, L.: 21.-23.09.2015, 5. International Workshop on Nuclear Resonance Scattering of Synchrotron Radiation: Status, Highlights, Methodology, and Trends, Hamburg, Germany: "Nuclear inelastic scattering and geophysics: Triumphs and setbacks"

MCGOWAN, N.; GRIFFIN, W.; PEARSON, N.; O'REILLY, S.; CLARK, S.; ROQUE-ROSELL, J.; MARCUS, M.; MCCAMMON, C.: 14.-18.12.2015, AGU Fall Meeting, San Francisco, USA[*B]: "The oxidation state of iron in chromite as a record of deep Earth processes", Abstract DI31A-2565, 2015

MILLOT, J.; RYGG, R.; HAMEL, S.; CELLIERS, P.M.; COLLINS, G.W.; EGGERT, J.H.; DUBROVINSKAIA, N.; CERNOK, A.; BLAHA, S.; DUBROVINSKY, L.S.; JEANLOZ, R.: 30.08.-04.09.2015, Joint AIRAPT-25 & EHPRG-53 Meeting, Madrid, Spain: "Exploring planetary interiors with laser shock compression: melting of silica and optical properties of superionic water"

MIYAJIMA, N.; KAWAZOE, T.: 16.-19.05.2015: 6th Mineral Sciences in the Carpathians Conference (MSCC2015), Veszprém, Hungary: "Iron partitioning between ringwoodite lamella and the host wadsleyite in the transformation"

MIYAJIMA, N.; LI, Y.; HEIDELBACH, F.: 04.-07.10.2015, GeoBerlin 2015, Berlin, Germany[*A]: "Electron channeling contrast imaging of dislocations in geological materials using a scanning electron microscope"

MOOKHERJEE, M.; SPEZIALE, S.; MARQUARDT, H.; JAHN, S.; WUNDER, B.; KOCH-MÜLLER, M.; LIERMANN, H.-P.: 14.-18.12.2015, AGU Fall Meeting, San Francisco, USA[*B]: "Equation of state and elasticity of the 3.65 A phase – constraining mantle hydration from the seismic x-discontinuity", Abstract DI13B-2671, 2015

MOROZOVA, N.V.; SHCHENNIKOV, V.V.; OVSYANNIKOV, S.V.: 30.08.-04.09.2015, Joint AIRAPT-25 & EHPRG-53 Meeting, Madrid, Spain: "Thermoelectric properties of rare-earth, transition, and other metals under high pressure"

MYHILL, R.; RUBIE, D.; FROST, D.J.: 08.-11.06.2015, Gordon Research Conference, Interior of the Earth, South Hadley, USA: "High pressure thermodynamics of Fe-Si-O compounds"

MYHILL, R.: 23.10.2015, University of Bristol, Department of Earth Sciences, Bristol, U.K.: "Water, water everywhere: H_2O in the deep mantle"

MYHILL, R.: 19.11.2015, University of Oslo, Centre for Earth Evolution and Dynamics (CEED), Oslo, Norway: "Getting into deep water: Experiments and observations of H_2O in the Earth's mantle"

MYHILL, R.; RUBIE, D.; FROST, D.J.: 14.-18.12.2015, AGU Fall Meeting, San Francisco, USA[*B]: "Light element partitioning between silicate and metallic melts: Insights into the formation and composition of Earth's core", Abstract MR23B-2653, 2015

NAMUR, O.; COLLINET, M.; CHARLIER, B.; HOLTZ, F.; GROVE, T.L.; MCCAMMON, C.: 16.-20.03.2015, 46th Lunar and Planetary Science Conference, The Woodlands, Houston, USA: "The mantle sources of surface lavas on Mercury"

NISHIHARA, Y.; OHUCHI, T.; KAWAZOE, T.; MARUYAMA, G.; HIGO, Y.; FUNAKOSHI, K.; SETO, Y.: 14.-18.12.2015, AGU Fall Meeting, San Francisco, USA*B: "Lattice preferred orientation of hcp-iron induced by shear deformation", Abstract DI33A-2622, 2015

OHUCHI, T.; KAWAZOE, T.; HIGO, Y.; FUNAKOSHI, K.; SUZUKI, A.; KIKEGAWA, T.; IRIFUNE, T.: 24.-28.05.2015, Japan Geoscience Union Meeting (JpGU), Makuhari Messe, Chiba, Japan: "Grain boundary sliding as the major deformation mechanism of olivine in Earth's upper mantle", Abstract SIT04-10

OHUCHI, T.; NISHIHARA, Y.; SETO, Y.; KAWAZOE, T.; NISHI, M.; MARUYAMA, G.; HASHIMOTO, M.; HIGO, Y.; FUNAKOSHI, K.; SUZUKI, A.; KIKEGAWA, T.; IRIFUNE, T.: 14.-18.12.2015, AGU Fall Meeting, San Francisco, USA*B: "*In situ* observation of crystallographic preferred orientation of deforming olivine at high pressure and high temperature", Abstract T33H-01, 2015

OVSYANNIKOV, S.V.: 23.-26.08.2015, 15th European Conference on Solid State Chemistry (ECSSC 15), Vienna, Austria (*invited*): "High-pressure high-temperature synthesis of simple oxide"

OVSYANNIKOV, S.V.; GOU, H.; KARKIN, A.E.; SHCHENNIKOV, V.V.; WIRTH, R.; DMITRIEV, V.; NAKAJIMA, N.; DUBROVINSKAIA, N.; DUBROVINSKY, L.: 15th European Conference on Solid State Chemistry (ECSSC 15), Vienna, Austria: "High-pressure high-temperature synthesis of bulk $Si_{1-x}B_x$ alloys: two semiconductors form an unusual metal"

OVSYANNIKOV, S.V.; GOU, H.; KARKIN, A.E.; SHCHENNIKOV, V.V.; WIRTH, R.; DMITRIEV, V.; NAKAJIMA, N.; DUBROVINSKAIA, N.; DUBROVINSKY, L.: 30.08.-04.09.2015, Joint AIRAPT-25 & EHPRG-53 Meeting, Madrid, Spain: "High-pressure high-temperature synthesis of bulk $Si_{1-x}B_x$ alloys: two semiconductors form an unusual metal"

OVSYANNIKOV, S.V.; MOROZOVA, N.V.; KOROBEINIKOV, I.V.; LUKYANOVA, L.N.; MANAKOV, A.Y.; LIKHACHEVA, A.Y.; ANCHAROVA, A.I.; VOKHMYANIN, A.P.; BERGER, I.F.; USOV, O.A.; KUTASOV, V.A.; KULBACHINSKII, V.A.; OKADA, T.; SHCHENNIKOV, V.V.: 30.08.-04.09.2015, Joint AIRAPT-25 & EHPRG-53 Meeting, Madrid, Spain: "Thermoelectric and structural properties of $(Bi,Sb)_2(Te,Se)_3$ thermoelectrics under pressure"

OVSYANNIKOV, S.V.; KARKIN, A.E.; MOROZOVA, N.V.; SHCHENNIKOV, V.V.; BYKOVA, E.; ABAKUMOV, A.M.; TSIRLIN, A.A.; GLAZYRIN, K.; DUBROVINSKY, L.: 23.-25.09.2015, 4th Joint Workshop on High Pressure, Planetary and Plasma Physics, Bayreuth, Germany: "Properties of metastable high-pressure polymorphs of manganese oxides"

OVSYANNIKOV, S.V.; GOU, H.; KARKIN, A.E.; SHCHENNIKOV, V.V.; WIRTH, R.; DMITRIEV, V.; NAKAJIMA, N.; DUBROVINSKAIA, N.; DUBROVINSKY, L.: 23.-25.09.2015, 4th Joint Workshop on High Pressure, Planetary and Plasma Physics, Bayreuth, Germany: "High-pressure high-temperature synthesis of bulk $Si_{1-x}B_x$ alloys: two semiconductors form an unusual metal"

PAKHOMOVA, A.; BOFFA BALLARAN, T.; KURNOSOV, A.; FROST, D.J.; LEONI, M.: 16.-21.08.2015, Goldschmidt 2015, Prague, Czech Republic: "Elastic properties of high pressures ices and their implication for the evolution of icy satellites", Goldschmidt Abstracts, 2015, 2381

PAKHOMOVA, A.S.; BOFFA BALLARAN, T.; KURNOSOV, A.V.; LEONI, M.: 30.08.-04.09.2015, Joint AIRAPT-25 & EHPRG-53 Meeting, Madrid, Spain: "Elastic properties of ice VI and VII and their implication for Ganymede-Callisto dichtonomy"

PAKHOMOVA, A.S.; BOFFA BALLARAN, T.; KURNOSOV, A.V.; LEONI, M.: 11.-13.11.2015, Joint meeting 'Paneth Kolloquium', 'The first 10 million years of the solar system' (DFG SPP 1385), Nördlingen, Germany: "Deformation of water ice VI: a single-crystal X-ray diffraction study"

PETITGIRARD, S.; MALFAIT, W.; SINMYO, R.; KUPENKO, I.; HARRIES, D.; RUBIE, D.: 16.-21.08.2015, Goldschmidt 2015, Prague, Czech Republic: "Fate of silicate melts at core-mantle boundary conditions", Goldschmidt Abstracts, 2015, 2470

PETITGIRARD, S.; MALFAIT, W.; SINMYO, R.; KUPENKO, I.; RUBIE, D.: 14.-18.12.2015, AGU Fall Meeting, San Francisco, USA[*B]: "Fate of silicate melts at core-mantle boundary", Abstract DI52A-01, 2015

PINTÉR, Zs.; KOVÁCS, I.; SZABÓ, Cs.: 16.-21.08.2015, Goldschmidt 2015, Prague, Czech Republic: "Insight into the evolution of lithosphere beneath Pannonian Basin through studying H_2O content in NAMs from Füzes-tó upper mantle xenoliths (Hungary)", Goldschmidt Abstracts, 2015, 4224

PINTER, Z.; ROSENTHAL, A.; FROST, D.; MCCAMMON, C.; HÖFER, H.; YAXLEY, G.; BERRY, A.; WOODLAND, A.; VASILYEV, P.; PEARSON, G.: 14.-18.12.2015, AGU Fall Meeting, San Francisco, USA[*B]: "High pressure experimental investigation of the interaction between partial melts of eclogite and mantle peridotite during upwelling", Abstract V33C-3113, 2015

POSNER, E.S.; RUBIE, D.C.; FROST, D.J.: 16.-21.08.2015, Goldschmidt 2015, Prague, Czech Republic: "Diffusion in liquid iron and peridotite melt at high pressure", Goldschmidt Abstracts, 2015, 2525

POSNER, E.S.; RUBIE, D.C.; FROST, D.J.; VLČEK, V.; STEINLE-NEUMANN, G.: 11.-13.11.2015, Joint meeting 'Paneth Kolloquium', 'The first 10 million years of the solar system' (DFG SPP 1385), Nördlingen, Germany: "High P-T experiments and first principles calculations of Si, O, Cr diffusion in liquid iron"

POSNER, E.S.; RUBIE, D.C.; FROST, D.J.; VLČEK, V.; STEINLE-NEUMANN, G.: 14.-18.12.2015, AGU Fall Meeting, San Francisco, USA[*B]: "High P-T diffusive transport properties of liquid iron alloys and peridotite melt", Abstract MR33D-04, 2015

RIVOLDINI, A.; VAN HOOLST, T.; DUMBERRY, M.; STEINLE-NEUMANN, G.: 23.-25.09.2015, 4th Joint Workshop on High Pressure, Planetary and Plasma Physics, Bayreuth, Germany: "Mercury's thermal evolution and core crystallisation regime"

RIVOLDINI, A.; VAN HOOLST, T.; DUMBERRY, M.; STEINLE-NEUMANN, G.: 27.09.-02.10.2015, European Planetary Science Congress 2015, Nantes, France: "Mercury's thermal evolution and core crystallisation regime"

ROSENTHAL, A.; YAXLEY, G.M.; GREEN, D.H.; FROST, D.J.; KOVACS, I.; SPANDLER, C.; HERMANN, J. (2015): 14.-18.12.2015, AGU Fall Meeting, San Francisco, USA[*B](*invited*): "Continuous eclogite melting and variable refertilisation in upwelling heterogeneous mantle", Abstract DI21B-01, 2015

RUBIE, D.C.: 11.03.2015, University of Bern, Center for Space and Habitability, Bern, Switzerland: "Accretion and early differentiation of the terrestrial planets"

RUBIE, D.C.: 13.-14.05.2015, ACCRETE Group Meeting, Bayreuth, Germany: "Earth's highly siderophile elements and the late veneer"

RUBIE, D.C.; DE VRIES, J.; NIMMO, F.; MELOSH, H.J.: 24.-28.05.2015, Japan Geoscience Union Meeting (JpGU), Makuhari Messe, Chiba, Japan: "Melting and core formation during accretion of the Earth"

RUBIE, D.C.: 24.-28.05.2015, Japan Geoscience Union Meeting (JpGU), Makuhari Messe, Chiba, Japan: "Accretion and early differentiation of the terrestrial planets"

RUBIE, D.C.: 29.05.2015, Tokyo Institute of Technology, Earth-Life Science Institute, Tokyo, Japan: "Accretion and early differentiation of the terrestrial planets"

RUBIE, D.; LAURENZ, V.; JACOBSON, S.; MORBIDELLI, A.; PALME, H.; FROST, D.: 16.-21.08.2015, Goldschmidt 2015, Prague, Czech Republic (*keynote lecture*): "The Hadean matte, magma ocean solidification and Earth's late veneer", Goldschmidt Abstracts, 2015, 2708

RUBIE, D.C.; LAURENZ, V.; JACOBSON, S.A.; MORBIDELLI, A.; PALME, H.; FROST, D.J.: 11.-13.11.2015, Joint meeting 'Paneth Kolloquium', 'The first 10 million years of the solar system' (DFG SPP 1385), Nördlingen, Germany: "Accreted metal did not strip Earth's mantle of HSEs during core formation"

RUBIE, D.C.: 16.11.2015, Universiät Münster, Institut für Planetologie, Münster, Germany: "Accretion and early differentiation of the terrestrial planets"

SCANDOLO, L.; ALVARO, M.; MCCAMMON, C.; DI PRIMA, M.; DOMENEGHETTI, M.C.; NESTOLA, F.: 02.-04.09.2015, SIMP-AIV-SoGeI-SGI 2015, Florence, Italy: "The role of oxidation on the high-temperature behavior of almandine"

SCHULZE, K.; MARQUARDT, H.; KAWAZOE, T.; KOCH-MÜLLER, M.; KURNOSOV, A.; BOFFA BALLARAN, T.: 16.-21.08.2015, Goldschmidt 2015, Prague, Czech Republic: "Direct quantification of the effects of iron content and hydration on the high-pressure elasticity of single-crystal ringwoodite", Goldschmidt Abstracts, 2015, 2820

SCHULZE, K.; MARQUARDT, H.; KAWAZOE, T.; KOCH-MÜLLER, M.; KURNOSOV, A.; BOFFA BALLARAN, T.: 04.-07.10.2015, GeoBerlin 2015, Berlin, Germany[*A]: "The effect of iron content and hydration on the high-pressure single-crystal elasticity of ringwoodite derived from an internally consistent approach"

SINMYO, R.; BYKOVA, E.; OVSYANNIKOV, S.V.; MCCAMMON, C.; KUPENKO, I.; ISMAILOVA, L.; DUBROVINSKY, L.: 04.-07.11.2015, Workshop 'The Earth's Mantle and Core: Structure, Composition, Evolution', Tokyo Institute of Technology, Earth-Life Science Institute, Tokyo, Japan: "Discovery of new iron oxide Fe_7O_9 and its solid solution, $(Mg,Fe^{2+})_3Fe^{3+}{}_4O_9$"

SINMYO, R.; BYKOVA, E.; OVSYANNIKOV, S.; MCCAMMON, C.; KUPENKO, I.; ISMAILOVA, L.; DUBROVINSKY, L.: 14.-18.12.2015, AGU Fall Meeting, San Francisco, USA[*B]: "Discovery of new iron oxide Fe_7O_9 and its solid solution, $(Mg,Fe^{2+})_3Fe^{3+4}O_9$", Abstract MR23B-2648, 2015

SMYTH, J.R.; KAWAZOE, T.; JACOBSEN, S.D.; ZHANG, L.: 16.-21.08.2015, Goldschmidt 2015, Prague, Czech Republic: "Transition metals in the transition zone: Crystal chemistry of Fe, Ti, Cr, V, Co, Ni, and Zn in wadsleyite", Goldschmidt Abstracts, 2015, 2931

SORBADERE, F.; FROST, D.; WENZ, M.; ROSENTHAL, A.; RIVARD, C.; LAURENZ, V.; MCCAMMON, C.: 16.-21.08.2015, Goldschmidt 2015, Prague, Czech Republic: "Behavior of ferric iron (Fe^{3+}) during partial melting of MORB-mantle source", Goldschmidt Abstracts, 2015, 2954

SPEZIALE, S.; LIERMANN, H.-P.; LO NIGRO, G.; MARQUARDT, H.; REICHMANN, H.J.: 04.-07.10.2015, GeoBerlin 2015, Berlin, Germany[*A]: "Compression of $(Mg_{0.9}Fe_{0.1})_2SiO_4$ olivine at ambient temperature to lower mantle pressures"

SPEZIALE, S.; MARQUARDT, H.; MIYAGI, L.; LIERMANN, H.-P.: 22.06.-02.07.2015, 26th General Assembly of the International Union of Geodesy and Geophysics (IUGG) Meeting, Prague, Czech Republic: "Studying the activity of slip systems in lower mantle minerals"

STIPP, M.; KEPPLER, R.; BEHRMANN, J.H.; HEIDELBACH, F.: 14.-18.12.2015, AGU Fall Meeting, San Francisco, USA[*B]: "Deformation processes of subduction and exhumation in Alpine eclogites with focus on the Tauern window", Abstract T51I-06, 2015

UENVER-THIELE, L.; WOODLAND, A.; BOFFA BALLARAN, T.; FROST, D.: 16.-21.08.2015, Goldschmidt 2015, Prague, Czech Republic: "Phase relations of $MgFe_2O_4$ and the stability of the new Fe^{3+}-oxide $Mg_2Fe_2O_5$ at conditions of the deep upper mantle and transition zone", Goldschmidt Abstracts, 2015, 3202

VASILYEV, P.; YAXLEY, G.; O'NEILL, H.; BERRY, A.; HÖFER, H.; WOODLAND, A.; ROSENTHAL, A.; KORSAKOV, A.: 16.-21.08.2015, Goldschmidt 2015, Prague, Czech Republic: "Redox state of deeply subducted altered oceanic crust: Experimental study and evidence from natural samples", Goldschmidt Abstracts, 2015, 3248

VASIUKOV, D.; DUBROVINSKY, L.; SOLOPOVA, N.; KUPENKO, I.; MCCAMMON, C.; CHUMAKOV, A.; DUBROVINSKAIA, N.: 30.08.-04.09.2015, Joint AIRAPT-25 & EHPRG-53 Meeting, Madrid, Spain: "Alkali halides are chemically active at high pressure and high temperature conditions"

VLČEK, V.; STEINLE-NEUMANN, G.; LEPPERT, L.; ARMIENTO, R.; KÜMMEL, S.: 15.-20.03.2016, 79. Jahrestagung der Deutschen Physikalischen Gesellschaft, Berlin, Germany: "Improved ground state electronic structure and optical dielectric constants with a semi-local exchange functional", Abstract O.85.8

VLČEK, V.; EISENBERG, H.; STEINLE-NEUMANN, G.; BAER, R.: 04.-05.05.2016, The Hebrew University of Jerusalem, Fritz-Haber Center for Molecular Dynamics, Institute of Chemistry, Jerusalem, Israel: "Length dependence of the ionization potential in thiophene and furan polymers"

WAGLE, F.; VLČEK, V.; STEINLE-NEUMANN, G.: 10.-13.03.2015, 5th PlanetMag Meeting, Nördlingen, Germany: "A back-of-the-envelope estimate for conductivity of metals at their melting point"

WAGLE, F.; VLČEK, V.; STEINLE-NEUMANN, G.: 23.-25.09.2015, 4th Joint Workshop on High Pressure, Planetary and Plasma Physics, Bayreuth, Germany: "Conductivity of iron along its melting curve"

WAGNER, J.; ADJAOUD, O.; MARQUARDT, K.; JAHN, S.: 14.-18.12.2015, AGU Fall Meeting, San Francisco, USA[*B]: "Mg_2SiO_4 forsterite grain boundary structures and self-diffusion from classical molecular dynamic simulations", Abstract MR32A-08, 2015

WANG, L.; BLAHA, S.; PINTÉR, S.; FARLA, R.J.M.; KAWAZOE, T.; MIYAJIMA, N.; MICHIBAYASHI, K.; KATSURA, T.: 22.06.-02.07.2015, 26th General Assembly of the International Union of Geodesy and Geophysics (IUGG) Meeting, Prague, Czech Republic: "Temperature dependence of [100](010) and [001](010) dislocation mobility in natural olivine"

WOODLAND, A.; UENVER-THIELE, L.; BOFFA BALLARAN, T.: 16.-21.08.2015, Goldschmidt 2015, Prague, Czech Republic: "Synthesis of Fe_5O_6 and the high-pressure stability of Fe^{2+}-Fe^{3+}-oxides related to Fe_4O_5", Goldschmidt Abstracts, 2015, 3446

[*A] **GeoBerlin 2015, Annual Meeting of DGGV • DMG, 'DYNAMIC EARTH – from Alfred Wegener to today and beyond', 04.-07.10.2015, Berlin, Germany**

[*B] **AGU: American Geophysical Union Fall Meeting, 14.-18.12.2015, San Francisco, USA**

4.4 Lectures and seminars at Bayerisches Geoinstitut

BALLMER, Maxim, ETH Zurich, Derpartment of Earth Sciences, Institute of Geophysics, Zurich, Switzerland: "The stagnation of slabs at ~ 1000 km depth indicates that dense basalt may be more abundant in the lower than the upper mantle", 27.10.2015

BLAHA, Stephan, Bayerisches Geoinstitut, Bayreuth, Germany: "Water-content dependence of dislocation mobility of olivine in the [100](010) slip system", 08.10.2015

BORCHERT, Manuela, Potsdam, Germany: "LOOKING INTO THE EARTH: Using brilliant hard X-rays to obtain chemical information directly at conditions of the Earth's crust and mantle", 19.01.2015

CAI, Nao, Ehime University, Geodynamics Research Center, Matsuyama, Japan: "A possible new Al-bearing hydrous phase (23 Å phase) as a water carrier in subduction zones", 15.06.2015

CERNOK, Ana, Bayerisches Geoinstitut, Bayreuth, Germany: "High-pressure behaviour of cristobalite: bridging the gap towards the 'seifertite enigma'", 15.05.2015

CHARITON, Stella, Bayerisches Geoinstitut, Bayreuth, Germany: "High-pressure behavior of rhodochrosite ($MnCO_3$) and spherocobaltite ($CoCO_3$)", 13.08.2015

DORFMAN, Susannah, École Polytechnique Fédérale de Lausanne, Earth and Planetary Science Laboratory, Physics Department, Lausanne, Switzerland: "Temperature gradients and chemical partitioning: FIB/TEM analysis of laser-heated diamond anvil cell experiments", 30.04.2015

DURHAM, William, Massachusetts Institute of Technology, Department of Earth, Atmospheric, and Planetary Sciences, Cambridge, USA: "Ice deformation at high P and low T: Developments in planetary applications of lab experiments", 01.10.2015

FAUL, Ulrich, Massachusetts Institute of Technology, Earth, Atmospheric and Planetary Sciences, Cambridge, USA: "Experimental constraints on seismic properties and rheology of the upper mantle: Effects of water and melt", 17.02.2015

FEI, Hongzhan, Bayerisches Geoinstitut, Bayreuth, Germany: "Dislocation mobility in ringwoodite and bridgmanite and implications to mantle rheology", 12.11.2015

GOLABEK, G., Bayerisches Geoinstitut, Bayreuth, Germany: "Modelling the evolution of planetary bodies", *Academy Commission Business Meeting*, 16.04.2015

GUO, Xinzhuan, China University of Geosciences, Wuhan, P.R. China: "Electrical conductivity of albite-(quartz)-water and albite-NaCl-water systems under high pressure and temperature and its implication to the high conductivity anomalies in the continental crust", 31.08.2015

HANSEN, Lars, University of Oxford, Department of Earth Sciences, Oxford, U.K.: "Laboratory constraints on plate boundary formation: Microstructural evolution and mechanisms of strain localization", 29.10.2015

HASHIM, Leila, Université d'Orléans, Institut des Sciences de la Terre d'Orléans, Orléans, France: "Experimental study of natural olivine grain growth: Effects of melt and its interconnectivity", 12.02.2015

JACOB, Damien, Université Lille 1, Unité Matériaux et Transformations, Villeneuve d'Ascq, France: "On the use of precession electron diffraction for minerals characterization: from winning identification to structure refinement", 26.03.2015

JACOBSON, S.A.: Bayerisches Geoinstitut, Bayreuth, Germany: "Importance of the last giant (Moon-forming) impact", *Academy Commission Business Meeting*, 16.04.2015

JENNINGS, Eleanor, University of Cambridge, Department of Earth Sciences, Cambridge, U.K.: "Recycled slabs in the mantle source of continental flood basalts", 12.08.2015

KAUS, Boris, Johannes Gutenberg-Universität Mainz, Institut für Geowissenschaften, Mainz, Germany: "Understanding the physics of the crust and lithosphere through geodynamic modelling", 18.06.2015

KAWAMOTO, Tatsuhiko, Kyoto University, Institute for Geothermal Sciences, Kyoto, Japan: "Importance of being salty: Salinity of fluid inclusions from subduction channels and mantle wedges", 25.08.2015

KOMABAYASHI, Tetsuya, University of Edinburgh, Grant Institute, Edinburgh, U.K.: "Experiment-based thermodynamics of Earth's core", 02.07.2015

LAUMONIER, Mickaël, Bayerisches Geoinstitut, Bayreuth, Germany: "Melt interconnectivity in the upper mantle", 21.10.2015

LIU, Zhaodong, Ehime University, Geodynamics Research Center, Matsuyama, Japan: "Phase relations, elastic properties of $MgSiO_3$ – Al_2O_3 system in Earth's interior", 01.06.2015

MARQUARDT, Katharina, Bayerisches Geoinstitut, Bayreuth, Germany: "Interfaces in olivine aggregates: frequency and impact on grain boundary related processes", 13.07.2015

MASOTTA, Matteo, Bayerisches Geoinstitut, Bayreuth, Germany: "Gas bubbles, eruption dynamics and sulfur release in volcanoes", 09.07.2015

MIYAGI, Lowell, University of Utah, Department of Geology and Geophysics, Salt Lake City, USA: "A mineral physics approach to seismic anisotropy in the deep Earth: Textures in perovskite and post-perovskite", 12.05.2015

MURAKAMI, Motohiko, Tohoku University, Department of Earth and Planetary Materials Science, Sendai, Japan: "Elasticity and thermal properties of Earth's deep materials", 25.06.2015

NAKAMURA, Michihiko, Tohoku University, Department of Earth and Planetary Materials Science, Sendai, Japan: "Shallow-level degassing of silicic magma: An experimental approach", 25.06.2015

NETTELMANN, Nadine, University of California Santa Cruz, Department of Astronomy and Astrophysics, Santa Cruz, USA: "Current prospects and challenges in our understanding of the internal structure of the solar system giant planets", 29.01.2015

NI, Huaiwei, China University of Geosciences, Wuhan, P.R. China: "Transport properties of silicate melts", 17.09.2015

PINTÉR, Zsanett, Bayerisches Geoinstitut, Bayreuth, Germany: "High pressure experimental investigation of the interaction between partial melts of eclogite and mantle along upwelling paths", 10.09.2015

PLESA, Ana-Catalina, Deutsches Zentrum für Luft- und Raumfahrt e.V., Berlin, Germany: "Thermo-chemical evolution and the present-day state of the Martian mantle", 23.04.2015

POZZO, Monica, University College London, Department of Earth Sciences, London, U.K.: "Transport properties of iron and iron mixtures at Earth's core conditions", 22.10.2015

RIVOLDINI, Attilio, Royal Observatory of Belgium, Brussels, Belgium: "Inferences on Mercury's interior structure from geodesy measurements, surface observations, and present day magnetic field", 16.07.2015

ROZEL, Antoine, ETH Zurich, Department of Earth Sciences, Institute of Geophysics, Zurich, Switzerland: "Thermochemical convection, grain size evolution and crust generation in the mantle of the Earth", 26.11.2015

RÜCKRIEMEN, Tina, Deutsches Zentrum für Luft- und Raumfahrt, Institut für Planetenforschung, Berlin, Germany: "Can the Fe-snow regime explain a present-day dynamo in Ganymede's core?", 05.02.2015

SCHMALHOLZ, Stefan, Université de Lausanne, Insitute of Earth Sciences, Lausanne, Switzerland: "Fundamental strain localization mechanisms for ductile shear zones", 05.11.2015

SIERSCH, Nicki Caroline, Bayerisches Geoinstitut, Bayreuth, Germany: "High-pressure behavior of $Mg_2Fe_2O_5$", 13.08.2015

SOLFERINO, Giulio, University College Cork, School of Biological, Earth and Environmental Sciences, Cork, Ireland: "Pallasite formation after a non-destructive impact. An experimental-, image analyses-, and numerical modeling-based study", 08.05.2015

SORBADÈRE, Fanny, Bayerisches Geoinstitut, Bayreuth, Germany: "Behavior of ferric iron (Fe^{3+}) during partial melting of MORB-mantle source", 10.08.2015

TOWNSEND, Joshua, Northwestern University, Department of Earth and Planetary Sciences, Evanston, USA: "First principles investigations of hydrous post-perovskite", 21.05.2015

WANG, Yanbin, University of Chicago, GSECARS, Chicago, USA: "Seeking links between structure and physical properties of silicate melts at high pressure", 20.02.2015

WERNER, Stephanie, University of Oslo, Department of Geosciences, Oslo, Norway: "Planetary time scales, Mars and shergottites", 19.11.2015

WENZ, Michelle, Bayerisches Geoinstitut, Bayreuth, Germany: "Formation and evolution of diamonds constrained through the study of their inclusions", 06.08.2015

WERNER, Stephanie, University of Oslo, Centre for Earth Evolution and Dynamics (CEED), Oslo, Norway: "Planetary time scales, Mars and shergottites", 19.11.2015

4.5 Conference organization

24.03.2015, Vesta workshop, Nürnberg, Germany (G. GOLABEK)

03.-07.05.2015, Joint Assembly 2015, Montreal, Canada: Session VGP23A: 'Perovskites Into the Next Millennium' (C.A. MCCAMMON, A. CHAKHMOURADIAN, P. WOODWARD, R. CARACAS)

22.06.-02.07.2015, 26th General Assembly of the International Union of Geodesy and Geophysics (IUGG) Meeting, Prague, Czech Republic: VS18: 'Rock Physics in Crustal Processes' (T. KATSURA, C.A. MCCAMMON)

22.06.-02.07.2015, 26th General Assembly of the International Union of Geodesy and Geophysics (IUGG) Meeting, Prague, Czech Republic: JS2/JS1/JA3 Physics and Chemistry of Earth and Planetary Interiors with Implications for their Structure, Process and Evolution / Planetary Physics / Geophysical Constraints on Geodynamical Processes, (J. CHEN, I. JACKSON, S. SPEZIALE, T. KATSURA, J. FEINBERG, C.A. MCCAMMON, T. SPOHN, R. GREVE, M. PURUCKER, C. CONSTABLE, G. HELFFRICH, G. HOUSEMANN)

16.-21.08.2015, Goldschmidt 2015, Prague, Czech Republic: Session 14b: 'Crystal Chemistry of Earth and Planetary Materials' (T. BOFFA BALLARAN, J.R. SMYTH)

23.-28.08.2015, 29th European Crystallographic Meeting (ECM29), Rovinj, Croatia: MS-21: 'Advances in high-pressure methods' (L.S. Dubrovinsky, R. Miletich)

28.08.2015, EosFit Satellite Workshop at the 29th European Crystallographic Meeting (ECM29), Rovinj, Croatia (R. ANGEL, T. BOFFA BALLARAN, M. ALVARO, D. PASQUAL)

23.-25.09.2015, 4th Joint Workshop on 'High Pressure Planetary and Plasma Physics', Bayerisches Geoinstitut, Bayreuth, Germany (G. STEINLE-NEUMANN)

27.09.-02.10.2015, European Planetary Science Congress 2015, Nantes, France: Oral and Poster Session 'Numerical Modelling of Planetary Dynamics' (G. GOLABEK)

04.-07.10.2015, GeoBerlin 2015, Berlin, Germany: Session A4-03: 'Properties of Earth Materials and Constraints on Mantle Flow' (H. MARQUARDT, R. FARLA, P. CORDIER)

04.-07.10.2015, GeoBerlin 2015, Berlin, Germany: Session A3-01: 'Meteorites and Planetary Evolution' (H. BECKER, A. GRESHAKE and T. KRUIJER)

04.-07.10.2015, GeoBerlin 2015, Berlin, Germany: Member of the Scientific Committee GeoBerlin 2015 (DGG, GV, DMG), Theme 'Mantle Dynamics'

14.-18.12.2015, American Geophysical Union Fall Meeting, San Francisco, USA: Session P11A: 'Accretion, Differentiation, and Early Planetary Evolution' (H. SAMUEL, G. GOLABEK, D. BARATOUX)

14.-18.12.2015, American Geophysical Union Fall Meeting, San Francisco, USA: Session MR32A: 'Atomic to Planetary Scales: Multiscale Understanding of Planetary Dynamics' (D. MAINPRICE, K. MARQUARDT, S.-i. KARATO, G. HELFFRICH)

14.-18.12.2015, American Geophysical Union Fall Meeting, San Francisco, USA: Session DI21B: 'Slabs in Earth's mantle: Where do they go and how do they interact with the mantle?' (H. MARQUARDT, S. JACOBSEN, M. LONG, M. JADAMEC)

14.-18.12.2015, American Geophysical Union Fall Meeting, San Francisco, USA: Session V21C: 'The Earth's geodynamic carbon cycle: subduction, storage, mirgration, and outgassing' (S. MIKHAIL, A. ROSENTHAL, V. STAGNO, T. LOPEZ)

14.-18.12.2015, American Geophysical Union Fall Meeting, San Francisco, USA: Session MR23: 'Physics and Chemistry of Earth's Deep Mantle and Core' (J. ZHICHENG, B. CHEN, T. KOMABAYASHI, R. SINMYO)

5. Visiting scientists

5.1 Visiting scientists funded by the Bayerisches Geoinstitut

ANGEL, Ross, Università degli Studi di Padova, Dipartimento di Geoscienze, Padova, Italy: 08.-19.06.2015

BALLMER, Maxim, ETH Zurich, Derpartment of Earth Sciences, Institute of Geophysics, Zurich, Switzerland: 26.-28.10.2015

BORCHERT, Manuela, Potsdam, Germany: 18.-21.01.2015

CAI, Nao, Ehime University, Geodynamics Research Center, Matsuyama, Japan: 14.-18.06.2015

CHUNYANG, Li, China University of Geosciences, Wuhan, P.R. China: 27.-31.01.2015

CIALDELLA, Laura, Università degli Studi di Padova, Dipartimento di Geoscienze, Padova, Italy: 31.08.-30.09.2015

CZEKAY, Laura, Universität Tübingen, Germany: 23.02.-03.04.2015

DATCHI, Frédéric, Université Paris 6, IMPMC, Paris, France: 23.-26.09.2015

DOLEJŠ, David, Charles University, Institute of Petrology and Structural Geology, Prague, Czech Republic: 16.-17.09.2015

FAUL, Ulrich, Massachusetts Institute of Technology, Earth, Atmospheric and Planetary Sciences, Cambridge, USA: 16.-18.02.2015

GUO, Xinzhuan, China University of Geosciences, Wuhan, P.R. China: 30.08.-04.09.2015

HASHIM, Leila, Université d'Orléans, Institut des Sciences de la Terre d'Orléans, Orléans, France: 09.-13.02.2015

HANSEN, Lars, University of Oxford, Department of Earth Sciences, Oxford, U.K.: 28.-31.10.2015

HAUBER, Markus, Universität Tübingen, Mineralogie & Geodynamik, Tübingen, Germany: 28.05.2015

JACOB, Damien, Université Lille 1, Unité Matériaux et Transformations, Villeneuve d'Ascq, France: 25.-27.03.2015

KAUS, Boris, Johannes Gutenberg-Universität Mainz, Institut für Geowissenschaften, Mainz, Germany: 17.-19.06.2015

KOMABAYASHI, Tetsuya, University of Edinburgh, Grant Institute, Edinburgh, U.K.: 01.-03.07.2015

LIU, Zhaodong, Ehime University, Geodynamics Research Center, Matsuyama, Japan: 31.05.-04.06.2015

MCWILLIAMS, Stewart, The University of Edinburgh, School of Physics and Astronomy, Edinburgh, U.K.: 22.-25.09.2015

MURAKAMI, Motohiko, Tohoku University, Department of Earth and Planetary Materials Science, Sendai, Japan: 23.-25.06.2015

NAKAMURA, Michihiko, Tohoku University, Department of Earth and Planetary Materials Science, Sendai, Japan: 23.-26.06.2015

NETTELMANN, Nadine, University of California Santa Cruz, Department of Astronomy and Astrophysics, Santa Cruz, USA: 28.-30.01.2015

OHTANI, Eiji, Tohoku University, Department of Earth and Planetary Materials Science, Sendai, Japan: 23.-25.06.2015

PALME, Herbert, Senckenberg Forschungsinstitut und Naturmuseum, Frankfurt/M., Germany: 19.-20.02.2015

PLESA, Ana-Catalina, Deutsches Zentrum für Luft- und Raumfahrt, Berlin, Germany: 22.-24.04.2015

POLEDNIA, Joana, Ruhr-Universität Bochum, Mineralogie – Petrologie, Bochum, Germany: 07.-08.06.2015

POZZO, Monica, University College London, Department of Earth Sciences, London, U.K.: 21.-23.10.2015

RITTER, Xenia, Westfälische Wilhelms-Universität Münster, Institut für Mineralogie, Münster, Germany: 31.05.-01.06.2015

RIVOLDINI, Attilio, Royal Observatory of Belgium, Brussels, Belgium: 15.-17.07.2015

ROZEL, Antoine, ETH Zurich, Derpartment of Earth Sciences, Institute of Geophysics, Zurich, Switzerland: 23.-27.11.2015

RÜCKRIEMEN, Tina, Deutsches Zentrum für Luft- und Raumfahrt, Institut für Planetenforschung, Berlin, Germany: 04.-06.02.2015

SCHMALHOLZ, Stefan, Université de Lausanne, Insitute of Earth Sciences, Lausanne, Switzerland: 04.-06.11.2015

SOLFERINO, Giulio, University College Cork, School of Biological, Earth and Environmental Sciences, Cork, Ireland: 06.-09.05.2015

STEGER, Simon, Universität Wien, Institut für Mineralogie und Kristallographie, Wien, Austria: 30.07.-01.08.2015

THOMAS, Christine, Westfälische Wilhelms-Universität Münster, Institut für Geophysik, Münster, Germany: 12.-13.10.2015

TOWNSEND, Joshua, Northwestern University, Department of Earth and Planetary Sciences, Evanston, USA: 18.-24.05.2015

VAN DRIEL, Jac, University College London, Department of Earth Sciences, London, U.K.: 01.07.-05.09.2015

WAGNER, Johannes, GeoForschungsZentrum Potsdam, Germany: 19.-23.10.2015

WERNER, Stephanie, University of Oslo, Department of Geosciences, Oslo, Norway: 18.-20.11.2015

WOODLAND, Alan, Johann Wolfgang Goethe-Universität, Physikalisch-Chemische Mineralogie, Frankfurt/M., Germany: 13.-15.07.2015

YAMAMOTO, Takafumi, Hiroshima University, Graduate School of Science, Hiroshima, Japan: 01.06.-05.07.2015

5.2 Visiting scientists supported by other externally funded BGI projects

CHAKRABORTY, Sumit, Ruhr-Universität Bochum, Institut für Geologie, Mineralogie und Geophysik, Bochum, Germany: 12.-14.11.2015 (DFG ^{*B})

DORFMAN, Susannah, École Polytechnique Fédérale de Lausanne, Earth and Planetary Science Laboratory, Lausanne, Switzerland: 29.04.-01.05.2015 (DFG [*B])

HAUBER, Stefanie, Universität Jena, Germany: 01.09.-31.10.2015 (DFG [*B])

IMMOOR, Julia, Universität Kiel, Germany: 01.-02.07.2015 (DFG [*B])

JENNINGS, Eleanor, University of Cambridge, Department of Earth Sciences, Cambridge, U.K.: 11.-13.08.2015 (ERC [*C])

LEIßNER, Lisa, Universität Hamburg, Geowissenschaften, Hamburg, Germany: 07.-08.06.2015 (DFG [*B])

MUKHINA, Elena, KTH Royal Institute of Technology, Stockholm, Sweden: 07.09.-31.12.2015 (DFG [*B])

NARDINI, Livia, Statoil ASA, Norway: 14.-15.06.2015 (DFG [*B])

VALKOVSKII, Gleb, Saint Petersburg State University, Russia: 14.-19.06.2015 (BMBF [*A])

[*A)] BMBF: Bundesministerium für Bildung und Forschung

[*B)] DFG: Deutsche Forschungsgemeinschaft

[*C)] ERC: European Research Council

5.3 Visiting scientists supported by the DFG Core Facility programme

DEMOUCHY, Sylvie, Université Montpellier 2, Géosciences, Montpellier, France: 07.-25.09.2015

FRACZEK, Elisabeth, University of Strathclyde, Institute of Photonics, Glasgow, U.K.: 01.-14.03.2015, 15.-30.10.2015

HULM, Walter, TU München, Forschungs-Neutronenquelle Heinz Maier-Leibnitz (FRM II), Garching, Germany: 10.-11.12.2015

LINSLER, Stefan, Leibniz Universität Hannover, Institut für Mineralogie, Hannover, Germany: 10.-17.05.2015

NAMUR, Olivier, Leibniz Universität Hannover, Institut für Mineralogie, Hannover, Germany: 10.-17.05.2015

ORTIZ PEREZ, David, Universitdad CEU San Pablo, Facultad de Farmacia, Boadilla del Monte, Spain: 01.-11.07.2015

PONCET, Melissa, Université Paris-Est Marne-la-Vallée, Laboratoire Géomatériaux et Environnement, Marne-la-Vallée, France: 16.-27.03.2015

SOFER, Zdenek, University of Chemistry and Technology, Prague, Czech Republic: 18.-20.11.2015

THOMSON, Andrew, University College London, Department of Earth Sciences, London, U.K.: 29.03.-02.04.2015

UENVER-THIELE, Laura, Johann Wolfgang Goethe-Universität, Physikalisch-Chemische Mineralogie, Frankfurt/M., Germany: 21.-27.11.2015

WOODLAND, Alan, Johann Wolfgang Goethe-Universität, Physikalisch-Chemische Mineralogie, Frankfurt/M., Germany: 28.09.-02.10.2015, 21.-27.11.2015

5.4 Visitors (externally funded)

ANTLAUF, Mathis, TU Bergakademie Freiberg, Institut für Anorganische Chemie, Freiberg, Germany: 29.11.-04.12.2015

BUHRE, Stephan, Johannes Gutenberg-Universität Mainz, Institut für Geowissenschaften, Mainz, Germany: 13.05.2015

CHANG, Jia, China University of Geosciences, Wuhan, P.R. China: 19.10.-31.12.2015

DOBSON, David, University College London, Department of Earth Sciences, London, U.K.: 30.03.-02.04.2015

DOLEJŠ, David, Charles University, Institute of Petrology and Structural Geology, Prague, Czech Republic: 23.-27.02.2015, 15.-16.06.2015, 19.-22.07.2015

DUCHOSLAV, Marguerita, Universität Tübingen, FB Mineralogie & Geodynamik, Arbeitsgruppe Petrologie, Tübingen, Germany: 19.-20.02.2015

DURHAM, William, Massachusetts Institute of Technology, Earth, Atmospheric and Planetary Sciences Department, Cambridge, USA: 23.-25.03.2015

FEI, Hongzhan, Bayerisches Geoinstitut, Bayreuth, Germany: 02.-13.08.2015

FUJINO, Kiyoshi, Ehime University, Geodynamics Research Center, Matsuyama, Japan: 21.-25.08.2015

IRIFUNE, Tetsuo, Ehime University, Geodynamics Research Center, Matsuyama, Japan: 24.08.2015, 28.08.2015

KAWAMOTO, Tatsuhiko, Kyoto University, Institute for Geothermal Sciences, Kyoto, Japan: 21.-28.08.2015

KOZLENKO, Denis, Frank Laboratory of Neutron Physics, Joint Institute for Nuclear Research, Dubna, Russia: 01.-09.06.2015

LEIßNER, Lisa, Universität Hamburg, Geowissenschaften, Hamburg, Germany: 09.-11.09.2015

LICHTENBERG, Tim, ETH Zurich, Derpartment of Physics, Institute for Astronomy, Zurich, Switzerland: 09.-12.09.2015

LOURENÇO, Diogo, ETH Zurich, Department of Earth Sciences, Institute of Geophysics, Zurich, Switzerland: 09.-13.09.2015

LUKIN, E., Frank Laboratory of Neutron Physics, Joint Institute for Nuclear Research, Dubna, Russia: 23.-27.11.2015

MACKWELL, Stephen, Lunar and Planetary Institute, Houston, USA: 03.-09.07.2015

MASHINO, Izumi, Tohoku University, Department of Earth and Planetary Materials Science, Sendai, Japan: 27.10.-24.11.2015

MEIER, Thomas, Universität Leipzig, Fakultät für Physik und Geowissenschaften, Leipzig, Germany: 26.06.2015

MIYAGI, Lowell, University of Utah, Department of Geology and Geophysics, Salt Lake City, USA: 10.-14.05.2015

NI, Huaiwei, China University of Geosciences, Wuhan, P.R. China: 01.08.-30.09.2015

PRESCHER, Clemens, Universität zu Köln, Institut für Geologie und Mineralogie, Abteilung Kristallographie, Köln, Germany: 01.-02.10.2015

RUDLOFF, Jennifer, Universität Frankfurt/Main, Institut für Geowissenschaften, Mineralogie, Frankfurt/M., Germany: 13.-17.04.2015

SAVITSKI, Vasili, University of Strathclyde, Institute of Photonics, Glasgow, U.K.: 01.-04.03.2015

SCHWARZ, Ulrich, Max-Planck-Institut für Chemische Physik fester Stoffe, Dresden, Germany: 27.-29.05.2015

SIMONOVA, Daria, Institute of Experimental Mineralogy, Chernogolovka, Moscow region, Russia: 01.07.-22.08.2015

SMYTH, Joseph R., University of Colorado at Boulder, Department of Geological Sciences, Boulder, USA: 09.-20.02.2015, 12.-15.08.2015

SPIVAK, Anna, Institute of Experimental Mineralogy, Chernogolovka, Moscow region, Russia: 01.07.-13.08.2015

UENVER-THIELE, Laura, Johann Wolfgang Goethe-Universität, Physikalisch-Chemische Mineralogie, Frankfurt/M., Germany: 13.-15.07.2015

VOLKOVA, Yana, Ural State University, Ekaterinburg, Russia: 15.-25.01.2015

WANG, Yanbin, University of Chicago, GSECARS, Chicago, USA: 20.03.2015

YANG, Xiaozhi, Nanjing University, School of Earth Sciences and Engineering, Nanjing, P.R. China: 10.09.-07.11.2015

ZAKHARCHENKO, Egor, Institute of Experimental Mineralogy, Chernogolovka, Moscow region, Russia: 01.07.-13.08.2015

ZHANG, Li, University of Colorado at Boulder, Department of Geological Sciences, Boulder, USA: 14.-28.02.2015

ZAKHAROV, Boris, Novosibirsk University, Department of Solid State Chemistry, Novosibirsk, Russia: 05.-07.10.2015

ZHANG, Li, China University of Geosciences, Wuhan, P.R. China: 01.08.-31.12.2015

6. Additional scientific activities

6.1 Theses

Ph.D. theses

BEYER, Christopher: Geobarometry, phase relations and elasticity of eclogite under conditions of Earth's upper mantle.

BYKOVA, Elena: Single-crystal X-ray diffraction at extreme conditions in mineral physics and material sciences.

CERNOK, Ana: Effect of pressure on polymorphism amongst tetrahedral SiO_2 phases: case of coesite and cristobalite.

VOGEL, Antje-Kathrin: Siderophile element partitioning at high pressures and temperatures – implications for core formation processes.

M.Sc. theses

CHARITON, Stella: High-pressure behavior of rhodochrosite ($MnCO_3$) and spherocobaltite ($CoCO_3$).

PINTÉR, Zsanett: High pressure experimental investigation of the interaction between partial melts of eclogite and mantle along upwelling paths.

SIERSCH, Nicki: High-pressure behavior of $Mg_2Fe_2O_5$.

WENZ, Michelle: Formation and evolution of diamonds constrained through the study of their inclusions.

6.2 Honours and awards

KATSURA, Tomoo — was appointed as a teaching guest professor at the *Department of Geosciences* at Tohoku University/Sendai, Japan starting from 01.10.2015. Professor Katsura will give individual lectures in Sendai as part of his duties as guest professor. Tohoku University is a partner within the DFG international research training graduate school "Deep Earth Volatile Cycles" (Prof. D. Frost)

ISMAILOVA, Leyla — a PhD student supervised by Prof. L. Dubrovinsky and Prof. N. Dubrovinskaia, was honored at the *Annual International Seminar of Experimental Mineralogy, Petrology, and Geochemistry* in Moscow in April 2015 for the best lecture in the session *Mineral Equilibrium at High PT*

6.3 Editorship of scientific journals

DUBROVINSKY, Leonid	Member, Editorial Board of the Journal of High Pressure Research
KATSURA, Tomoo	Associate Editor "Reviews of Geophysics"
KEPPLER, Hans	Editorial Board "Contributions to Mineralogy and Petrology"
MCCAMMON, Catherine	Chief Editor and Managing Editor "Physics and Chemistry of Minerals" Advisory Editor "Springer Briefs in Earth Sciences"
MIYAJIMA, Nobuyoshi	Associate Editor "European Journal of Mineralogy"

6.4 Membership of scientific advisory bodies

DUBROVINSKY, Leonid	Co-Chair of SIG "Crystallography at extreme conditions" of the European Crystallography Union Member, Review Panel for allocation of beam-time at ESRF Member, Review Panel of Canadian Light Source Member, Review Panel of SPRING8 Chair, Subcomission on Spectroscopy, Diffraction, and new Instrumentations in Mineral Physics of the International Mineralogical Association Member, Deep Carbon Observatory Scientific Steering Committee Member, Review Panel of PETRA III
FROST, Dan	Member of the council of the European Association of Geochemistry (EAG) - (Chair of the communications committee) Member, Geochemical Fellows Selection Committee (EAG-GSA) Member of the Scientific Committee for Goldschmidt 2015 Member of the Elements Executive Committee
Keppler, Hans	Member, Committee ANR CES 31 for subatomic physics, sciences of the universe, structure and history of the Earth, Agence National de Recherche, Paris Member, Abraham Gottlob Werner Medal Committee, German Mineralogical Society (DMG)

	Member, Commission for Research of Bayreuth University (Präsidialkommission für Forschung und wissenschaftlichen Nachwuchs) Member, German National Academy of Sciences (Leopoldina) Member, Bavarian Academy of Sciences Member, Deep Carbon Observatory Scientific Steering Committee Member, Alexander von Humboldt Foundation Selection Panel for Humboldt Awardees
McCammon, Catherine	Past-President, Volcanology, Geochemistry & Petrology Section of the American Geophysical Union Chair, Nominations Committee, Volcanology, Geochemistry & Petrology Section of the American Geophysical Union Member, Affiliation and Engagement Task Force of the American Geophysical Union Member, Centennial Task Force of the American Geophysical Union Member, Governance Committee of the American Geophysical Union Chair, Bunsen Medal Committee, European Geosciences Union Chair, Sub-committee “Earth’s Deep Interior” of the Commission of the Physics of Minerals, International Mineralogical Association Member, IASPEI/IAVCEI/IAGA Commission on Physics and Chemistry of Earth Materials

7. Scientific and Technical Personnel

Name		Position	Duration in 2015	Funding source
ADAMS, Andrea	B.Sc.	Student. Hilfskraft	from 15.04.	UBT[2]
ARATO, Robert	M.Sc.	Wiss. Mitarbeiter		DFG
ARMSTRONG, Katherine	M.Sc.	Wiss. Mitarbeiterin	from 01.02.	DFG
AUDÉTAT, Andreas	Dr.	Akad. Rat		BGI
BEYER, Christopher	M.Sc.	Wiss. Mitarbeiter		DFG
BLAHA, Stephan	M.Sc.	Wiss. Mitarbeiter	to 31.07.	DFG
BÖHM, Ulrich		Mechaniker		BGI
BOFFA BALLARAN, Tiziana	Dr.	Akad. Oberrätin		BGI
BOLLINGER, Caroline	Dr.	Wiss. Mitarbeiterin	to 14.09.	BGI/VP
		Forschungsstipendiatin	from 15.09.	AvH
BUCHEN, Johannes	Dipl.-Min.	Wiss. Mitarbeiter		DFG
BUCHERT, Petra		Fremdsprachen-sekretärin		BGI
BYKOV, Maxim	Dr.	Wiss. Mitarbeiter	from 01.03.	DFG
BYKOVA, Elena	Dr.	Wiss. Mitarbeiterin		BMBF/ DFG
CERANTOLA, Valerio	M.Sc.	Stipendiat,	to 30.04.	UB e.V.
		Wiss. Hilfskraft	to 30.04.	DFG
CHARITON, Stella	M.Sc.	Wiss. Mitarbeiterin	from 01.10.	DFG
CHAUDHARI, Alok	B.Sc.	Student. Hilfskraft		UBT[2]
CHUST, Thomas	Dipl. Geophys.	Wiss. Mitarbeiter	to 30.04.	DFG
DE VRIES, Jellie	Dr.	Wiss. Mitarbeiterin	to 30.06.	EU
DOBSON, David	Prof.	Forschungspreisträger	20.07.-11.09.	AvH
DRUZHBIN, Dmitry	M.Sc.	Wiss. Mitarbeiter		DFG
DUBROVINSKY, Leonid	Apl. Prof. Dr.	Akad. Direktor		BGI
DURHAM, William	Prof.	Forschungspreisträger	19.08.-20.11.	AvH
EL GORESY, Ahmed	Prof. Dr.			BGI/VP[1]
EMILIEN, Joanna	M.Sc.	Nebenberufliche	to 31.03.	BGI
		Wiss. Hilfskraft	from 01.04.	UBT[2]
FARLA, Robert	Dr.	Forschungsstipendiat		AvH
FEI, Hongzhan	Dr.	Wiss. Mitarbeiter	from 01.10.	DFG
FISCHER, Heinz		Mechaniker		BGI
FISCHER, Nicole	ROI	Verwalt. Beamtin		BGI
FROST, Daniel	Prof. Dr.	Stellvertr. Leiter	to 30.09.	BGI
		Leiter	from 01.10.	BGI
GOLABEK, Gregor	Prof. Dr.	Professor	from 09.03.	BGI

GOLLNER, Gertrud		Chem.-Techn. Assistentin	to 30.06.	BGI
GUO, Haihao	M.Sc.	Stipendiat		CSC
HEIDELBACH, Florian	Dr.	Wiss. Mitarbeiter		DFG
HUANG, Rong	M.Sc.	Wiss. Mitarbeiterin		DFG
IMMOOR, Julia	Dipl.-Geol.	Wiss. Mitarbeiterin	from 01.09.	DFG
ISHII, Takayuki	Dr.	Stipendiat	from 01.04.	JSPS
JABAROV, Sakin	Dr.	Stipendiat	to 30.06.	ANAS
JACOBSEN, Steven	Prof.	Forschungspreisträger	to 08.07.	AvH
JACOBSON, Seth	Dr.	Wiss. Mitarbeiter		EU
JENNINGS, Eleanor	Dr.	Wiss. Mitarbeiterin	from 01.11.	EU
KATSURA, Tomoo	Prof. Dr.	Leiter	to 30.09.	BGI
		Stellvertr. Leiter	from 01.10.	BGI
KAWAZOE, Takaaki	Dr.	Akad. Rat		BGI
KEPPLER, Hans	Prof. Dr.	Professor		BGI
KEYSSNER, Stefan	Dr.	Akad. Oberrat		BGI
KISON-HERZING, Lydia		Sekretärin		BGI
KLASINSKI, Kurt	Dipl.-Ing. (FH)	Techn. Angestellter		BGI
KRAUßE, Detlef	Dipl.-Inform. (FH)	Techn. Angestellter		BGI
KRIEGL, Holger		Haustechniker		BGI
KULIK, Eleonora	Dipl.-Physik-ingenieurin	Wiss. Mitarbeiterin		DFG
KUPENKO, Ilya	Dr.	Wiss. Mitarbeiter		BMBF
KURNOSOV, Alexander	Dr.	Wiss. Mitarbeiter		EU
LAUMONIER, Mickaël	Dr.	Forschungsstipendiat	to 26.10.	AvH
LAURENZ-HEUSER, Vera	Dr.	Wiss. Mitarbeiterin		EU
LI, Yang	B.Sc.	Student. Hilfskraft		DFG
LINHARDT, Sven		Elektrotechniker		BGI
LIU, Zhaodong	Dr.	Wiss. Mitarbeiter	from 01.12.	BGI/VP
MALLIK, Ananya	Dr.	Wiss. Mitarbeiterin	from 03.02.	BGI/VP
MARQUARDT, Hauke	Dr.	Nachwuchs-gruppenleiter		DFG
MARQUARDT, Katharina	Dr.	Akad. Rätin		BGI
MASOTTA, Matteo	Dr.	Forschungsstipendiat	to 30.09.	AvH
		Wiss. Mitarbeiter	from 01.10.	BGI/VP
MELAI, Caterina	B.Sc.	Student. Hilfskraft	15.10.-20.10.	BGI
			21.10.-16.11.	HiWi
			from 17.11.	DFG
MCCAMMON, Catherine	Dr.	Akad. Direktorin		BGI
MIYAJIMA, Nobuyoshi	Dr.	Akad. Rat		BGI

MUKHINA, Elena	M.Sc.	Stipendiatin	from 07.09.	DAAD
MYHILL, Robert	Dr.	Wiss. Mitarbeiter	from 15.01.	EU
NJUL, Raphael		Präparator		BGI
OVSYANNIKOV, Sergey	Dr.	Wiss. Mitarbeiter		DFG
PAKHOMOVA, Anna	Dr.	Wiss. Mitarbeiterin	to 31.08.	DFG
			from 01.09.	BGI/VP
PETIGIRARD, Sylvain	Dr.	Forschungsstipendiat	to 30.09.	AvH
		Wiss. Mitarbeiter	from 01.10.	DFG
PINTÉR, Zsanett	M.Sc.	Nebenberufliche Wiss. Hilfskraft	01.12.-31.12.	EU
POLEDNIA, Joana	M.Sc.	Wiss. Mitarbeiterin	from 15.10.	DFG
POMMIER, Anne	Prof.	Forschungs-preisträgerin	15.06.-12.09.	AvH
POSNER, Esther	M.Sc.	Wiss. Mitarbeiterin		DFG
POTAPKIN, Vasily	Dr.	Wiss. Mitarbeiter	from 05.08.	DFG
POTZEL, Anke		Chem.-Techn. Assistentin		BGI
RAMMING, Gerd		Elektroniker		BGI
RAUSCH, Oliver		Mechaniker		BGI
ROSENTHAL, Anja	Dr.	Wiss. Mitarbeiterin	to 08.05.	EU
			09.05.-31.10.	UBT[2]
			from 01.11.	DFG
RUBIE, David C.	Prof. Dr.	Professor		EU
SCHARFENBERG, Romina	B.Sc.	Sekretärin		BGI
SCHULZE, Hubert		Präparator		BGI
SCHULZE, Kirsten	M.Sc.	Wiss. Mitarbeiterin		DFG
SEROVAISKII, Aleksandr	M.Sc.	Stipendiat	to 26.02.	DAAD
SHCHEKA, Svyatoslav	Dr.	Wiss. Mitarbeiter		DFG
SHI, Lanlan	M.Sc.	Wiss. Mitarbeiterin	to 10.09.	DFG
SIERSCH, Nicki	B.Sc.	Student. Hilfskraft	to 30.09.	UBT[2]
	M.Sc.	Wiss. Mitarbeiterin	from 01.11.	DFG
SINMYO, Ryosuke	Dr.	Wiss. Mitarbeiter	to 15.07.	DFG
SORBADERE, Fanny	Dr.	Forschungsstipendiatin	to 31.08.	AvH
STEINLE-NEUMANN, Gerd	Dr.	Akad. Oberrat		BGI
THIELMANN, Marcel	Dr.	Wiss. Mitarbeiter	from 01.09.	BGI/VP
TRENZ, Ulrike		Biol.-Techn. Assistentin		BGI
ÜBELHACK, Stefan		Mechaniker		BGI
VLCEK, Vojtech	M.Sc.	Wiss. Mitarbeiter		DFG

WAGLE, Fabian	M.Sc.	Wiss. Mitarbeiter		DFG
WALTE, Nicolas	Dr.	Wiss. Mitarbeiter		BMBF
WANG, Lin	M.Sc.	Wiss. Mitarbeiter		DFG
WENZ, Michelle	B.Sc.	Student. Hilfskraft	to 14.10.	BGI
WIESNER, Dorothea		Techn. Assistentin	from 07.10.	BGI
YOSHIOKA, Takahiro	M.Sc.	Wiss. Mitarbeiter	to 30.09.	UBT[2]
			from 01.10.	DFG
ZAREI, Alireza	B.Sc.	Student. Hilfskraft	from 20.10.	DFG
ZHANG, Daohan	M.Sc.	Stipendiat		CSC

Abbreviations/explanations:

ANAS	Azerbaijan National Academy of Sciences
AvH	Alexander von Humboldt Foundation
BGI	Staff Position of Bayerisches Geoinstitut
BGI/VP	Visiting Scientists' Program of Bayerisches Geoinstitut
BMBF	Federal Ministry of Education and Research
CSC	Chinese Science Council
DAAD	German Academic Exchange Service
DFG	German Science Foundation
EU	European Union
HiWi	Hilfskraftmittel BGI
JSPS	Japanese Society for the Promotion of Science
UB e.V.	Universität Bayern e.V.
UBT	Universität Bayreuth

[1] partially funded by the Visiting Scientists' Program of Bayerisches Geoinstitut

[2] Profilfeld Hochdruckforschung

Index